Mathematical Modelling of Metabolism and Acidity in Cancer

Jessica Buono McGillen

St Catherine's College

University of Oxford

A thesis submitted for the degree of

Doctor of Philosophy

Hilary Term 2014

Mathematical modelling of metabolism and acidity in cancer

Jessica Buono McGillen
St Catherine's College
University of Oxford
Hilary Term 2014

A thesis submitted for the degree of Doctor of Philosophy

Abstract

Human cancers exhibit the common phenotype of elevated glycolytic metabolism, which causes acidification of the tissue microenvironment and may facilitate tumour invasion. In this thesis, we use mathematical models to address a series of open problems underlying the glycolytic tumour phenotype and its attendant acidity.

We first explore tissue-scale consequences of metabolically-derived acid. Incorporating more biological detail into a canonical model of acidity at the tumour-host interface, we extend the range of tumour behaviours captured by the modelling framework. We then carry out an asymptotic travelling wave analysis to express invasive tumour properties in terms of fundamental parameters, and find that interstitial gaps between an advancing tumour and retreating healthy tissue, characteristic of aggressive invasion and comprising a controversial feature of the original model, are less significant under our generalised formulation.

Subsequently, we evaluate a potential role of lactate—historically assumed to be a passive byproduct of glycolytic metabolism—in a perfusion-dependent metabolic symbiosis that was recently proposed as a beneficial tumour behaviour. Upon developing a minimal model of dual glucose-lactate consumption *in vivo* and employing a multidimensional sensitivity analysis, we find that symbiosis may not be straightforwardly beneficial for our model tumour. Moreover, new *in vitro* experiments, carried out by an experimental collaborator, place U87 glioblastoma tumours in a weakly symbiotic parameter regime despite their clinical malignancy. These results suggest that intratumoural metabolic cooperation is unlikely to be an important role for lactate.

Finally, we examine the complex pH regulation system that governs expulsion of metabolically derived acid loads across tumour cell membranes. This system differs from the healthy system by expression of only a few key proteins, yet its dynamics are non-intuitive in the crowded and poorly perfused *in vivo* environment. We systematically develop a model of tumour pH regulation, beginning with a single-cell scenario and progressing to a spheroid, within a Bayesian framework that incorporates information from *in vitro* data contributed by a second experimental collaborator. We predict that a net effect of pH regulation is a straightforward transmembrane pH gradient, but also that existing treatments are unable to disrupt the system strongly enough to cause tumour cell death.

Taken together, our models help to elucidate previously unresolved features of glycolytic tumour metabolism, and illustrate the utility of a combined mathematical, statistical, and experimental approach for testing biological hypotheses. Opportunities for further investigation are discussed.

For my parents.

Acknowledgements

I would like to extend heartfelt thanks to Professor Philip Maini, Dr. Eamonn Gaffney, and Dr. Natasha Martin, for being the best supervisors anyone could hope for. I have benefitted immensely from their wisdom, care, patience, and high standards, and it is an honour to have been their student.

Thank you to my collaborators for helping me to make what I believe are vital connections between mathematics and biological meaning: Dr. Catherine Kelly, Dr. Pawel Swietach, and the group of Professor Victor Pérez-García; and especially to Professor Pérez-García and the University of Castilla-La Mancha for their hospitality.

I could not have come this far without some exceptional teachers over the years. Thanks to Mrs. Gill, who first suggested that I pursue biology, and to my favourite high school teacher, Mr. Prokay, who introduced me to statistics and demanded my best academic effort. Without the example set by Professor Shlomo Ta'asan, I might not have realised how fulfilling a career in mathematical biology could be; and I am privileged to call Professor David Kinderlehrer a mentor and friend.

My experiences in the Systems Biology Doctoral Training Centre and Wolfson Centre for Mathematical Biology have been wonderful, due in no small part to my friends and colleagues. I hope that my friendships with Duncan Palmer*, Struan Murray*, Aidan Russell, and Jonas Schlüter will be lifelong. It has been a pleasure sharing an office with Aaron Lim, Gabriel Rosser, Louise Dyson, Suruchi Bakshi, Abdullah Al-Shammari, Alhaji Cherif, Jochen Kursawe, Linus Schumacher, and Jackie Liao (and honourary office-mate Deborah Markham)—thanks to them for the fun times and tea trains.

It is difficult to express how grateful I am to my family for their unfailing support. My sister, Steff, is the most caring person I know, makes me laugh so hard I can't breathe, and keeps me sane. She is the best (just the best). My mom has been my emotional anchor, for my whole life but especially during these past few years; I could not imagine being without her guidance. And from shape-sorter geometry when I was three to calculus at the dining room table, my dad never missed a chance to impart a mathematical mindset. He has been a constant inspiration to me and it fills me with pride to follow in his footsteps.

Finally, I am very lucky to have found Gregory Ross, whose scientific insight and boundless curiosity make me a better researcher and person.

This work was generously supported by NIH National Cancer Institute grant U54CA143970 and by an Overseas Graduate Scholarship from St. Catherine's College, Oxford.

*These gentlemen have contributed equally to this friendship.

The following publications have resulted from this work:

McGillen JB, Martin NK, Gaffney EA, Maini PK, 2012. Applications of mathematical analysis to tumour acidity modelling. *RIMS Kôkyûroku Bessatsu*, B31: 31-59.

McGillen JB, Gaffney EA, Martin NK, and Maini PK, 2014. A general reaction-diffusion model of acidity in cancer invasion. *Journal of Mathematical Biology*, 68: 1199-1224.

McGillen JB, Kelly CJ, Mártinez-González A, Martin NK, Gaffney EA, Maini PK, and Pérez-García VM. Glucose-lactate metabolic cooperation in cancer: insights from a spatial mathematical model and implications for targeted therapy. Under review.

McGillen JB, Martin NK, Gaffney EA, Swietach P, Maini PK. A spatial continuum model of the tumour pH regulation system in a Bayesian framework. In preparation.

Contents

List of Figures

List of Tables

Glossary

α-cyano-4-hydroxycinnamate (CHC) A selective inhibitor of the monocarboxylate transporter 1 (MCT1) sort. 8, 117, 123

44'-diisothiocyanatostilbene-22'-disulfonic acid (DIDS) An inhibitor of sodium bicarbonate import across cell membranes. 102, 116

5(NN-dimethyl)amiloride (DMA) An inhibitor of sodium/proton exchange across cell membranes. 102

acetazolamide (ATZ) A membrane-permeable inhibitor of carbonic anhydrase activity. 116

activation energy The minimum energy required for initiation of a chemical reaction. 87

aerobic glycolysis Cytosolic conversion of glucose to lactic acid under oxygenated conditions. 2, 135

angiogenesis Growth of new capillary networks from pre-existing vessels. 13, 135

apoptosis Programmed cell suicide. 10

astrocytes Characteristic star-shaped glia in the brain and spinal cord. 135

ATP Adenosine triphosphate; the molecular energy carrier of a cell. 4

buffer therapy Treatment strategy against tumours expressing the glycolytic phenotype whereby a buffer is applied to neutralise tissue acidity. 6, 20

carbonic anhydrase IX (CAIX) An isoform of the carbonic anhydrase family of enzymes which is tethered to the tumour cell membrane facing extracellular space and catalyses the reversible bicarbonate buffering reaction. 11, 83

carcinoma A malignant tumour derived from epithelial cells. 8, 19

catabolism The set of metabolic pathways that break down molecules into small units to release energy in the form of ATP. 2, 17

catalysis Acceleration of a chemical reaction by an enzyme. 11, 126

fibroblasts Type of cell that synthesises the extracellular matrix, the structural framework that supports animal tissues. 10, 135

glioblastoma multiforme The most common and most aggressive malignant primary brain tumour in humans. 13

glutamatergic signalling Activation of multiple intracellular signalling pathways by binding of glutamate. 136

glycolysis Metabolic pathway by which glucose is converted into pyruvate. 2, 54, 131

glycolytic phenotype Constitutive upregulation of aerobic glycolysis in tumour cells. 4, 17, 131

HCT116 A human colon carcinoma cell line. 85

Hepes An artificial buffer. 101

hypoxia Oxygen deprivation. 2, 57

indanesulfonamide A lead compound for designing selective inhibitors of isoforms of the carbonic anhydrase enzyme family. 11

ionophores Lipid-soluble molecules that disrupt transmembrane ion concentration gradients. 10

MDA-MB-468 A human breast cancer cell line. 119

melanoma A malignant human tumour derived from pigment-producing cells in the skin, bowl, and eye. 136

microfluidics A class of experimental devices for precisely manipulating the flow of fluids through microchannels. 136

necrosis Death of cells in living tissue by self-digestion, caused by factors external to the cell or tissue (in contrast to apoptosis). 8, 133

neoplasia A tumour characterised by uncontrolled cell proliferation. 2

normoxia Normal oxygen supply. 10

oncogene A gene that has the potential to cause cancer through mutation or overexpression. 2

oxidative phosphorylation Metabolic pathway by which mitochondria break down nutrients and generate ATP. 2, 54, 84

p53 A tumour suppressor gene involved in the initiation of cell cycle arrest or apoptosis in response to cellular damage or stress. 117

PBS Phosphate buffered saline; a common buffer solution. 70

pH Measure of acidity of an aqueous (water-based) solution, calculated by taking the negative log of the molar concentration of free protons. 6, 20, 49, 83, 108, 133, 171

phenotype An observable physical or biochemical characteristic of a cell or individual. 4

pK$_a$ Negative log of the acid dissociation constant. 85, 108, 134

quiescence An inactive state, for example the resting phase of the cell cycle. 134

somatic evolution The effect of accumulated mutations on the fitness of body cells during the lifetime of an organism (distinct from heritable mutations in sex cells). 4, 18

stroma Connective tissue that supports a tissue or organ, comprised of cellular and acellular components. 51, 135

superfusate Solution in *in vitro* experiments that is flushed over the outside of a cell or spheroid to sustain its activity. 85

U87 A human primary glioblastoma cell line. 15, 70

vasoactive Causing constriction or dilation of blood vessels. 135

Warburg effect Expression of the glycolytic phenotype in cancer cells. 2, 17, 54, 131

xenograft Surgical graft of tissue from one species to another. 8

Chapter 1

Cancer metabolism

History repeats, but science reverberates. —Siddhartha Mukherjee

Cancer presents one of the most daunting challenges facing global health today. Its reach extends across all ages, ethnicities, lifestyles, and socio-economic levels, leaving no human population untouched. In 2008 alone, cancer claimed the lives of 7.6 million people globally (World Health Organisation, www.who.int). Once viewed primarily as a disease of the ageing developed world, roughly 70% of all cancer deaths now occur in resource-poor regions; and worldwide deaths are projected to rise to over 13.1 million in 2030, with developing countries shouldering a disproportionate share of the burden (World Health Organisation, www.who.int).

1.1 A very brief history of oncology

Humanity has always been plagued by cancer; the earliest written record dates to circa 1600 BC in Egypt, on a papyrus that described eight cases of breast tumours and stated, "There is no treatment" (Hajdu et al. 2011). In 400 BC, Hippocrates gave cancer its name: *carcinos*, Greek for "crab", after the shape taken by a solid vascularised tumour under the skin (Mukherjee 2010). For more than two millenia after Hippocrates, medical science was based on the theory of four humours of the body (black and yellow bile, blood, and phlegm), leading to treatment strategies centred on blood-letting and laxatives, and in the 16th and 17th centuries—once dissection of human cadavers became acceptable—many causes for tumours were hypothesised, from acidic lymph fluid to contagious poison (Yalom 1997). However, it was not until the advent of the microscope in the 18th century that modern cancer research begin to take shape. Metastasis (the spread of cancer from its primary site to other locations in the body) was discovered in the mid 19th century (Grange et al. 2002),

and in the same period the humour-centred theory of medicine was finally superceded by a new understanding that the body was composed of tissues which in turn were composed of millions of cells.

During the 1920s, a golden age for biochemical discovery (Koppenol et al. 2011), the nascent field of oncology was transformed by Dr. Otto Heinrich Warburg—an acclaimed German chemist, physician, soldier in the First World War, and Nobel prize-winner (for his discovery of the respiratory enzyme cytochrome *c* oxidase), who was motivated from a young age by an ambition to cure cancer (Krebs 1972). While using quantitative approaches derived from physics and chemistry to investigate neoplasia (abnormal growth) of rat liver carcinoma cells (Koppenol et al. 2011), Warburg discovered that the cells accomplished glucose catabolism (metabolic breakdown for energy), not by converting the nutrient into carbon dioxide and water in the oxygen-dependent mitochondrial pathway of oxidative phosphorylation—as healthy cells do under normal conditions—but by a truncated pathway that converted pyruvate, an intermediate product of glycolysis, into lactic acid in the cytosol. This truncated pathway is independent of oxygen, and hence is commonly utilised by healthy tissue under conditions of hypoxia (oxygen deprivation), such as muscle cells during exercise; but Warburg observed that cancer cells favoured this pathway even in the presence of oxygen (Figure 1.1) (Warburg 1930). This finding led him to propose a metabolism-centred theory of tumourigenesis, translated from the original German by Koppenol et al. (2011):

> "The origin of cancer lies in the anaerobic metabolic component of normal growing cells, which is more resistant to damage than is the respiratory component. Damage to the organism favours this anaerobic component and, therefore, engenders cancer."

Warburg labelled this constitutively active "anaerobic component" as aerobic glycolysis, to differentiate it from non-constitutive, normal use under oxygen deprivation; others have called it the Warburg effect. Initially, Warburg's theory of aerobic glycolysis as a central factor in cancer was well-received and prominent in oncology; but as molecular biology advanced, it was eventually eclipsed by the oncogene revolution of the 1970s and 1980s (Morange 1997), and metabolic perspectives on cancer fell out of favour for several decades. During this time, a gene-centred paradigm developed in which neoplastic transformation was viewed as driven solely by cell-autonomous genotypic alterations (Land et al. 1983, Varmus et al. 2005).

In recent years, however, high-throughput and next-generation sequencing (Stratton et al. 2009, Meyerson et al. 2010, Christoforides et al. 2013) and a wealth of bioinformatics data (Parsons et al. 2008) have revealed that mutations underlying tumourigenesis are far more

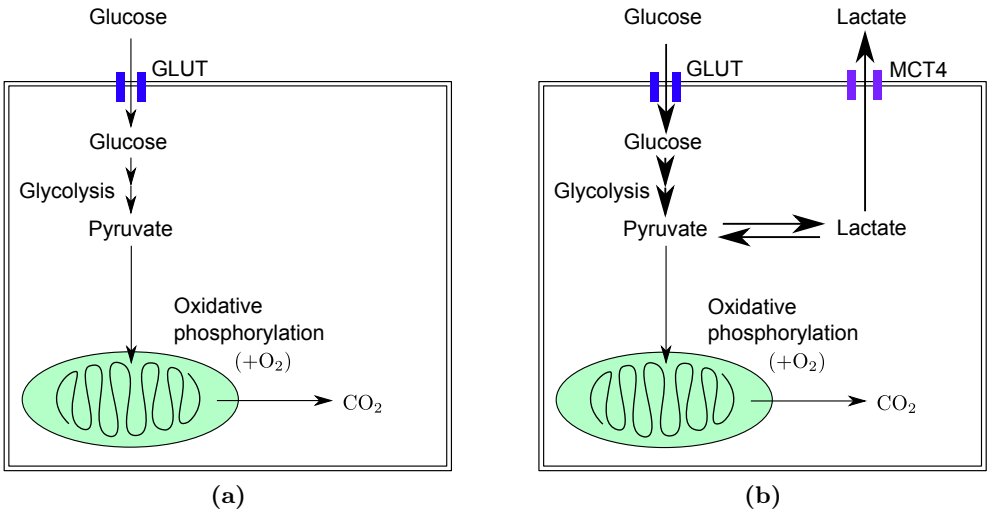

Figure 1.1: The Warburg effect. Healthy cells consume glucose primarily by oxidative phosphorylation in the mitochondria, as in (a), under normoxic conditions, and under hypoxic conditions they temporarily switch to a truncated, oxygen-independent pathway in the cytosol, as in (b). Warburg (1930) observed that tumour cells constitutively exhibit highly enhanced use of the latter pathway, even under normoxic conditions. Glucose is imported across the cell membrane by glucose transporters (GLUT), and lactate is exported by the monocarboxylate transporter MCT4.

numerous and varied than originally supposed, with immense genotypic heterogeneity at every level: across cancer types, tumours of the same type in different patients, different sites in a single patient, and even different regions within a single tumour (Gerlinger et al. 2012, Shibata 2012). These genotypic multitudes have largely resisted enumeration and mutation-specific targeting (Gerlinger et al. 2012); and the central therapeutic paradigm of surgery/chemotherapy/radiation—though incrementally improved by advances in, for example, imaging technology (Frangioni 2008, Majumdar et al. 2010, Bai and Bornhop 2012)—has remained fundamentally unchanged for half a century.

Problems with the surgery/chemotherapy/radiation paradigm abound. First, chemotherapeutic agents are highly cytotoxic poisons that indiscriminantly kill proliferative cells in the body, subjecting the patient to painful side effects and prolonged regimens that are difficult to withstand. Radiotherapy, although administered with more precision than chemotherapy, also causes collateral damage to healthy tissue. Secondly, cytotoxic treatments and surgical resections are costly and labour-intensive, which renders them unattainable to resource-poor populations. Thirdly, the growing spectre of therapeutic resistance (Vaupel et al. 2001) suggests that existing strategies may inadvertently be selecting for, rather than eliminating, aggressive tumours (Gatenby et al. 2009). Broad shifts in both perspective and treatment strategy are needed if profound headway against cancer is to be gained in the coming years.

As it becomes increasingly evident that the oncogene revolution has failed to deliver the

breakthroughs that were anticipated at its dawn, science is now branching out in search of alternative conceptual frameworks: phenotype-driven scaffolds onto which genotypic heterogeneity can be collapsed to build a more comprehensive understanding of cancer. For this, it is returning to metabolism.

1.2 A revitalised role for tumour glucose metabolism

Carcinogenesis is now understood as a dynamic, multi-step reversion of abnormal cells to a more primitive, less ordered state (Volpe 1988, Chang et al. 1995) via the accumulation of genetic and epigenetic alterations that enable them to evolve out from under the many constraints on growth and replication that are placed on normal cells in the body (Vogelstein et al. 1988, Clarke et al. 1990, Anderson et al. 2006). Often termed somatic evolution (Nowell 1976), this process is intricately connected with the tumour microenvironment and produces several phenotypic hallmarks which appear to be common to many or all cancers, and which may be important or even essential for the attainment of invasive capability (Hanahan and Weinberg 2000). Deregulated cellular energetics—or, altered metabolism—is thought to be one of these hallmarks of malignancy (Hanahan and Weinberg 2011).

Accumulation of neoplastic tumour cells causes a progressive harshening of the local tissue environment as conditions become more crowded and cellular waste cannot be cleared away, forcing cells to alter their metabolic pathways in order to optimise energy production and continue dividing (Cairns et al. 2011). Central carbon metabolism, which includes glucose processing, is a vital component of the cellular metabolic network (DeBerardinis and Thompson 2012), and thus Warburg's theory of aerobic glycolysis is now experiencing a renaissance (Ferreira 2010, Koppenol et al. 2011, Lunt and Vander Heiden 2011). However, this renewed interest has raised significant issues, one of which is that the advantages for a tumour cell of diverting glucose from its mitochondria are not fully understood.

For a time, Warburg and others thought that the mitochondria of tumour cells became damaged, such that the Warburg effect—now also called the glycolytic phenotype—provided a compensatory mechanism (Koppenol et al. 2011); but subsequently it was established that tumour mitochondria are typically very active (Zu and Guppy 2004, Fantin et al. 2006, Moreno-Sánchez et al. 2007). The advantages of enhanced glycolysis thus remain controversial, chiefly because the pathway is dramatically less efficient than oxidative phosphorylation at producing ATP (generating 2, rather than 36, ATP per glucose molecule consumed). An intuitive argument would suggest that cells relying heavily on glycolysis proliferate more

slowly than those relying on oxidative phosphorylation, due to this reduced energetic efficiency. But glycolysis, though inefficient in terms of yield, is a *fast* ATP generator (Pfeiffer et al. 2001), and tumour cells exhibit upregulated expression of membrane-bound glucose transporters (GLUT) such that glucose can flood into the cytosol; in other words, tumours appear to substitute pace of glucose processing for efficiency. In fact, elevated glucose flux into tumour cells is sufficiently widespread for exploitation by fluoro-deoxy-D-glucose positron emission tomography (FDG-PET), an imaging technique that uses a radiolabelled analogue of glucose to diagnose cancers and monitor treatments (Jabour et al. 1993, Kherlopian et al. 2008, Jakoby et al. 2011, Vriens et al. 2012, Gillings 2013).

Despite this, it remains arguable whether proliferation under glycolysis is actually faster or slower than under oxidative phosphorylation. Studies have shown that a large portion of ATP in a cell is contributed by oxidative phosphorylation (Zu and Guppy 2004, Rodríguez-Enríquez et al. 2006, Maher et al. 2012), and hence an ATP-centred argument again leads to the idea that enhancing glycolysis slows proliferation. However, it is now understood that ATP likely supports the maintenance of basic cellular functions, rather than being a limiting factor for proliferation. Proliferation does require, though, that cells replicate the entirety of their contents; and glycolytic intermediates are precursors for many of the macromolecules essential to this biosynthesis. Hence, from a biomass-centred perspective, aerobic glycolysis is favourable for proliferation, with mitochondria-generated ATP maintaining basic function underneath this proliferative programme (Hume and Weidemann 1979, Kroemer and Pouyssegur 2008, DeBerardinis et al. 2008, Vander Heiden et al. 2009, Lunt and Vander Heiden 2011, Shlomi et al. 2011).

It is possible that the role of the glycolytic phenotype is to stabilise, rather than accelerate, a proliferative cellular programme—indeed, Ma et al. (2007) found nearly equivalent growth rates in glycolytic and oxidative cells, and Haberkorn et al. (1994) observed a lack of correlation between FDG uptake and proliferation rate—but, in our opinion, the evidence in favour of the biomass-centred justification for enhanced glycolysis is very strong. Even so, ATP-centred assertions that glycolysis leads to slower proliferation continue to surface, for example in (Archetti 2014), indicating that the issue may not be fully resolved.

Beyond all of this, however, lies another important—and incompletely understood—feature of the Warburg effect: its consequences for the tissue microenvironment. These consequences are complex and multi-faceted, and, as we will discuss in the following sections, they form the cornerstones of the biological motivations that drive this thesis.

1.3 The acid-mediated invasion hypothesis

Continual elevation of the glycolytic pathway results in the conversion of large amounts of pyruvate to lactic acid in the cytosols of tumour cells, which the cells then extrude into the surrounding space. Accumulation of metabolically-derived acid in the local tissue environment is toxic, and hence this consequence would seem to render the glycolytic phenotype a detriment. However, Gatenby and Gawlinski (1996) hypothesised that if tumour cells can evolve acid resistance concurrently with the glycolytic phenotype, they may be able to thrive in the toxic tissue environment while neighbouring, acid-vulnerable, healthy cells are killed; and, taking the line of reasoning a step further, this selective destruction of healthy tissue may even be essential for the tumour to overcome spatial constraints and invade (Figure 1.2). This idea, termed the **acid-mediated invasion hypothesis**, has generated steady interest over the past two decades.

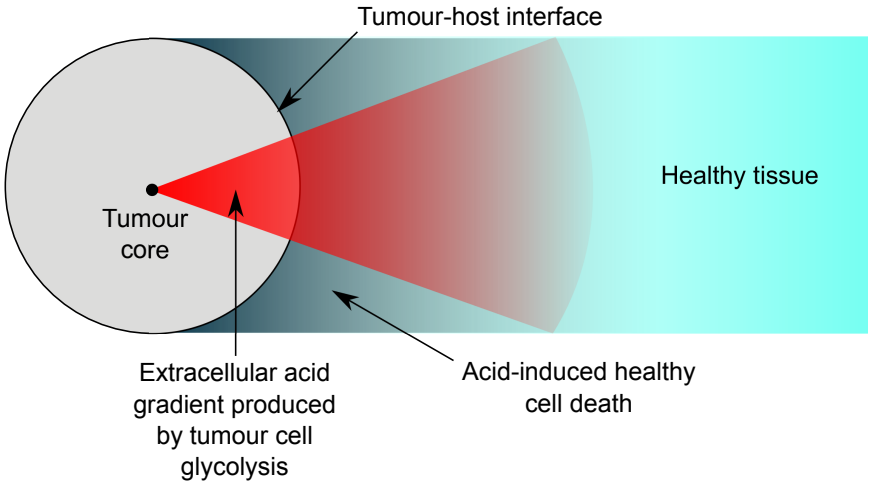

Figure 1.2: Acid-mediated invasion hypothesised by Gatenby and Gawlinski (1996). If tumour cells collectively leach acid due to expressing the glycolytic phenotype, and concurrently have the capacity to resist the toxic effects of acidity, they may be able to invade into space that is opened by the death of neighbouring acid-vulnerable healthy tissue.

Multiple experiments have confirmed the existence of correlations between tumour malignancy and acidity gradients in the local tissue (Rofstad et al. 2006, Estrella et al. 2013), suggesting that the acid-mediated invasion hypothesis plays at least a frequent, if not ubiquitous, role in tumour development. A novel treatment strategy, buffer therapy, has emerged from this hypothesis, and aims to strip a developing tumour of its acid-derived selective advantage by applying a buffer to neutralise the tissue pH (Robey et al. 2009, Silva et al. 2009, Martin et al. 2010, 2011, Alfarouk et al. 2011, Robey and Martin 2011). Pre-clinical

studies with bicarbonate have seen success in reducing metastatic but not primary tumours in mice (Robey and Martin 2011) for reasons possibly relating to tissue density (McGillen et al. 2012) but not fully known. Even so, investigations into buffer therapy are ongoing, and thus it is timely and important to better understand the full implications of the acid-mediated invasion hypothesis.

In theory, it may be the case that the acid effect of the glycolytic phenotype is sufficient to render a tumour invasive, independently of the phenotype also having an explicit impact on proliferation rate. This possibility will be considered in Chapters 2 and 3. The following sections address two further factors underlying the glycolytic phenotype that remain to be elucidated: the role of lactate (Section 1.4) and the complex acid-extrusion system employed by tumours (Section 1.5).

1.4 The role of lactate

The acid-mediated invasion hypothesis implicitly considers lactate to be simply a passive byproduct of the glycolytic phenotype, but recent years have seen advances that necessitate a revision of this view. Experimental evidence is building that tumour cells can take up extracellular lactate and use it as a substrate for oxidative phosphorylation (Cheeti et al. 2006, Pavlides et al. 2009, 2010, Kennedy and Dewhirst 2010). Sonveaux et al. (2008) demonstrated that tumour cells can exhibit an elevated level of expression of the passive monocarboxylate transporter 1 (MCT1), and furthermore that lactate-fueled ATP production in these cells occurs and is gated by MCT1 *in vitro* (Figure 1.3).

On the basis of these results, Sonveaux et al. (2008) put forward the hypothesis that

> "...lactate, the end-product of glycolysis, is the keystone of an exquisite symbiosis in which glycolytic and oxidative tumour cells mutually regulate their access to energy metabolites,"

in a spatially compartmentalised manner dependent upon oxygen gradients in the tumour tissue. Additionally, the authors proposed a novel treatment strategy, which centred on radio-sensitising a tumour by inhibiting MCT1 to force oxygenated cells to consume glucose and thereby starving nearby hypoxic, radiation-invulnerable, cells. Figure 1.4 provides a graphical interpretation of these ideas.

Despite the elegance of the *in vitro* evidence for MCT1-gated lactate consumption that was presented in the paper by Sonveaux et al. (2008), the strength of the *in vivo* evidence for symbiosis and radio-sensitisation has since been questioned, chiefly by Busk et al. (2011).

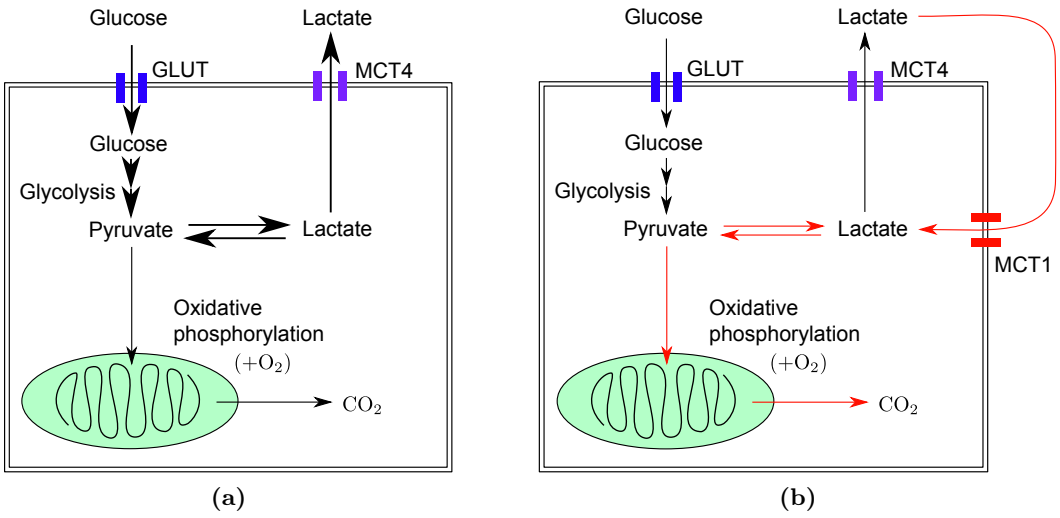

Figure 1.3: Lactate consumption gated by MCT1. Rather than lactate being purely an extruded waste product of the glycolytic phenotype, as in (a), it is now known to be taken back up into cells for oxidative consumption, as in (b). It was shown by Sonveaux et al. (2008) that this uptake is gated by the monocarboxylate transporter MCT1 *in vitro*, whose expression is cell line-dependent. Additionally, glucose is imported by glucose transporters (GLUT) and lactate extruded by the monocarboxylate transporter MCT4.

In particular, the *in vivo* evidence presented by Sonveaux et al. (2008), and discussed further by Feron (2009), is non-quantitative and based mainly on a metabolic outlier—the oxidative cervical cancer line SiHa—as most tumours are highly glycolytic. Furthermore, the symbiosis hypothesis posits a correlation between glucose consumption and hypoxia that is at odds with ubiquitous observations of tumour glycolysis uncoupled from tissue oxygenation (the Warburg effect) (Warburg 1930, 1956, Aisenberg 1961, Rajendran et al. 2004, Gatenby and Gillies 2004, Hanahan and Weinberg 2011).

Busk et al. (2011) carried out an independent experimental test of the symbiosis hypothesis *in vivo*. They examined human xenograft tumours in mice of both SiHa and the more typical, highly glycolytic, head and neck squamous cell carcinoma FaDu_{dd}. Upon treating these tumours with α-cyano-4-hydroxycinnamate (CHC), a selective MCT1 inhibitor, the authors expected—in accordance with the symbiosis hypothesis—that they would observe an immediate reduction in the hypoxia-dependence of glucose consumption (due to oxygenated cells being unable to consume lactate and instead becoming glycolytic), a reduced overall glucose concentration in the tumour tissue, and necrosis induced by glucose starvation over prolonged or repeated treatment. In both treated cancers, the authors indeed observed a reduction, albeit transient, in the hypoxia-dependence of glycolysis, supportive of a disrupted metabolic compartmentalisation; however, they found neither an accompanying reduction in tissue glucose levels nor an increase in necrosis (Busk et al. 2011).

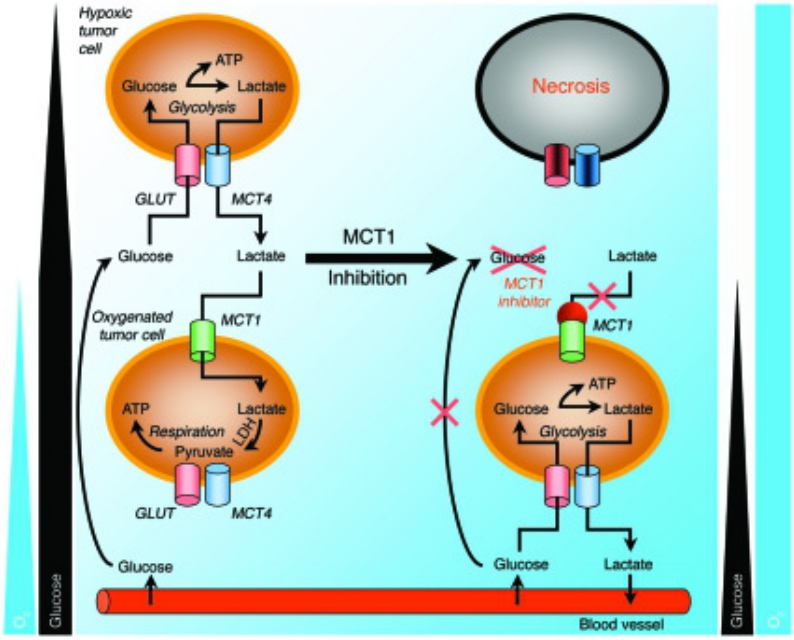

Figure 1.4: Metabolic symbiosis hypothesised by Sonveaux et al. (2008). In a wildtype tumour (left panel), cells in the oxygenated environment near a capillary take up lactate for consumption by oxidative phosphorylation, gated by monocarboxylate transporter 1 (MCT1), while cells in the hypoxic environment of the tumour interior take up glucose for consumption by glycolysis, gated by glucose transporters (GLUT) and producing lactate. This cooperation is thought to preserve glucose for the tumour interior. Sonveaux et al. postulated that inhibiting MCT1 (right panel) would force cells near the capillary to consume glucose instead of lactate, starving interior cells. Image reprinted with permission from the *Journal of Clinical Investigation*.

These conflicting experimental results call into question the therapeutic potential of MCT1 inhibition and emphasise the need for further investigation of the symbiosis hypothesis, in order to clarify the role of lactate in tumour metabolism and acid-mediated invasion. We will pursue this topic in Chapter 4.

1.5 Mechanisms underlying acid resistance in tumours

As was mentioned in Section 1.3, correlations between tumour malignancy and acidic tissue pH (Rofstad et al. 2006, Estrella et al. 2013) have supported the acid-mediated invasion hypothesis. However, the *mechanisms* by which tumour cells might achieve acid resistance—necessary to render acid production a selective advantage—comprise an important open question (Gillies et al. 2012). Tumour acidity is highly complicated, with intricate coupling between intracellular and extracellular pH at the cellular scale (Aisenberg 1961), and we postulate that for comprehensive insight into the impact of the Warburg effect on tumours, one must consider the full complexity, not only of extracellular pH, but also of intracellular

pH. With the notable exception of work by Webb et al. (1999b,c), Al-Husari and Webb (2013a,b), and Al-Husari et al. (2013), most theoretical studies to date have considered only extracellular pH, and hence fall short of this.

Extracellular pH influences the activity of acid/base transporters that regulate intracellular pH (Boron 2004), and intracellular pH in turn plays a multi-faceted role in cellular physiology, such as in the induction of many mediators of cell growth (Pouyssegur et al. 1984, Chambard and Pouyssegur 1986). The result is a great deal of cross-talk between intracellular and extracellular pH (Jean et al. 1985, Stewart et al. 2009), and the intracellular-extracellular pH difference impacts the distribution of membrane-permeant weak acids and bases, including many clinical drugs (Swietach et al. 2009). Importantly, a spatially uniform intracellular pH of close to 7.2 (that is, slightly alkaline) must be tightly maintained for optimal cellular functioning; hence, under conditions of the internal acid load resulting from expression of the glycolytic phenotype, tumour cells must have a strategy for continually disposing of this load and regulating their intracellular pH that remains functional even in increasingly stressed conditions (Hulikova et al. 2011).

While no empirical studies have yet directly analysed the degree of intracellular acidification that can induce cell death in hypoxic tumours (Parks et al. 2013), indirectly applicable data from fibroblasts (which do not express the full suite of intracellular pH-regulation proteins) and tumour lines treated with ionophores in normoxia, gathered by Pouyssegur et al. (1984), Rotin et al. (1986, 1987), and Newell and Tannock (1989), indicate that a reduction in intracellular pH by 0.3 units induces a (reversible) cytostatic growth arrest and a drop below 6.0 induces apoptosis. A promising treatment approach, then, may be to disrupt tumour cells' mechanisms for intracellular pH regulation and thus force their internal acid loads to lethal levels.

The strategy by which a tumour cell regulates its intracellular pH pivots on three interrelated mechanisms. Recent years have seen a thorough characterisation of each of these (Pouyssegur et al. 2006, Swietach et al. 2008, 2009, 2010, Casey et al. 2010, Chiche et al. 2010, Neri and Supuran 2011, Parks et al. 2011, Hulikova et al. 2011, Parks et al. 2013), and they remain of great interest to the oncology community. This is chiefly because the tumour pH regulation system differs from the (far less robust) healthy system by differential expression of only a few key proteins (Parks et al. 2013), and hence there are clear potential targets for therapy if only the complex interactions between the regulatory components can be understood in such a way as to identify points of vulnerability to disruption. We briefly discuss each component here.

The first pH regulation mechanism is extrusion of protons by sodium-proton exchangers. These are the predominant proteins for intracellular pH regulation in healthy cells, and expression levels vary by cell type and oxygen availability (Lucien et al. 2011, Hulikova et al. 2013). In tumour cells, sodium-proton exchangers are thought to directly manage free intracellular protons upon exhaustion of the buffering capacity (Cardone et al. 2005).

Secondly, tumour cells utilise the mechanism—anti-parallel to sodium-proton extrusion—of biochemical buffering of free protons in the cytosol by bicarbonate that is imported from the extracellular space (Swietach et al. 2007, 2008). The exact mechanism of bicarbonate import for intracellular buffering is not fully known, although it is thought to involve sodium-bicarbonate co-transporters (Casey et al. 2010); but, importantly, the reaction is catalysed by cytosolic carbonic anhydrases, such as the isoform CAII. A further connected feature is the catalysis of *extracellular* bicarbonate buffering by carbonic anhydrase IX (CAIX), which is tethered to the cell membrane facing extracellular space and which accelerates the hydration of freely-permeating carbon dioxide as it exits the cell (Swietach et al. 2009, 2010, Hulikova et al. 2011). CAIX expression occurs almost exclusively in tumour cells, making it one of the main points of interest for therapeutic targeting (Parks et al. 2013); however, it is also a subtle enzyme, accelerating the (reversible) bicarbonate buffering reaction by only an order of magnitude. Blocking its activity, for example with indanesulfonamide (Dubois et al. 2011), has seen some early success, but a more precise understanding of its effect on pH regulation would be beneficial (McDonald et al. 2012).

Finally, the passive movement of weak acids and bases across the cell membrane may play an important role in counteracting intracellular acidity. Specifically, the Warburg effect produces lactic acid, whose dissociation leaves lactate anions and free protons in the cytosol which cells must continually extrude; this is accomplished via the co-transport of the two ions by MCT4 (Manning-Fox et al. 2000), a hypoxia-induced isoform of the passive monocarboxylate transporter (MCT) family. Additionally, as discussed in the previous section, re-uptake of extruded lactate by MCT1 for consumption by oxidative phosphorylation may also play a significant role in the tumour metabolic system. Because monocarboxylate transporters are passive, they are sensitive to the dynamic concentrations of both protons and lactate inside and outside cells, and thus their role in the pH regulation system may be non-intuitive. Furthermore, although the pK_a (negative log of the acid dissociation constant) of lactic acid is 3.86, such that it is predominantly dissociated at an intracellular pH of 7.2, a drop in intracellular pH of a full pH-unit would mean a ten-fold increase in the protonated form of lactic acid, to which the cell membrane is permeable (Parks et al. 2013).

The passive movements of both the protonated and dissociated forms of lactic acid must therefore be considered carefully in the context of intracellular pH regulation.

We summarise these three interconnected mechanisms for pH regulation in Figure 1.5. While the mechanisms are well-characterised individually and/or in a single-cell setting, their interactions are not fully understood in the crowded, poorly-perfused environment of a tumour spheroid (Hulikova et al. 2013). In particular, sodium-proton exchange, sodium-bicarbonate co-import, and monocarboxylate transport are all sensitive, at least in part, to both intracellular and extracellular pH, and hence the pH-regulation network is subject to highly nonlinear feedback; this makes prediction of its dynamic response to clinically relevant scenarios immensely difficult. Additionally, some species integral to the system (for example, intracellular lactate) currently cannot be measured experimentally. There is thus great scope for generating novel insight into tumour spheroids by uniting the three mechanisms in a detailed, comprehensive theoretical model of intracellular-extracellular pH regulation. This will be pursued in Chapters 5 and 6.

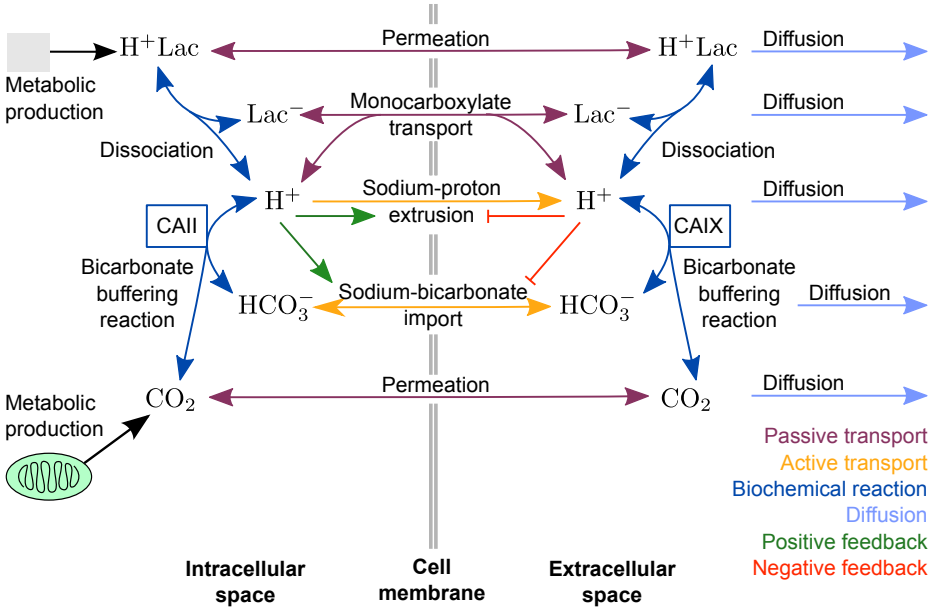

Figure 1.5: The pH regulation system in tumours. Interrelated biochemical mechanisms for handling of metabolically-derived acid loads and maintenance of pH in the intracellular space of a tumour cell, across the cell membrane, and in the local extracellular space of the microenvironment, as detailed in Section 1.5. Species in this system are protonated lactic acid (H^+Lac), lactate ions (Lac^-), free protons (H^+), bicarbonate ions (HCO_3^-), and carbon dioxide (CO_2). The bicarbonate buffering reaction is catalysed by carbonic anhydrase II (CAII) inside the cell, and by membrane-tethered carbonic anhydrase IX (CAIX) in the local extracellular space.

1.6 Mathematical oncology in the literature

Experiments can elucidate features or components of a complicated biological system, but mathematics is uniquely powerful for synthesising experimental insights and forcing explicit consideration of the assumptions involved in a given hypothesis. Translating a biological system into the language of mathematics enables us to distill it to those components thought to be essential for a process of interest, and thus to elucidate cause and effect in a rigorous, testable framework. Furthermore, mathematics is uniquely capable of accommodating the multiscale, highly nonlinear interactions characteristic to many biological systems, and can provide insight where linear or intuitive thinking might lead us astray (Gatenby and Maini 2003).

Modelling frameworks for studying tumour development span an enormous range, from discrete and stochastic (Bellomo et al. 2008), to tissue mechanical—including adhesion effects with cell-cell contact either implicit (Byrne and Chaplain 1996, Chaplain 1996, Byrne and Gourley 1997, Cristini et al. 2003, Frieboes et al. 2006, Friedman 2007, Macklin and Lowengrub 2007) or explicit (Armstrong et al. 2006, Sherratt et al. 2009), stress versus strain (Jones et al. 2000), and a theory of mixtures arising from viewing the tumour as a solid phase embedded in viscous fluid (Chen et al. 2001, Jackson and Byrne 2002, Byrne et al. 2003, Byrne and Preziosi 2003, Roose et al. 2003)—as well as game theoretic (Tomlinson 1997, Gatenby and Vincent 2003), and multiscale (Alarcon et al. 2004, Bellomo and Delitala 2008, Osborne et al. 2010, Lowengrub et al. 2010).

Areas of application are equally diverse, encompassing angiogenesis and vascular growth (Mantzaris et al. 2004, Byrne 2010), gene interactions and their evolution (Komarova et al. 2003, Michor et al. 2004, Spencer et al. 2004, Gatenby et al. 2005, Merlo et al. 2006, Komarova 2006, 2007), and phenotypic evolution (Anderson et al. 2006). Moreover, models of a variety of types have been developed to describe organ-specific cancers, such as colorectal (d'Onofrio and Tomlinson 2007, Mirams et al. 2012, Kershaw et al. 2013) and glioblastoma multiforme (Hatzikirou et al. 2005, Swanson et al. 2008, Rockne et al. 2010).

Clearly, the vastness of the field of mathematical oncology precludes a comprehensive review here. Instead we will focus on the sub-field of continuum modelling of aspects of cancer metabolism. Continuum modelling is a deterministic framework that enables the elucidation of averaged or emergent features in sufficiently large populations—here, populations of tumour and healthy cells in their joint microenvironment. At the tissue level, the microenvironment is comparable to an ecosystem, with tumour and healthy populations competing

for the space and resources necessary for survival or proliferation; this scale-invariant property allows the application of reaction-diffusion and other continuum modelling strategies that were originally used in the study of populations of organisms comprising ecosystems (Pienta et al. 2008).

This long-developed branch of mathematical oncology began with the first mathematical descriptions of early tumour growth by Burton (1966) and Greenspan (1972, 1976); and in the decades since, continuum frameworks have been employed to explore, among many topics, the role of growth factors (Chaplain et al. 1994, Byrne and Gourley 1997, Chaplain et al. 2001), dynamics of migration and metastasis (Anderson et al. 2000, Adam 1996, Pettet et al. 2000), and drug transport (Ward and King 1999, 2003, Wein et al. 2002, Norris et al. 2006). More information can be found in reviews by Araujo and McElwain (2004), Roose et al. (2007), Bellomo et al. (2008), and Byrne (2010).

Problems of tumour metabolism can be framed as reaction-diffusion, and hence continuum mathematical, problems: how do nutrients of interest flow in tumour tissue, and what spatial features develop as a consequence of consumption of these nutrients across the tumour domain? Prior to vascularisation—or, alternatively, locally within a large tumour exhibiting leaky or dysfunctional tumour-induced vasculature—delivery of nutrients into the tissue space becomes diffusion-limited, which presents challenges to a growing tumour (Roose et al. 2007, Gatenby et al. 2007, Gillies and Gatenby 2007, Basanta et al. 2011). The late 20th century was principally concerned with the effects of oxygen and its insufficient perfusion on tumour growth, as evidenced by the continuum models of McElwain and Ponzo (1977), Grossmann (1984), Mueller-Klieser (1984), Arve and Liapis (1988), Degner and Sutherland (1988), and Måaseide and Rofstad (2000). More recently, the spatio-temporal dynamics of glucose and lactate in combination with oxygen have received growing interest. Dual delivery of glucose and oxygen was explored by Casciari et al. (1992), Kirkpatrick et al. (2003), Jiang et al. (2005), and Schaller and Meyer-Hermann (2006), and additional models by McElwain and Morris (1978), Byrne (1999), Smallbone et al. (2005), Venkatasubramanian et al. (2006), Bianchini and Fasano (2009), and Bertuzzi et al. (2007, 2010) have considered the evolution of the tumour boundary in response to these nutrients.

1.7 Thesis overview and aims

To summarise, we see three important unresolved problems in the glycolytic phenotype, now well-established as a widespread and important feature of tumour glucose metabolism. First, what are the consequences of lactic acid production for the tumour microenvironment?

Is acid sufficient to render the glycolytic phenotype a selective advantage without also requiring that replication be enhanced? Secondly, what is the true role of lactate? Can dual consumption of glucose and lactate give rise to spatial cooperative features, and if so, are these important for tumour survival? Thirdly, what are the comprehensive dynamics of the tumour pH regulation system, and what aspects can best be exploited for treatment?

Without resolving these substantial unknowns, we argue that it is impossible to comprehensively understand the tumour metabolic phenotype that they underpin, or to evaluate the acid-mediated invasion hypothesis. The biological aim of this thesis is thus to investigate the above open questions, in order to shed light on these uncertain details and thereby contribute to the advancement of our understanding of altered glucose metabolism in cancer.

In the following chapters, we will develop partial differential equation models to describe each of our three issues in turn. These models, though kept as minimal as possible throughout, are necessarily of increasing complexity, and thus each requires a different approach for characterisation of its behaviour. From a theoretical perspective, then, this thesis can be viewed as an exploration of the range of approaches available across mathematics and statistics for comprehensively understanding the behaviour of biologically motivated continuum mathematical models as they increase in complexity.

In Chapters 2 and 3 we develop a general model of acidity in the tumour-host microenvironment based on a canonical model, and carry out an asymptotic analysis in a travelling wave framework to gain a comprehensive understanding of the fundamental parameter space. We thus demonstrate that our generalised model captures a wider range of tumours behaviours than did the original formulation, and also remains amenable to mathematical analysis. In addition, we use our analytical results to investigate interstitial gaps, a feature of the canonical model formulation that has met with some skepticism in the oncological community, and find that they become smaller and less likely to arise under our generalised model.

In Chapter 4, we develop a model to test whether, in principle, a spatial metabolic symbiosis based on lactate can arise in glioma, and employ a statistics-inspired multivariate sensitivity analysis to gain insight into the model parameter space. We find that metabolic symbiosis is not straightforwardly beneficial for tumour growth under our model formulation. We also present a set of new experiments, carried out in collaboration with an experimentalist, which suggest that U87 glioblastoma tumours do not exhibit strongly symbiotic behaviour. Moreover, we predict that treatments designed to disrupt this symbiosis are unlikely to cause a significant amount of necrosis in the tumour core, although they may increase the extent of oxygenation.

In Chapters 5 and 6, we systematically develop and validate a model of the tumour pH regulation system in a Bayesian framework, beginning with a single-cell modelling scenario and progressing to a spatial description of a tumour spheroid. We incorporate data from an experimental collaborator into our estimation of some of the model parameters and validate our modelling against known experimental dynamics at multiple steps. Subsequently, we predict that the pH regulation system in spheroids is highly sensitive to several parameters which are poorly characterised experimentally. We also find, in agreement with Parks et al. (2013), that protonated lactic acid can play a significant role in pH regulation under large intracellular acid loads. Moreover, upon considering a suite of treatment strategies proposed by Parks et al. (2013), we predict that they are unlikely to disrupt intracellular pH regulation sufficiently to cause cell death. Finally, our model predicts a straightforward "reverse" transmembrane pH gradient in the tumour core, suggesting that extracellular pH may be a valid proxy for the full pH regulation system in coarse-grained models of tumour metabolism.

Finally, in Chapter 7, we review the main findings of this thesis and reflect on some limitations of the modelling approaches we have employed, before suggesting possible ways in which the work can be taken forward in the future.

Chapter 2

A generalised model of acid-mediated tumour invasion

In Chapter 1 we introduced the Warburg effect, a constitutive enhancement of the truncated, oxygen-independent glycolytic pathway for glucose catabolism that comprises one of the best-characterised features of altered metabolism in cancer. A candidate explanation for the prevalence of this feature in tumours is the acid-mediated invasion hypothesis, which proposes that the Warburg effect may give tumour cells a selective advantage over nearby healthy tissue if they exhibit acid resistance concurrently with the acid-producing glycolytic phenotype (visualised in Chapter 1 and reproduced in Figure 2.1 for the reader's convenience).

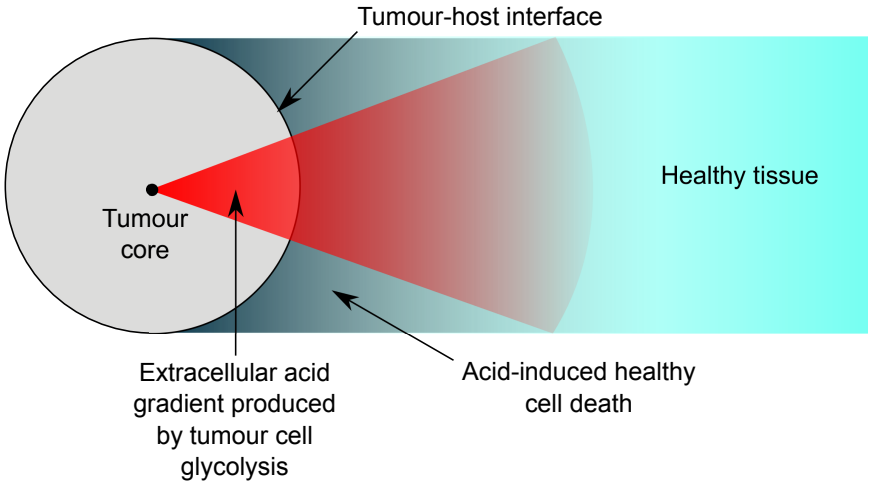

Figure 2.1: Acid-mediated invasion hypothesised by Gatenby and Gawlinski (1996). If tumour cells collectively leach acid due to expressing the glycolytic phenotype, and concurrently have the capacity to resist the toxic effects of acidity, they may be able to invade into space that is opened by the death of neighbouring acid-vulnerable healthy tissue.

The acid-mediated invasion hypothesis is motivated by viewing a tumour as an invasive species experiencing increasingly harsh selective pressures and undergoing somatic evolution within the microenvironment of a healthy population (Nowell 1976, Fidler and Hart 1982, Kallinowski et al. 1988, Vogelstein et al. 1988, Clarke et al. 1990, Gatenby 1991, Pienta et al. 2008); hence, like the systems discussed in Section 1.6, it is amenable to mathematical representation as a reaction-diffusion system at the tissue scale. The first to put the acid-mediated invasion hypothesis into a reaction-diffusion framework were Gatenby and Gawlinski (1996).

2.1 A canonical model of acid-mediated invasion

Restricting their range of consideration to avascular tumours that had acquired the glycolytic phenotype—that is, tumours whose metabolism was uncoupled from oxygen supply—Gatenby and Gawlinski (1996) isolated the consequences of the glycolytic phenotype for invasion at the interface between the growing tumour and the surrounding healthy tissue. Letting $U(X,T)$ denote the density of healthy cells (a function of the spatial variable X in units of centimetres and time T in seconds), $V(X,T)$ the density of tumour cells, and $W(X,T)$ the concentration of extracellular lactic acid in excess of normal tissue acid concentrations, the resulting system of nonlinear partial differential equations presented by Gatenby and Gawlinski (1996) is:

$$\frac{\partial U}{\partial T} = \underbrace{\rho_1 U\left(1-\frac{U}{\kappa_1}\right)}_{\substack{\text{logistic}\\ \text{growth}}} - \underbrace{\delta_1 UW}_{\substack{\text{acid-}\\ \text{mediated}\\ \text{healthy}\\ \text{cell death}}}, \tag{2.1}$$

$$\frac{\partial V}{\partial T} = \underbrace{\rho_2 V\left(1-\frac{V}{\kappa_2}\right)}_{\substack{\text{logistic}\\ \text{growth}}} + \underbrace{\frac{\partial}{\partial X}\left[\Delta_2\left(1-\frac{U}{\kappa_1}\right)\frac{\partial V}{\partial X}\right]}_{\substack{\text{density-limited tumour}\\ \text{cell diffusion}}}, \tag{2.2}$$

$$\frac{\partial W}{\partial T} = \underbrace{\rho_3 V - \delta_3 W}_{\substack{\text{acid production}\\ \text{by tumour cells}\\ \text{and clearance}\\ \text{by vasculature}}} + \underbrace{\Delta_3 \frac{\partial^2 W}{\partial X^2}}_{\substack{\text{chemical}\\ \text{diffusion}\\ \text{of excess}\\ \text{acid}}}. \tag{2.3}$$

Here the subscript '1' represents parameter association with healthy cells, '2' with tumour cells, and '3' with excess extracellular lactic acid. The constants $\kappa_{1,2}$ represent the tissue carrying capacities, δ_1 the rate of acid-mediated healthy cell death, δ_3 the rate of clearance of excess acid by combined buffering and vascular evacuation, $\rho_{1,2}$ the cell proliferation rates, ρ_3 the rate of production of excess acid by tumour cells, Δ_2 the free-space diffusion

coefficient of tumour cells, and Δ_3 the chemical diffusion coefficient of excess acid. A key feature of this model is the density-limited tumour diffusion term in Equation (2.2), the idea being that a healthy tissue operating at full carrying capacity will spatially constrain a tumour unless diminished.

In Gatenby and Gawlinski (1996), numerical solution of Equations (2.1)-(2.3) indicated the capture of two types of behaviour: invasion by a heterogeneous tumour consisting of both healthy and malignant cells, and invasion by a homogeneous tumour killing all healthy cells behind its leading edge; both are reproduced in Figure 2.2. Further, for sufficiently aggressive tumours, the authors predicted the opening of an interstitial gap between advancing malignant cells and regressing healthy cells (visible in Figure 2.2b)—a previously unreported behaviour—and went on to report gaps in *in vitro* specimens of human squamous cell carcinoma (Figure 2.3). This prediction and apparent detection of the interstitial gap has been recognised as an elegant illustration of the benefits of a hybrid mathematical-experimental approach to the study of cancer (Byrne 2010), and the gap could, perhaps, have diagnostic potential as a marker for aggressive tumours.

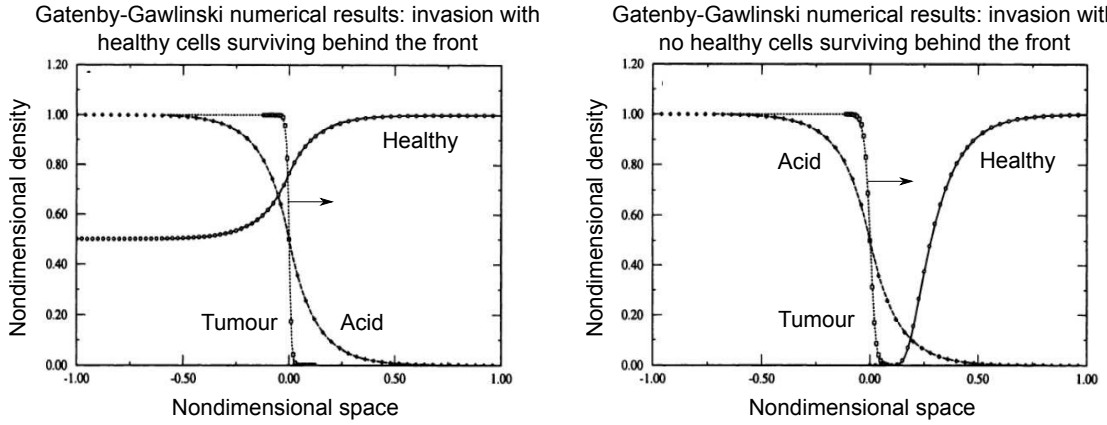

Figure 2.2: Numerical results from Gatenby and Gawlinski (1996). Results presented by Gatenby and Gawlinski (1996) for Equations (2.1)-(2.3) showing (a) invasion that leaves healthy tissue alive behind the advancing tumour front, obtained by setting (in our notation) $d = 0.5$, with a nondimensional tumour wavespeed of 0.0064 and (b) invasion that kills all healthy tissue behind the front, obtained by setting $d = 12.5$, with a nondimensional tumour wavespeed of 0.0128. The latter image also exhibits an interstitial gap between the advancing tumour profile and retreating healthy profile. Other parameter values are (in our notation) $r_2 = 1$, $d = 12.5$, $D = 4 \cdot 10^{-5}$, and $c = 70$. Images reprinted with permission from *Cancer Research*.

We note that Gatenby and Gawlinski (1996) drew a distinction between their observed tumour behaviours which we believe to be too strong; they claimed a bifurcation between

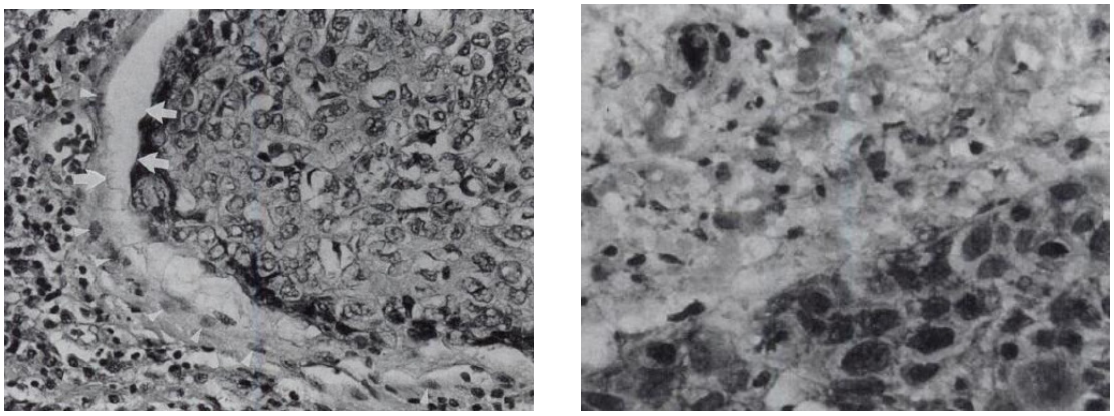

(a) **(b)**

Figure 2.3: Experimental results from Gatenby and Gawlinski (1996). Stained micrographs of the tumour-host interface (large arrows) in (a) formalin-fixed and (b) flash-frozen specimens from human squamous cell carcinomas of the head and neck. A hypocellular gap at the interface (arrowheads) is visible in the fixed specimen and less clearly visible in the unfixed specimen. Images reprinted with permission from *Cancer Research*.

'benign' (Figure 2.2a) and invasive (Figure 2.2b) behaviours according to the parameter d. However, as the 'benign' tumours established invasive travelling waves, we suggest that the bifurcation simply distinguished between two types of invasive behaviour, rather than an invasive from a non-invasive type. Subsequently we will refer to these two behaviours as heterogeneous invasion (as in Figure 2.2a) and homogeneous invasion (as in Figure 2.2b).

The Gatenby and Gawlinski (1996) model is one of a number of studies suggesting that acidity may play an important role in tumour progression (Gillies et al. 2012). If true, this could lead to novel therapeutic strategies. Mentioned briefly in Chapter 1, one such treatment currently in development—buffer therapy—was motivated by the modelling conclusions in Gatenby and Gawlinski (1996) and aims to strip a developing tumour of its selective advantage by neutralising the pH of the microenvironment (Robey et al. 2009, Silva et al. 2009, Martin et al. 2010, Alfarouk et al. 2011, Martin et al. 2011, Robey and Martin 2011).

2.2 Motivations for generalising the canonical model

Despite the elegance of the Gatenby and Gawlinski (1996) model and its success in predicting a novel feature of the microenvironment, some unresolved problems remain. First, in the years since its publication, the gap has been met with skepticism from the experimental community, with some members suggesting informally that it may be an artefact of *in vitro* specimen fixation. To our knowledge, however, no independent experimental verifications

have been published to follow up on this issue, and it may therefore be enlightening to look further into the gap in a mathematical modelling context. Secondly, the goal of Gatenby and Gawlinski (1996) was to provide the first mathematical formulation of the acid-mediated invasion hypothesis, and thus their modelling assumptions are necessarily pared-down and minimal. For the purpose of current applications, however, we argue that these assumptions are *too* restrictive, as they allow consideration of only the most aggressive tumours that arise *in vitro* and thus miss slightly less aggressive tumours that may be relevant in a clinical context. Relaxing some of the model assumptions could enable consideration of these wider tumour scenarios, and also would permit an exploration of the robustness of the modelling framework.

In this chapter we pursue this by augmenting the Gatenby and Gawlinski (1996) model with biologically motivated terms. We then look numerically into the tumour behaviours captured by this extended model. Subsequently, in Chapter 3, we will explore our generalised system analytically, and also examine the parameter conditions governing the occurrence of interstitial gaps, as these were considered an important feature of the Gatenby and Gawlinski (1996) formulation.

2.3 The generalised model

To generalise the Gatenby and Gawlinski (1996) model and explore the sensitivity of the modelling framework to the inclusion of more biological information, we incorporate two new elements. First, we add classical Lotka-Volterra mutual competition (Murray 2002) between healthy and tumour cells for resources needed for growth, which may be postulated to be a relevant feature of the tumour-host interface where the two cell types are in close proximity.

Secondly, we add a term for acid-mediated tumour cell death that parallels that for healthy cells, which we conjecture is biologically realistic as tumours are rarely observed at a pH more acidic than 6.3 (Casciari et al. 1992, Park et al. 1999) and so would not exhibit complete acid resistance even under the most aggressive cases. This term also gives our model the capacity to consider tumours with varying degrees of acid resistance, which again may prove clinically relevant.

Retaining the notation used for Equations (2.1)-(2.3), our reaction-diffusion partial differ-

ential equations are:

$$\frac{\partial U}{\partial T} = \underbrace{\rho_1 U\left(1 - \frac{U}{\kappa_1} - \alpha_2\frac{V}{\kappa_1}\right)}_{\substack{\text{logistic growth with}\\ \text{cellular competition}}} - \underbrace{\delta_1 UW}_{\substack{\text{acid-}\\ \text{mediated}\\ \text{healthy}\\ \text{cell death}}}, \tag{2.4}$$

$$\frac{\partial V}{\partial T} = \underbrace{\rho_2 V\left(1 - \frac{V}{\kappa_2} - \alpha_1\frac{U}{\kappa_2}\right)}_{\substack{\text{logistic growth with}\\ \text{cellular competition}}} - \underbrace{\delta_2 VW}_{\substack{\text{acid-}\\ \text{mediated}\\ \text{tumour}\\ \text{cell death}}} + \underbrace{\frac{\partial}{\partial X}\left[\Delta_2\left(1 - \frac{U}{\kappa_1}\right)\frac{\partial V}{\partial X}\right]}_{\substack{\text{density-limited tumour}\\ \text{cell diffusion}}}, \tag{2.5}$$

$$\frac{\partial W}{\partial T} = \underbrace{\rho_3 V - \delta_3 W}_{\substack{\text{acid production}\\ \text{by tumour cells}\\ \text{and clearance}\\ \text{by vasculature}}} + \underbrace{\Delta_3\frac{\partial^2 W}{\partial X^2}}_{\substack{\text{chemical}\\ \text{diffusion}\\ \text{of excess}\\ \text{acid}}}. \tag{2.6}$$

In these equations, terms repeated from Equations (2.1)-(2.3) carry the same meanings as before, but now δ_2 represents the rate of acid-mediated tumour cell death and $\alpha_{1,2}$ the relative competitive strengths of the two cell types. Values and, where appropriate, order-of-magnitude estimates for our dimensional parameters are listed in Table 2.1. To facilitate comparison with the Gatenby and Gawlinski (1996) system, we employ a density-limited diffusion term rather than an alternative such as contact inhibition (Sherratt 2000, Painter and Sherratt 2003) to capture movement in the interacting cell populations.

Table 2.1: Dimensional parameter values for Equations (2.4)-(2.6).

Parameter	Value	Units	Source
ρ_1	1×10^{-6}	s^{-1}	Gatenby and Gawlinski (1996)
ρ_2	1×10^{-6}	s^{-1}	Gatenby and Gawlinski (1996)
ρ_3	2.2×10^{-17}	$\mathrm{cm}^3\mathrm{s}^{-1}\mathrm{M}$	Martin and Jain (1994)
δ_1	$\mathcal{O}(1)$	$\mathrm{M}^{-1}\mathrm{s}^{-1}$	Gatenby and Gawlinski (1996)
δ_2	$\mathcal{O}(1)$	$\mathrm{M}^{-1}\mathrm{s}^{-1}$	chosen to be $\mathcal{O}(\delta_1)$
δ_3	$\mathcal{O}(10^{-4})$	s^{-1}	Gatenby and Gawlinski (1996)
κ_1	5×10^7	cm^{-3}	Tracqui et al. (1995)
κ_2	5×10^7	cm^{-3}	Tracqui et al. (1995)
Δ_2	2×10^{-10}	$\mathrm{cm}^2\mathrm{s}^{-1}$	Dale et al. (1994)
Δ_3	5×10^{-6}	$\mathrm{cm}^2\mathrm{s}^{-1}$	Lide (2004)
α_1	$\mathcal{O}(1)$	dimensionless	Murray (2002)
α_2	$\mathcal{O}(1)$	dimensionless	Murray (2002)

Letting $\kappa_1 = \kappa_2 = \kappa$ and making the substitutions $u = \frac{U}{\kappa}$, $v = \frac{V}{\kappa}$, $w = \frac{\delta_3 W}{\rho_3 \kappa}$, $t = \rho_1 T$, and $x = \sqrt{\frac{\rho_1}{\Delta_3}} X$ in Equations (2.4)-(2.6) produces the nondimensionalised system

$$u_t = u(1 - u - a_2 v) - d_1 uw, \tag{2.7}$$

$$v_t = r_2 v(1 - v - a_1 u) - d_2 vw + D[(1-u)v_x]_x, \tag{2.8}$$

$$w_t = c(v - w) + w_{xx}, \tag{2.9}$$

where $a_{1,2} = \alpha_{1,2}$, $r_2 = \frac{\rho_2}{\rho_1}$, $d_{1,2} = \frac{\delta_{1,2}\rho_3\kappa}{\rho_1\delta_3}$, $c = \frac{\delta_3}{\rho_1}$, and $D = \frac{\Delta_2}{\Delta_3}$. While Equations (2.4)-(2.6) allow for a choice of scaling different from the one presented here—for example, a scaling which retains the rates of tumour acid production (ρ_3) and acid-mediated tumour cell death (δ_2) as independent parameters—we employ the same nondimensionalisation as that in Gatenby and Gawlinski (1996) to facilitate later comparisons with the Gatenby and Gawlinski (1996) model, now a special case of our generalised model. Values, order-of-magnitude estimates, and some biologically motivated constraints for our nondimensional parameters are listed in Table 2.2. Importantly, we require that $d_2 \leq d_1$ to capture the tumour capacity for acid resistance. The Gatenby and Gawlinski (1996) model is then the limiting case of complete tumour resistance to acid, for which $d_2 = 0$ (and competition is negligible), with the other extreme being a tumour that lacks any resistance to acid ($d_2 = d_1$).

Table 2.2: Nondimensional parameters in Eq (2.7)**-**(2.9)**.** Table of nondimensionalised parameter estimates for all numerical solutions of Equations (2.7)-(2.9) carried out in this chapter. In an absolute sense all parameters are order-of-magnitude estimates due to between-tumour differences and intrinsic experimental error (Fasano et al. 2009), but for our purposes we allow more variation in some parameters than others. Beyond all parameters being non-negative, we impose the constraint that $d_2 \leq d_1$ to capture tumour capacity for acid resistance, and additionally require that $a_1 \neq a_2$ as tumour and healthy cells are unlikely to consume resources with precisely the same efficiency. We do not otherwise immediately restrict a_1 and a_2 as we wish to allow for the possibility of a tumour consuming resources more aggressively ($a_2 > a_1$) or experiencing a cost of acid resistance ($a_2 < a_1$ in cases of low d_2).

Parameter	Value or range	Constraint	Derivation
r_2	1		ρ_2/ρ_1
$d_{1,2}$	$\mathcal{O}(1)$ to $\mathcal{O}(10)$	$d_2 \leq d_1$	$\delta_{1,2} \cdot (\rho_3\kappa)/(\rho_1\delta_3)$
c	$\mathcal{O}(10^2)$		δ_3/ρ_1
D	4×10^{-5}		Δ_2/Δ_3
$a_{1,2}$	$\mathcal{O}(1)$	$a_1 \neq a_2$	$\alpha_{1,2}$

After nondimensionalisation, the spatial domain extends along a one-dimensional ray from the tumour core at $x = -1$ out into the bulk healthy tissue at $x = 1$. We impose zero-flux

boundary conditions at both spatial boundaries, $x = -1$ and $x = 1$, and initial conditions as depicted in Figure 2.4, with a piece-wise linear decreasing tumour density extending out from the core and attaining zero within the domain, an analogous but reflected healthy density, and no excess extracellular acid. These boundary and initial conditions are appropriate for a travelling wave framework, to be discussed in Chapter 3, in which the tumour evolves from an invaded state in the core toward a homogeneous healthy state far from the core.

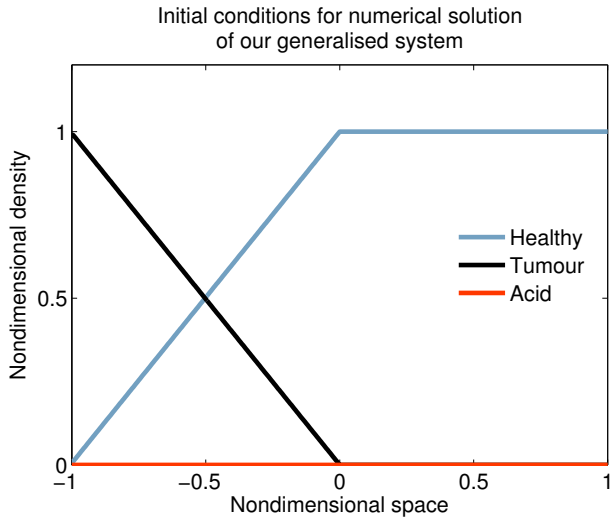

Figure 2.4: Initial conditions for numerical solution of Eq (2.7)-(2.9)**.** Conditions at $t = 0$ for the nondimensional healthy tissue density, u (blue), tumour density, v (black), and excess acid, w (red) in all numerical simulations of Equations (2.7)-(2.9). This imposes a tumour-only population declining from carrying capacity across the left-hand portion of the domain ($x < 0$), representing the tumour core, and a healthy-only population increasing to carrying capacity to the right of the core ($x > 0$), with no excess acid present initially.

Examining the linear stability of our system under spatial and temporal invariance (see Appendix A) indicates the attainable types of tumour behaviour as governed by the model parameters. Equations (2.7)-(2.9) exhibit four equilibrium points, as did the original system (Gatenby and Gawlinski 1996); but whereas the healthy state was globally unstable in the Gatenby and Gawlinski (1996) formulation, leading exclusively to invasive behaviours, it is now conditionally stable in our formulation, allowing both invasive and non-invasive behaviours. The stationary points for Equations (2.7)-(2.9) are:

1. a trivial absence of all species, $(u, v, w) = (0, 0, 0)$, globally unstable;
2. a healthy state, $(u, v, w) = (1, 0, 0)$, linearly unstable if $a_1 < 1$ and stable if $a_1 > 1$;
3. a heterogeneous state, $(u, v, w) = (1 - (a_2 + d_1)\tilde{v}, \tilde{v}, \tilde{v})$, with u, v, and $w > 0$,

where $\tilde{v} = \dfrac{1 - a_1}{1 - a_1 a_2 + \frac{d_2}{r_2} - a_1 d_1}$,
linearly unstable if $d_1 > 1 + \frac{d_2}{r_2} - a_2$ and stable if $0 < d_1 < 1 + \frac{d_2}{r_2} - a_2$; and

4. a homogeneous tumour state, $(u, v, w) = \left(0, \frac{1}{1+\frac{d_2}{r_2}}, \frac{1}{1+\frac{d_2}{r_2}}\right)$,
linearly unstable if $0 < d_1 < 1 + \frac{d_2}{r_2} - a_2$ and stable if $d_1 > 1 + \frac{d_2}{r_2} - a_2$,

noting again that we always require $d_2 \leq d_1$ to capture tumour capacity for acid resistance.

Our initial conditions (Figure 2.4) impose a tumour-only state at $x = -1$ and a healthy-only state at $x = 1$, and we expect the system to evolve over time according to the above analysis, producing four types of tumour behaviour. If $a_1 < 1$, then the healthy state is linearly unstable and we expect the tumour to propagate in the positive x-direction, establishing behind the tumour-healthy interface either a heterogeneous state with both cell types coexisting at reduced densities, if $0 < d_1 < 1 + d_2/r_2 - a_2$, or a homogeneous tumour state if $d_1 > 1 + d_2/r_2 - a_2 > 0$. If $a_1 > 1$, then we expect the linearly stable healthy state to prevent tumour invasion, instead either clearing the tumour if $0 < d_1 < 1 + d_2/r_2 - a_2$ or establishing a stationary interface with the stable tumour population if $d_1 > 1 + d_2/r_2 - a_2$.

2.4 Methods for numerical solution

We solve Equations (2.7)-(2.9) numerically using the Method of Lines (Schiesser 1991), with the system of partial differential equations discretised with a spatial step of $\mathrm{d}x = 0.005$ and the resulting system of coupled ordinary differential equations solved through time using Matlab's inbuilt ODE15s algorithm to accommodate stiffness. The speed of an invasive tumour—here, one that propagates in the positive x-direction—is measured by tracking the midpoint of the front as it evolves near the endtime of each simulation. Further details of our Method of Lines implementation and wavespeed calculation are in Appendix B.

All simulations are run to at least $t = 20$, corresponding to approximately 0.6 years, to ensure complete decay of transients, and initial and boundary conditions are imposed as described in Section 2.3. The particular initial configuration shown in Figure 2.4 is chosen simply for clear delineation of tumour versus healthy tissue, with the interface positioned at the domain midpoint ($x = 0$) to allow enough space in the domain for us to observe either leftward- or rightward-propagating waves. Changing the initial conditions does not alter the overall system behaviour, provided the biologically-motivated boundary constraints are met; that is, one end of the domain (here $x = -1$) is primarily tumour, and the other end (here $x = 1$) is exclusively healthy tissue.

The accuracy of our numerical method is confirmed by setting $a_1 = a_2 = d_2 = 0$ in Equations (2.7)-(2.9) to recover the two behaviours captured by the Gatenby and Gawlinski (1996) model, heterogeneous invasion and homogeneous invasion, with wavespeeds closely matching those measured in Gatenby and Gawlinski (1996) (Figure 2.5). Additionally, upon setting $d_1 = d_2 = 0$ in Equations (2.7)-(2.9) to remove acid-mediated cell death, we attain, as expected, the dynamics of a classical mutual-competition system (discussed later in Section 2.5.2) in which the competition parameters, here a_1 and a_2, govern the linear stability of the system (Murray 2002).

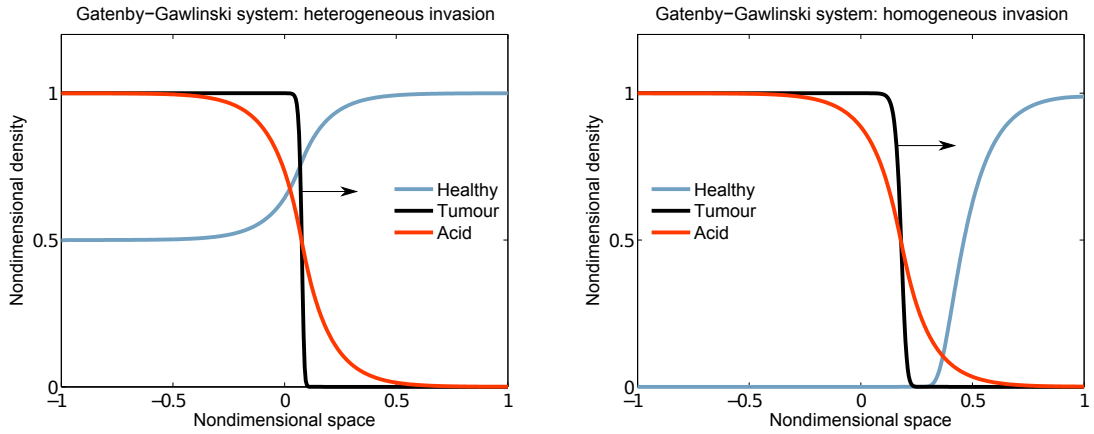

Figure 2.5: Recovery of dynamics in Gatenby and Gawlinski (1996). Profiles of healthy density, u (blue), tumour density, v (black), and excess acid, w (red), from numerical simulations of Equations (2.1)-(2.3), nondimensionalised and subject to the initial and boundary conditions detailed in Section 2.3, with arrows indicating the direction of tumour propagation. a) Heterogeneous invasion is obtained by setting $d_1 = 0.5$, producing a nondimensional wavespeed of 0.0063, as compared with a speed of 0.0064 in Gatenby and Gawlinski (1996); redimensionalised, this corresponds to a speed of approximately 0.01 mm/day. b) Homogeneous invasion with an interstitial gap is obtained by setting $d_1 = 12.5$, producing a nondimensional wavespeed of 0.0127, as compared with a speed of 0.0128 in Gatenby and Gawlinski (1996); redimensionalised, this is a speed of approximately 0.03 mm/day. Each simulation was run to a final time of $t = 20$ (approximately 0.6 years) to ensure complete decay of transients. Other parameter values are $r_2 = 1$, $D = 4 \cdot 10^{-5}$, and $c = 70$.

2.5 Results

2.5.1 Our model captures an expanded range of tumour behaviours

Numerical solution of our full system, Equations (2.7)-(2.9) with all parameters non-zero, produces the four expected types of tumour behaviour (Figure 2.6). While the two invasive

types seen by Gatenby and Gawlinski (1996) are still present in our model—when $a_1 < 1$ and $d_1 < 1 + d_2/r_2 - a_2$ we see heterogeneous invasion (Figure 2.6a) and when $a_1 < 1$ and $d_1 > 1 + d_2/r_2 - a_2$ we see homogeneous invasion (Figure 2.6b)—we also capture two other types of behaviour.

First, when $a_1 > 1$ and $d_1 > 1 + d_2/r_2 - a_2$ we see a non-aggressive tumour which appears stationary for a time (Figure 2.6c). This behaviour is unlikely to persist, however, as our simulations indicate that a truly stationary outcome requires a tumour with both no acid resistance (i.e. the limiting case of $d_2 = d_1$) and a competitive strength precisely equivalent to that of the healthy cells (i.e. $1 < a_1 = a_2$); but these are biologically unlikely conditions and, in the case of the latter, dependent upon mathematical parameter fine-tuning. Instead, the delicate balance between the two stable homogeneous states will be tipped in one direction or the other by inequalities between the two populations. If the tumour has no acid resistance ($d_2 = d_1$) and the healthy population is the stronger competitor ($a_1 > a_2$), then the tumour will eventually be cleared in a manner similar to Figure 2.6d; but if the tumour does exhibit acid resistance ($d_2 < d_1$), as is more plausible biologically, then it will invade. Nevertheless, the speed of invasion is extremely slow—for example, the parameter set $\{a_1, a_2, d_1, d_2\} = \{1.4, 1.6, 10, 8\}$ produces a tumour which advances by less than half a millimetre over a year of simulation time—and hence tumours in this regime, while not strictly stationary, can be considered non-aggressive, at least in comparison with the faster-moving types in the $a_1 < 1$ regimes (Figures 2.6a and 2.6b) which travel on the order of 4 millimetres per year.

The final observed behaviour is truly non-invasive: when $a_1 > 1$ and $d_1 < 1 + d_2/r_2 - a_2$, the healthy cells clear away the tumour (Figure 2.6d).

2.5.2 Acid produces a non-monotonic tumour profile

Although our method for numerical solution of Equations (2.7)-(2.9) successfully recovered the Gatenby and Gawlinski (1996) dynamics with $a_1 = a_2 = d_2 = 0$ (Figure 2.5), the non-monotonic shapes of the tumour profiles in the full generalised system (Figure 2.6) are surprising and did not occur under the Gatenby and Gawlinski (1996) formulation. In the following we examine these localised peaks at the tumour-healthy interface, and conclude that they comprise, not a numerical artefact, but a real feature of our system.

First, we first simulate Equations (2.7)-(2.9) with no acid or tumour diffusion ($c = D = 0$), and observe that the system becomes one of classical mutual competition with linear stability governed by the competition parameters a_1 and a_2 (Murray 2002), and the waves

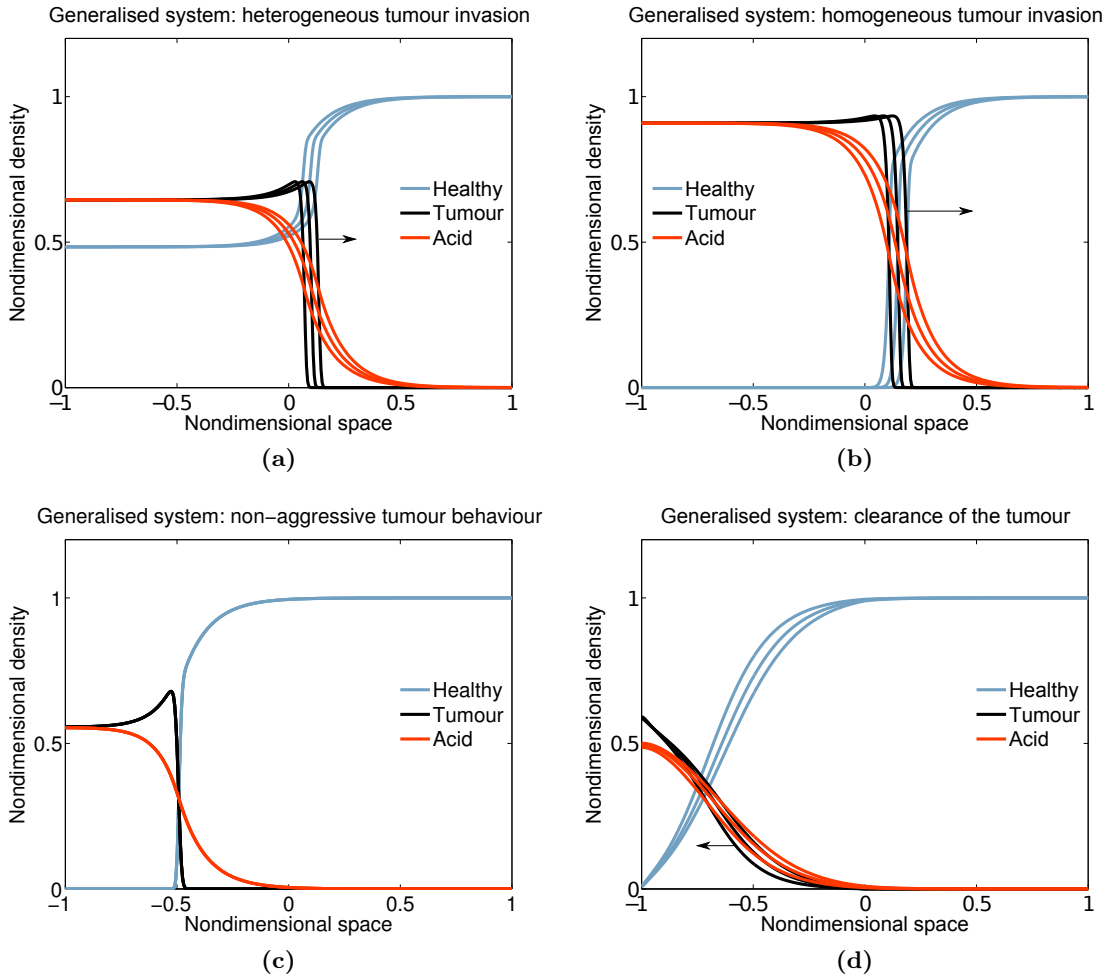

Figure 2.6: Behaviours of numerical solutions of Eq (2.7)-(2.9)**.** Representative time-evolving profiles of the healthy density (blue), tumour density (black), and excess acid (red) from numerical solutions of Equations (2.7)-(2.9) according to parameter regime, with arrows indicating the direction of tumour propagation. a) Heterogeneous tumour invasion with healthy cells surviving behind the tumour-healthy interface, b) homogeneous tumour invasion with no healthy cells remaining behind the interface, c) establishment of a non-aggressive tumour which can progress either toward clearance, in the limiting case of no tumour acid-resistance, or toward very slow invasion, and d) clearance of the tumour by the healthy population. Each simulation was run to a final time of $t = 20$ (approximately 0.6 years). Parameter choices shown are $\{a_1, a_2, d_1, d_2\} = \{0.2, 0.3, 0.5, 0.4\}$ in (a), $\{a_1, a_2, d_1, d_2\} = \{0.2, 1.2, 0.6, 0.1\}$ in (b), $\{a_1, a_2, d_1, d_2\} = \{1.6, 1.4, 1, 0.8\}$ in (c), and $\{a_1, a_2, d_1, d_2\} = \{1.1, 0.8, 1, 0.8\}$ in (d), with the remaining parameters set to $r_2 = 1$, $D = 4 \cdot 10^{-5}$, and $c = 70$.

do not travel (Figure 2.7a). In Matlab's inbuilt solver 'PDEPE', the use of finite elements in the Method of Lines can result in a diffusion artefact that allows movement even with a zero diffusion coefficient (Martin 2009). Figure 2.7a confirms that the use of finite differences in our Method of Lines implementation (see Appendix B) has avoided this problem.

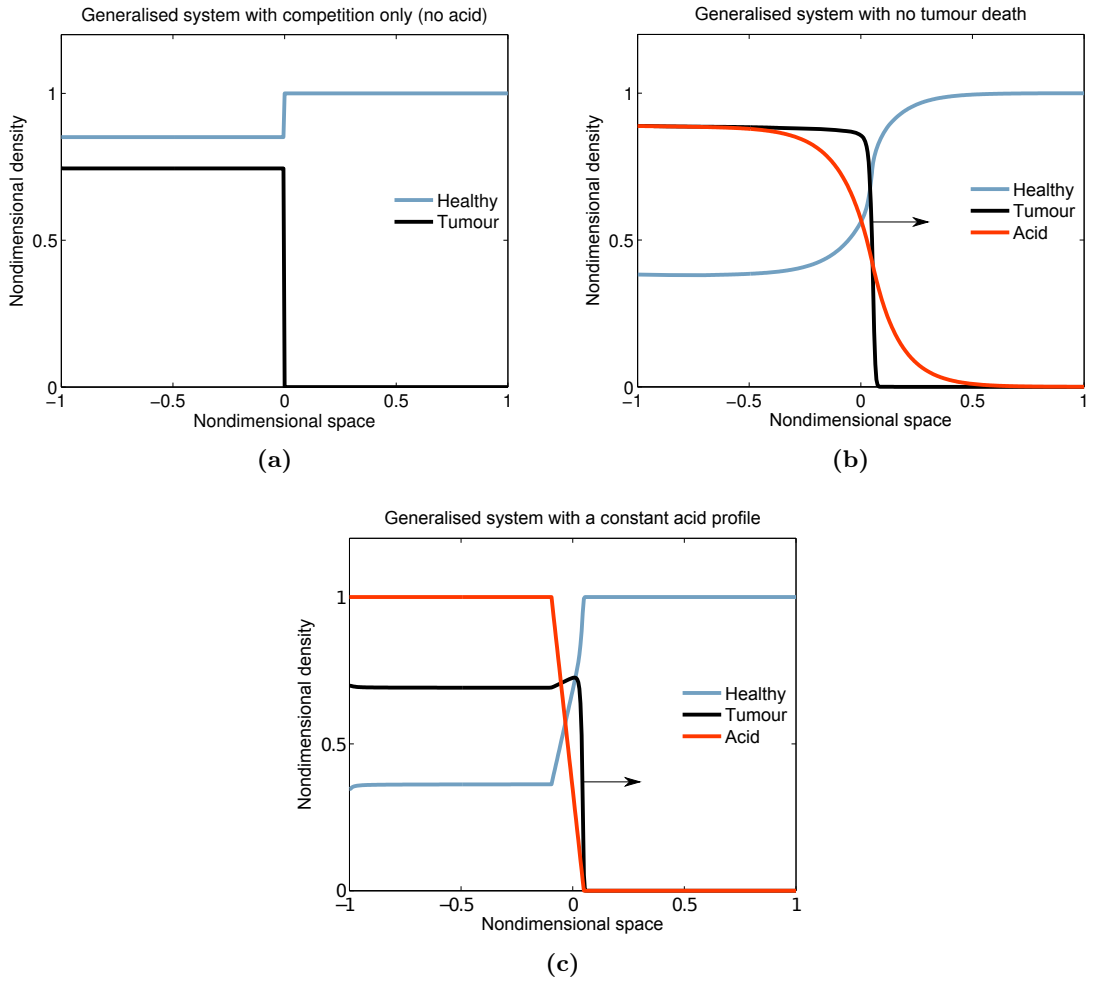

Figure 2.7: Verification of the non-monotonic tumour profile. Investigation of the localised peaks seen in the tumour profiles in Figure 2.6. Numerical simulation of Equations (2.7)-(2.9) with (a) $c = D = 0$ to remove acid and tumour diffusion, to verify that the waves do not exhibit diffusion artefacts; (b) $d_2 = 0$ to remove acid-mediated tumour cell death and confirm that tumours do not exhibit the peaks when they are not killed by acid; and (c) a temporally constant and spatially fixed acid profile to demonstrate its influence on the shape of the tumour (and healthy) profiles. All simulations were run to an end-time of $t = 20$ (approximately 0.6 years) to ensure decay of transients, and representative parameters were selected to be $r_2 = 1$, $c = 70$, $D = 4 \cdot 10^{-5}$, $a_1 = 0.3$, $a_2 = 0.2$, $d_1 = 0.5$, and $d_2 = 0.2$, unless set to zero as described.

Simulating Equations (2.7)-(2.9) with $d_2 = 0$ to remove acid-mediated tumour death, we observe that, similarly to the Gatenby and Gawlinski (1996) cases (Figure 2.5), invasion occurs without a localised peak in the tumour profile (Figure 2.7b), suggesting that peaks are a consequence of acid-mediated tumour death. Finally, we impose a constant acid profile that declines linearly across the middle portion of the spatial domain and does not travel with the tumour, and find that the resulting tumour profile exhibits a non-monotonic shape that is clearly dependent upon the acid profile (Figure 2.7c). This confirms that the

tumour peaks are not a numerical artefact, but rather a consequence of our inclusion of acid-mediated tumour cell death in the system. These non-monotonic tumour fronts are an intriguing feature of our model for which we do not yet have an experimental analogue, although similar non-monotonicity has been observed in healthy tissue encapsulating benign tumours (Perumpanani et al. 1997, Jackson and Byrne 2002), healthy tissue surrounding an invasive tumour that secretes growth signals (Sherratt 1993), tumours under treatment with macrophages (Byrne et al. 2006, Webb et al. 2007), and tumours with invasive speeds exhibiting biphasic dependence on healthy tissue properties (Marchant et al. 2006).

2.6 Discussion

In this chapter we have incorporated additional, potentially important, biological features into the canonical Gatenby and Gawlinski (1996) model of acid-mediated invasion to generalise its descriptive power beyond the highly aggressive cases considered by Gatenby and Gawlinski (1996). By rendering the healthy state conditionally stable rather than globally unstable, we have obtained four tumour behaviours, two of which are non-invasive or non-aggressive and were not captured by the original model (Figure 2.6).

We would caution, however, against translating these non-invasive and non-aggressive cases directly to an *in vivo* or clinical setting, not least because competitive strength of the healthy population (a_1) is a somewhat abstract term and finding a one-to-one correspondence between it and an adjustable property of the biological system may prove difficult. Nevertheless, it is promising that we have attained such behaviours, in part because they may provide good targets for model validation. Additionally, the tumour profiles in our generalised system exhibit localised peaks at the tumour-healthy interface (Figure 2.6), which comprise an acid-dependent feature of the system. This feature may hold potential as another target for experimental validation of the model.

As we have succeeded in obtaining additional targets for model validation beyond what was suggested by Gatenby and Gawlinski (1996), our generalised model fits into a larger goal of assessing possible experiments that will test the acid-mediated invasion hypothesis, an important task in light of novel treatment strategies, such as buffering therapy (Robey et al. 2009, Silva et al. 2009, Martin et al. 2010, 2011, Alfarouk et al. 2011, Robey and Martin 2011), to which the hypothesis has given rise.

However, while the numerical exploration detailed here has provided us with a high-level understanding of the attainable tumour behaviours, it does not indicate where in parameter space interstitial gaps can occur, or indeed whether they are permissible under our

generalised system. Moreover, from numerical simulations alone we cannot elucidate explicitly how the system behaviours depend on fundamental model parameters; and as the parameter space is high-dimensional, an implicit description is inadequate for building a comprehensive picture of the system. In the following chapter we will address these issues by carrying out an analysis of our generalised model of acid-mediated invasion.

Chapter 3

Analysis of the generalised model of acid-mediated invasion

In this chapter we carry out an analysis of the generalised model of acid-mediated invasion that we developed in Chapter 2, motivated by the aim of elucidating explicitly how fundamental parameters influence the model behaviours and thereby building a comprehensive picture of the system. This analysis hinges on two observations: first, that our numerical solutions of Equations (2.7)-(2.9) exhibit travelling waves of constant velocity and shape, which arise due to propagation into the unstable healthy steady state (van Saarloos 1988); and secondly, that there is a boundary layer at the tumour-healthy interface (Figure 3.1).

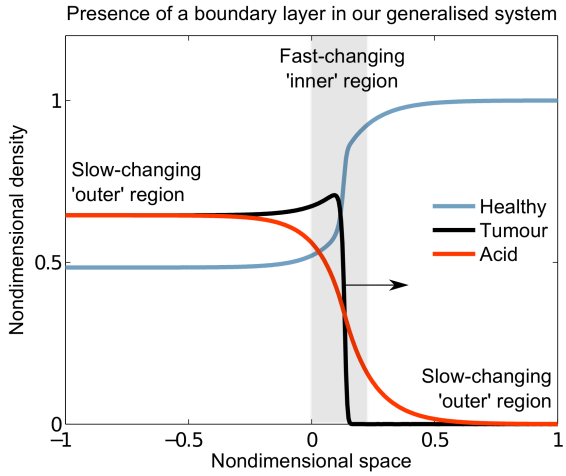

Figure 3.1: Presence of a boundary layer in Eq (2.7)-(2.9)**.** Representative numerical solution of Equations (2.7)-(2.9), as in Figure 2.6a, showing the presence of a rapidly-changing boundary layer at the tumour-host interface flanked by two slowly-changing regions at the periphery of the domain.

We will exploit these features with a strategy that is broadly analogous to the one taken by Fasano et al. (2009) on the Gatenby and Gawlinski (1996) system, but with substantial extra subtleties due to increased coupling in our more comprehensive model. In preparation for this analysis, we now briefly discuss the mathematics behind travelling waves.

3.1 Travelling waves in general

Wave phenomena are widespread in the biomedical sciences, and cancer is no exception. Realistic models of biological systems typically involve many dimensions and species, but sometimes these can be reduced to a single-species form that captures key features and is amenable to a travelling wave analysis. Properties of interest, such as the speed of the wave, can thus be elucidated explicitly in terms of the fundamental model parameters. An in-depth introduction to travelling wave analyses can be found in the canonical textbook by Murray (2002), and hence we confine our discussion here to a brief overview of the general approach.

We can convert a reaction-diffusion equation from the standard coordinate system—in space, x, and time, t—into a coordinate system that travels with the wave. If the wave propagates in the positive x-direction, the new coordinate becomes $z = x - ct$ where c is the (positive) constant wave speed. (A wave propagating in the negative x-direction takes the coordinate $z = x + ct$.) This change of coordinates transforms a partial differential equation in x and t into an ordinary differential equation in the wave variable, z.

The simplest case of a nonlinear reaction-diffusion equation is the Fisher equation, which was first developed to describe the spatial spread of a gene through a population (Fisher 1937) and which is a natural extension of classical logistic growth to include population dispersion (Murray 2002). Letting k represent the growth rate of population u and D the diffusion coefficient, the Fisher equation is:

$$\frac{\partial u}{\partial t} = ku(1-u) + D\frac{\partial^2 u}{\partial x^2} \quad \text{for } k, D > 0.$$

Nondimensionalising by $t^* = kt$ and $x^* = x\sqrt{k/D}$ and omitting the asterisks, this equation becomes

$$\frac{\partial u}{\partial t} = u(1-u) + \frac{\partial^2 u}{\partial x^2}. \tag{3.1}$$

Under spatial homogeneity the steady states of Equation 3.1 are $u = 0$, which is linearly unstable, and $u = 1$, which is linearly stable. (Negative values of u are non-physical.) If

a travelling wave exists for this system, then it can be written as $u(x,t) = U(z)$, where $z = x - ct$ and the wavespeed is $c \geq 0$. Making this change of coordinates, $U(z)$ satisfies

$$U'' + cU' + U(1-U) = 0, \tag{3.2}$$

with $'$ denoting differentiation with respect to the wave coordinate z. While there are many types of travelling waves, including fronts (exhibited by the Gatenby and Gawlinski (1996) model) and pulses (occurring in a recent extension of the Gatenby and Gawlinski (1996) model by Holder et al. (2014) to accommodate a nonlinear acid production term), we will consider only front-type waves in this thesis. A typical wavefront solution is one where U attains one steady state as $z \to -\infty$ and the other as $z \to +\infty$. The particular configuration of this solution is problem-dependent, as it evolves from a partial differential equation with biologically-motivated initial and boundary conditions framing the problem.

To determine the wavespeed at which our species U is travelling, $c \geq 0$, we consider the (U, V) phase-plane of Equation 3.2, where

$$\begin{aligned} U' &= V \quad \text{and} \\ V' &= -cV - U(1-U). \end{aligned}$$

The phase-plane trajectories are then solutions of $\mathrm{d}U/\mathrm{d}V = (-cV - U(1-U))/V$, which has two singular points: $(U,V) = (0,0)$ and $(U,V) = (1,0)$. A linear stability analysis (Appendix A) reveals that the eigenvalues, λ, are

$$\begin{aligned} \lambda_{\pm} &= \frac{1}{2}[-c \pm \sqrt{c^2+4}] \quad \text{for } (U,V) = (1,0), \text{ and} \\ \lambda_{\pm} &= \frac{1}{2}[-c \pm \sqrt{c^2-4}] \quad \text{for } (U,V) = (0,0). \end{aligned}$$

The former is a saddle point, and the latter is a stable node if $c \geq 2$ (degenerate if $c = 2$) and a stable spiral if $c < 2$. A stable spiral means that U oscillates in the vicinity of the origin, which is physically unrealistic as U must always be non-negative. Indeed, from a mathematical point of view it can be shown that the solution to the Fisher equation for non-negative initial conditions is always non-negative. If the origin is a stable node, however, it can be reasoned from the (U,V) phase plane (see Figure 3.2) that a trajectory connecting $(1,0)$ to $(0,0)$ which lies entirely in the lower right quadrant, i.e. where $U \geq 0$ and $U' \leq 0$ with non-negative U, exists for all wavespeeds $c \geq 2$. Transforming this back to the original dimensions, the range of possible wavespeeds satisfies $c \geq 2\sqrt{kD}$.

As this is an infinite range of wavespeeds, it remains to be determined what kind of initial condition, $u(x,0)$, evolves to a travelling wave solution to the Fisher equation, and, if such

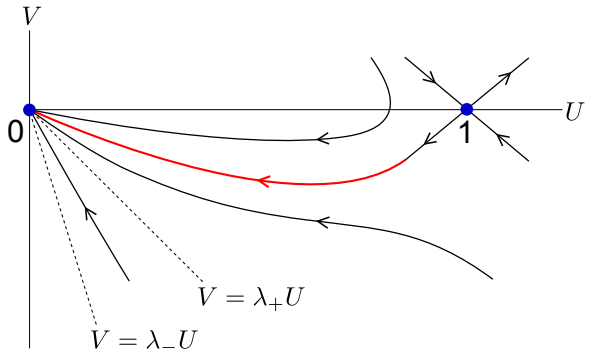

Figure 3.2: Phase plane for Fisher travelling waves. If a travelling wave solution exists for Equation (3.2), then there will be a trajectory (red) connecting the saddle stationary point $(U, V) = (1, 0)$ to the stable stationary point $(U, V) = (0, 0)$ (both blue). Other trajectories in the phase plane are shown as solid black curves, and dotted lines mark where $V = \lambda_- U$ and $V = \lambda_+ U$.

a solution exists, what wavespeed it establishes. Kolmogorov et al. (1937) proved that if the initial condition has semi-compact support—that is, if $u(x, 0) = u_0(x)$ where $u_0(x) = 1$ for $x \leq x_1$ and $u_0(x) = 0$ for $x \geq x_2$, with $x_1 < x_2$ and $u_0(x)$ being continuous—then the solution $u(x, t)$ evolves to the *minimum* wave speed, $c = 2$. For other initial data, the solution may depend critically on the behaviour of $u(x, 0)$ far ahead of the front; and for many systems more complicated than the Fisher equation, particularly those with multiple species, it remains an open question whether any travelling wave trajectories exist. For our purposes in this chapter, however, we will consider it sufficient to observe the establishment of the minimum wavespeed in numerical simulations of our model.

3.2 Asymptotic analysis of our model in a travelling wave framework

To begin, we transform the generalised system that we developed in Chapter 2—Equations (2.7)-(2.9) in nondimensionalised form—into travelling wave coordinates by letting, with a mild abuse of notation, $u(x, t) = u(z)$, $v(x, t) = v(z)$, and $w(x, t) = w(z)$ where $z = x - \theta t$ is our travelling wave coordinate and θ the (constant, positive) wavespeed. Extending the spatial domain to the real line to allow for travelling waves, we obtain, with $\dot{}$ denoting differentiation with respect to z:

$$-\theta \dot{u} = u(1 - u - a_2 v) - d_1 uw, \tag{3.3}$$

$$-\theta \dot{v} = D(\ddot{v}(1 - u) - \dot{u}\dot{v}) + r_2 v(1 - v - a_1 u) - d_2 vw, \tag{3.4}$$

$$-\theta \dot{w} = \ddot{w} + c(v - w). \tag{3.5}$$

In Equations (3.3)-(3.5) the wavefront is now fixed through translational invariance at $z = 0$, with $z < 0$ behind the advancing wavefront and $z > 0$ ahead. Accordingly, we impose the healthy state at the boundary far ahead of the tumour wavefront and one of the two invaded states (heterogeneous or homogeneous) far behind, such that the travelling-wave boundary conditions are:

$$(u, v, w)(\infty) = (1, 0, 0), \quad \text{and} \tag{3.6}$$

$$(u, v, w)(-\infty) = \begin{cases} (1 - (a_2 + d_1)\tilde{v}, \tilde{v}, \tilde{v}) & \text{if } d_1 < 1 + \frac{d_2}{r_2} - a_2, \text{ or} \\ \left(0, \frac{1}{1+\frac{d_2}{r_2}}, \frac{1}{1+\frac{d_2}{r_2}}\right) & \text{if } d_1 > 1 + \frac{d_2}{r_2} - a_2, \end{cases} \tag{3.7}$$

where $\tilde{v} = \dfrac{1 - a_1}{1 - a_1 a_2 + \frac{d_2}{r_2} - a_1 d_1}$ as before.

In Equation (3.4) the parameter D, the ratio between the free-space tumour and acid diffusion coefficients, is very small, and we exploit it as an asymptotically small parameter by relating it to the wavespeed via consideration of the fast and slow dynamics of Equations (3.3)-(3.5). That is, we let $z = x - \epsilon\theta_0 t$ where $\epsilon = \sqrt{D} \ll 1$ and θ_0 is $O(1)$. The system becomes:

$$-\epsilon\theta_0 \dot{u} = u(1 - u - a_2 v) - d_1 uw, \tag{3.8}$$

$$-\epsilon\theta_0 \dot{v} = \epsilon^2(\ddot{v}(1 - u) - \dot{u}\dot{v}) + r_2 v(1 - v - a_1 u) - d_2 vw, \tag{3.9}$$

$$-\epsilon\theta_0 \dot{w} = \ddot{w} + c(v - w). \tag{3.10}$$

We can now take advantage of the boundary layer exhibited by the system (Figure 3.1): within and near the tumour wavefront is a region of rapid change for the species and their derivatives, while far behind and ahead of the wavefront the changes are much slower. A brief overview of asymptotic and boundary layer theory can be found in Appendix C.

To asymptotic (leading order) accuracy, the solution in the slowly-varying outer regions satisfies Equations (3.8)-(3.10) with $\epsilon = 0$:

$$0 = u(1 - u - a_2 v) - d_1 uw, \tag{3.11}$$

$$0 = r_2 v(1 - v - a_1 u) - d_2 vw, \tag{3.12}$$

$$0 = \ddot{w} + c(v - w). \tag{3.13}$$

Rescaling the narrow wavefront region by setting $z = \epsilon\zeta$, the leading order solution in the wavefront region satisfies, with the subscript 'in' denoting a profile in this inner region and

$'$ denoting differentiation with respect to the 'stretched' inner coordinate ζ,

$$-\theta_0 u'_{in} = u_{in}(1 - u_{in} - a_2 v_{in}) - d_1 u_{in} w_{in}, \tag{3.14}$$

$$-\theta_0 v'_{in} = v''_{in}(1 - u_{in}) - u'_{in} v'_{in} + r_2 v_{in}(1 - v_{in} - a_1 u_{in}) - d_2 v_{in} w_{in}, \tag{3.15}$$

$$w''_{in} = 0. \tag{3.16}$$

The Gatenby and Gawlinski (1996) model, a subset of our generalised model, exhibits interstitial gaps and sharp fronts—profiles under semi-compact support with a discontinuity in the derivative where zero density is reached—under certain parameter regimes (Fasano et al. 2009). Hence, we must allow for these possibilities in our model.

We proceed by first finding an approximate solution for the healthy profile (u) to asymptotic accuracy, then finding an asymptotic approximation for the excess acid profile (w) and using both of these to determine the dynamics in the tumour wavefront.

3.2.1 Asymptotic approximation for the healthy profile

Before considering the asymptotic structure of the problem for evaluating u, from Equation (3.8) we have exactly that

$$\dot{u} = \frac{u^2 - A(z)u}{\epsilon\theta_0}, \quad \text{where} \tag{3.17}$$

$$A(z) = 1 - a_2 v - d_1 w \tag{3.18}$$

and $A(+\infty) = 1$. In the outer regions this will invoke a fast relaxation to one of the roots, $u = 0$ or $u = A(z)$, and in the inner region the u derivatives are larger still, so the same behaviour will occur; hence to asymptotic accuracy we will expect to have $u \approx 0$ or $u \approx A(z)$.

As a preliminary analysis of Equation (3.17) in detail, let us consider $A(z) = A$ where A is a constant different from $u(\infty)$. Beginning at the right-hand boundary at $z = +\infty$ and moving leftward toward in the inner wavefront region, we see that

$$\dot{u} = \frac{-Au + u^2}{\epsilon\theta_0}. \tag{3.19}$$

If $A > 0$, then as we move inward along z from $+\infty$, the $(u, -\dot{u})$ phase plane will exhibit an attractor at $u = A$ (Figure 3.3a), while if $A < 0$ then u will be driven to zero (Figure 3.3b). Based upon this initial reasoning, and the fast response of the system given $\epsilon \ll 1$ in the

denominator of Equation (3.19), in explicitly solving Equation (3.17) we expect *a priori* to find that, for all z,

$$\begin{aligned} u &\approx \begin{cases} 0 & \text{if } A(z) < 0, \\ \mathrm{A(z)} & \text{if } 0 < A(z) \leq 1, \end{cases} \\ &= \max\{0, A(z)\}, \end{aligned}$$

where the sign of $A(z)$ will depend upon the behaviour of the tumour profile, v, and acid profile, w, in the outer regions. A full analysis of Equation (3.17) follows.

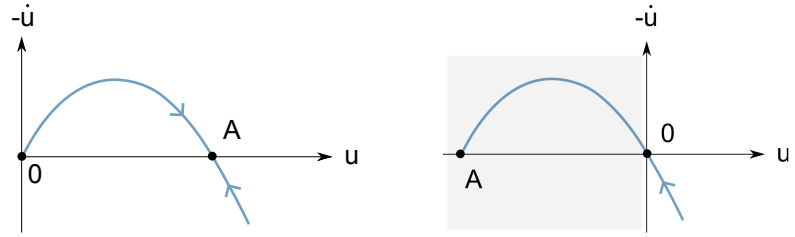

Figure 3.3: Possibilities in the $(u, -\dot{u})$ phase plane. Schematics of the possible behaviour in the $(u, -\dot{u})$ phase plane arising from Equation (3.19), which is Equation (3.17) with the simplification that A is constant rather than a function of the travelling wave coordinate z, as we move inward along z from $z = +\infty$. Shown are trajectories (blue) in the phase plane (a) if $A > 0$, in which case the point $u = A$ is an attractor; and (b) if $A < 0$, in which case the point $u = 0$ is an attractor and the point $u = A$ is unattainable, as we must start with $u > 0$ and therefore from Equation (3.17) we cannot have u go negative (shaded region).

With the substitution $u = 1/q$, Equation (3.17) becomes

$$\epsilon\theta_0 \dot{q} = A(z)q - 1,$$

a linear equation which we solve directly to obtain

$$q(z) = e^{-\frac{1}{\epsilon\theta_0}\int_z^{\tilde{z}} A(s)ds} q(\tilde{z}) + \frac{1}{\epsilon\theta_0} e^{\frac{1}{\epsilon\theta_0}\int_0^z A(s)ds} \int_z^{\tilde{z}} e^{-\frac{1}{\epsilon\theta_0}\int_0^s A(x)dx} ds,$$

where $\tilde{z}$ is a judicious choice of z. Choosing $\tilde{z}$ to be very large, but not infinite since $\int_z^\infty A(s)ds$ is ill-defined, we have $q(\tilde{z}) = 1/u(\tilde{z}) \approx 1$ because of the healthy-state boundary conditions imposed on $u(z)$ as $z \to +\infty$. Substituting $u(z)$ back into the equation, we obtain

$$u(z) \approx \frac{e^{\frac{1}{\epsilon\theta_0}\int_z^{\tilde{z}} A(s)ds}}{1 + \frac{1}{\epsilon\theta_0} e^{\frac{1}{\epsilon\theta_0}\int_0^{\tilde{z}} A(s)ds} \int_z^{\tilde{z}} e^{-\frac{1}{\epsilon\theta_0}\int_0^s A(x)dx} ds},$$

and with

$$\phi(s) = -\frac{1}{\theta_0}\int_0^s A(x)dx \text{ and}$$
$$I(z) = \int_z^{\tilde{z}} e^{\frac{1}{\epsilon}\phi(s)}ds,$$

this becomes

$$u(z) \approx \frac{e^{\frac{1}{\epsilon\theta_0}\int_z^{\tilde{z}} A(s)ds}}{1 + \frac{1}{\epsilon\theta_0}e^{\frac{1}{\epsilon\theta_0}\int_0^{\tilde{z}} A(s)ds}I(z)}, \tag{3.20}$$

where $I(z)$ is a Laplace integral (Appendix D).

These expressions implicitly assume that $u \approx \max\{0, A(z)\}$ is such that $A(z) = 1 - a_2 v - d_1 w$ has at most one root. Ahead of the wavefront, $v \approx 0$ and hence $A(z) = 1 - d_1 w$, which is increasing as w always decreases (this is evident from numerical solutions and also will be seen in Section 3.2.2); thus there can be at most one root ahead of the wavefront. This root is illustrated by Case 1c of Figure 3.4, which depicts the possible locations of the tumour wavefront in relation to the zeros of $A(z)$. Considering two or three roots, as illustrated in the third and fourth rows of Figure 3.4, respectively, we immediately have an absence of monotonicity in u which is not consistent with our numerical results. Furthermore, Case 1b in Figure 3.4 requires parameter fine tuning, and hence we do not consider it, in view of the variability in our parameters imparted by between-tumour variation and intrinsic experimental error (Fasano et al. 2009). We are left with Cases 0a, 1a, or 1c from Figure 3.4, which we explore below.

For fixed z, suppose that $A > 0$ on the interval $[z, \tilde{z}]$, with $\tilde{z} \gg 1$, and hence has no roots; this is Case 0 in Figure 3.4. Then we have that $\dot{\phi}(s) = -\frac{1}{\theta_0}A(s) < 0$ for all s in $[z, \tilde{z}]$, indicating that on the interval $[z, \tilde{z}]$, $\frac{1}{\epsilon}\phi(s)$ has its maximum at $s = z$, and we Taylor expand $I(z)$ about this point:

$$\begin{aligned} I(z) &\approx \int_z^{\tilde{z}} e^{\frac{1}{\epsilon}\left[\phi(z) + (s-z)\dot{\phi}(z)\right]}ds \\ &\approx -\frac{\epsilon}{\dot{\phi}(z)}e^{\frac{1}{\epsilon}\phi(z)}, \end{aligned}$$

where the second line follows from the first by extension of the upper limit of integration to ∞ in accordance with the Laplace Method (Appendix D), introducing only exponentially

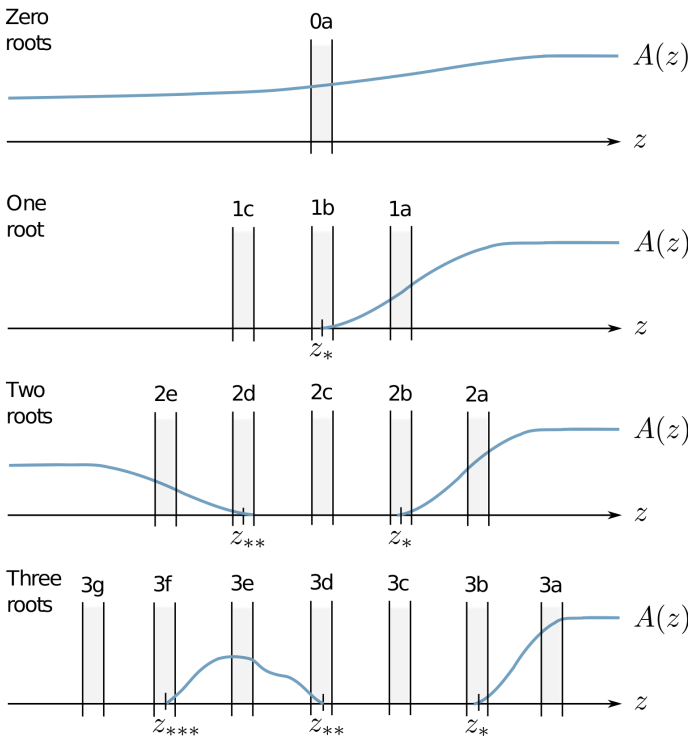

Figure 3.4: Possibilities for the roots of Eq (3.18)**.** Locations along z where the inner wavefront region can fall (shaded columns) in relation to the roots of $A(z)$, a function given by Equation (3.18) and shown as a blue curve, for four possible scenarios: no roots (top), a single root at z_* (second from top), two roots at z_* and z_{**} (second from bottom), or three roots at z_*, z_{**}, and z_{***} (bottom).

small errors. Substituting this into Equation (3.20), we obtain

$$\begin{aligned} u(z) &\approx \frac{e^{\frac{1}{\epsilon\theta_0}\int_z^{\tilde{z}} A(s)ds}}{1+\frac{1}{A(z)}e^{\frac{1}{\epsilon\theta_0}\int_z^{\tilde{z}} A(s)ds}} \\ &\approx \frac{e^{\frac{1}{\epsilon\theta_0}\int_z^{\tilde{z}} A(s)ds}}{\frac{1}{A(z)}e^{\frac{1}{\epsilon\theta_0}\int_z^{\tilde{z}} A(s)ds}} \\ &= A(z), \end{aligned}$$

with the second line following from the first by the observation that $A(s) > 0$ for all s in $[z, \tilde{z}]$ and hence the exponential dominates unity.

If $A(s)$ has one root at $s = z_*$, then for $z > z_*$ the asymptotics are analogous to the no-root case and $u \approx A(z)$; here we consider $z < z_*$, corresponding to Case 1a or 1c in Figure 3.4. We have at z_* that $\dot{\phi}(z_*) = -\frac{1}{\theta_0}A(z_*) = 0$, and it follows that $\ddot{\phi}(z_*) = -\frac{1}{\theta_0}A'(z_*) \leq 0$. Excluding the mathematically fine-tuned degenerate case for which $\ddot{\phi}(z_*) = 0$, we assume

that $\ddot{\phi}(z_*) < 0$ and expand $I(z)$ about $s = z_*$:

$$\begin{aligned} I(z) &\approx \int_z^{\tilde{z}} e^{\frac{1}{\epsilon}\left[\phi(z_*)+\frac{(s-z_*)^2}{2}\ddot{\phi}(z_*)\right]} ds \\ &\approx e^{\frac{1}{\epsilon}\phi(z_*)} \sqrt{\frac{2\pi\epsilon}{-\ddot{\phi}(z_*)}}, \end{aligned}$$

with the second line following from the first by extension of the limits of integration to $-\infty$ and $+\infty$, again introducing only exponentially small errors. Substituting this into Equation (3.20) gives us

$$\begin{aligned} u(z) &\approx \frac{e^{\frac{1}{\epsilon\theta_0}\int_z^{\tilde{z}} A(s)ds}}{1 + \frac{1}{\epsilon\theta_0} e^{\frac{1}{\epsilon\theta_0}\int_{z_*}^{\tilde{z}} A(s)ds} \sqrt{\frac{2\pi\epsilon\theta_0}{\dot{A}(z_*)}}} \\ &\approx \frac{e^{\frac{1}{\epsilon\theta_0}\int_z^{\tilde{z}} A(s)ds}}{\frac{1}{\epsilon\theta_0} e^{\frac{1}{\epsilon\theta_0}\int_{z_*}^{\tilde{z}} A(s)ds} \sqrt{\frac{2\pi\epsilon\theta_0}{\dot{A}(z_*)}}} \\ &= \sqrt{\frac{\epsilon\theta_0\dot{A}(z_*)}{2\pi}} e^{\frac{1}{\epsilon\theta_0}\int_z^{z_*} A(s)ds} \\ &\approx 0, \end{aligned}$$

where the final line comes from letting $\epsilon \to 0$ for an approximation to leading order in ϵ, noting that in the interval from z to z_* we have $A(s) < 0$ and hence the exponential vanishes.

Consistent with our initial expectation, we have found that

$$u \approx \max\{0, A(z)\} \tag{3.21}$$

to leading order. In the following section we incorporate this solution into an asymptotic approximation for the excess acid profile, w.

3.2.2 Asymptotic approximation for the acid profile

Depending on the type of invasive behaviour as determined by the imposed boundary conditions, either heterogeneous invasion or homogeneous invasion is possible, with the limit in $z < 0$ corresponding to the appropriate boundary condition at $z = -\infty$ from Equation (3.7). Furthermore, ahead of the wavefront, Equation (3.12) governs the tumour density and hence we have either $v = 1 - a_1 u - d_2 w/r_2$ or $v = 0$ to asymptotic accuracy. The former can be discounted immediately as it is inconsistent with the boundary condition

at spatial infinity, except for the mathematical fine tuning $a_1 = 1$, which corresponds to the confluence of two of the steady states and is excluded by the conditions for invasion. Therefore, for invading waves we have, to asymptotic accuracy, $v = 0$ for all $z > 0$. In this region, Equation (3.13) becomes $0 = \ddot{w} - cw$, and from this we find the leading-order solution for w for z sufficiently large:

$$w_+ = k_1 e^{-\sqrt{c}z}, \tag{3.22}$$

where k_1 is to be determined. In $z < 0$ we have $0 = \ddot{w} + c(v - w)$, and the profiles in $z < 0$ then depend on invasive type as follows.

When we enforce the boundary conditions for heterogeneous invasion by requiring that $a_1 < 1$ and $d_1 < 1 + \frac{d_2}{r_2} - a_2$, for all $z < 0$ we have $v \neq 0$ and $u > 0$ everywhere; hence from Equation (3.21) we have $u = A(z) > 0$ (Case 0 in Figure 3.4). Under these conditions, Equation (3.13) becomes

$$-\frac{c(1-a_1)}{1-a_1a_2} = \ddot{w} - c\left(1 + \frac{\frac{d_2}{r_2} - a_1d_1}{1-a_1a_2}\right)w.$$

Letting

$$\lambda = 1 + \frac{\frac{d_2}{r_2} - a_1d_1}{1-a_1a_2} \text{ and, as before,}$$
$$\tilde{v} = \frac{1-a_1}{1-a_1a_2+\frac{d_2}{r_2}-a_1d_1},$$

solving this linear ordinary differential equation and applying the heterogeneous boundary condition for w at $z = -\infty$ yields the leading-order solution for w,

$$w_- = k_2 e^{z\sqrt{c\lambda}} + \tilde{v},$$

for all $z < 0$. To find the unknown constants k_1 and k_2 and determine the inner solution for the acid, w_{in}, we match the functional forms of the leading-order approximations for w in each of the outer regions with those in the inner region within the overlapping boundary regions. To leading order w_{in} is given by Equation (3.16); this equation could be satisfied by a linear w_{in}, but as w_{in} must be bounded in order to match with the bounded outer regions, it must be constant rather than linear. Consequently, matching the outer solutions to the inner boundaries is equivalent to matching the functional forms of $w_-(0)$ and $w_+(0)$ with one another across the constant inner region where both take the value of w_{in}. We match

the functions, $w_-(0) = w_+(0)$, and their derivatives, $\dot{w}_-|_0 = \dot{w}_+|_0$, to obtain at leading order in ϵ:

$$w = \begin{cases} \tilde{v}\left(1 - \dfrac{e^{z\sqrt{c\lambda}}}{1+\sqrt{\lambda}}\right) & \text{for } z < 0, \\ \dfrac{\tilde{v}e^{-z\sqrt{c}}}{1+\sqrt{\frac{1}{\lambda}}} & \text{for } z > 0, \end{cases} \tag{3.23}$$

and it follows that for all ζ,

$$w_{in} = \frac{\tilde{v}}{1+\sqrt{\frac{1}{\lambda}}} \tag{3.24}$$

in the heterogeneous invasion case. The sign of λ exerts an extra constraint on our parameter space, in that λ must be positive for solutions for w to be real, and hence we must have

$$d_1 < \frac{1}{a_1}\left(1 + \frac{d_2}{r_2}\right) - a_2. \tag{3.25}$$

When we enforce the boundary conditions for homogeneous invasion by requiring that $a_1 < 1$ and $d_1 > 1 + \frac{d_2}{r_2} - a_2$, ahead of the wavefront we have $v \approx 0$ and the behaviour of w is as previously, but in $z < 0$ the limit as $z \to -\infty$ now tends to the homogeneous boundary condition. Again we find from Equation (3.13) that

$$-\frac{c(1-a_1)}{1-a_1a_2} = \ddot{w} - c\lambda w,$$

and solving this ODE, now with the homogeneous boundary condition imposed on w, gives

$$w_- = k_3 e^{z\sqrt{c\lambda}} + \frac{1}{1+\frac{d_2}{r_2}}$$

for $z < 0$. Matching the functional form of this solution with the solution in $z > 0$, given by Equation (3.22), we obtain the outer solution for w to asymptotic accuracy:

$$w = \begin{cases} \dfrac{1}{1+\frac{d_2}{r_2}}\left(1 - \dfrac{e^{z\sqrt{c\lambda}}}{1+\sqrt{\lambda}}\right) & \text{for } z < 0, \\ \dfrac{e^{-z\sqrt{c}}}{\left(1+\frac{d_2}{r_2}\right)\left(1+\sqrt{\frac{1}{\lambda}}\right)} & \text{for } z > 0, \end{cases} \tag{3.26}$$

and it follows that for all ζ,

$$w_{in} = \frac{1}{\left(1+\frac{d_2}{r_2}\right)\left(1+\sqrt{\frac{1}{\lambda}}\right)} \tag{3.27}$$

in the homogeneous invasion case, again subject to the parameter restriction in Equation (3.25). We now use the solutions from this section and Section 3.2.1 to extract the tumour wavespeed, θ, from the equation governing the tumour wavefront, Equation (3.15).

3.2.3 Determination of the invasive speed and interstitial gap

To find the wavespeed, θ, of an invading tumour wave, we again consider each type of invasion—heterogeneous and homogeneous—as dictated by parameter conditions.

When $a_1 < 1$ and $d_1 < 1 + \frac{d_2}{r_2} - a_2$, leading to heterogeneous invasion, in order to match with the appropriate boundary conditions we must have from Section 3.2.1 that $u \approx A(z) > 0$ everywhere in the domain. Incorporating our solution for w, Equation (3.24), we have

$$u_{in} \approx 1 - a_2 v_{in} - \frac{d_1 \tilde{v}}{1 + \sqrt{\frac{1}{\lambda}}}$$

to leading order in ζ in the inner region, and it follows that $u'_{in} = -a_2 v'_{in}$. With these leading-order solutions for u_{in} and w_{in}, the asymptotic equation for the wavefront, Equation (3.15), becomes

$$0 = a_2[v_{in}v'_{in}]' + \alpha v''_{in} + \theta_0 v'_{in} + v_{in}(\beta - \gamma v_{in}), \tag{3.28}$$

where

$$\begin{aligned}
\alpha &= \frac{d_1 \tilde{v}}{1 + \sqrt{\frac{1}{\lambda}}}, \\
\beta &= r_2 \left(1 - a_1 - \tilde{v} \frac{\frac{d_2}{r_2} - a_1 d_1}{1 + \sqrt{\frac{1}{\lambda}}} \right), \quad \text{and} \\
\gamma &= r_2(1 - a_1 a_2).
\end{aligned}$$

Recalling that the healthy state imposed at $z = +\infty$ is unstable, we have the type of propagation in which the wave is pulled by the instability at its leading edge (van Saarloos 1988). At this leading edge the tumour density, v_{in}, is very small and the degenerate term in Equation (3.28), $a_2[v_{in}v'_{in}]'$, becomes negligible, allowing us to consider only

$$0 \approx \alpha v''_{in} + \theta_0 v'_{in} + v_{in}(\beta - \gamma v_{in}),$$

which is a Fisher-type equation and by marginal stability exhibits an asymptotic front speed of $\theta_0 = 2\sqrt{\alpha\beta}$. Substituting back to the original parameters and recalling that $\theta = \epsilon\theta_0 = \sqrt{D}\theta_0$, we obtain the speed

$$\theta \approx 2\sqrt{D} \sqrt{\frac{d_1 r_2 \tilde{v}}{1 + \sqrt{\frac{1}{\lambda}}} \left(1 - a_1 - \tilde{v} \frac{\frac{d_2}{r_2} - a_1 d_1}{1 + \sqrt{\frac{1}{\lambda}}} \right)} \tag{3.29}$$

in the heterogeneous invasion case.

When $a_1 < 1$ and $d_1 > 1 + \frac{d_2}{r_2} - a_2$, leading to homogeneous invasion, for attainment of the appropriate boundary conditions we must have u tending to zero somewhere in the domain; thus, $A(z)$ must have a root, and whether or not u plays a role in the inner region depends on where this root is located. Using Equation (3.26) and our previous argument that $v \approx 0$ in $z > 0$, we have, for all $z > 0$,

$$u \approx \max\left\{0, 1 - \frac{d_1 e^{-z\sqrt{c}}}{\left(1 + \frac{d_2}{r_2}\right)\left(1 + \sqrt{\frac{1}{\lambda}}\right)}\right\}. \tag{3.30}$$

The system behaviour in the wavefront now depends on whether the root of $A(z)$ falls in $z > 0$; that is, whether the magnitude of d_1 is sufficient to drive u to zero ahead of the tumour wavefront. For notational convenience we let

$$\sigma = \left(1 + \frac{d_2}{r_2}\right)\left(1 + \sqrt{\frac{1}{\lambda}}\right).$$

If $d_1 < \sigma$, then u is driven to zero in $z < 0$ by matching to the limit as $z \to -\infty$ (Case 1a from Figure 3.4). We thus expect u_{in} to be nonzero, resulting in homogeneous tumour invasion with no interstitial gap and the inner travelling wave equation

$$0 = \alpha v_{in}'' + \theta_0 v_{in}' + v_{in}(\beta - \gamma v_{in}),$$

where

$$\begin{aligned}
\alpha &= \frac{d_1}{\sigma}, \\
\beta &= r_2\left(1 - a_1 - \frac{\frac{d_2}{r_2} - a_1 d_1}{\sigma}\right), \text{ and} \\
\gamma &= r_2(1 - a_1 a_2).
\end{aligned}$$

It follows that the asymptotic front speed is

$$\theta \approx 2\sqrt{D}\sqrt{\frac{d_1 r_2}{\sigma}\left(1 - a_1 - \frac{\frac{d_2}{r_2} - a_1 d_1}{\sigma}\right)}. \tag{3.31}$$

If $d_1 = \sigma$, then $u \approx \max\{0, 1 - e^{-z\sqrt{c}}\}$, and u attains zero inside the narrow inner region; this is the mathematically fine-tuned Case 1b from Figure 3.4, and considering the potential variance in parameter values across tumours, we do not proceed further with it.

If $d_1 > \sigma$, then this condition is sufficient to push u to zero at some $z_* > 0$ (Case 1c from Figure 3.4), resulting in homogeneous invasion with an interstitial gap. In this case, $u_{in} = 0$, and Equation (3.15) simplifies to

$$0 \approx v_{in}'' + \theta_0 v_{in}' + v_{in}\left(r_2 - \frac{d_2}{\sigma} - r_2 v_{in}\right),$$

exhibiting a tumour wavespeed of

$$\theta \approx 2\sqrt{D}\sqrt{r_2 - \frac{d_2}{\sigma}}. \tag{3.32}$$

Finally, recalling that the wavefront is fixed at $z = 0$ through translational invariance, we find the width of the interstitial gap to be given by the location where u attains zero, z_*:

$$z_* = \frac{1}{\sqrt{c}}\ln\left(\frac{d_1}{\sigma}\right). \tag{3.33}$$

3.3 Results

We now have a comprehensive picture of the parameter space belonging to Equations (2.7)-(2.9), and the types of behaviours that can arise within this space, shown in Figure 3.5.

3.3.1 Comparison of analytical and numerical results

Comparing our analytical solutions—Equations (3.29)-(3.33)—with estimates measured from our numerical solutions from Chapter 2, we see good agreement (Figure 3.6). Discrepancies on the order of our asymptotic parameter, ϵ, arise due to our use of leading-order approximations in the asymptotics, but the correspondence is sufficiently close that we do not consider it necessary to include higher-order terms.

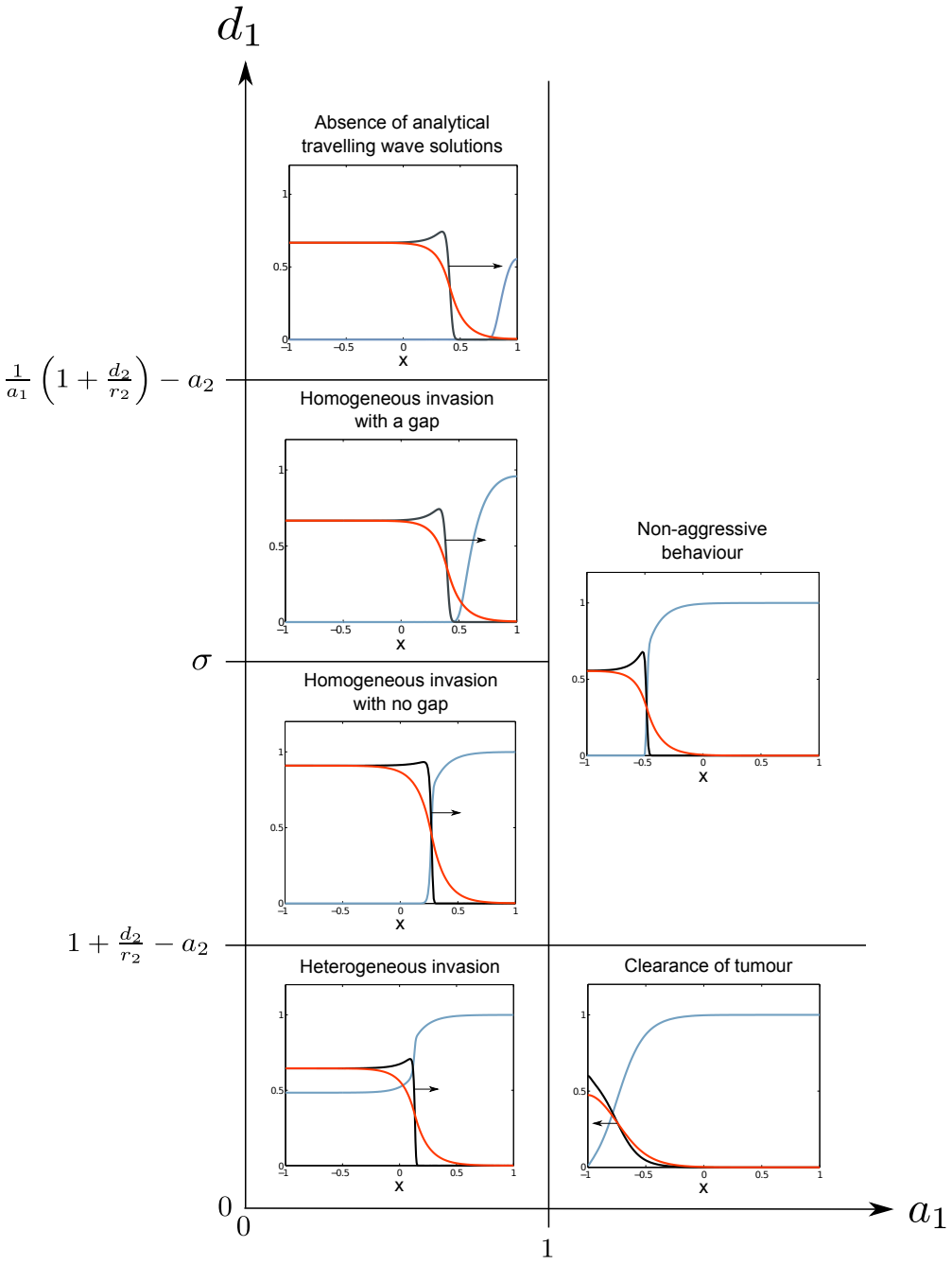

Figure 3.5: Comprehensive picture of the parameter space for Eq (2.7)-(2.9)**.** Behaviours permitted by Equations (2.7)-(2.9) in parameter space, with the additional, biologically motivated, constraint in all regimes that $d_2 \leq d_1$ to capture tumour capacity for acid resistance. Shown are late-time healthy (blue), tumour (black), and acid (red) profiles over space (x-axes) for representative simulations in each parameter regime. In the regime labelled "absence of analytical travelling wave solutions" we have complex analytical solutions that do not exhibit travelling waves, stemming from a negative value of λ in the exponentially decaying approximation for the acid profile (see Section 3.2.2)—here correspondence with our numerical solutions breaks down.

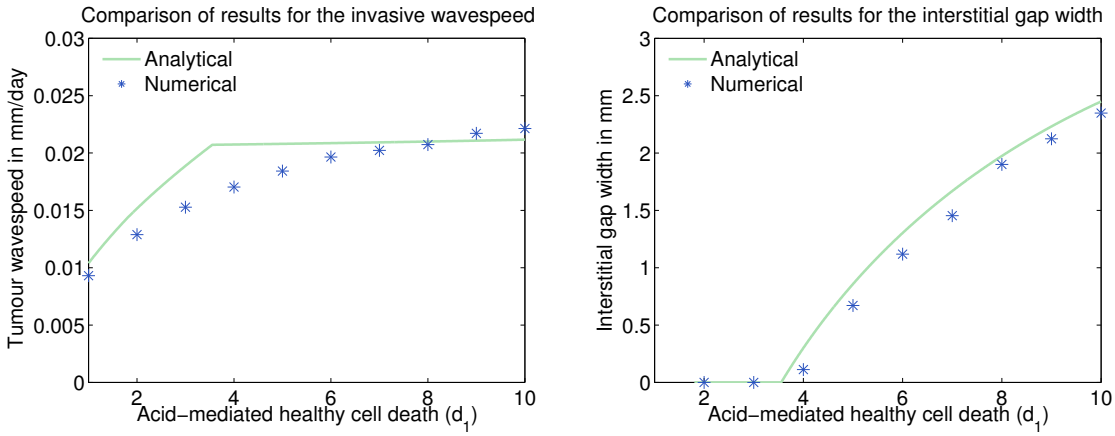

Figure 3.6: Comparison of analytical and numerical solutions of Eq (2.7)-(2.9)**.** Comparison of (a) invasive tumour wavespeeds and (b) interstitial gap widths produced by our analysis in this chapter (green curves) and numerical simulations detailed in Chapter 2 (blue stars), over increasing rates of acid-mediated healthy cell death, d_1, from $d_1 = 1$ to $d_1 = 10$. Other parameters are held constant at $r_2 = 1$, $d_2 = 1$ (maintaining $d_1 \geq d_2$ as required from Section 2.3), $D = 4 \cdot 10^{-5}$, $c = 70$, $a_1 = 0.1$, and $a_2 = 0.2$. Errors of $\mathcal{O}(\epsilon)$ in the analytical curves arise due to our use of leading-order approximations in the asymptotics.

3.3.2 Impact of tumour aggressiveness

To understand the behaviour of Equations (3.29)-(3.33), we view the 'aggressiveness' of a tumour in terms of the values of its competitive strength and acid-mediated death parameters (d_2 and a_2, respectively) relative to those of the healthy population (d_1 and a_1, respectively). We consider 'low' aggressiveness to mean that the tumour death rate and competitive strength parameters are similar to those for the healthy tissue; 'moderate' aggressiveness to indicate a tumour with a death rate approximately half, and competitive strength twice, the values for the healthy tissue; and 'high' aggressiveness to mean a tumour with a death rate an order of magnitude lower, and competitive strength an order of magnitude higher, than those of the healthy tissue.

Under these three aggressiveness characterisations, we vary the healthy cell death rate and competitive strength parameters (d_1 and a_1, respectively) and plot the resulting wavespeeds (Figure 3.7). Broadly speaking the wavespeeds increase with tumour aggressiveness as one would expect. Increasing aggressiveness also compresses the regime of valid travelling wave solutions, as a result of the parameter condition in Equation (3.25), which produces a complex solution for the acid profile when violated (see Section 3.2.2).

Returning to the interstitial gap, we again vary the healthy death and competition parameters under three degrees of tumour aggressiveness, but plot interstitial gap width rather

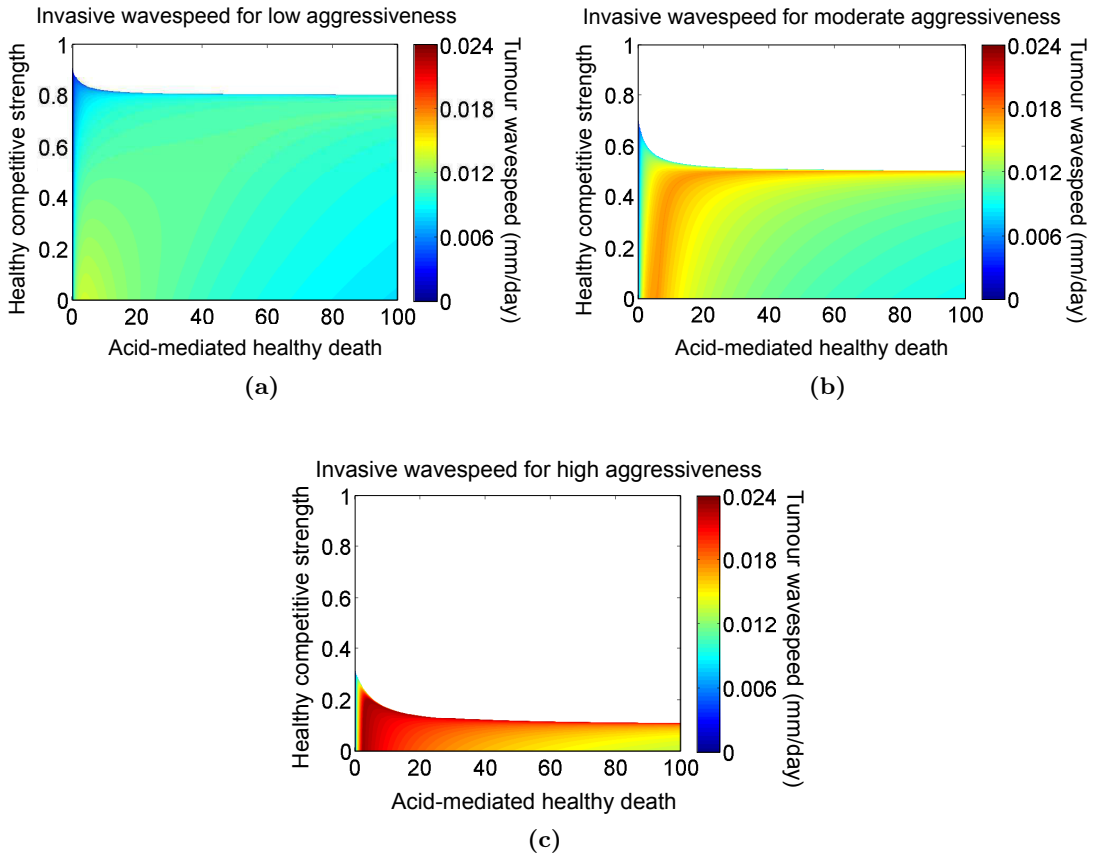

Figure 3.7: Effect of tumour aggressiveness on the speed of invasion. Tumour wavespeed, found in Section 3.2.3, is plotted (colour gradients, redimensionalised to millimetres per day) with the healthy acid-mediated death rate (d_1) and healthy competitive strength (a_1) on the x and y axes, respectively. White regions mark parameter combinations that are outside the regime of travelling wave solutions. (a) The tumour acid-mediated death rate (d_2) is set to $0.8d_1$ and tumour competitive strength (a_2) to $1.2a_1$, representing tumours which are only mildly aggressive; (b) d_2 is set to $0.5d_1$ and a_2 to $2a_1$, representing moderately aggressive tumours; (c) d_2 is set to $0.1d_1$ and a_2 to $10a_1$, representing highly aggressive tumours. Remaining parameters are $r_2 = 1$, $D = 4 \cdot 10^{-5}$, and $c = 70$.

than wavespeed (Figure 3.8). We find that gap width increases with aggressiveness, from no gaps in much of the parameter space for 'low' aggressiveness to gaps as large as 5 millimetres in the parameter space for 'high' aggressiveness. To be realistic, however, interstitial gaps must fulfil two criteria. First, their size must fall within the range observed experimentally by Gatenby and Gawlinski (1996); that is, on the order of 0.1 millimetres. Second, the tissue pH established inside the tumour, which comes from our solution for w near the core, must be experimentally plausible; the core was assumed *a priori* to be non-necrotic (Gatenby and Gawlinski 1996), meaning that the pH must be higher (less acidic) than 6.3, the commonly observed threshold for tumour cell survival (Park et al. 1999), and hence model tumours that are acid-resistant enough to thrive below this threshold can be deemed clinically unrealistic. Taking these two criteria together, it emerges that while gaps in gen-

eral arise over a large portion of parameter space, *realistic* gaps occur in a fairly restricted space that shrinks as the aggressiveness of the tumour increases, indicating that realistic gaps are sensitive to parameter choice.

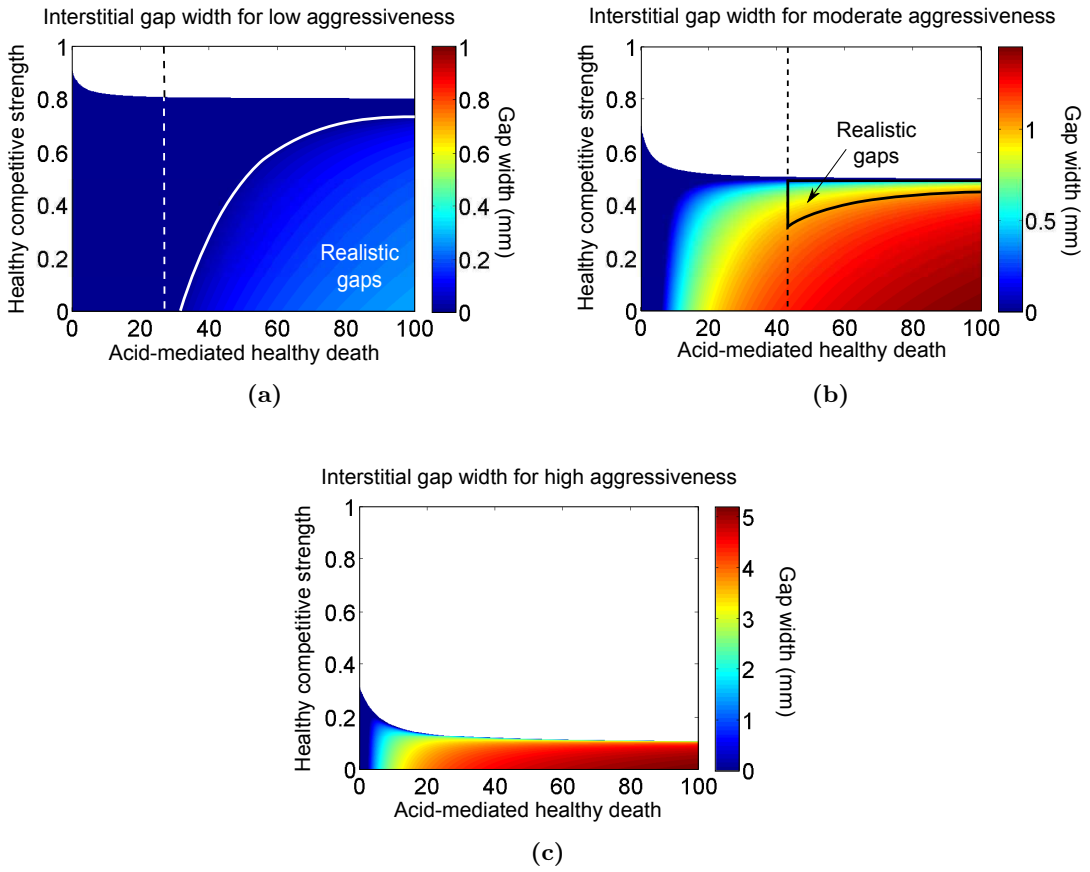

Figure 3.8: Effect of tumour aggressiveness on the interstitial gap width. Interstitial gap width, as found in Section 3.2.3, is plotted (colour gradients, redimensionalised to millimetres) with the healthy acid-mediated death rate (d_1) and healthy competitive strength (a_1) on the x and y axes, respectively. White regions mark parameter combinations that are outside the regime of travelling wave solutions. (a) The tumour acid-mediated death rate (d_2) is set to $0.8d_1$ and tumour competitive strength (a_2) to $1.2a_1$, representing mildly aggressive tumours; (b) d_2 is set to $0.5d_1$ and a_2 to $2a_1$, representing moderately aggressive tumours; (c) d_2 is set to $0.1d_1$ and a_2 to $10a_1$, representing highly aggressive tumours. The remaining parameters are $r_2 = 1$, $D = 4 \cdot 10^{-5}$, and $c = 70$. The dashed lines represent the threshold pH value of 6.3, below which tumours are not seen clinically (Park et al. 1999). To the right of the dashed lines, the tissue pH near the tumour core—calculated by converting the acid profile (w) near the left domain boundary to pH units—is above this threshold, meaning the tumours are clinically plausible. In (c) the pH is lower than the threshold of 6.3, and hence the tumours are unrealistic, for all parameter choices. Gap widths on the order of 0.1 millimetres are within the range observed experimentally in Gatenby and Gawlinski (1996); allowing widths of up to 1 millimetre, and incorporating the pH information, regions of parameter space giving rise to biologically realistic interstitial gaps are outlined by the solid curves (white in (a) and black in (b)). Despite the occurrence of gaps ranging to 5 millimetres in width in (c), none is realistic due to the implausibly low pH values.

3.3.3 Tumour morphology and invasive speed

Some past experiments have indicated a lack of correlation between speed of invasion and the density of healthy cells, stroma, and other material mixed in with the tumour (Dvorak et al. 1983). Sampling our (a_1, a_2, d_1, d_2) parameter space while holding all other parameters constant reveals the presence of a negative correlation between wavespeed and healthy density (Figure 3.9a); and a positive non-linear correlation between wavespeed and tumour density, albeit with considerable spread (Figure 3.9b). In the following section we summarise the implications of the results presented here.

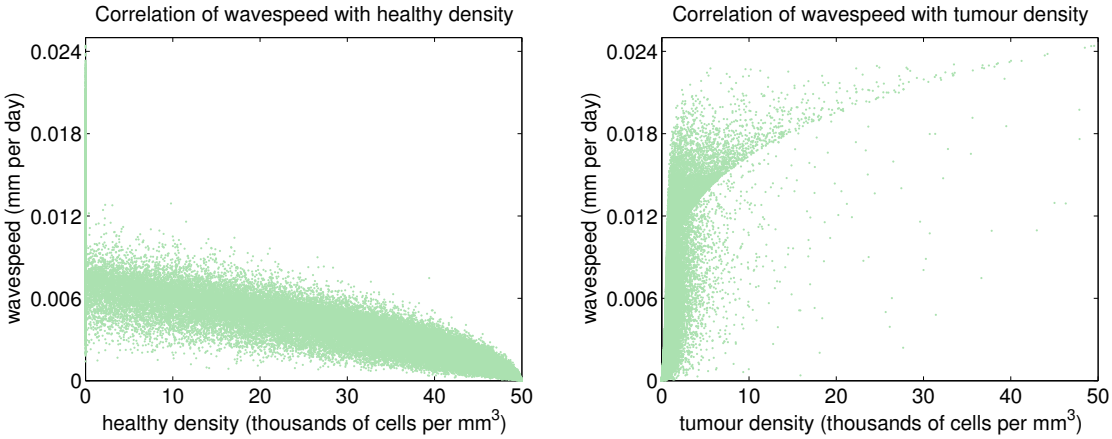

Figure 3.9: Correlation of invasive speed with densities behind the front. Correlation between invasive speed and density of cells remaining behind the advancing front, obtained by taking 10^5 random samples from uniform distributions of a_1, a_2, d_1, and d_2 in the invasive regimes, subject to the ranges and biologically motivated constraints listed in Table 2.2 (that is, $a_{1,2} = \text{Unif}(0, 1)$ and $d_{1,2} = \text{Unif}(0, 100)$), with the remaining parameters held constant at $r_2 = 1$, $D = 4 \cdot 10^{-5}$, and $c = 70$, and applying the results from our travelling wave analysis. (a) Tumour wavespeed, in millimetres per day, is plotted against the density of healthy cells near the core, in thousands of cells per cubic millimetre. (b) Tumour wavespeed is plotted against the density of tumour cells near the core, with the same units as in (a). The tissue carrying capacity for both cell types is 50 thousand cells per cubic millimetre.

3.4 Conclusions from our generalised model of acid-mediated tumour invasion

In this chapter we have demonstrated that our generalised model of acid-mediated invasion, which we developed in Chapter 2, remains amenable to mathematical analysis. Through a travelling wave analysis in an asymptotic framework, we have fully characterised the

invasive behaviours in the parameter space, finding these to be consistent both with our own numerical solutions (Figure 3.6) and with previous experimental and mathematical descriptions of the system (Gatenby and Gawlinski 1996, Fasano et al. 2009). It should be noted that existence of the minimum wavespeed has not been proven here, and this remains a general open problem for travelling wave systems with multiple species. Our numerical simulations in Chapter 2 have indicated, however, that the minimum wavespeed is indeed established, at least for the parameter ranges we have considered.

We note that our asymptotic analysis was concerned with dynamics at the leading edge of the tumour front and cannot provide insight into the non-monotonic tumour peaks observed numerically in Chapter 2. It would be interesting to pursue an analysis of this feature, following travelling wave analyses carried out on non-monotonic waves of tumour-encapsulating connective tissue (Sherratt 1993, 1999) and tumour profiles with invasive speeds exhibiting biphasic dependence on healthy tissue properties (Marchant et al. 2006).

Additionally, we have made references to "healthy tissue" throughout Chapters 2 and 3, but this is an abstract term that encompasses multiple cell types making up the stroma (for example, fibroblasts and immune cells) as well as the extracellular matrix and a diverse set of chemical signals. Many models address the composition of this healthy tissue more directly, such as those by Perumpanani et al. (1996), Jackson and Byrne (2002), Sherratt et al. (2009), Painter et al. (2010), and Martin et al. (2010) which explicitly consider interactions between the tumour and the extracellular matrix.

Our finding that the interstitial gap is sensitive to parameter choice (Figure 3.8) leads to the modelling prediction that the gap is perhaps unlikely to be a widespread feature of tumour invasion. This finding is not inconsistent with the experimental results in Gatenby and Gawlinski (1996), in which hypocellular interstitial gaps along tumour-host interfaces were observed in 14 out of 21 fixed specimens and appeared less well-defined in unfixed specimens (see Figure 2.3 for a representative fixed versus unfixed specimen). We note that our model predicts gaps in mildly aggressive tumours rather than the highly aggressive tumours predicted by the Gatenby and Gawlinski (1996) formulation, most likely due to our inclusion of the biologically realistic, but aggression-limiting, features of tumour cell death and cellular competition, as well as our experimentally-motivated lower limit on tissue pH.

The Gatenby and Gawlinski (1996) model was an elegant first investigation of the acid-mediated invasion hypothesis, and the generalisation we presented in Chapter 2 and have analysed here provides a formulation applicable to a wider variety of tumour scenarios; but some implicit over-simplifications underlying the hypothesis remain to be investigated. This is highlighted by the discrepancy between the correlations we have found between invasive

speed and cell densities inside the tumour (Figure 3.9) and past experimental results that saw no such correlations (Dvorak et al. 1983), which indicate that something more must be influencing the system dynamics than we have considered here. We will next examine two possible factors as follows.

First, as discussed in Chapter 1, the acid-mediated invasion hypothesis characterises lactate as a cellular waste product and assumes that tumour metabolism is exclusively glycolytic. Recently, however, it has been shown that even highly glycolytic tumours retain at least some mitochondrial function (Bouzier-Sore et al. 2001, DeBerardinis et al. 2008, Vander Heiden et al. 2009, Mathupala et al. 2010), and furthermore that tumour cells can consume lactate oxidatively as a metabolic substrate (Cheeti et al. 2006, Sonveaux et al. 2008, Pavlides et al. 2009, 2010). In Chapter 4 we will develop a minimal reaction-diffusion model to explore the possibility of glucose-lactate metabolic cooperation within tumours.

Secondly, the acid-mediated invasion hypothesis is a coarse-grained description of tumour dynamics that considers only extracellular acidity. It is likely, though, that tissue-scale consequences of the glycolytic phenotype emerge from the intricate biochemical mechanisms by which tumour cells handle their metabolically-derived intracellular acid loads and govern the spatial coordination of their intracellular pH (Webb et al. 2011, Jean et al. 1985, Stewart et al. 2009, Swietach et al. 2009, 2010, Hulikova et al. 2011), as was introduced in Chapter 1; hence, a finer-scale understanding of tumour pH may be necessary for true insight into acid-mediated invasion. We will pursue this topic in Chapters 5 and 6.

Chapter 4

A minimal spatial model of glucose-lactate metabolic cooperation

This chapter is the product of a collaboration, with the work divided as follows: The project was conceived by Prof. Philip Maini and Prof. Victor Pérez-García[*]; the model was developed by Jessica McGillen and the group of Prof. Pérez-García; numerical solutions and strategies for parameter space exploration were designed and implemented by Jessica McGillen; and experiments were planned by Jessica McGillen and Dr. Catherine Kelly[†] and carried out by Dr. Kelly.

Historically, studies of the Warburg effect in developing tumours characterised lactate, generated by conversion of pyruvate during glycolysis, as merely a cellular waste product, and a view of tumours as greedy glucose consumers prevailed. The past several years have brought changes to these ideas, however, beginning with the discovery that even highly glycolytic tumours retain at least some mitochondrial function (Bouzier-Sore et al. 2001, DeBerardinis et al. 2008, Vander Heiden et al. 2009, Mathupala et al. 2010). Several sets of experiments by Cheeti et al. (2006), Pavlides et al. (2009, 2010), and Sonveaux et al. (2008) now indicate that tumour cells can consume lactate oxidatively as a metabolic substrate, either as a replacement fuel for glucose or concurrently with it. This lactate consumption has been shown to occur via oxidative phosphorylation (OXPHOS) and to depend upon uptake through the monocarboylate transporter MCT1. On the basis of these discover-

[*]Institute of Applied Mathematics in Science and Engineering, University of Castilla-La Mancha, Spain
[†]Gray Institute for Radiation Oncology and Biology, Oxford University

ies, Sonveaux et al. (2008) put forward the symbiosis hypothesis for spatial glucose-lactate metabolic cooperation in tumours, discussed in Chapter 1 and summarised in Figure 4.1 (reproduced from Chapter 1 for the reader's convenience).

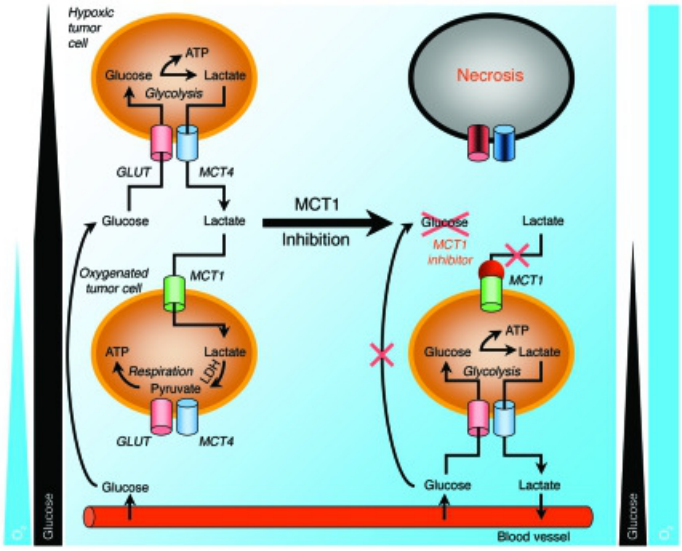

Figure 4.1: Metabolic symbiosis as hypothesised by Sonveaux et al. (2008). In a wild-type tumour (left panel), cells in the oxygenated environment near a capillary take up lactate for consumption by oxidative phosphorylation, gated by monocarboxylate transporter 1 (MCT1), while cells in the hypoxic environment of the tumour interior take up glucose for consumption by (anaerobic) glycolysis, gated by glucose transporters (GLUT) and producing lactate, which is then extruded by monocarboxylate transporter 4 (MCT4). This cooperation is thought to preserve glucose for the tumour interior. Sonveaux et al. postulated that inhibiting MCT1 (right panel) would force cells near the capillary to consume glucose instead of lactate, starving interior cells and increasing oxygenation into the tumour. Image reproduced with permission from the *Journal of Clinical Investigation*.

As was discussed in Chapter 1, the evidence in favour of *in vivo* symbiosis presented by Sonveaux et al. (2008) was later questioned by Busk et al. (2011), and controversy remains as to whether the symbiosis hypothesis is an important feature of tumours and, especially, whether MCT1 inhibition of this symbiosis can cause the detrimental effects claimed by Sonveaux et al. (2008). There is scope for mathematics to help resolve some of this controversy: by translating the dual glucose-lactate metabolic system into a mathematical model, with underlying assumptions made explicit, it may be possible to shed light on whether *in vivo* symbiosis as proposed by Sonveaux et al. (2008) is plausible in principle, and which of the two sets of experimental results is more likely to represent clinical reality.

4.1 A non-spatial metabolic model by Mendoza-Juez et al. (2012)

Mendoza-Juez et al. (2012) developed a preliminary mathematical description of dual glucose-lactate tumour metabolism *in vitro*. This model was non-spatial and captured the metabolic behaviour of two fractional populations of tumour cells, one oxidative and the other glycolytic, in the presence of glucose and lactate. Denoting these oxidative and glycolytic fractions as $P_o(t)$ and $P_g(t)$, respectively, and the concentrations of glucose and lactate as $G(t)$ and $L(t)$, respectively, all as functions of time t, and assuming that cellular consumption of metabolites follows Michaelis Menten-type kinetics, the Mendoza-Juez et al. (2012) equations are

$$\frac{dP_o}{dt} = \overbrace{\frac{1}{\tau_o}\left(1 - \frac{P_o + P_g}{P^*}\right)P_o}^{\text{logistic cell growth}} + \overbrace{\frac{1}{\tau_{go}}\chi_L(L)P_g}^{\substack{\text{switch from}\\ \text{glycolytic to}\\ \text{oxidative}\\ \text{metabolism}}} - \overbrace{\frac{1}{\tau_{og}}(1-\chi_L(L))\chi_G(G)P_o}^{\substack{\text{switch from}\\ \text{oxidative to}\\ \text{glycolytic}\\ \text{metabolism}}}, \tag{4.1}$$

$$\frac{dP_g}{dt} = \overbrace{\frac{1}{\tau_g}\left(1 - \frac{P_o + P_g}{P^*}\right)P_g}^{\text{logistic cell growth}} + \overbrace{\frac{1}{\tau_{go}}\chi_L(L)P_g}^{\substack{\text{switch from}\\ \text{glycolytic to}\\ \text{oxidative}\\ \text{metabolism}}} - \overbrace{\frac{1}{\tau_{og}}(1-\chi_L(L))\chi_G(G)P_o}^{\substack{\text{switch from}\\ \text{oxidative to}\\ \text{glycolytic}\\ \text{metabolism}}}, \tag{4.2}$$

$$\frac{dG}{dt} = -\overbrace{\beta_o\frac{\alpha_G G}{\alpha_G G + \alpha_L L + N_*}P_o}^{\substack{\text{oxidative}\\ \text{consumption}\\ \text{of glucose}}} - \overbrace{\beta_g\frac{G}{G+G^*}P_g}^{\substack{\text{glycolytic}\\ \text{consumption}\\ \text{of glucose}}}, \tag{4.3}$$

$$\frac{dL}{dt} = -\overbrace{\beta_L\frac{\alpha_L L}{\alpha_G G + \alpha_L L + M_*}P_o}^{\substack{\text{oxidative}\\ \text{consumption}\\ \text{of lactate}}} + \overbrace{2\beta_g\frac{G}{G+G_*}P_g}^{\substack{\text{glycolytic}\\ \text{production}\\ \text{of lactate}}}. \tag{4.4}$$

Here, τ_o and τ_g denote the doubling times of oxidative and glycolytic cells, respectively; τ_{go} and τ_{og} the time taken for a cell to switch its metabolism from glycolytic to oxidative or from oxidative to glycolytic, respectively; β_o and β_L the maximal consumption rates of glucose and lactate, respectively, by oxidative phosphorylation; β_G the maximal consumption rate of glucose by glycolysis; M_*, N_*, and G_* the half-saturation points of the corresponding Michaelis Menten consumption curves; and α_G and α_L the relative expression of glucose and monocarboxylate transporters, respectively, at the cell membrane. Additionally, χ_L and χ_G are Heaviside functions that capture the dependence of the metabolic switching on lactate levels (such that cells switch to oxidative consumption of lactate when lactate is

high) and of glycolysis on the availability of glucose, as follows:

$$\chi_L(L) = \frac{1}{2}[1 + \tanh(\gamma(L - L_*))], \tag{4.5}$$

$$\chi_G(G) = \begin{cases} 0 & \text{if } G \leq G_{\min}, \\ 1 & \text{if } G > G_{\min}, \end{cases} \tag{4.6}$$

where $G_{\min}$ represents the minimum concentration of glucose that cells can take up. Further details and justification of Equations (4.1)-(4.4) can be found in Mendoza-Juez et al. (2012).

In brief, Mendoza-Juez et al. (2012) validated Equations (4.1)-(4.4) against five human cancer cell lines with varying characteristic metabolic rates (Elstrom et al. 2004, Sonveaux et al. 2008, Voisin et al. 2010) and successfully replicated the experimentally observed behaviours. Their study supports the idea that tumour cells can consume lactate and that this capability, conferred by MCT1 expression, varies among cell lines in an *in vitro* environment; but it leaves unanswered the question of whether, in principle, metabolic symbiosis is plausible *in vivo*.

The symbiosis hypothesis is intrinsically related to spatial tumour features, as the metabolism of each cell is responsive to hypoxia cues in the local microenvironment and hence based, at least in part, on relative distance from the capillary bed. Consequently, to fully capture the symbiosis hypothesis, a spatial model is needed.

In this chapter we develop a minimal spatial model of glucose-lactate metabolism and use it to interrogate both the plausibility of metabolic symbiosis *in vivo* and the potential effectiveness of blocking this symbiosis as a radiosensitisation strategy. We find that symbiosis is a robust feature of our model system, and, although it does not directly rescue tumours from necrosis, on average its effects on the tumour dynamics are in line with expectations. However, symbiosis does require the cells' metabolic activity to be several orders of magnitude higher than what is commonly observed *in vitro*. Whether such levels are plausible remains an open question. Furthermore, we demonstrate experimentally that U87 glioblastoma tumours are likely to fall in a parameter regime that produces only weakly symbiotic behaviour, raising the question of whether symbiosis is likely to be exhibited by highly malignant tumours in general. Finally, we simulate MCT1 inhibition and discover that, in agreement with Busk et al. (2011), this blocking of symbiosis does not cause the expected increase in necrosis. MCT1 inhibition does, however, cause an increase in tissue oxygenation that is highly correlated with the extent of hypoxia that was exhibited by the wildtype system, suggesting that it may be an effective strategy for radiosensitising lactate-consuming tumours with or without symbiosis.

4.2 Our model

Throughout this study, we will aim for a model of minimal complexity, conjecturing that if metabolic symbiosis is not possible in a simplified scenario where glucose and lactate dominate the metabolic landscape, then it is unlikely to be a significant feature in more complicated scenarios. We do consider it vital for our model to be spatial, however, as the metabolic symbiosis hypothesis *in vivo* is a spatial feature; hence, a minimal system of partial differential equations provides the relevant level of complexity.

4.2.1 Motivation and framework

The model we develop here is a direct extension, with simplifications, of the model proposed by Mendoza-Juez et al. (2012) to a spatial tumour scenario. As such, it captures behaviours that are qualitatively similar to those with which the non-spatial model was verified, namely patterns of dual consumption of glucose and lactate that vary across tumour cell lines depending on the relative expression of membrane transporters. However, we simplify the modelling framework considerably by avoiding the assumption of metabolic switching, and instead suppose that cells can use both glycolysis and oxidative phosphorylation given their relative expression of the requisite membrane transporters and the appropriate environment conditions (e.g. oxidative phosphorylation (OXPHOS) requires oxygen). This change allows us to avoid imposing an artificial dichotomy between the metabolic pathways. We also depart slightly from the Mendoza-Juez et al. (2012) model by neglecting consumption of glucose by oxidative phosphorylation, as experiments have shown this to be a minor factor relative to glycolysis in proliferative cells (Pfeiffer et al. 2001, Vander Heiden et al. 2009, Koppenol et al. 2011).

We model a one-dimensional ray in polar coordinates extending out from the core of a tumour, under the assumption of spherical symmetry, to a spherical shell of capillaries 0.02 cm from the core. This modelling scenario corresponds either to a small avascular tumour or, more interestingly (and more realistically biologically), to pockets of tissue inside a larger vascularised tumour. Large tumours exhibit heterogeneities in oxygen supply due to capillary crushing and leakiness of tumour-induced vascular networks (Gatenby et al. 2007, Gillies and Gatenby 2007, Basanta et al. 2011), and hence our model can be viewed as a simplified representation of localised metabolic features in a heterogeneous tumour.

4.2.2 Equations and terms

The species in our model are dependent upon time, t, in days, and one-dimensional spatial coordinate, r, in centimetres from the tumour core, or interior of the local tumour pocket. These species are cell density, $C(r,t)$, normalised by the tissue carrying capacity; the tissue concentration of glucose, $G(r,t)$, in mM; the tissue concentration of lactate, $L(r,t)$, in mM; and the partial pressure of oxygen, $O(r,t)$, in mM. In Chapters 2 and 3 we considered the impact of tumour-healthy competition on tumour invasion; but here we model only the tumour tissue, as inclusion of the underlying stroma could introduce complicated metabolic interactions (Pavlides et al. 2009, 2010), and we wish to keep the modelling scenario restricted to a simple in-principle test of the symbiosis hypothesis as it was stated in Sonveaux et al. (2008).

We let ρ represent the rate of tumour cell growth; δ the rate of tumour cell necrosis; and κ_G and κ_L the maximal rates of consumption of glucose and lactate, respectively, by the tumour population. Additionally defining switch functions capturing tumour sensitivity to hypoxia, glucose deprivation, severe acidosis, and severe anoxia as ψ_H, ψ_G, ψ_A, and ψ_N, respectively, our model equations are

$$C_t = \overbrace{\frac{\Delta_C}{r^2}[r^2 C_r]_r}^{\text{cellular diffusion}} + \overbrace{\rho C\left(1-\frac{C}{C_*}\right)}^{\text{logistic growth}} - \overbrace{\delta\left(\psi_G+\psi_A+\psi_N\right)C}^{\substack{\text{necrosis by starvation,}\\ \text{acidosis, or anoxia}}}, \tag{4.7}$$

$$G_t = \overbrace{\frac{\Delta_G}{r^2}[r^2 G_r]_r}^{\text{diffusion}} - \overbrace{\kappa_G \frac{\alpha_G G}{\alpha_G G+\alpha_L L+\eta_G} C}^{\text{consumption by glycolysis}}, \tag{4.8}$$

$$L_t = \overbrace{\frac{\Delta_L}{r^2}[r^2 L_r]_r}^{\text{diffusion}} + \overbrace{2\kappa_G \frac{\alpha_G G}{\alpha_G G+\alpha_L L+\eta_G} C}^{\text{production by glycolysis}} - \overbrace{\kappa_L \frac{\alpha_L L}{\alpha_G G+\alpha_L L+\eta_L}\psi_H C}^{\text{consumption by OXPHOS}}, \tag{4.9}$$

$$O_t = \overbrace{\frac{\Delta_O}{r^2}[r^2 O_r]_r}^{\text{diffusion}} - \overbrace{3\kappa_L \frac{\alpha_L L}{\alpha_G G+\alpha_L L+\eta_L}\psi_H C}^{\text{consumption by OXPHOS}}, \tag{4.10}$$

where Δ_C, Δ_G, Δ_L, and Δ_O denote the diffusion coefficients of tumour cells, glucose, lactate, and oxygen, respectively. We assume a Michaelis-Menten form for the metabolite uptake functions such that η_G and η_L represent the half-saturation points for uptake of glucose and lactate, respectively.

Although expression of metabolite transporters is tied to the microenvironment *in vivo*, with GLUT expression being hypoxia-induced (Burgman et al. 2001, Airley et al. 2001, Williams et al. 2002, Wincewicz et al. 2007, Liu et al. 2009) and MCT1 expression being hypoxia-repressed (Berra et al. 2003, Marxsen et al. 2004, Sonveaux et al. 2008, Feron 2009,

Semenza 2010), different cell lines exhibit different characteristic levels of expression *in vitro* (Elstrom et al. 2004, Sonveaux et al. 2008, Voisin et al. 2010) and it is possible that cells retain these features *in vivo* in the form of characteristic maximal levels of expression. The parameters α_G and α_L in Equations (4.8)-(4.10) allow for this possibility: if the cells' characteristic capacity for MCT1 expression is high relative to that for GLUT, then we will have $\alpha_L > \alpha_G$; conversely, if the characteristic capacity for MCT1 expression is low relative to that for GLUT, then we will have $\alpha_L < \alpha_G$. If $\alpha_G = \alpha_L$ then the cells have no characteristic capacities *in vivo* and instead transporter expression is determined entirely by the microenvironment. We note that Equations (4.8)-(4.10) preserve the appropriate stoichiometry of the metabolic pathways; that is, two molecules of lactate are produced per molecule of glucose consumed by the glycolytic pathway and three molecules of oxygen are consumed per molecule of lactate processed by OXPHOS.

Tumour cells may become necrotic under severely glucose-starved, acidic, or anoxic conditions. We model this in Equation (4.7) as a sum of simple sensitivity switches—ψ_G for glucose starvation, ψ_A for acidosis, and ψ_N for anoxia—such that the speed of cell death increases as conditions become harsher. Additionally, OXPHOS is sensitive to hypoxia, which we represent as an oxygen-dependent switch, ψ_H, multiplying the uptake of lactate in Equations (4.9) and (4.10). These four sensitivity switches are

$$\psi_G = \begin{cases} 0 & \text{if } G > \sigma_G, \\ 1 & \text{otherwise;} \end{cases} \tag{4.11}$$

$$\psi_A = \begin{cases} 1 & \text{if } L > \sigma_A, \\ 0 & \text{otherwise; and} \end{cases} \tag{4.12}$$

$$\psi_N = \begin{cases} 0 & \text{if } O > \sigma_N, \\ 1 & \text{otherwise;} \end{cases} \tag{4.13}$$

$$\psi_H = \begin{cases} 1 & \text{if } O > \sigma_H, \\ 0 & \text{otherwise;} \end{cases} \tag{4.14}$$

where σ_G denotes the minimum glucose concentration that cells require for survival, σ_A the lactate concentration corresponding to the maximum tolerable level of tissue acidity, σ_N the oxygen threshold for severe anoxia, and σ_H the oxygen threshold for hypoxia. We note that σ_G and σ_A are difficult to measure experimentally—the latter due to the non-linear relationship between metabolically-derived lactate and resultant tissue acidity (to be explored further in Chapter 5 and 6)—and hence these constants are somewhat abstract. Nevertheless, we will make the reasonable choices of setting σ_G to be small and σ_A to be above the lactate level typically observed in tumour tissue (Herholz et al. 1992).

We can make the slight simplification of scaling the tumour cell density by the tissue carrying capacity, such that $\tilde{C} = C/C_*$. Further letting $a = \alpha_L/\alpha_G$, $n_G = \eta_G/\alpha_G$, $n_L = \eta_L/\alpha_L$, $k_G = \kappa_G C_*$, and $k_L = \kappa_L C_*$, and dropping the tilde for convenience, we have

$$C_t = \frac{\Delta_C}{r^2}[r^2 C_r]_r + \rho C(1-C) - \delta\left(\psi_G + \psi_A + \psi_N\right) C, \tag{4.15}$$

$$G_t = \frac{\Delta_G}{r^2}[r^2 G_r]_r - k_G \frac{G}{G + a_L L + n_G} C, \tag{4.16}$$

$$L_t = \frac{\Delta_L}{r^2}[r^2 L_r]_r + 2k_G \frac{G}{G + aL + n_G} C - k_L \frac{L}{G/a + L + n_L} \psi_H C, \tag{4.17}$$

$$O_t = \frac{\Delta_O}{r^2}[r^2 O_r]_r - 3k_L \frac{L}{G/a + L + n_L} \psi_H C. \tag{4.18}$$

In keeping with Mendoza-Juez et al. (2012), we have only partially nondimensionalised our system, but for comparison a full nondimensionalisation is presented in Appendix E. Finally, for later notational convenience we define the uptake functions

$$\phi_G = \frac{G}{G + aL + n_G}, \tag{4.19}$$

$$\phi_L = \frac{L}{G/a + L + n_L}. \tag{4.20}$$

Boundary conditions are zero-flux for all species in the tumour core, under our assumption of spherical symmetry, and we retain this zero-flux condition for the tumour population at the edge of the tumour (at $r = R$ where R is the radius of a typical avascular tumour, taken here to be 0.02 cm), such that the cells cannot migrate beyond the capillary shell. Metabolites are permitted to exchange with the capillary shell as follows (for a generic metabolite, M):

$$\frac{\partial M}{\partial r}|_{r=R} = J_M(M_v - M), \tag{4.21}$$

where J_M is the coefficient of exchange and M_v the concentration of the metabolite in the vessels. The vessels act as a source for glucose and oxygen and, commonly, as a sink for lactate. In exceptional cases of chronic hyperlactatemia (Huckabee 1961, Levraut et al. 1998, Boubaker et al. 2001) or insulin-induced hypoglycemia (Boumezbeur et al. 2010), the capillary shell may act instead as a source for lactate, but we do not consider this relatively rare phenomenon here. The vessel concentrations of glucose, lactate, and oxygen (G_v, L_v, and O_v, respectively) and corresponding exchange coefficients (J_G, J_L, and J_O) can be found in Table 4.1.

We impose initial conditions such that the tumour cells have a uniform density of half the carrying capacity across the domain, and metabolite concentrations take a uniform value equal to their vessel concentrations. The steady-state results of our system are qualitatively insensitive to our choice of initial conditions, and we have chosen this particular configuration to facilitate a clear interpretation of any necrosis in the tumour core that we may see relative to the edge.

4.2.3 Metrics for model exploration

'Symbiosis' as proposed by Sonveaux et al. (2008) is a qualitative and imprecisely defined feature of the tumour system. Nevertheless, we can consider it by determining the fraction of total metabolic consumption occupied by glycolysis, denoted Φ_g, and the fraction occupied by oxidative phosphorylation of lactate, denoted Φ_l; these are given by:

$$\Phi_g = \frac{k_G \phi_G}{k_G \phi_G + k_L \phi_L \psi_H}, \tag{4.22}$$

$$\Phi_l = \frac{k_L \phi_L \psi_H}{k_G \phi_G + k_L \phi_L \psi_H}. \tag{4.23}$$

We consider symbiosis to occur when glycolysis dominates over oxidative phosphorylation of lactate (OXPHOS) in the hypoxic core, and OXPHOS dominates over glycolysis in the oxygenated region near the tumour edge. Further, we can consider the 'strength' of symbiosis to be given by the degree of dominance OXPHOS takes over glycolysis in the oxidative region. We are also interested in the occurrence of necrosis, or a reduction in tumour density in the core relative to the edge, and the extent of hypoxia, or the location along the tumour domain where oxygen crosses the hypoxia threshold, σ_H. Accordingly, letting θ denote symbiosis, γ denote necrosis, and λ denote the extent of hypoxia, we define the metrics

$$\theta = \begin{cases} \max\{\Phi_l(\text{edge}) - \Phi_g(\text{edge})\} & \text{if } \Phi_g > \Phi_l \text{ in core and } \Phi_l > \Phi_g \text{ near edge,} \\ 0 & \text{otherwise;} \end{cases} \tag{4.24}$$

$$\gamma = C(\text{edge}) - C(\text{core}); \tag{4.25}$$

$$\lambda = r(O = \sigma_H); \tag{4.26}$$

with λ subject to the limiting cases that $\lambda = 0$ if the whole tissue is normoxic and $\lambda = R$ if the whole tissue is hypoxic.

4.3 Mathematical and statistical methods

4.3.1 Numerical solutions

Throughout this chapter, Equations (4.15)-(4.18) are solved numerically using the Method of Lines (Appendix B.5). By this method, we discretise space using a very fine step ($dr = 10^{-4}$ cm) and solve the resulting system of coupled ordinary differential equations through time using Matlab's inbuilt ODE15s solver to accommodate stiffness.

Numerically simulating Equations (4.15)-(4.18) with a representative choice of parameters reveals that an end-time of 200 days is sufficient to achieve a steady state in which all species have reached a plateau (Figure 4.2).

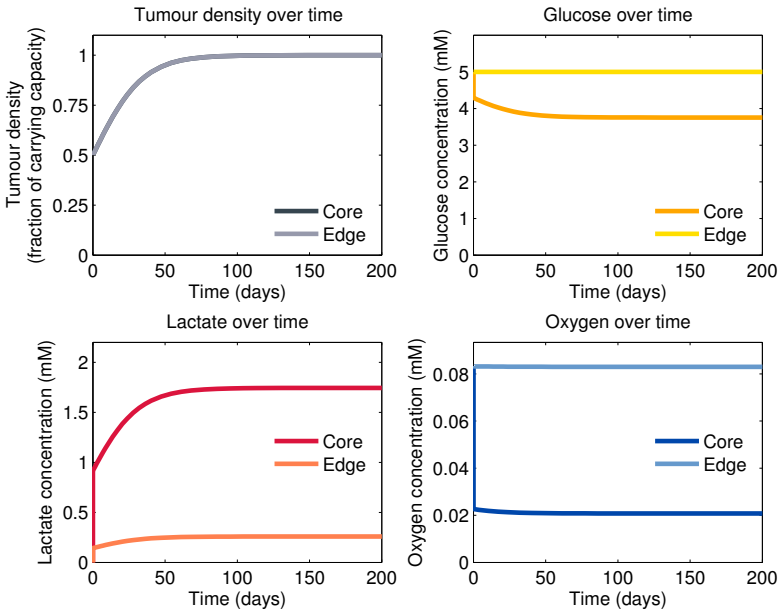

Figure 4.2: Temporal behaviour of Equations (4.15)-(4.18)**.** Over-time profiles in the tumour core (darker colours) and at the tumour edge (lighter colours) for the tumour cell density (greys) and concentrations of glucose (oranges), lactate (reds), and oxygen (blues), for a representative choice of parameters: $a = 1$, $n_L = 1$, $n_G = 1$, $k_L = 10^4$, and $k_G = 10^3$, with the remaining parameters as listed in the top portion of Table 4.1. All profiles reach steady state well before the simulation end-time of 200 days.

For the remainder of this chapter, we will be concerned with spatial behaviours established at steady state. Hence, all simulations are run to an end-time of 200 days; parameters are listed in Table 4.1 and discussed further in Section 4.3.2.

In Figure 4.2 it appears that we have fast early-time dynamics, possibly due to the magnitude of the uptake rate parameters k_G and k_L. A nondimensionalisation (for example, along the lines of the one presented in Appendix E) could help to elucidate the relative timescales driving the system, and an asymptotic analysis could potentially generate insight. However, we wish to explore the full range of possible parameter values for our model—including smaller choices for k_L and k_G—and therefore turn our attention to an exploration of some effective numerical methods by which to obtain a comprehensive picture of the fundamental parameter space of the model. Such methods can serve as a kind of proxy for analytical insight in differential equation settings, and have an elegance and power of their own.

4.3.2 Multivariate sensitivity analysis

In any given model of a biological system, some of the fundamental model parameters may be well-determined, but others either cannot be measured accurately due to experimental limitations, or are of interest where variation is an important biological feature—for example, across different tumours. To explore the sensitivity of a system to its parameters that fall into the latter category, i.e. are of interest as having the potential to vary, it is possible to carry out a standard single-parameter or local sensitivity analysis in which one parameter is varied at a time while the others are held constant at 'baseline' or reference values (Marino et al. 2008). However, such an approach, while common, loses information about underlying uncertainties—for example in estimation of the 'baseline' values—and also about parameter interaction effects, and so would provide incomplete insight into the system (James and McCulloch 1990, Marino et al. 2008, Saltelli and Annoni 2010).

To escape the limitations of one-at-a-time sensitivity, we can simply allow the parameters of interest to vary simultaneously, and take random samples from the resulting multidimensional parameter space (Saltelli et al. 2008) for use in repeated numerical solutions of the model system. We can then examine the resulting distribution of model behaviours using histograms, scatterplots, and further statistical methods as required. While more sophisticated methods for sensitivity analysis exist (Wu et al. 2013), this straightforward sampling approach is sufficient to avoid the pitfalls of single-parameter sensitivity analyses while remaining computationally tractable.

The parameters in Equations (4.15)-(4.18) which we fix and consider 'background' parameters, are listed with their sources in the top portion of Table 4.1. The remaining five parameters, which are the metabolic parameters and therefore of interest as potentially varying across tumours, are sampled from the ranges listed in the lower portion of Table

4.1, for repeated numerical solutions of Equations (4.15)-(4.18) to steady state as described in Section 4.3.1.

Global, multidimensional sensitivity analyses have been gaining traction in systems biology (Marino et al. 2008) and nonlinear modelling (Homma and Saltelli 1996), particularly of ecology (De'ath and Fabricius 2000, Fieberg and Jenkins 2005, Cutler et al. 2007, Cariboni et al. 2007) and infectious diseases (Wu et al. 2013). Yet, to our knowledge, we are the first to apply such approaches to tumour metabolism modelling. In the following, we introduce a selection of statistical algorithms that exploit this multidimensional, sampling-based method for sensitivity analysis.

4.3.2.1 Principal component analysis

Principal component analysis (PCA) is a simple, non-parametric approach for extracting relevant information from large, complex datasets by reducing their dimensionality (Hastie et al. 2009). The PCA transformation is defined such that the first principal component captures as much variability in the data as possible, and each subsequent component captures the largest possible amount of the remaining variability, subject to the constraint that the new component is uncorrelated with (i.e. orthogonal to) the preceding components. Computationally, principal components are determined by calculating the eigenvectors and eigenvalues of the data covariance matrix, equivalent to finding an axis system that renders the covariance matrix diagonal; as such, PCA is the simplest of many eigenvector-based techniques for multivariate analysis. We outline the process in more detail below.

If a dataset $\mathbf{X}$ is arranged as an m-by-n matrix such that each of n observations comprises a column vector of m variables (here, parameters), then each observation (here, a sampled point from our model parameter space) is a vector that lies in an m-dimensional vector space spanned by a basis. The goal of PCA is to find an alternative basis which is a linear combination of the original basis vectors and expresses the dataset more meaningfully. Note that PCA is a linear method; as such, it is stringent, because most complex systems are nonlinear, but also powerful, because it renders the problem amenable to linear algebra.

Letting $\mathbf{X}$ and $\mathbf{Y}$ denote m-by-n matrices related by a linear transformation $\mathbf{P}$, such that $\mathbf{X}$ is the original dataset and $\mathbf{Y}$ is a re-representation of it, and further defining $\vec{p}_i$ as the rows of $\mathbf{P}$, $\vec{x}_i$ as the columns of $\mathbf{X}$, and $\vec{y}_i$ as the columns of $\mathbf{Y}$, a change of basis is represented by the equation $\mathbf{PX} = \mathbf{Y}$. The rows of $\mathbf{P}$, $\{\vec{p}_1, ..., \vec{p}_m\}$ are a set of new basis vectors for expressing the columns of $\mathbf{X}$: by construction, the principal components.

Table 4.1: Parameters in Equations (4.15)-(4.18). Model parameters (with dimensions, as we have only partially scaled the system): listed are value estimates for parameters that we consider fixed in order to set up a consistent background against which to view the dynamics of tumour glucose-lactate consumption (top portion), and ranges for our metabolic parameters that are of interest as varying in a meaningful way across tumours (bottom portion).

	Parameter	Value	Units	Source
Fixed	Δ_C	$5.7 \cdot 10^{-6}$	cm^2/day	Rockne et al. (2010)
	Δ_G	0.0346	cm^2/day	Jiang et al. (2005)
	Δ_L	0.0518	cm^2/day	$1.5\Delta_G$, due to size
	Δ_O	0.864	cm^2/day	Rockne et al. (2010)
	ρ	1/17	1/day	Rockne et al. (2010)
	δ	1/10	1/day	Estimated
	σ_H	0.0278	mM	Daşu et al. (2003)
	σ_G	0.1	mM	Chosen to be small
	σ_A	20	mM	Chosen to be large
	σ_N	0.001	mM	Chosen to be small
	J_G	10^3	1/cm	High as diffusion across vessel wall is facilitated (McEwen and Reagan 2004)
	J_O	10^3	1/cm	High as the capillary wall offers negligible resistance to oxygen diffusion (Blum 1960)
	J_L	10	1/cm	Assumed moderate for functioning vessels
	G_v	5	mM	Physiological (Sherwood 2007)
	L_v	0	mM	Physiological (Figley 2011)
	O_v	0.0834	mM	Physiological (Sherwood 2007)
Varied	k_G	$[1, 10^5]$	mM/day	Chosen to cover a large range
	k_L	$[1, 10^5]$	mM/day	Chosen to cover a large range
	n_L	$[0.01, 10]$	mM	Mendoza-Juez et al. (2012)
	n_G	$[0.01, 10]$	mM	Mendoza-Juez et al. (2012)
	a	$[10^{-3}, 10^3]$	none	Chosen to cover a large range

The covariance matrix for the dataset $\mathbf{X}$ is then given by $\mathbf{S}_x = \frac{1}{n-1}\mathbf{X}\mathbf{X}^T$, a square symmetric m-by-m matrix. As our goal is to capture meaningful features of the data, we want to remove the redundancy (i.e. covariance) from the variables, which, in turn, means diagonalising $\mathbf{X}\mathbf{X}^T$. This operation ensures that all basis vectors $\{\vec{p}_1, ..., \vec{p}_m\}$ are orthonormal, and carries the assumption that the directions with the largest variances are the most important, i.e. principal. In brief, PCA selects a normalised direction in m-dimensional space along which the variance in $\mathbf{X}$ is maximised ($\vec{p}_1$), then the direction along which the remaining variance is maximised ($\vec{p}_2$), restricted by the orthonormality condition to those perpendicular to $\vec{p}_1$; and so on, generating the ordered set of principal components, $\{\vec{p}_1, ..., \vec{p}_m\}$. These principal components are the eigenvectors of the covariance matrix $\mathbf{X}\mathbf{X}^T$, with the i^{th} eigenvalue capturing the variance of $\mathbf{X}$ along $\vec{p}_i$ (Lay 2000).

Often, large variances are associated with the first $k < m$ principal components, with a steep decline in the size of the remaining eigenvalues; in such cases the most interesting dynamics are captured by the first k dimensions and the rest can be ignored.

4.3.2.2 Analysis of parameter importance using classification trees

We can explore the sensitivity of a model output of interest to the fundamental model parameters—or, equivalently, the relative importance of the parameters for classifying that output—by applying a tree-based statistical classifier (Pappenberger et al. 2006). A system of partial differential equations can be translated into a classification problem by first generating a large random sample of the multidimensional parameter space, then numerically simulating the system of partial differential equations to steady state and applying the binary classification

$$y = \begin{cases} 1 & \text{if the behaviour of interest is obtained, and} \\ 0 & \text{if not,} \end{cases}$$

for each of the sampled parameter points. Our model parameters subsequently comprise the set of variables for a tree analysis and our vector y the classified responses. Tree-based methods iteratively determine which variable best classifies the training data, progressively segmenting the data by further classifications as the tree grows deeper (Figure 4.3).

Trees can capture complex interaction structures in data, but also are inherently noisy (Hastie et al. 2009), as a small error near the top may propagate into a large effect at the bottom. A remedy for this is the popular machine-learning algorithm RandomForest, developed by Breiman (2001), which grows a forest of trees, each on an independent bootstrapped sample (random sample with replacement) from the training data, and averages

over the predictions from all trees to reduce the variance in the final result. RandomForest is fast, accurate, and capable of handling a high-dimensional variable space.

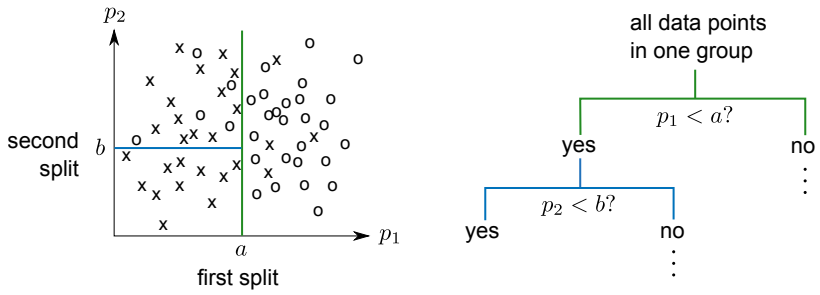

Figure 4.3: Construction of a classification tree. A simple example of building a classification tree for a dataset with two parameters, p_1 and p_2. The first split, a, is the location at which a line splits the $\{p_1, p_2\}$ plane (at left) according to a loss function to produce the greatest classification accuracy; that is, such that the data are divided into two groups of mostly x's and mostly o's. (Note that p_1 being the first split dimension is incidental, and parameters can appear in more than one split.) Next, the location b determines the line which best further splits one of these groups. On the $(p_1 < a) \rightarrow (p_2 < b)$ branch of the corresponding tree (at right), we have arrived at a node as all the data points in the sub-group are x's. For a higher-dimensional parameter space, the splits are hyperplanes through the data rather than lines, but the overall procedure remains similar.

Each tree in a given forest has a built-in test set—the out-of-bag data, or data not included in the bootstrapped sample for that tree—which can be exploited to determine the relative importance of the variables for accurate classification. After growing a forest, the class of each point in the training data is predicted using each tree for which that point is out-of-bag. The values of a variable x are then randomly permuted while holding the others fixed, and the permuted data are passed down the tree. The relative importance of variable x for the behaviour of interest is the difference in out-of-bag error before and after the permutation, averaged over all trees (Breiman 2001).

4.4 Experimental methods

The experiments described in this section were designed by Jessica McGillen and Dr. Catherine Kelly[‡]*, and carried out by Dr. Kelly.*

Sonveaux et al. (2008) and Busk et al. (2011) considered the highly oxidative cervical cell line SiHa, the glycolytic colon line WiDr, and the glycolytic squamous carcinoma line FaDu_{dd} *in*

[‡]Gray Institute for Radiation Oncology and Biology, Oxford University

vitro and *in vivo*. Mendoza-Juez et al. (2012) additionally considered results from *in vitro* experiments on two glycolytic glioma lines (LN18 and LN229) and a more oxidative glioma line (C6). We supplement these data further with a set of *in vitro* experiments carried out on the highly malignant glioblastoma cell line U87. This extends our modelling scenario to glioblastoma tumours, which are notoriously challenging clinically and hence of special interest. Moreover, the blood-brain barrier renders glioma tumours slightly metabolically simplified—at least in terms of the variety of metabolic substrates present in the local tissue—in comparison to body tumours (Terpstra et al. 1998, Moreno-Sánchez et al. 2007), and thus U87 may be a good target for future model validation *in vivo*. Finally, considering this cell line opens the possibility for an eventual connection of tumour metabolic dynamics with healthy metabolic cooperation that is known to occur between glutamatergic neurons and glia (Kirchhoff et al. 2001, Pellerin and Magistretti 2004, Gladden 2004, Magistretti 2006, Pellerin et al. 2007, Bélanger et al. 2011).

We carried out a set of experiments to explore the metabolic characteristics of U87 glioblastoma cultures *in vitro* using three metrics: glucose uptake, extracellular acidification, and oxygen consumption. Glucose was measured using a radiolabelled analogue, [18F] fluorodeoxyglucose (FDG), which has similar uptake kinetics to glucose. Unlike glucose, FDG is trapped in cells, and is frequently used as an estimator of glycolytic flux. The rate of media acidification (i.e. the change in pH over time) provides an estimate for the rate of lactate production and additional marker of glycolysis. The rate of oxygen consumption reflects the rate of oxidative phosphorylation.

4.4.1 Acidification and oxygen consumption

In a pair of experiments, U87 cells were seeded in a Seahorse XF Analyser 96-well cellplate (Seahorse Biosciences, USA) and grown in standard tissue culture under high-glucose conditions (25 mM) for 48 hours to allow full adhesion. For the assay, cells were incubated with 180 μl Seahorse medium (5mM glucose, 4mM glutamine, and 0.1mM sodium pyruvate) to replicate physiological conditions. Basal rates of oxygen consumption and extracellular acidification were measured using the Seahorse XF Analyser. Sodium lactate was then injected at concentrations of 0, 3, 6, 9, 12, and 15mM and further rate data were collected. Rate data were normalised to cell density as determined using Hoechst fluorescence staining.

4.4.2 Uptake of glucose

U87 cells were trypsinised to a single cell suspension and transferred to counting tubes. Cells were washed twice with PBS and the growth medium was replaced with a medium containing 100kBq [18F]FDG, 4mM glutamine, and sodium lactate at concentrations of 0, 3, 6, 9, 12, and 15mM. Cells were incubated for one hour at 37C; thereafter, cells were washed in PBS and activity in the cells was counted using a Beckman Coulter counter.

We note that these experiments consider only low to moderate lactate concentrations. Although lactate has been estimated to potentially reach as high as 35 mM in human brain tumours, maximum accumulation tends to occur in necrotic and cystic regions, with concentrations remaining below 15 mM in the more peripheral regions (Herholz et al. 1992) which are of interest for the symbiosis hypothesis.

4.5 Results

Application of the complementary statistical techniques for multivariate sensitivity analysis that we discussed in 4.3.2—importance analysis of symbiosis (θ), necrosis (γ), and hypoxia (λ) using classification trees, and principal component analysis of symbiosis (θ)—enables us to elucidate features of our multidimensional parameter space, as follows.

4.5.1 Consumption rates and substrate preference govern symbiosis

Our principal component analysis, a linear method, shows that the first two principal components for symbiosis (θ) comprise mainly the rates of glucose and lactate consumption by the tumour—k_G and k_L, respectively—and the characteristic preference for lactate uptake, a (Figure 4.4a). Our complementary, nonlinear, importance analysis is in agreement with this result (Figure 4.4b), suggesting that we are capturing robust dependencies.

Figure 4.4b also reveals that the importance weighting for the extent of hypoxia is similar (though not identical) to that for symbiosis, with lactate consumption (k_L) the most important parameter for both, followed by glucose consumption (k_G) and then preference for lactate (a). However, the importance weighting for necrosis is markedly different from these (Figure 4.4b), with necrosis depending primarily on consumption of glucose (k_G), secondarily on preference for lactate (a), and much less on consumption of lactate (k_L).

This difference in parameter dependence is further illustrated by projecting each of the three characteristics—symbiosis, necrosis, and hypoxia—onto the principal component space for

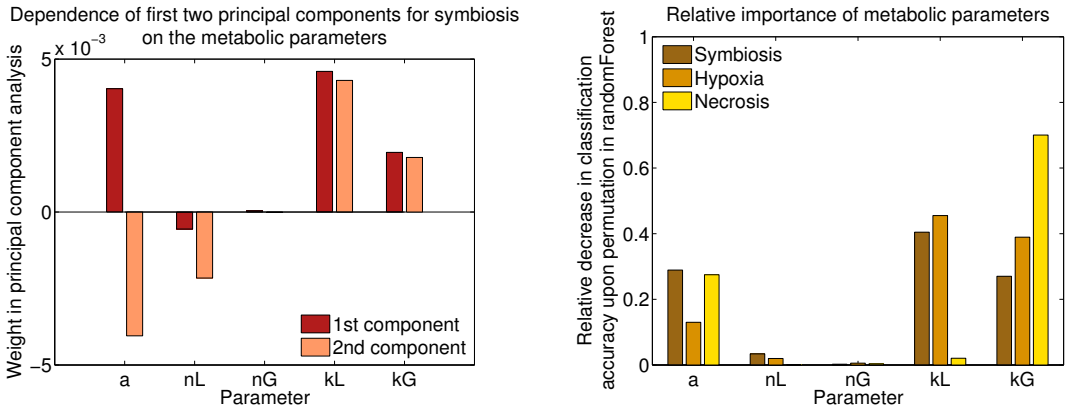

Figure 4.4: Principal component weighting and importance of parameters. (a) Weights assigned to each parameter from the original parameter space of Equations (4.15)-(4.18) in linear combinations comprising the first two principal components for symbiosis, described in Section 4.3.2.1; and (b) relative importance, as defined in Section 4.3.2.2, of the parameters for classifying the presence of symbiosis, θ (brown), tissue hypoxia, λ (tan), and necrosis, γ (yellow). The parameters are: expression of MCT1 relative to GLUT (a), the half-saturation point for uptake of lactate (n_L) and glucose (n_G), and the rates of consumption of lactate (k_L), and glucose (k_G).

symbiosis (Figure 4.5). Symbiosis and hypoxia project similarly (though not identically) to one another, while necrosis projects differently from both.

The Michaelis-Menten constants for glucose and lactate uptake (n_G and n_L, respectively) have relatively small principal component weightings for symbiosis and are relatively unimportant for all three characteristics. This is perhaps surprising in view of the variability in n_L across tumour cell lines *in vitro* (Mendoza-Juez et al. 2012).

4.5.2 Symbiosis exhibits the expected effects

Plotting symbiosis, necrosis, and hypoxia each against the three most important parameters pairwise (Figure 4.6) indicates that symbiosis can occur when consumption of glucose (k_G) and of lactate (k_L) are both high and the preference for lactate (a) is not small (top row of Figure 4.6). Additionally, broadly speaking it appears that symbiosis is more pronounced when $k_L > k_G$. We note that symbiosis requires the tumour to be extremely active metabolically, as k_G must be above 10^2 mM/day and k_L above 10^3 mM/day for it to occur. Quantitative measurements of *in vivo* metabolic consumption are, to our knowledge, difficult to come by, but future experiments could potentially be focussed in this direction to help determine whether these are plausible parameter ranges for tumours *in vivo*.

The extent of hypoxia is highest when consumption of glucose and lactate (k_G and k_L, respectively) are both very high, though it is less dependent than symbiosis on the preference

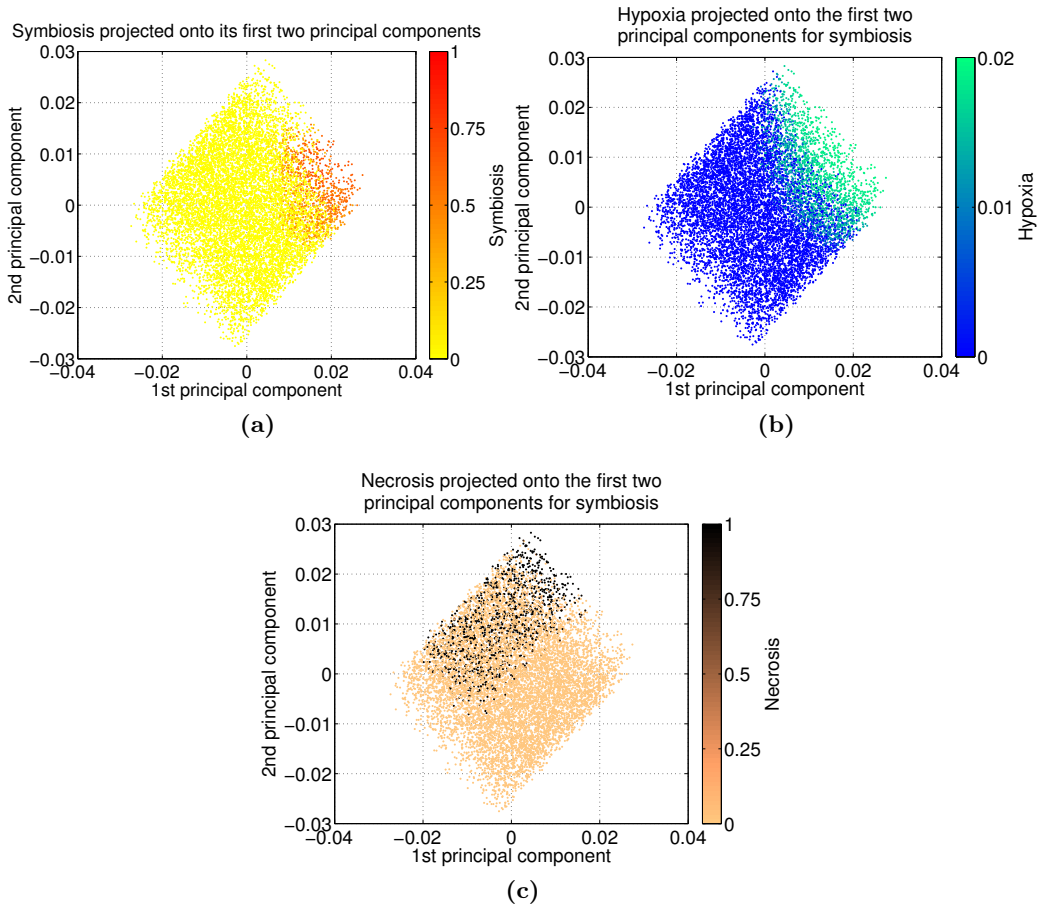

Figure 4.5: Projection onto the symbiosis principal component space. Projection onto the first two principal components for symbiosis, as defined in Section 4.3.2.1, of (a) symbiosis, θ, (b) hypoxia, λ, and (c) necrosis, γ. The projection of symbiosis onto the space of its first two principal components is similar to the projection of hypoxia onto the same space, while the projection of necrosis onto the same space is different from these.

for lactate (a) (middle row of Figure 4.6). The fact that hypoxia does not occur in the regime of lower metabolic consumption rates suggests that metabolically less-active tumours of the size considered here do not exhibit the nutrient gradients that are needed to drive the development of a spatial symbiosis.

Necrosis is mostly—though not entirely—mutually exclusive to symbiosis, reaching high values when glucose consumption (k_G) is very high and the preference for lactate (a) is small (bottom row of Figure 4.6). Plotting a representative sample from this region of parameter space over time reveals that the cause of this necrosis is glucose starvation, rather than acidosis or severe anoxia (Figure 4.7). There is, however, a small region of parameter space in which symbiosis and necrosis are not mutually exclusive: when the preference for lactate (a) is on the order of one, and consumption of glucose (k_G) is on the order of 10^4, both

symbiosis and necrosis can occur. It would be informative to determine whether or not this small parameter region is narrow enough to be considered a biological fine-tuning; but this would require a mapping between this model parameter region and the space of clinically plausible tumour characteristics, which again points to the need for quantitative *in vivo* measurements of the metabolic parameters.

Figures 4.8 and 4.9 illustrate the averaged steady-state system behaviours over the tumour domain for the parameter regimes which produce either strongly symbiotic behaviour, with lactate consumption dominating over glucose consumption near the oxygenated tumour edge (Figure 4.8), or weakly- or non-symbiotic behaviour, with lactate consumption at the tumour edge which does not strikingly dominate over glucose consumption at the tumour edge (Figure 4.9). On average, the strongly-symbiotic regime exhibits lower lactate, higher glucose, and a greater extent of hypoxia over the tumour domain than does the less-symbiotic regime. The latter additionally exhibits considerable necrosis in the tumour core.

Overall, these results suggest that a highly oxidative tumour—which would have a high rate of OXPHOS relative to glycolysis and a high preference for lactate as a metabolic substrate (Mendoza-Juez et al. 2012)—is likely to fall in the strongly symbiotic regime of our model parameter space, provided it is sufficiently metabolically active. In contrast, a highly glycolytic tumour, which would have a high rate of glycolysis relative to OXPHOS and low preference for lactate, is likely to fall into the regime of weak or no symbiosis. In the following section we present and analyse the results of our experiments, outlined in Section 4.4, to determine where U87 tumours may lie in this parameter space.

4.5.3 Experiments suggest weak symbiosis in U87 tumours

One of the model criteria for strongly symbiotic behaviour is that the tumour exhibits a strong characteristic preference for lactate over glucose as a metabolic substrate (i.e. that a is large). From our *in vitro* experiments on the metabolic characteristics of U87 tumours (outlined in Section 4.4), it is evident that increasing the amount of available lactate leads to a reduction in the extracellular acidification rate (Figure 4.10a) and a corresponding increase in the oxygen consumption rate (Figure 4.10b), which together signal consumption of lactate by oxidative phosphorylation. However, there is only a slight decrease in glucose uptake with increasing lactate concentration (Figure 4.10c), indicating that the cells do not exhibit a strong characteristic preference for lactate but instead consume glucose at a similar rate whether or not lactate is available.

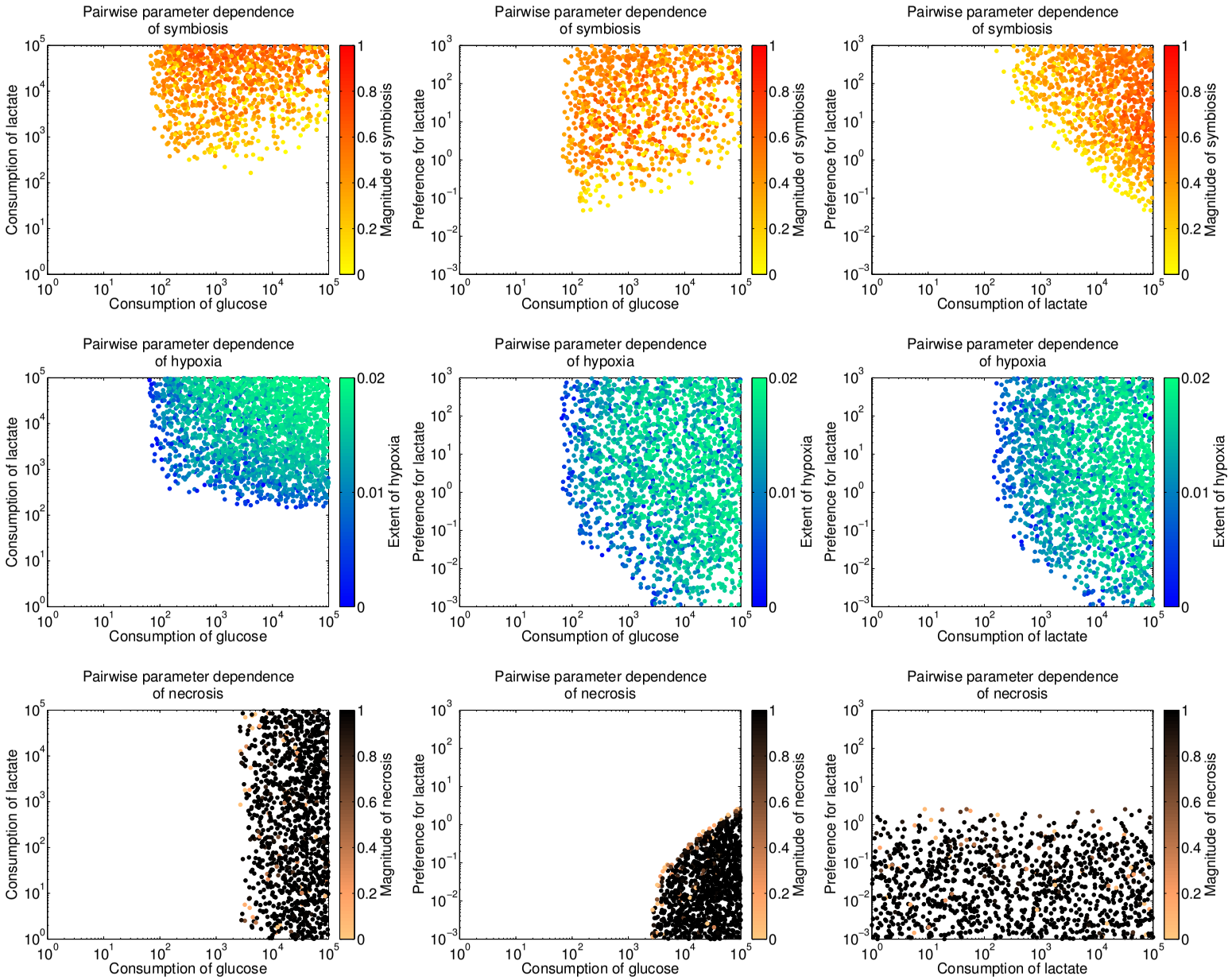

Figure 4.6: Symbiosis, hypoxia, and necrosis in the space of important parameters. Symbiosis (top row), hypoxia (middle row), and necrosis (bottom row), for numerical simulations of Equations (4.15)-(4.18) with 10^4 random samples of the parameter space, plotted pairwise against the three most important parameters: rates of consumption of glucose (k_G) and lactate (k_L), and characteristic preference for lactate (a).

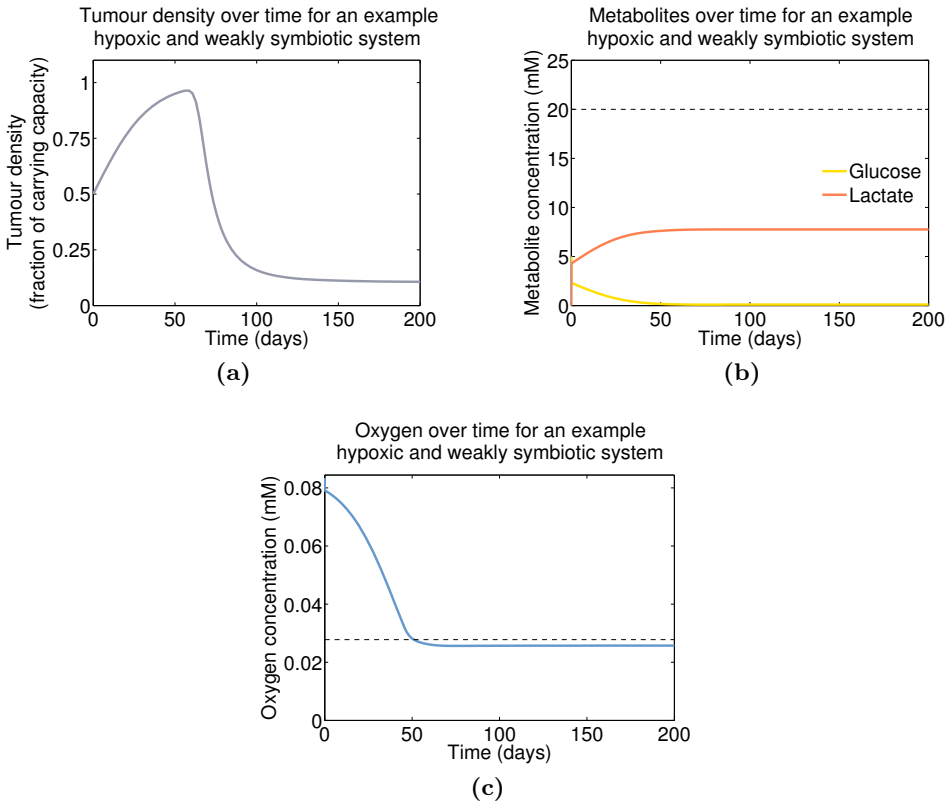

Figure 4.7: Cause of necrosis under weak/no symbiosis. Species profiles in the tumour core over time for a representative sample from the weakly-/non-symbiotic parameter regime governing Equations (4.15)-(4.18). Shown are the (a) tumour density (grey), (b) glucose (yellow) and lactate (red) concentrations, and (c) oxygen concentration (blue). Dotted lines in (b) and (c) indicate the acidosis threshold σ_A and the hypoxia threshold σ_H, respectively.

These experiments thus suggest that the preference for lactate (a) is likely to be small, which places U87 glioblastoma tumours approximately into the regime in which only weakly symbiotic behaviour develops—but U87 tumours are highly malignant. This raises the question of whether symbiosis is likely to have any correlation with tumour aggressiveness. It is perhaps possible that symbiotic tumours are stabilised by their metabolic cooperation and insulated from oxygen-dependent treatments, but at the cost of being less malignant than non-symbiotic tumours. This connection, or lack thereof, remains to be explored.

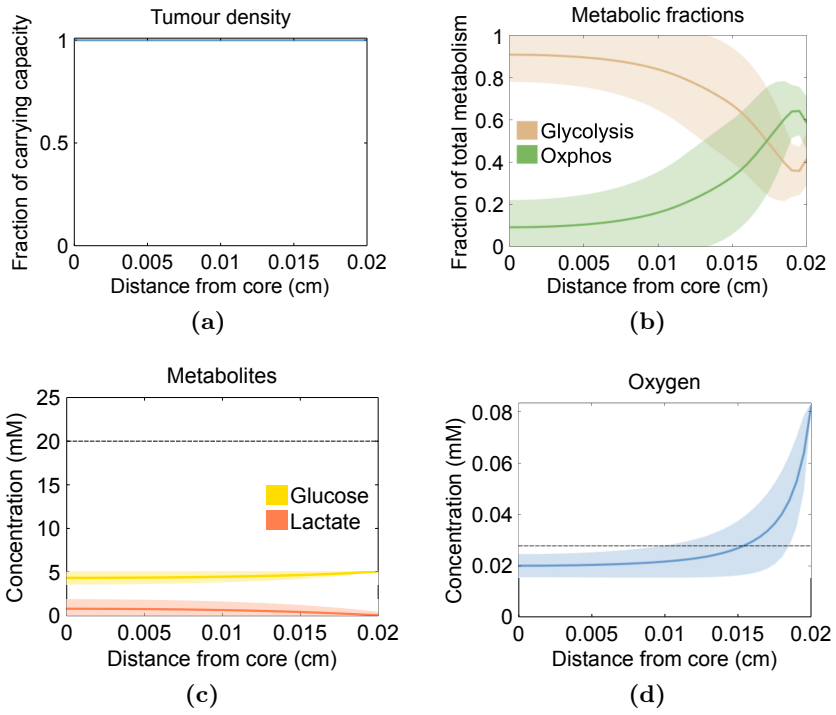

Figure 4.8: Symbiotic behaviour of Equations (4.15)-(4.18)**.** Averaged spatial behaviours of the (a) tumour density, (b) metabolic fractions, (c) metabolite concentrations, and (d) oxygen concentration, at steady state. Shown are the means (curves) and standard deviations (shaded areas) from 10^4 uniformly distributed samples from the parameter region giving rise to symbiotic behaviour; that is, from the region in which consumption of lactate (k_L) and glucose (k_G) are high with $k_L > k_G$, and the characteristic preference for lactate (a) is high. Fixed parameters are listed in the top portion of Table 4.1.

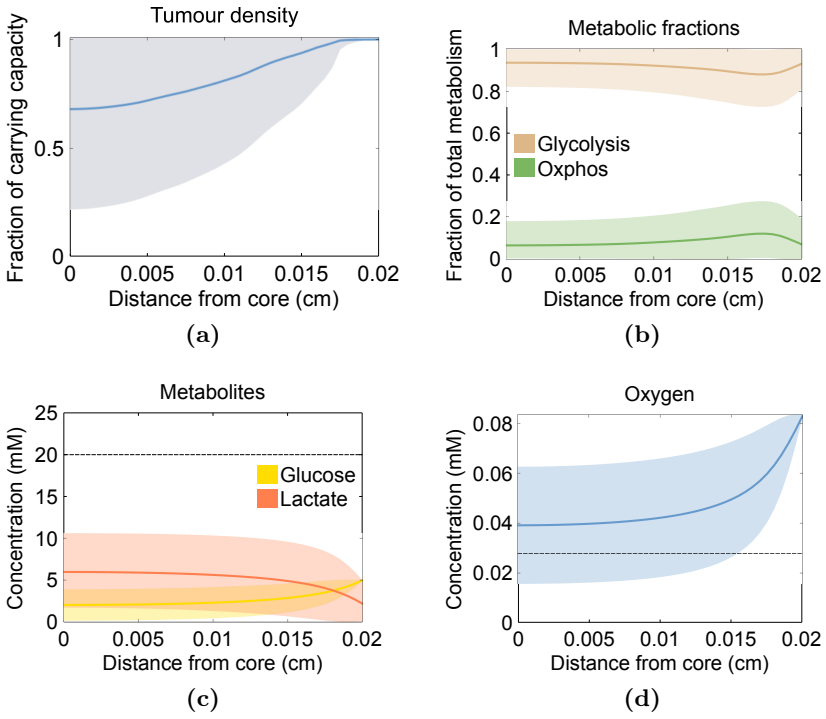

Figure 4.9: Weakly- or non-symbiotic behaviour of Equations (4.15)-(4.18)**.** Averaged spatial behaviours of the (a) tumour density, (b) metabolic fractions, (c) metabolite concentrations, and (d) oxygen concentration, at steady state. Shown are the means (curves) and standard deviations (shaded areas) from 10^4 uniformly distributed samples from the parameter region giving rise to weakly- or non-symbiotic behaviour; that is, from the region in which consumption of lactate (k_L) and glucose (k_G) are high with $k_G > k_L$, and the characteristic preference for lactate (a) is low. Fixed parameters are listed in the top portion of Table 4.1.

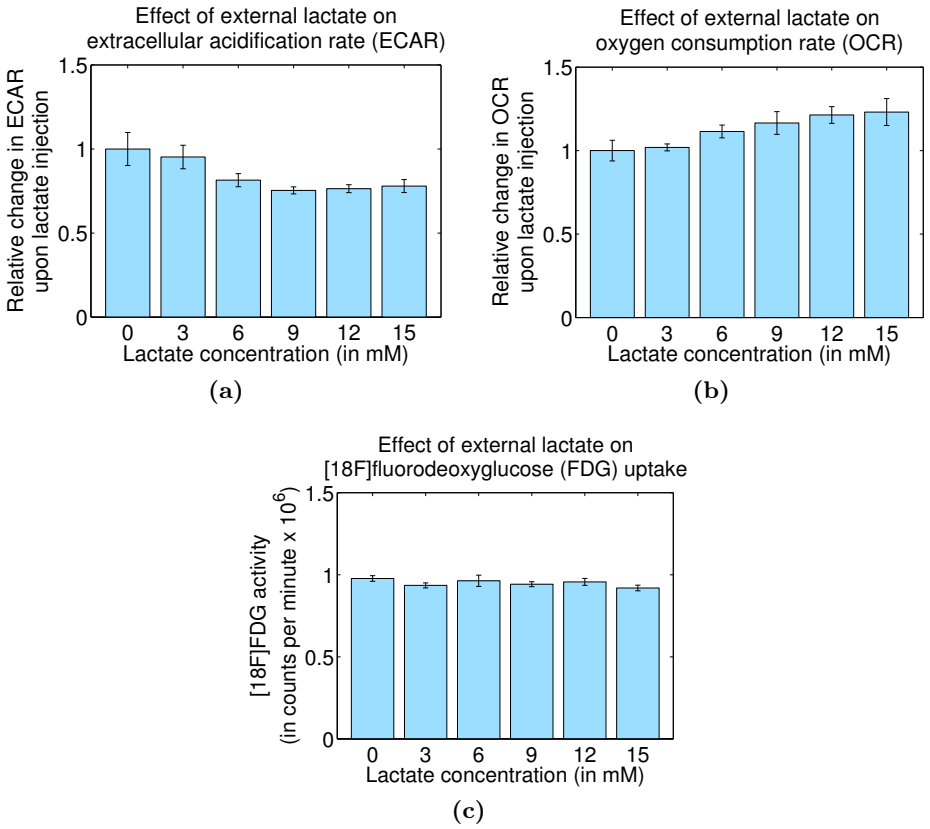

Figure 4.10: Experimental metabolic dynamics of U87 glioma cells *in vitro*. Metabolic rate dynamics in U87 glioma cells cultured *in vitro* over varying concentrations of lactate in the medium, as outlined in Section 4.4. (a) Extracellular acidification rate (ECAR), a marker of the net effect of glycolysis and lactate consumption; (b) oxygen consumption rate (OCR), a marker of oxidative phosphorylation; and (c) activity of fluorodeoxyglucose ([18F]FDG), a marker of glycolysis. Increasing the concentration of available lactate leads to a decrease in ECAR and an increase in OCR, but a negligible change in [18F]FDG, signifying consumption of lactate by oxidative phosphorylation without a strong characteristic preference for lactate over glucose as a metabolic substrate. These data are provided in Appendix F.

4.5.4 MCT1 inhibition increases oxygenation but not necrosis

The first part of the symbiosis hypothesis concerns the establishment and beneficial effects of a well-defined spatial symbiosis, which we have considered thus far. The second part proposes that inhibiting symbiosis by blocking the monocarboxylate transporter 1 (MCT1) forces cells near the tumour edge that were consuming lactate by OXPHOS to instead consume glucose by glycolysis, such that MCT1-inhibition has the dual effect of starving the tumour core and increasing the extent of tissue oxygenation (Sonveaux et al. 2008). The latter effect, if confirmed, would make MCT1-inhibition a promising method for radiosensitising symbiotic tumours.

We simulate MCT1-inhibition by CHC—the treatment strategy employed by both Sonveaux et al. (2008) and Busk et al. (2011) *in vivo*—by numerically solving Equations (4.15)-(4.18) with the same parameter values from our multi-dimensional parameter space as before, but now with lactate uptake blocked by setting $k_L = 0$. Contrary to the prediction of Sonveaux et al. (2008), blocking MCT1 has no effect on necrosis in our model system—except when, in cases of high hypoxia, it *decreases* necrosis (Figure 4.11a-c). These latter cases are mostly, but not not entirely, limited to tumours which were non-symbiotic in wildtype, and thus the effect of CHC may be less straightforward than assumed.

CHC treatment does have the expected effect on hypoxia in our model system, in that the extent of oxygenation is increased when lactate uptake is inhibited (Figure 4.11b-f). However, this effect correlates only loosely with the amount of symbiosis exhibited by the wildtype system, with substantial reductions in the extent of hypoxia occurring even in the absence of wildtype symbiosis. Instead, the effect correlates exactly with the extent of hypoxia that was already present in the wildtype system, with greater reductions occurring for tumours with more extensive wildtype hypoxia.

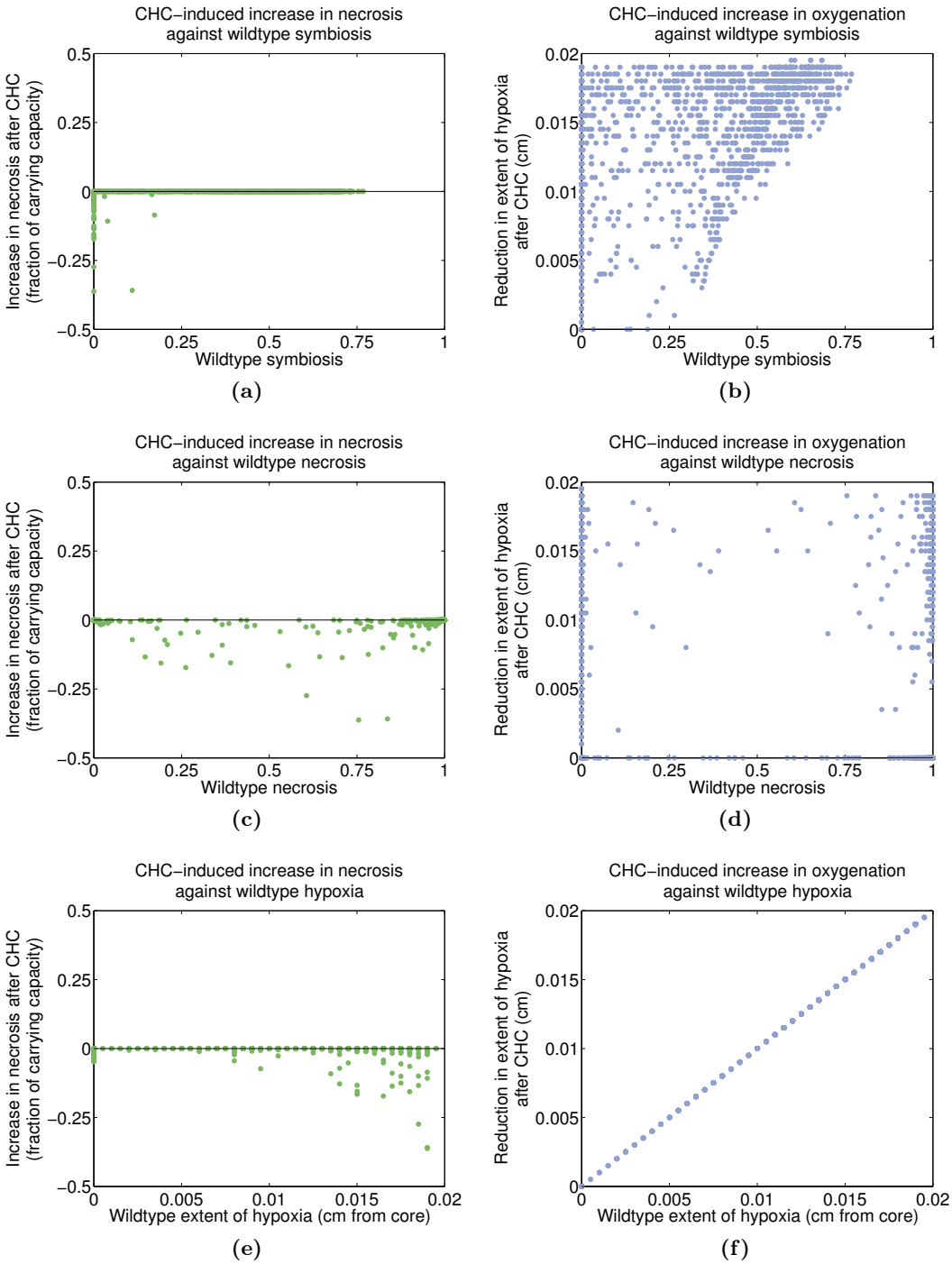

Figure 4.11: Effect of MCT1 inhibition on necrosis and hypoxia. Increase in necrosis (left column) and extent of tissue oxygenation (right column) relative to wildtype, obtained by numerically solving Equations (4.15)-(4.18) with 10^4 parameter points sampled uniformly from the ranges in the bottom portion of Table 4.1, and comparing these to solutions for the same parameter points but with $k_L = 0$ to simulate MCT1 inhibition by CHC. Shown are the increase in necrosis and increase in oxygenation as functions of the amount of symbiosis (top row), necrosis (middle row), and hypoxia (bottom row) that were already occurring in the wildtype systems.

4.6 Discussion

Our aim in this chapter was to examine the symbiosis hypothesis put forward by Sonveaux et al. (2008) and to address the disagreement between their *in vivo* experimental results and those of Busk et al. (2011). We have pursued this by developing a minimal spatial model of dual glucose-lactate consumption. Our main findings from this model are that, while symbiosis arises over a substantial portion of the parameter space, it requires cells to be extremely metabolically active, and whether such a parameter regime is clinically realistic remains to be established. For the most part, the occurrence of symbiosis is mutually exclusive with the occurrence of necrosis in the tumour core, and the latter is caused by nutrient deprivation (rather than by acidosis or severe anoxia) as predicted by Sonveaux et al. (2008). However, symbiosis and necrosis do not exhibit the same dependence on the model parameters, indicating that symbiosis may not directly 'rescue' tumours from nutrient starvation.

Furthermore, we have demonstrated experimentally that U87 glioma tumours consume lactate but do not exhibit a discernible characteristic preference for lactate over glucose as a metabolic substrate (Figure 4.10), one of the conditions required for strongly symbiotic behaviour under our modelling framework. U87 tumours are known to be highly malignant, and thus our experimental results compel us to take a step beyond the original hypothesis and raise the new question of whether symbiosis, if indeed it occurs *in vivo*, may be advantageous or disadvantageous (or neither) for clinical malignancy. In particular, under some conditions necrosis is associated with tumour-promoting inflammation and accelerated tumour growth (Degenhardt et al. 2006), such that the relationship between necrosis-reducing symbiotic behaviour and malignancy may not be a simple one.

We also have found that simulation of MCT1 inhibition does not cause the increase in necrosis in the tumour core that was expected to result from increased glucose consumption by cells at the formerly lactate-consuming tumour edge. This places our results in line with those of Busk et al. (2011), who saw no increase in necrosis upon CHC administration. MCT1 inhibition does cause an increase in the extent of tissue oxygenation in our model system, as predicted by Sonveaux et al. (2008), but this correlates with the extent of hypoxia that was present in the wildtype system rather than with its strength of symbiosis. This result gives the promising indication that CHC may be a viable strategy for radiosensitisation wherever there is oxidative lactate consumption in a tumour, regardless of whether or not the tumour exhibits a spatially well-defined symbiosis.

We caution that our model is a minimal representation of tumour glucose-lactate metabolism, and real tumour metabolic systems are a great deal more complicated than what we have considered here. As such, our conclusions should be taken more as theoretical, in-principle statements than as prescriptive of what occurs in real tumours *in vivo*. Well-defined experimental measurements of local glucose and lactate consumption rates *in vivo* could help to refine the placement of tumours in our model parameter space and thereby more conclusively establish whether symbiosis is likely to be a significant feature of tumours *in vivo*. Nevertheless, the minimal spatial model presented herein has enabled some predictions which can be tested experimentally—in particular, the relationship (or lack thereof) between the occurrence of symbiosis and degree of clinical malignancy can be investigated—and which support the *in vivo* observations of Busk et al. (2011) with regard to CHC-induced necrosis over those of Sonveaux et al. (2008). Hence, in our view this chapter is illustrative of the insights that can be gained by integrating mathematical modelling with experiments for clearer and more rigorous hypothesis testing.

We will now take such integration a step further: Chapters 5 and 6 will detail the systematic development of a spatial continuum model of pH regulation in tumours, using a Bayesian approach that incorporates information from data into the modelling framework to facilitate a clearer understanding of parameter uncertainty and variability.

Chapter 5

A model of pH regulation in single tumour cells

The majority of modelling studies of tumour metabolism and acidity—including those we have presented thus far in Chapters 2-4—consider only extracellular pH. In light of the complex mechanisms and potentially non-intuitive dynamics underpinning tumour maintenance of intracellular and extracellular pH that we discussed in Chapter 1, however, this is likely to prove insufficient for gaining a comprehensive understanding of tumour glucose metabolism.

A complete model of tumour pH should take into account the interrelated transmembrane processes of proton extrusion, bicarbonate import, and concurrent proton-lactate export, as well as the bicarbonate buffering reaction catalysed in intracellular space by bulk carbonic anhydrases (namely CAII) and in extracellular space by carbonic anhydrase IX (CAIX) (Parks et al. 2013). Our ultimate goal is to develop a comprehensive model of this system in a spatial framework.

In this chapter we will begin from first principles and derive a model of pH regulation in single tumour cells. We will then employ a Bayesian framework to incorporate information from *in vitro* experimental datasets on transmembrane fluxes (to be detailed later) into our estimation of some of the parameters, before validating our system against known single-cell dynamics. Finally, we will confirm that our single-cell model predicts a straightforward relationship between intracellular and extracellular pH that is consistent with expectations.

Chapter 6 will then detail an embedding of our validated single-cell model into a spatial framework to capture metabolic tumour dynamics in a spheroid setting.

5.1 The model

To begin, we isolate components that are currently thought to drive the maintenance of a favourable intracellular pH: sodium/proton exchange, bicarbonate buffering, and proton/lactate co-transport (Parks et al. 2013). As molecular transport within the cytoplasm of eukaryotic cells is facilitated, we can assume that the cytoplasm is well-mixed and hence neglect diffusion in the intracellular domain of our model cell. The metabolic species of interest are lactic acid, H^+-Lac (also commonly called protonated lactate), lactate anions, Lac^-, free protons, H^+, bicarbonate ions, HCO_3^-, and carbon dioxide, CO_2. Figure 5.1 summarises the processes that govern the dynamics of these metabolites in a single tumour cell. Below we discuss each feature that we will include in our model of this system, before stating the model itself.

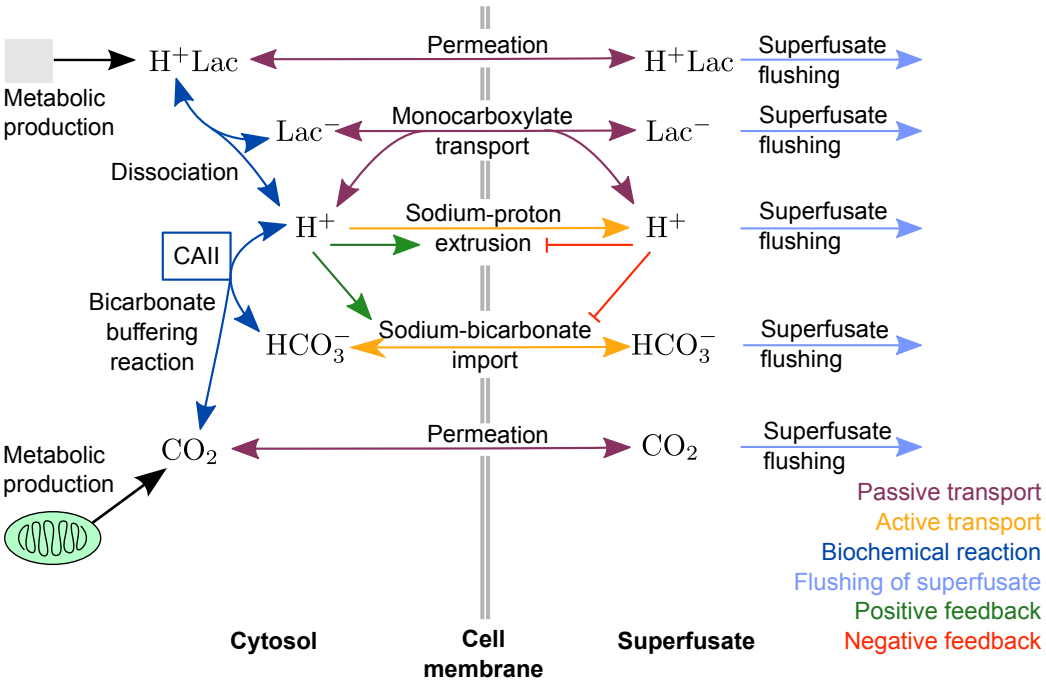

Figure 5.1: The pH regulation system in single tumour cells. Interrelated biochemical mechanisms for handling of a metabolically-derived acid load in the cytoplasm, across the cell membrane, and in the superfused space of a single-cell experimental setting. Species in this system are protonated lactic acid (H^+Lac), lactate ions (Lac^-), free protons (H^+), bicarbonate ions (HCO_3^-), and carbon dioxide (CO_2). The bicarbonate buffering reaction is catalysed by carbonic anhydrase II (CAII).

First, we must capture metabolic production of lactic acid by glycolysis and of carbon dioxide by oxidative phosphorylation. We denote these rates as υ_A and υ_C, respectively, and

assume they are constant in the single-cell environment. This is a reasonable assumption as the environmental factors to which cellular metabolism is responsive—for example, nutrient supply—are controllable in a single-cell experimental setting via manipulation of the superfusate, and hence can be considered stable. Representing the two metabolic pathways (glycolysis and oxidative phosphorylation) as independent, as we do here, allows for the consideration of a variety of tumour metabolic phenotypes.

As the pK_a (negative log of the acid dissociation constant; see Appendix G) of lactic acid is 3.65 (Berg et al. 2002), it dissociates virtually completely in the cytosolic space, producing free protons and lactate ions. The reversible chemical reaction for this dissociation is:

$$\mathrm{H^+\text{-}Lac} \underset{\kappa_a}{\overset{\kappa_d}{\rightleftharpoons}} \mathrm{Lac^-} + \mathrm{H^+}, \tag{5.1}$$

with κ_d and κ_a representing the rates of dissociation and association, respectively.

Once they have been generated, intracellular free protons ($\mathrm{H^+}$) do not persist as free for long; rather, they are rapidly buffered away via attachment onto proteins and other bulk material in the cytosol (Roos and Boron 1981, Leem et al. 1999). This exerts an intrinsic dampening effect on the changes in total concentration of free intracellular protons, known as the intrinsic buffering power. Supposing that we have a single collective (unknown) buffer species comprising the cytosol of our single tumour cell, the intrinsic buffering power, β, is

$$\beta = \frac{\ln(10) S \kappa_s [\mathrm{H^+}]}{(\kappa_s + [\mathrm{H^+}])^2}, \tag{5.2}$$

in mM per unit of pH, where S is the total concentration of the collective buffer species and κ_s its dissociation constant (both in mM). This equation is derived in Appendix G.

For our model, the parameters S and κ_s will be determined by fitting to *in vitro* measurements of intrinsic buffering power in single HCT116 cells, to be detailed further in Section 5.3. Buffering capacity is measured in mM (per dimensionless unit of pH), and we can turn it into a dimensionless scaling factor by converting β to units of M and taking the negative log (Swietach et al. 2009), such that we have

$$\mathrm{p}\beta = -\log_{10}(\beta/10^3). \tag{5.3}$$

This will allow us to appropriately scale our equation for the rate of change of free protons in the cell, as will be seen later.

Any free protons not buffered away by bulk intracellular material are handled by three mechanisms in the cell. The first mechanism is direct extrusion by sodium-proton ($\mathrm{Na^+/H^+}$)

exchangers, an active transport process that is sensitive to positive feedback by accumulation of intracellular protons and negative feedback by accumulation of extracellular protons (Parks et al. 2013). The kinetics of this feedback-controlled transport are commonly approximated by a Hill function in two variables, intracellular protons and extracellular protons (Swietach et al. 2009). Letting Hi denote the concentration (in mM) of free protons in the intracellular space and He the concentration (in mM) of free protons in the extracellular space (controlled through the superfusate in single-cell experiments), the rate of efflux of free protons due to Na^+/H^+ exchange, F_{nhe}, is given by:

$$F_{nhe} = \gamma_1 \frac{Hi^\eta}{Hi^\eta + \gamma_2^\eta} \left(1 - \frac{He^\eta}{He^\eta + \gamma_3^\eta}\right), \tag{5.4}$$

with γ_1 denoting the maximum speed of transport; γ_2 and γ_3 the concentrations of Hi and He, respectively, at which transport is half-saturated; and η the Hill coefficient. Equation (5.4) captures the basic kinetics of Na^+/H^+ exchange as follows: if intracellular acidity is high, then efflux of free protons will occur at a rate close to the maximum transporter capacity; but if the extracellular acidity is also high, efflux will be inhibited. If intracellular acidity is low, then efflux will be slow, and slower still if extracellular acidity is high.

The second mechanism for proton handling is the carbon dioxide/bicarbonate (CO_2/HCO_3^-) buffering system, a crucial component of the physiological pH-buffering system in healthy tissues and the bloodstream (Berg et al. 2002). For buffering by this system, bicarbonate ions (HCO_3^-) must be imported into the cell; this is thought to be accomplished mainly by sodium/bicarbonate (Na^+/HCO_3^-) co-transport (Parks et al. 2013). Here, we denote influx of HCO_3^- due to Na^+/HCO_3^- co-transport as F_{nbc}. Similarly to Na^+/H^+ exchange, Na^+/HCO_3^- co-transport is an active process that is subject to positive feedback by intracellular acidity and negative feedback by extracellular acidity. Hence, the kinetics of bicarbonate influx due to this transport, F_{nbc}, can be represented by a Hill curve,

$$F_{nbc} = \gamma_4 \frac{Hi^\xi}{Hi^\xi + \gamma_5^\xi} \left(1 - \frac{He^\xi}{He^\xi + \gamma_6^\xi}\right), \tag{5.5}$$

with γ_4 denoting the maximum speed of transport; γ_5 and γ_6 the concentrations of Hi and He, respectively, at which transport is half-saturated; and ξ the Hill coefficient. As with proton efflux, bicarbonate influx is fastest when intracellular acidity is high, and is impeded by high extracellular acidity and/or low intracellular acidity.

Once bicarbonate has been imported into the cytosol, it combines biochemically with free protons to form carbon dioxide and water via the reversible CO_2/HCO_3^- reaction,

$$CO_2 + H_2O \underset{\kappa_r}{\overset{\kappa_f}{\rightleftharpoons}} H^+ + HCO_3^-, \tag{5.6}$$

where κ_f and κ_r are the rates of the forward and reverse reactions, respectively. Equation (5.6) is derived fully in Appendix G. The CO_2/HCO_3^- buffering reaction proceeds slowly in solution, but is catalysed in the intracellular space by cytosolic carbonic anhydrases, such as the isoform CAII. As with all catalysts, carbonic anhydrases lower the activation energy for the reaction, which dramatically increases the reaction rate but does not alter its equilibrium (Berg et al. 2002).

The third proton-handling mechanism is co-transport of free protons (H^+) and lactate anions (Lac^-) across the cell membrane by H^+-linked monocarboxylate transporters (MCTs). Though commonly described as unidirectional—shuttling protons and lactate either out of the cell (if MCT4) or into the cell (if MCT1)—MCTs are, in fact, passive co-transporters of protons and lactate (Swietach et al. 2009). MCTs are also membrane-bound, and thus the transport process can be described as a combination of binding and unbinding events of H^+ and Lac^- ions with the transporters:

$$H^+_{intracellular} + Lac^-_{intracellular} \underset{\kappa_u}{\overset{\kappa_b}{\rightleftharpoons}} MCT \underset{\kappa_b}{\overset{\kappa_u}{\rightleftharpoons}} H^+_{extracellular} + Lac^-_{extracellular}, \tag{5.7}$$

with κ_b and κ_u denoting the rates of binding to and unbinding from the membrane-bound monocarboxylate transporter, respectively. These binding and unbinding rates are sufficiently rapid that the co-transport process can be approximated as co-permeation (Swietach et al. 2009) and thus considered to be governed by the transmembrane concentration gradients of H^+ and Lac^-. By the law of mass action, the rate of change in the concentration of each species, denoted as F_{mct} below, is then given by

$$F_{mct} = \frac{3}{c}\rho_L(HiLi - HeLe), \tag{5.8}$$

where c is the radius of a typical tumour cell, such that $\frac{3}{c}$ is its surface-area-to-volume ratio, and ρ_L is the rate of co-transport (effectively, the co-permeation rate), with Li and Le representing the lactate concentration in the intracellular and extracellular space, respectively.

Finally, the cell membrane is permeable to carbon dioxide (CO_2) and lactic acid (H^+Lac). Each is lost from (or gained by) the cytosol at a rate proportional to its concentration gradient across the cell membrane. The rates of change of the concentrations of CO_2 (Ci) and of H^+Lac (Ai) due to this permeation, denoted below as F^C_{per} and F^A_{per}, respectively, are given by

$$F^C_{per} = \frac{3}{c}\rho_C(Ci - Ce), \tag{5.9}$$

$$F^A_{per} = \frac{3}{c}\rho_A(Ai - Ae), \tag{5.10}$$

where again the factor $\frac{3}{c}$ is the surface-area-to-volume ratio of a single cell, and ρ_C and ρ_A are the respective rates of permeation.

We assume that changes over time in the concentrations of our intracellular metabolic species (Hi, Li, Ai, Ci, and the intracellular concentration of bicarbonate, Bi) are completely characterised by: the chemical reactions in Equations (5.1) and (5.6); loss or gain across the cell membrane due to active transporters in Equations (5.4) and (5.5) or permeation-equivalent processes in Equations (5.8), (5.9), and (5.10); and dampening of the free proton dynamics by the intrinsic buffering factor given by Equation (5.3). We note that this assumption relies on the current opinion of Parks et al. (2013) and others that Na^+/H^+ exchange, Na^+/HCO_3^- co-import, and H^+/Lac^- co-transport are the drivers of pH regulation in tumour cells. Thus our model will enable us to comment on whether these features are indeed sufficient to explain observed pH dynamics.

Letting $'$ denote differentiation with respect to time, and applying the law of mass action to the chemical reactions in (5.1) and (5.6), the ordinary differential equations governing the rates of change of our metabolite concentrations are shown on the following page.

$$Hi' = \overbrace{\left(-\log_{10}\left(\frac{\ln(10)S\kappa_s Hi}{(\kappa_s+Hi)^2}/10^3\right)\right)^{-1}}^{\text{intrinsic buffering}}\left(\overbrace{\kappa_d Ai-\kappa_a HiLi}^{\text{H}^+\text{Lac dissociation}}+\overbrace{\alpha_{II}(\kappa_f Ci-\kappa_r HiBi)}^{\substack{\text{CAII-catalysed}\\ \text{CO}_2/\text{HCO}_3^- \text{ buffering}}}-\overbrace{\gamma_1\frac{Hi^\eta}{Hi^\eta+\gamma_2^\eta}\left(1-\frac{He^\eta}{He^\eta+\gamma_3^\eta}\right)}^{\text{Na}^+/\text{H}^+ \text{ exchange}}-\overbrace{\frac{3}{c}\rho_L(HiLi-HeLe)}^{\text{H}^+/\text{Lac}^- \text{ co-transport}}\right) \tag{5.11}$$

$$Li' = \overbrace{\kappa_d Ai-\kappa_a HiLi}^{\text{H}^+\text{Lac dissociation}}-\overbrace{\frac{3}{c}\rho_L(HiLi-HeLe)}^{\text{H}^+/\text{Lac}^- \text{ co-transport}} \tag{5.12}$$

$$Ai' = \overbrace{v_A}^{\substack{\text{glycolytic}\\ \text{metabolic}\\ \text{production}}}-\overbrace{(\kappa_d Ai-\kappa_a HiLi)}^{\text{H}^+\text{Lac dissociation}}-\overbrace{\frac{3}{c}\rho_A(Ai-Ae)}^{\text{H}^+\text{Lac permeation}} \tag{5.13}$$

$$Bi' = \overbrace{\gamma_4\frac{Hi^\xi}{Hi^\xi+\gamma_5^\xi}\left(1-\frac{He^\xi}{He^\xi+\gamma_6^\xi}\right)}^{\text{Na}^+/\text{HCO}_3^- \text{ co-import}}+\overbrace{\alpha_{II}(\kappa_f Ci-\kappa_r HiBi)}^{\substack{\text{CAII-catalysed}\\ \text{CO}_2/\text{HCO}_3^- \text{ buffering}}} \tag{5.14}$$

$$Ci' = \overbrace{v_C}^{\substack{\text{oxidative}\\ \text{metabolic}\\ \text{production}}}-\overbrace{\alpha_{II}(\kappa_f Ci-\kappa_r HiBi)}^{\substack{\text{CAII-catalysed}\\ \text{CO}_2/\text{HCO}_3^- \text{ buffering}}}-\overbrace{\frac{3}{c}\rho_C(Ci-Ce)}^{\text{CO}_2 \text{ permeation}} \tag{5.15}$$

The first term in Equation (5.11) is the dimensionless scaling factor that comes from taking the negative log of the intrinsic buffering power, i.e. pβ in Equation (5.3) with β given by Equation (5.2). This term is a departure from the standard biomathematical approach of mass action, but is derived from an assumption that the uptake of protons onto bulk buffers obeys fast kinetics such that intrinsic buffering emerges as a modulation term (Roos and Boron 1981, Leem et al. 1999).

Several of the parameters in this model are experimentally well-determined or establish the background for the metabolic dynamics of interest, and hence can be considered fixed; these are listed in Table 5.1. The others, however, are either poorly determined experimentally—such as the metabolic production rates υ_A and υ_C—or are of interest for varying across tumours and serving as potential therapeutic targets. We will therefore allow them to behave as random variables governed by distributions, similarly to the approach we took in Chapter 4. Moreover, we have available to us small sets of experimental data that provide information about some of the parameters (described in detail in Appendix F and discussed in Section 5.3). To integrate information from these data into the appropriate parameter distributions in our model formulation, we will employ Bayesian inference. We now discuss the general approach to Bayesian inference before applying it to our model.

5.2 Bayesian inference for parameter selection

Mathematical models can be leveraged for increased insight with the application of Bayesian inference, a powerful statistical framework for formalising our knowledge of a given model system, and for considering both system sensitivity to model parameters and the underlying uncertainty in estimation of those parameters. To our knowledge, the present work is the first to consider the utility of a Bayesian approach for continuum models in mathematical oncology.

We contend that a Bayesian approach can be immensely beneficial to mathematical oncology (and indeed to mathematical biology in general), as it facilitates the development of theory in step with experiment, updating our mathematical description when new information about the system is acquired. Furthermore, with Bayesian reasoning we can confront, and handle in a formal way, our prior knowledge of a system, uncertainty in parameter estimation, and the variation intrinsic to tumours (and other biological systems). This is accomplished by representing fundamental model parameters as random variables—that is, as governed by distributions—and thus wrapping uncertainty and variability into the model itself, rather than attempting to gauge one or both of these as external properties after the

model has been developed. Bayesian inference incorporates any information we have *a priori* about these distributions governing the parameters, and updates them according to new information provided by data, iteratively if necessary, such that the final product is a probabilistic and fully informed model. The following sections provide a brief discussion of the theory behind this approach.

5.2.1 Analysis using Bayes' Theorem

A Bayesian analysis proceeds according to the following steps. Initially, a probability model for the data must be formulated. Letting θ represent our vector of model parameters which are unknown but which we wish to estimate, and $y_1, ..., y_n$ the n data points to be collected, then—assuming the data observations are independent—we are interested in choosing a probability function, $p(y_i|\theta)$, for the data (Glickman and van Dyk 2007). (Throughout this thesis, $p(a|b)$ denotes the probability of observing a conditioned on having observed b.) For biological experiments that measure continuous properties of a given system, it can usually be assumed that the data are normally distributed, and we will do so here. This assumption is justified by viewing the total experimental error as the sum of many individual sources of error, which are uncorrelated random variables and thus sum to a normal distribution by the central limit theorem.

The second step in Bayesian analysis is to quantify our uncertainty regarding the unknown model parameters *before* the data are observed. This is accomplished by constructing a **prior distribution**, here denoted $\pi(\theta)$, that represents the current state of knowledge regarding the model parameters, θ. Choosing a Bayesian prior is not a trivial step, and approaches fall into two main categories, with entire chapters of Bayesian textbooks devoted to each. Some priors, known as informative, use knowledge of the substantive problem, perhaps by interpreting existing data or eliciting expert opinion; others, known as noninformative, are constructed to represent objectivity and ignorance about the model parameters. Many common methods for constructing noninformative priors—for example, always assuming uniform distributions—are subject to pitfalls and inconsistencies. Namely, it can be difficult to construct a flat (uniform) prior whose probabilistic information is invariant to the scale at which the parameter is measured, and approaches may result in priors which are improper (that is, they do not integrate to one) and hence are not true probability distributions. In general, an effective strategy is to construct a proper, *relatively* flat prior distribution that is closely related to the data distribution in such a way as to simplify later calculations. This is done with a conjugate prior; that is, a distribution which is in the same family as the data distribution. Common examples of conjugate priors include

Beta-distributed priors for Bernoulli-distributed data and normally distributed priors for normally distributed data (Hastie et al. 2009).

Once data have been observed, we construct a **likelihood function**. This is the joint probability function of the data, viewed as a function of the parameters with the observed data as fixed quantities, and hence is well-determined. Again assuming the data values $y = y_1, ..., y_n$ were obtained independently, the likelihood function, denoted $f(y|\theta)$, is given by

$$f(y|\theta) = p(y_1, ..., y_n|\theta) = \Pi_{i=1}^{n} p(y_i|\theta). \tag{5.16}$$

Under the Bayesian framework, all information about the parameters θ that comes directly from the data is contained in $f(y|\theta)$. Parameters that are well-supported by the data are those whose values correspond with large values of the likelihood function.

The goal of Bayesian analysis is to obtain a **posterior distribution**, $P(\theta|y)$, which is the probability distribution of the parameters once the data have been observed. For this, we apply Bayes' Theorem:

$$P(\theta|y) = \frac{f(y|\theta)\pi(\theta)}{\int f(y|\theta)\pi(\theta)d\theta}. \tag{5.17}$$

The denominator of this equation, $\int f(y|\theta)\pi(\theta)d\theta$, is the likelihood function marginalised over all parameter choices; this is simply a normalising constant that can be omitted so that the quantity of interest is the non-normalised distribution,

$$P^*(\theta|y) = f(y|\theta)\pi(\theta) \propto P(\theta|y). \tag{5.18}$$

For complex problems relevant to biological systems, it is often infeasible to compute the full posterior distribution, $P(\theta|y)$, analytically, as this would demand high-dimensional integration which is difficult or even intractable. However, often the non-normalised component, $P^*(\theta|y)$, is amenable to calculation for a given single choice of θ. In the next section we discuss some techniques for exploiting $P^*(\theta|y)$ to approximate $P(\theta|y)$ through sampling.

5.2.2 Techniques for sampling from Bayesian posteriors

Having defined a Bayesian model, we can numerically sample from the (analytically intractable) posterior distribution by applying **Markov chain Monte Carlo (MCMC)** methods, a broad class of statistical algorithms which generate a sample by progressing through a sequence of states in a Markov chain—a stochastic system that undergoes transitions from one state to another on a state space, such that the next state depends only on the current state and not on the sequence of states that preceded it (MacKay 2003).

Visualising an infinite number of identical Markov chain simulators running in parallel, we can denote the probability of the current state of a simulator as $p^{(t)}(\mathbf{x})$. A Markov chain is then specified by an initial probability distribution, $p^0(\mathbf{x})$, and by the probability of transitioning to a new state $\mathbf{x}'$, denoted $T(\mathbf{x}';\mathbf{x})$; and the probability distribution of the state at the $(t+1)$th iteration is given by $p^{(t+1)}(\mathbf{x}') = \int T(\mathbf{x}';\mathbf{x})p^{(t)}(\mathbf{x})\mathrm{d}\mathbf{x}$. In a MCMC model, samples are dependent due to their generation as successive states in the Markov chain; the goal is then to run the model for long enough to obtain *effectively* independent samples from the target distribution, $P(\mathbf{x})$. This occurs when the Markov chain converges to its stationary (time-invariant) distribution, $\Pi(\mathbf{x})$, which by construction is $P(\mathbf{x})$. In addition to constructing the chain such that $\Pi(\mathbf{x}) = P(\mathbf{x})$, we also require it to be ergodic, i.e. that $p^{(t)}(\mathbf{x}) \to \Pi(\mathbf{x})$ as $t \to \infty$ for any $p^0(\mathbf{x})$; in other words, every state must be reachable from every other state in a finite number of steps. Proving that an MCMC will converge to the target distribution often relies on it exhibiting the property of detailed balance, whereby transitions are symmetric and reversible: $T(\mathbf{x}_a;\mathbf{x}_b)p(\mathbf{x}_b) = T(\mathbf{x}_b;\mathbf{x}_a)p(\mathbf{x}_a)$ for all $\mathbf{x}_a$ and $\mathbf{x}_b$.

A number of algorithms are available for implementing MCMC methods. We will briefly discuss a few of the most popular options.

5.2.2.1 Metropolis methods

The first MCMC approach we consider, known as Metropolis-Hastings (or simply Metropolis), is a collection of algorithms for sampling from a non-normalised distribution $P^*(\mathbf{x})$ that can be evaluated at any point $\mathbf{x}$ (MacKay 2003). Metropolis methods utilise a proposal density, Q, which depends on the current state $\mathbf{x}^{(t)}$. The density $Q(\mathbf{x}';\mathbf{x}^{(t)})$ might be a simple Gaussian centred at the current $\mathbf{x}^{(t)}$ but does not need to look similar to the target distribution $P(\mathbf{x})$; rather, any fixed density from which we can draw samples is permissible.

A single iteration of a Metropolis method begins with the tentative drawing of a new state $\mathbf{x}'$ from the proposal density $Q(\mathbf{x}';\mathbf{x}^{(t)})$, for which an acceptance criterion is calculated:

$$A = \frac{P^*(\mathbf{x}')Q(\mathbf{x}^{(t)};\mathbf{x}')}{P^*(\mathbf{x}^{(t)})Q(\mathbf{x}';x^{(t)})}.$$

If $A \geq 1$, the new state is accepted; otherwise, the new state is accepted with probability A. If the state was accepted, we update $\mathbf{x}^{t+1} = \mathbf{x}'$, and if the state was rejected, we write the current state again onto the list by setting $\mathbf{x}^{(t+1)} = \mathbf{x}^{(t)}$. Computing the acceptance probability A requires computation of the probability ratios $P(\mathbf{x}')/P(\mathbf{x}^{(t)})$ and $Q(\mathbf{x}^{(t)};\mathbf{x}')/Q(\mathbf{x}';\mathbf{x}^{(t)})$; this is straightforward if the proposal density is a simple symmetric

density, in which case the latter ratio is $Q(\mathbf{x}^{(t)};\mathbf{x}')/Q(\mathbf{x}';\mathbf{x}^{(t)}) = 1$ and we only need to compare the value of the target density at the proposed and current states.

It can be shown that for any positive proposal density Q, a Metropolis algorithm will converge (that is, the probability distribution of $\mathbf{x}^{(t)}$ will tend to $P(\mathbf{x}) = P^*(\mathbf{x})/Z$, where Z is the normalising constant, as $t \to \infty$); but determining how *long* this will take is another problem entirely. In fact, Metropolis methods are notoriously slow to converge, and other algorithms are often preferred.

5.2.2.2 Gibbs sampling

If the distribution to be sampled has at least two dimensions, then Gibbs sampling—a Metropolis method in which a sequence of proposal distributions Q is defined in terms of the *conditional* distributions of the joint distribution $P(\mathbf{x})$—can be employed. This relies on the assumption that, while $P(\mathbf{x})$ is too complicated to draw samples from, its conditional distributions $P(x_i|\{x_j\}_{j\neq i})$ are tractable; and indeed, for many models it is straightforward to sample from these one-dimensional conditional distributions (MacKay 2003).

For the simplest case—a two-dimensional scenario where $\mathbf{x} = (x_1, x_2)$—on each iteration the Gibbs sampling algorithm starts from the current state $\mathbf{x}^{(t)}$ and samples x_1 from the conditional density $P(x_1|x_2)$ with x_2 fixed at $x_2^{(t)}$. A sample x_2 is then taken from the conditional density $P(x_2|x_1)$ using this new value of x_1, completing the iteration and bringing the algorithm to the new state $\mathbf{x}^{(t+1)}$.

In the general case of a system with n dimensions, a single iteration involves sampling each parameter sequentially as follows, with $\sim$ denoting sampling from a density:

$$\begin{aligned}
x_1^{(t+1)} &\sim P(x_1|x_2^{(t)}, x_3^{(t)}, ..., x_n^{(t)}) \\
x_2^{(t+1)} &\sim P(x_2|x_1^{(t+1)}, x_3^{(t)}, ..., x_n^{(t)}) \\
x_3^{(t+1)} &\sim P(x_3|x_1^{(t+1)}, x_2^{(t+1)}, ..., x_n^{(t)}) \\
&\vdots
\end{aligned}$$

Because Gibbs sampling is a Metropolis method, the probability distribution of $\mathbf{x}^{(t)}$ tends to $P(\mathbf{x})$ as $t \to \infty$. Gibbs sampling is subject to the same defects as Metropolis methods, namely that the state space is explored by a slow random walk; however, it is often favoured over Metropolis methods because the latter require the specification of adjustable parameters, such as the proposal state $\mathbf{x}'$.

5.2.2.3 Slice sampling

A third MCMC algorithm with similarities to both Metropolis methods and Gibbs sampling—but often preferable to both for reasons that will be discussed—is slice sampling, which can be applied wherever Metropolis methods can be applied; that is, to any system for which the target density, $P^*(\mathbf{x})$, can be evaluated at any point $\mathbf{x}$ (MacKay 2003).

Assuming for the moment that our goal is to sample from a one-dimensional density $P^*(x) \propto P(x)$, where x is a real number, slice sampling makes transitions from a two-dimensional point (x, y) that lies under the curve $P^*(x)$ to another point (x', y') that also lies under the curve. This results in the probability distribution of (x, y) tending to a uniform distribution over the interval(s) along x that lie under the curve $P^*(x)$.

To make a single transition from (x, y) to (x', y'), the slice sampling algorithm first evaluates $P^*(x)$, then draws a vertical coordinate y' from a uniform distribution over the interval $[0, P^*(x)]$. A horizontal interval, $[x_L, x_R]$, is created that encloses x (this is the 'slice'); a popular method for creating this interval is 'stepping out', whereby outward steps of length w are taken until endpoints x_L and x_R are found at which $P^* < y$. The next horizontal candidate x' is then drawn from a uniform distribution over the interval $[x_L, x_R]$, the function $P^*(x')$ is evaluated, and a new vertical coordinate y' is drawn from the uniform distribution over $[0, P^*(x)]$. If $P^*(x') > y'$, then the next transition can occur. If not, the interval $[x_L, x_R]$ must first be modified, commonly by a 'shrinking' step in which one of its endpoints is replaced with x'.

This algorithm is easily extendable to a multidimensional density $P^*(\mathbf{x}) \propto P(\mathbf{x})$; we can simply choose a sequence of directions $\mathbf{y}^{(1)}, \mathbf{y}^{(2)}, ...$ and define $\mathbf{x} = \mathbf{x}^{(t)} + x\mathbf{y}^{(t)}$. The function $P^*(x)$ from the one-dimensional case above is then replaced by the function $P^*(\mathbf{x}) = P^*(\mathbf{x}^{(t)} + x\mathbf{y}^{(t)})$. The choice of directions $\mathbf{y}^{(1)}, \mathbf{y}^{(2)}, ...$ is flexible: if they are the coordinate axes, then Gibbs sampling is recaptured, but they may be selected at random in any manner so long as the overall procedure satisfies detailed balance.

Slice sampling is similar to both Metropolis methods and Gibbs sampling—like Metropolis methods it involves a random walk, and like Gibbs sampling it consists of one-dimensional transitions in state space—but is more robust than either of these. For Metropolis methods the choice of proposal state $\mathbf{x}'$ is critical to the rate at which the algorithm progresses, but in slice sampling the step size w is self-tuning; and, unlike Gibbs sampling, slice sampling does not require easily-sampled conditional distributions.

5.3 Application of Bayesian methods to our model

We have three sets of data from *in vitro* experiments on dynamics in single HCT116 tumour cells: one for intrinsic cellular buffering power, one for flux due to Na^+/H^+ exchange across the membrane, and one for flux due to Na^+/HCO_3^- co-import; these data are discussed further and graphed in Appendix F. We want to use information from these data to estimate the parameters involved in Equations (5.2), (5.4), and (5.5). Under the assumption that our data are normally distributed (reasonable as discussed previously due to the central limit theorem), we assign normal prior distributions to these parameters so that they are conjugate to the posterior, but use proportionally large standard deviations to ensure that they are relatively non-informative. These prior distributions are visualised in Figure 5.2.

For each of the functions given by Equations (5.2), (5.4), and (5.5) in turn, we apply Bayes' Theorem, given by Equation (5.18), to the corresponding experimental data set and the relatively flat priors we have assigned to each of the relevant parameters. We then employ a slice sampling algorithm (the inbuilt *slicesample* function in Matlab), the general theory behind which was discussed in Section 5.2.2.3, to sample from the three resulting (non-normalised) joint posterior distributions.

A convenient way to visualise a joint posterior distribution is by looking at the marginal posterior distribution for each parameter; that is, the probability distribution of each parameter averaged over the other parameters. To confirm that our slice sampling algorithm correctly samples from our three joint posterior distributions—defined by S and κ_s from Equation (5.2), γ_{1-3} from Equation (5.4), and γ_{4-6} from Equation (5.5)—we plot the sampling traces, or paths along the x-axis underlying the curve $P^*(x)$ that the slice sampling algorithm takes, for the marginal distribution of each parameter as a function of sample number (Figure 5.3). We observe that these marginal traces resemble high-frequency noise, which indicates that they exhibit no discernible autocorrelation between adjacent samples. The sampling also clearly exhibits convergence to stationarity; that is, moving averages of the traces stay roughly constant with an increasing number of samples. Therefore, we can safely conclude that our slice sampler is generating samples for each parameter which are effectively independent and converge on the desired joint posterior distributions.

Calculating the mean and covariance of each of our slice samples, then, provides us with approximations to the mean and covariance matrix for each joint posterior distribution. Taking the square root of the diagonal entries of the covariance matrix gives us the marginalised standard deviation for each parameter (Hastie et al. 2009). Using this information, we can plot the approximate (non-normalised) marginal posterior distribution for each parameter,

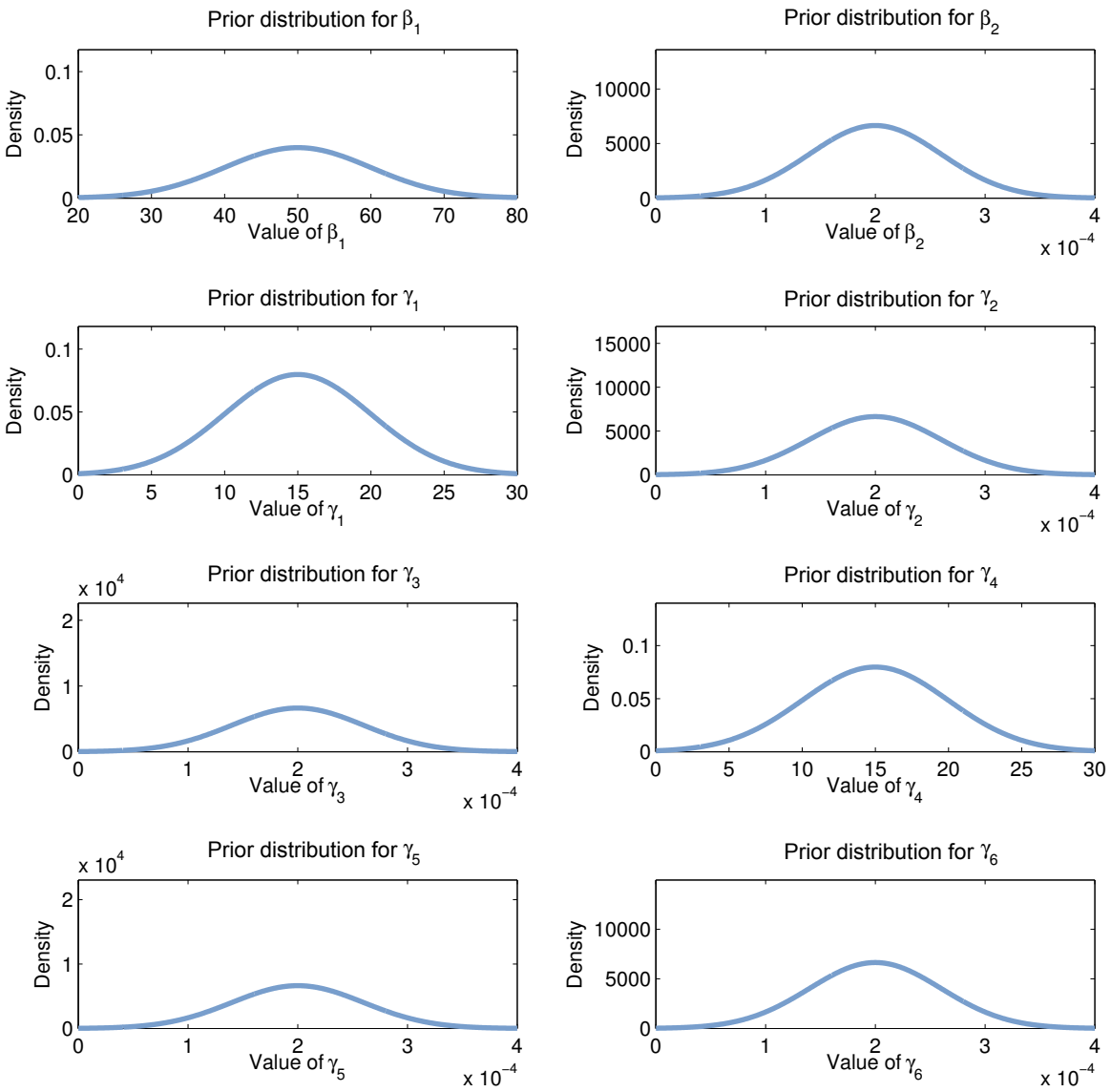

Figure 5.2: Bayesian prior distributions. Relatively flat normal prior distributions (blue curves) for the coefficients governing Equations (5.2), (5.4), and (5.5), chosen to be conjugate to the normal posterior distributions but with proportionally large standard deviations to minimise our *a priori* assumptions about the parameter values.

and observe how our Bayesian method has updated the prior distributions that we had originally assigned to the parameters before seeing the data (Figure 5.4).

We can draw some conclusions from Figure 5.4 about relative sensitivities of the buffering power, Na^+/H^+ efflux, and Na^+/HCO_3^- influx to our model parameters. For example, the maximal rates of Na^+/H^+ efflux and Na^+/HCO_3^- influx—the parameters γ_1 and γ_4, respectively—have (approximate) marginal posterior distributions which are nearly as wide as their prior distributions. This indicates that Na^+/H^+ efflux and Na^+/HCO_3^- influx are not very sensitive to our choice of the maximal flux rates. In contrast, the (approximate)

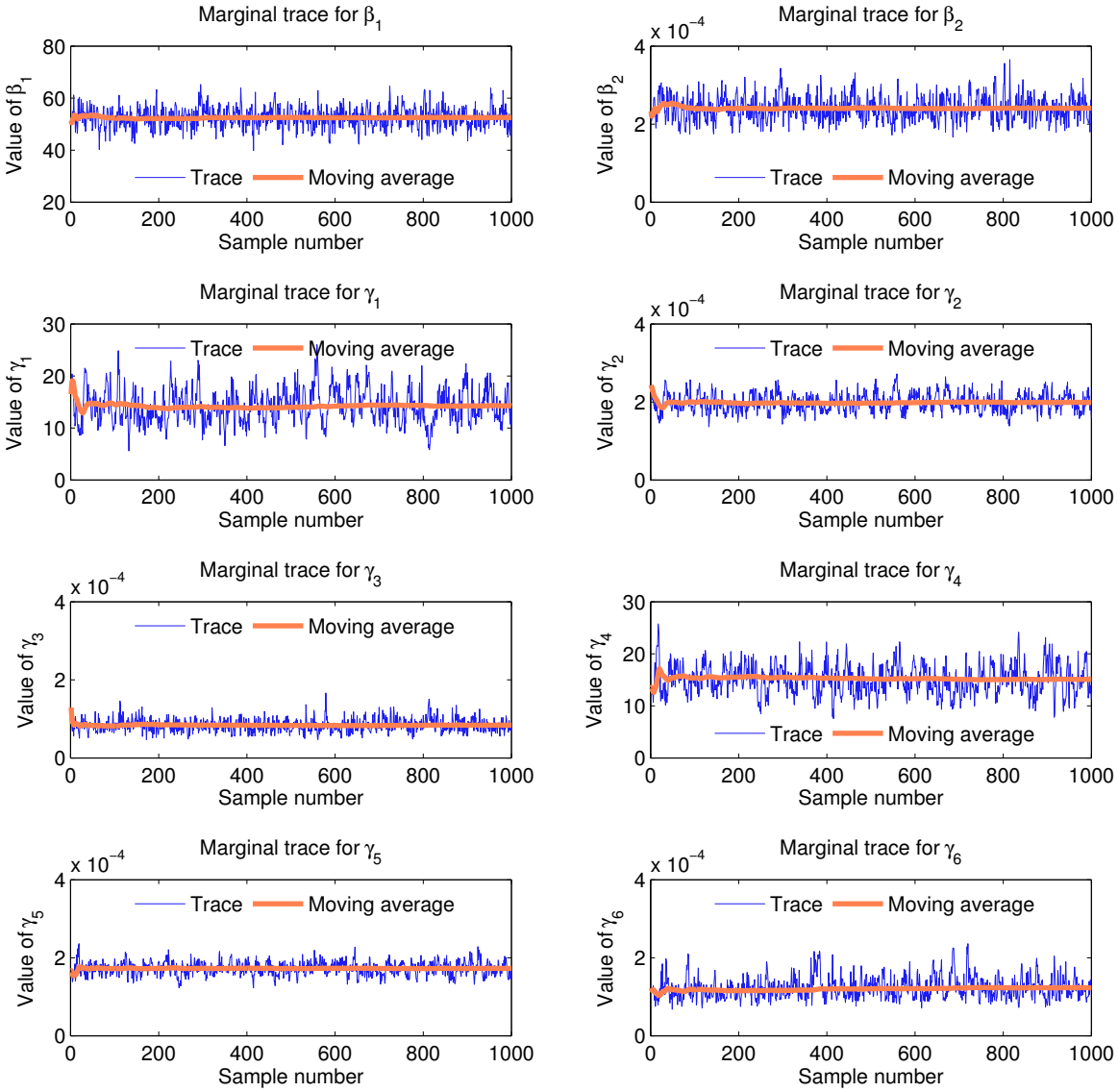

Figure 5.3: Convergence of slice sampling of Bayesian posteriors. Traces (blue) from slice samples of our Bayesian posteriors (described in Section 5.3) show no discernible autocorrelation between adjacent samples. If autocorrelation were present, the traces would resemble low-frequency noise. The sampling also exhibits convergence to stationarity; that is, the moving averages (orange) stay roughly constant as the number of samples increases.

marginal posterior distributions for the intracellular half-saturation parameters γ_3 and γ_5 are considerably narrower than their prior distributions, suggesting that Na^+/H^+ efflux and Na^+/HCO_3^- influx are sensitive to the intracellular pH at which the capacity of Na^+/H^+ exchangers and Na^+/HCO_3^- importers, respectively, become half-saturated. This makes sense, as both transporters are known to be highly sensitive to intracellular acidity (Parks et al. 2013).

As a final confirmation of our Bayesian method, Figures 5.5 shows that our Bayesian fit for

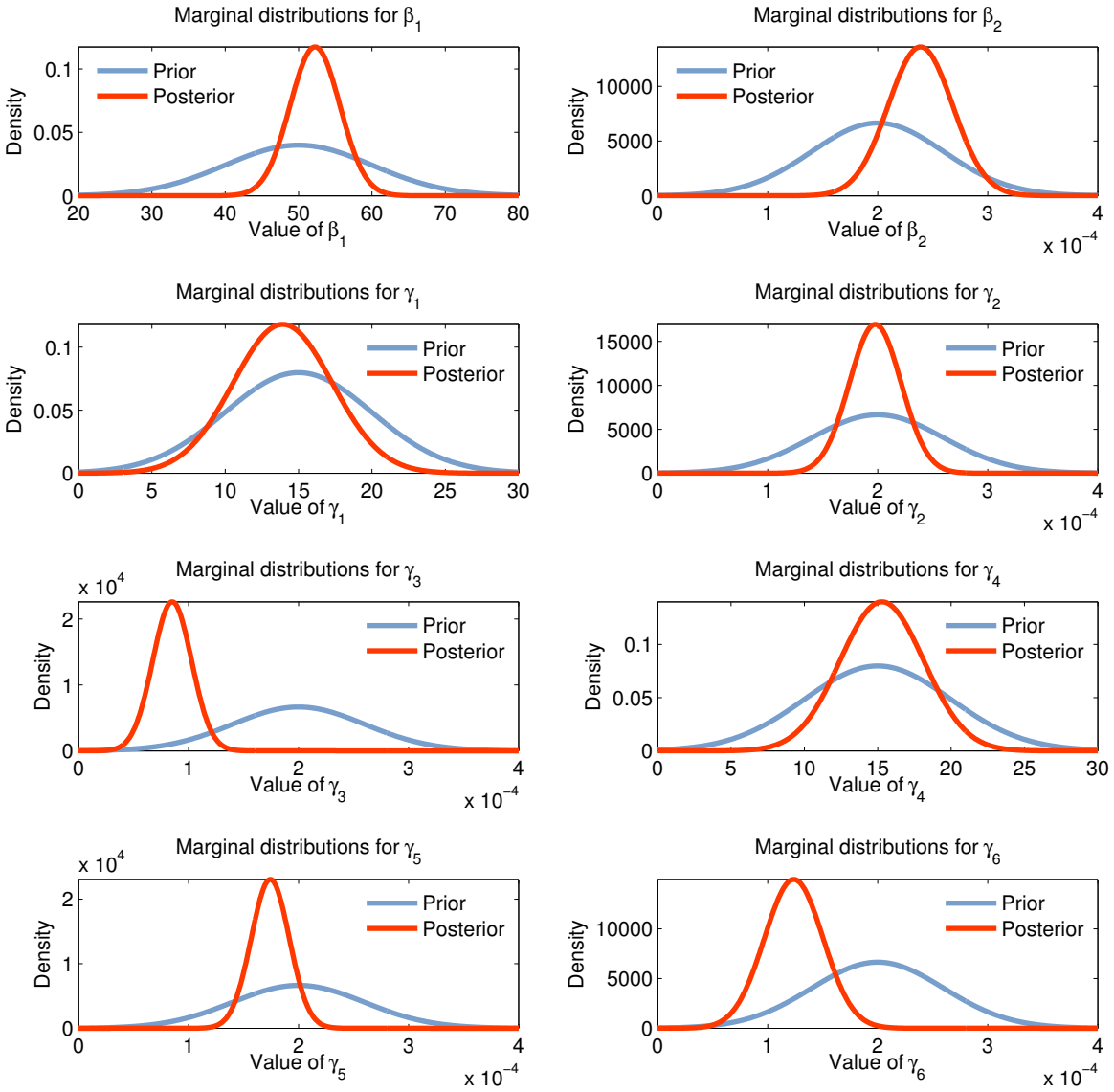

Figure 5.4: Bayesian priors and posteriors. Relatively flat normal priors (blue) chosen for the coefficients governing Equations (5.2), (5.4), and (5.5) as shown in Figure 5.2, overlaid with the approximate marginal posterior distributions (red) for those same coefficients that result from the Bayesian updating and slice sampling procedure outlined in Section 5.3.

the parameters in Equations (5.2), (5.4), and (5.5) provides good coverage of the data. The statistics specifying the (approximate) joint posterior distributions for these parameters are listed in Table 5.2.

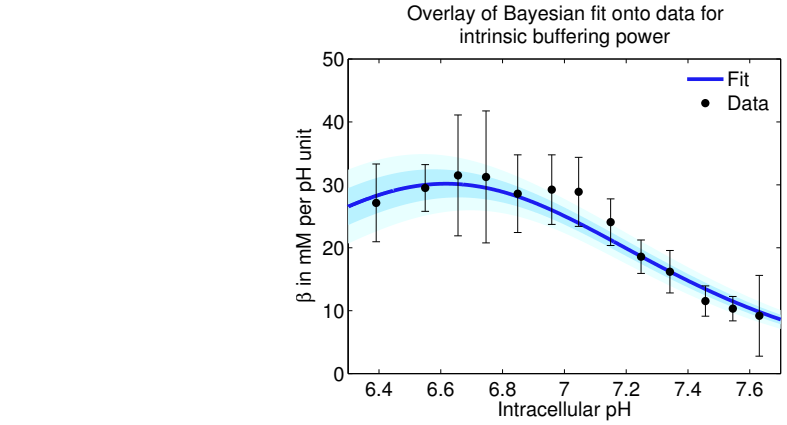

(a)

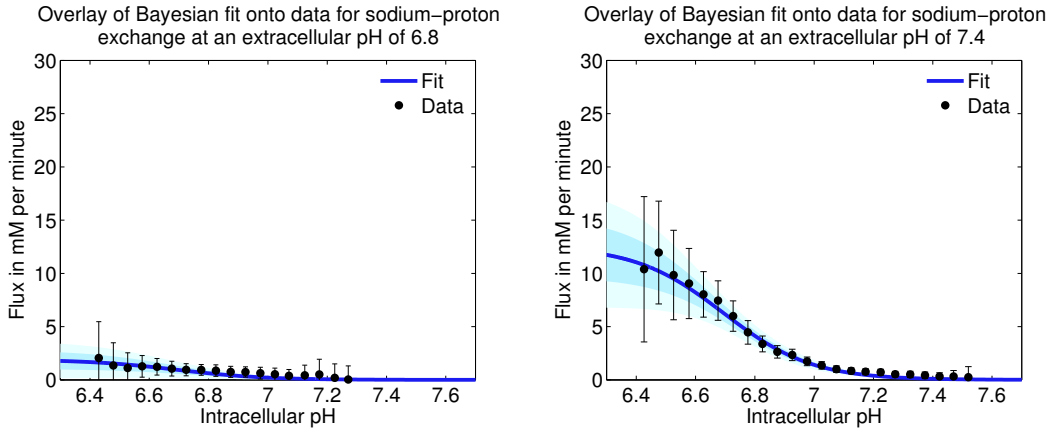

(b)

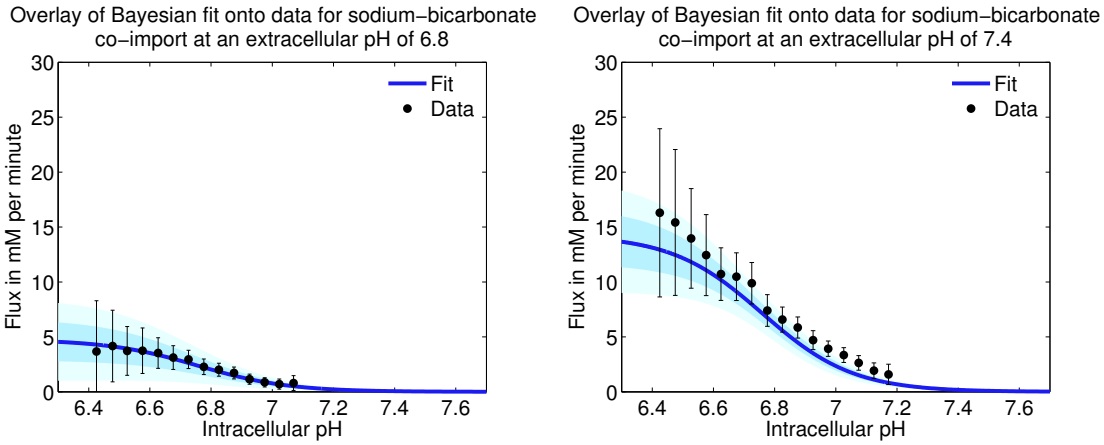

(c)

Figure 5.5: Overlay of our Bayesian fits onto data. Our Bayesian fitting procedure outlined in Section 5.3 results in good coverage of the data we have for (a) buffering power, which we model with Equation (5.2), (b) two representative slices through the extracellular pH dimension of H^+ efflux due to Na^+/H^+ exchange, which we model with Equation (5.4), and (c) two representative slices through the extracellular pH dimension of HCO_3^- influx due to Na^+/HCO_3^- co-transport, which we model with Equation (5.5). Shown are the mean (dark blue curve), one standard deviation from the mean (medium blue shading), and two standard deviations from the mean (pale blue shading) of 10^3 samples from our approximate joint posterior distributions, overlaid on the *in vitro* data (black dots) with error bars showing the data standard deviations. These data are listed in Appendix F.2.

5.4 Validation against experimental dynamics

Having calibrated the distributions for the parameters in Equations (5.2), (5.4), and (5.5) against experimental data in a Bayesian framework, we return to our full system for pH regulation in single cells, Equations (5.11)-(5.15). Some of our model parameters are well-established or help to set up the geometry of our simulations (for example, the radius of a single cell, c, is fixed at 6μm as representative of an average tumour cell); these are listed in Table 5.1. Against this background, we represent the remaining parameters in Equations (5.11)-(5.15) as random variables, allowing them to vary according to normal distributions about their estimated mean values, which we take from experimental estimates in the literature. Proportionally larger standard deviations are chosen for parameters which are less well-characterised experimentally. These are detailed in Table 5.2.

Table 5.1: Fixed parameters for Eq (5.11)**-**(5.15)**.** Parameters that we consider to be either well-determined or important for a consistent set-up for numerical solutions of Eq (5.11)-(5.15).

	Value	Units	Source
κ_d	$6 \cdot 10^7$	1/min	Not limiting
κ_a	$6 \cdot 10^8$	1/(mM·min)	Formula, $k_r = K_a k_f$
κ_f	8.4	1/min	Appendix G.2
κ_r	$1.1 \cdot 10^4$	1/(mM·min)	Appendix G.2
c	6	μm	Swietach et al. (2009)
η	3	None	Bayesian fitting
ξ	3	None	Bayesian fitting

We now validate Equations (5.11)-(5.15) by simulating a number of experimental scenarios that explore the varying capacity of single HCT116 tumour cells to recover a favourable (slightly alkaline) intracellular pH following an acid spike under different conditions.

By imposing an initial intracellular pH of 6.6—that is, by setting $Hi(t = 0) = 10^{-6.6}10^3$ mM—we simulate an ammonium prepulse-induced acid spike. This is a common experimental strategy for observing pH recovery dynamics *in vitro* (Leem et al. 1999, Swietach et al. 2009). We then specify a healthy extracellular pH of 7.4 by setting $He = 10^{-7.4}10^3$mM, and set $Be = Ce = 0$ to simulate an experimental situation where the cell is flushed with an artificial buffer such as Hepes (Figure 5.6A). Keeping $Be = Ce = 0$ but setting $He = 10^{-6.8}10^3$ mM allows us to simulate the same artificial buffer in the presence of extracellular acidity (Figure 5.6C). Furthermore, we simulate physiological buffering (5.5% CO_2/22mM HCO_3^-) at a healthy extracellular pH of 7.4 by setting $Be = 22$ mM,

Ce = 1.1 mM, and $He = 10^{-7.4}10^3$ mM (Figure 5.6B). Finally, we simulate CO^2/HCO_3^- buffering at an acidic extracellular pH by setting $He = 10^{-6.8}10^3$ mM, Be = 5.5 mM, and Ce = 0.275 mM (Figure 5.6D). In each of these figures, the effects of inhibiting Na^+/H^+ extrusion and/or Na^+/HCO_3^- import are explored by setting $\gamma_1 = 0$ to mimic treatment with 5(NN-dimethyl)amiloride (DMA) and/or $\gamma_4 = 0$ to mimic treatment with 44'-diisothiocyanatostilbene-22'-disulfonic acid (DIDS), respectively.

The dynamics in Figure 5.6 are in good agreement with published experimental data (Figure 5.7). Similarly to the cells in the experiments, our model cells are able to recover a favourable intracellular pH within ten minutes under a wildtype scenario in artificial buffer, but this recovery is inhibited by treatment with DMA (Figure 5.6A), indicating that Na^+/H^+ exchange is the dominant pH regulation mechanism in the absence of the CO_2/HCO_3^- buffering system. In an acidic extracellular medium, however, the effectiveness of Na^+/H^+ exchange is impeded, and this is exacerbated by the addition of DMA (Figure 5.6C). Under physiological conditions of a healthy pH and CO_2/HCO_3^- buffering (Figure 5.6B), our model wildtype cells recover from the initial acid spike within ten minutes; and furthermore, treatment with a combination of DMA and DIDS is more detrimental to this recovery than DMA alone, indicating that both Na^+/H^+ exchange and CO_2/HCO_3^- buffering (facilitated by Na^+/HCO_3^- import) are important for pH regulation. Finally, Figure 5.6D again confirms the inhibitory effect of extracellular acidity on intracellular pH recovery: the recovery of our model wildtype cells is slower at an extracellular pH of 6.8 than at 7.4 in Figure 5.6B, with the addition of DMA impeding it further.

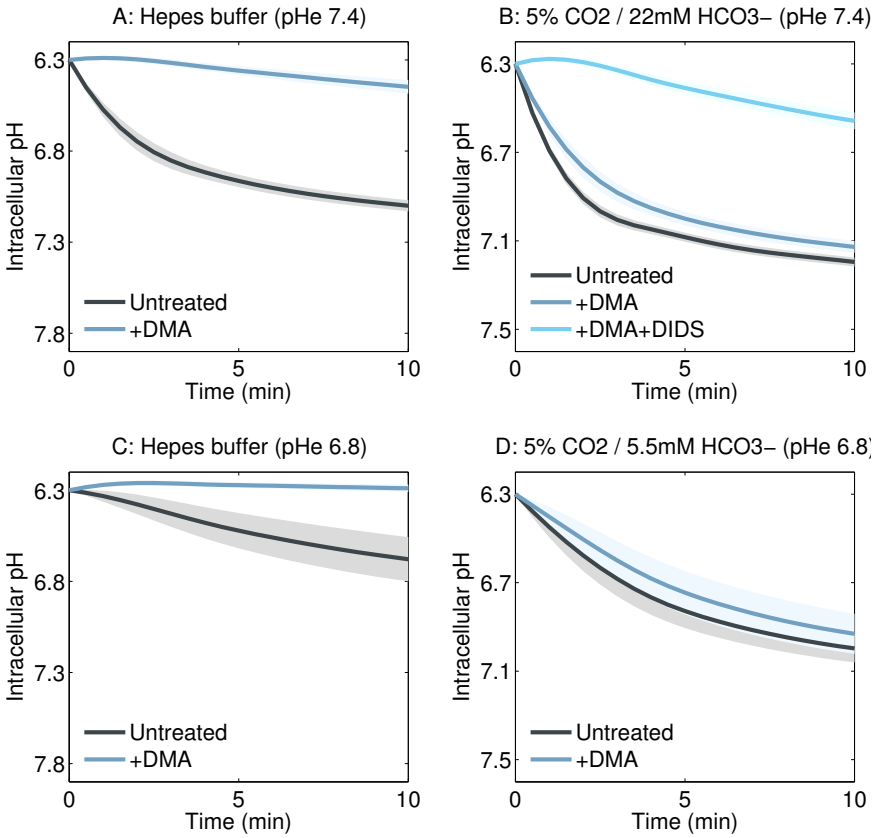

Figure 5.6: Simulated pH recovery in single cells. Means (curves) and standard deviations (shading), each from 10^3 numerical simulations of Equations (5.11)-(5.15) with an initial intracellular acid spike imposed by setting $Hi(t=0) = 10^{-6.6}10^3$ mM, corresponding to a pH of 6.6. Parameters are fixed at the values listed in Table 5.1 or sampled randomly from the distributions in Table 5.2. We show how the intracellular pH recovers from the acid spike under a series of simulated experimental scenarios: A, at physiological extracellular pH (here denoted pHe) in the absence of CO_2/HCO_3^- buffering, which we simulate by setting $He = 4 \cdot 10^{-5}$ (corresponding to a pH of 7.4), $Be = 0$, and $Ce = 0$, all in mM; B, at physiological extracellular pH in the presence of CO_2/HCO_3^- buffering, simulated by setting $He = 4 \cdot 10^{-5}$, $Be = 22$, and $Ce = 1.1$ mM; C, at acidic extracellular pH in the absence of CO_2/HCO_3^- buffering, simulated by setting $He = 1.6 \cdot 10^{-4}$ (corresponding to a pH of 6.8), $Be = 0$, and $Ce = 0$ mM; and D, at acidic extracellular pH in the presence of CO_2/HCO_3^- buffering, simulated by setting $He = 1.6 \cdot 10^{-4}$, $Be = 5.5$, and $Ce = 0.275$ mM. Shown are the wildtype system (black), the system with $\gamma_1 = 0$ to represent inhibition of Na^+/H^+ exchange by 5-(N,N-dimethyl)amiloride (DMA; blue), and the system with $\gamma_4 = 0$ to represent inhibition of Na^+/HCO_3^- import by 4,4'-diisothiocyanatostilbene-2,2'-disulfonic acid (DIDS; turquoise). Note that we have reversed the direction of the y-axis such that pH decreases as we move up the axis (i.e. acidity increases); this is done according to convention. Our simulated recovery dynamics agree with experimental results from Hulikova et al. (2011), shown for comparison in Figure 5.7.

Table 5.2: Variable parameters for Eq (5.11)-(5.15)**.** Parameters we view as random variables and sample for numerical solutions of Eq (5.11)-(5.15), calibrated by the Bayesian procedure outlined in Sections 5.2 or varied about a mean value taken from literature estimates. The statistic μ denotes the mean of a univariate normal distribution or vector of means for a multivariate normal distribution; Σ denotes the covariance matrix of a multivariate normal distribution and σ the standard deviation of a univariate normal distribution.

	Statistics	Source	Units
β_1	$\mu = \begin{pmatrix} 53.4 \\ 2 \cdot 10^{-4} \end{pmatrix}$ $\Sigma = \begin{pmatrix} 1.7 & 10^{-5} \\ 10^{-5} & 9.8 \cdot 10^{-11} \end{pmatrix}$	Bayesian fitting of Eq (5.2)	mM/pH-unit
β_2			mM
γ_1	$\mu = \begin{pmatrix} 13.6 \\ 10^{-4} \\ 2 \cdot 10^{-4} \end{pmatrix}$ $\Sigma = \begin{pmatrix} 0.04 & 5 \cdot 10^{-7} & -4 \cdot 10^{-7} \\ 5 \cdot 10^{-7} & 10^{-10} & 4 \cdot 10^{-11} \\ -3 \cdot 10^{-7} & 4 \cdot 10^{-11} & 5 \cdot 10^{-10} \end{pmatrix}$	Bayesian fitting of Eq (5.4)	mM/min
γ_2			mM
γ_3			mM
γ_4	$\mu = \begin{pmatrix} 18.1 \\ 2 \cdot 10^{-4} \\ 4 \cdot 10^{-4} \end{pmatrix}$ $\Sigma = \begin{pmatrix} 0.4 & 6 \cdot 10^{-6} & 7 \cdot 10^{-6} \\ 6 \cdot 10^{-6} & 3 \cdot 10^{-9} & 10^{-11} \\ 7 \cdot 10^{-6} & 10^{-11} & 10^{-8} \end{pmatrix}$	Bayesian fitting of Eq (5.5)	mM/min
γ_5			mM
γ_6			mM
α_{II}	$\mu = 4$ $\sigma = 0.8$	Swietach et al. (2009)	None
ρ_L	$\mu = 10^5$ $\sigma = 2 \cdot 10^4$	Swietach et al. (2009)	μm/(mM·min)
ρ_A	$\mu = 60$ $\sigma = 36$	Parks et al. (2013)	μm/min
ρ_C	$\mu = 60$ $\sigma = 12$	Swietach et al. (2003, 2008)	μm/min
υ_A	$\mu = 30$ $\sigma = 18$	Kunz-Schughart et al. (2000), Walenta et al. (2000)	mM/min
υ_C	$\mu = 30$ $\sigma = 18$	Kunz-Schughart et al. (2000), Walenta et al. (2000)	mM/min

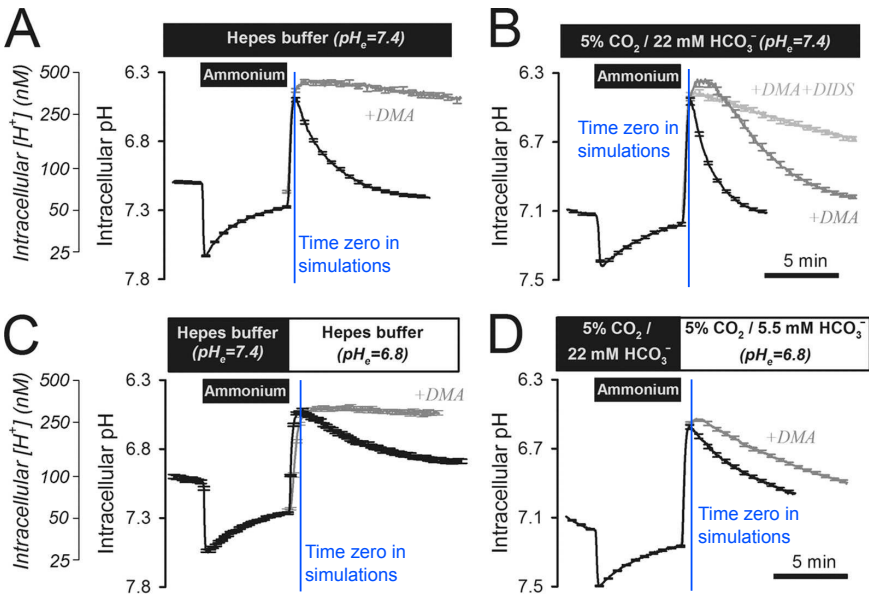

Figure 5.7: pH recovery in single HCT116 cells. Experimental results presented by Hulikova et al. (2011). A, ammonium prepulse, at an extracellular pH (pH_e) of 7.4, performed to acid load HCT116 cells superfused with CO_2/HCO_3^- free, 20mM Hepes buffer. Intracellular pH recovery was inhibited by DMA (30μM). Mean of >30 cells. B, ammonium prepulse (at pH_e 7.4) performed to acid load HCT116 cells, superfused with 5% CO_2/22mM HCO_3^- buffer. On removal of ammonium, intracellular pH recovery was partly inhibited by DMA (30μM). The remainder of acid extrusion was sensitive to 300μM DIDS. Mean of >30 cells. C, at the reduced pH_e of 6.8, intracellular pH recovery in Hepes buffer remained DMA-sensitive but was considerably slower than at pH_e 7.4. D, in CO_2/HCO_3^- buffer, intracellular pH recovery was slower at low pH_e attained by reducing [HCO_3^-] to 5.5mM. Mean of >30 cells. Error bars indicate standard error. Image reproduced with permission from the *Journal of Biological Chemistry*.

5.5 Our model predicts a "reverse" pH gradient

Upon varying the extracellular pH in our single-cell model, and plotting the resulting trans-membrane gradient from intracellular to extracellular pH, we predict a "reverse" pH gradient (that is, a positive gradient indicating the intracellular pH is higher than the extracellular pH) for acidic extracellular pH values. This reverse pH gradient is a distinctive feature of tumours (Webb et al. 1999a), and in this regard our model succeeds where the single-cell model of Al-Husari and Webb (2013a), which obtained the reverse pH gradient only under unphysiological pH values, did not. We further predict a non-monotonic dependence of the gradient on extracellular pH, such that the size of the gradient is maximised at an extracellular pH of 6.8. Our results are consistent with expectations: near physiological values of extracellular pH, the tumour pH regulation mechanisms operate optimally and maintain a favourable intracellular pH; but as the extracellular space grows more acidic, pH-dependent trans-membrane fluxes become inhibited, preventing the cell from extruding its acid load. We note that our Bayesian-and-sampling based approach to model exploration reveals an increasing variability in this relationship as the extracellular acidity increases; this captures the uncertainty that arises from difficulties in obtaining experimental flux measurements at lower pH values (Swietach 2011).

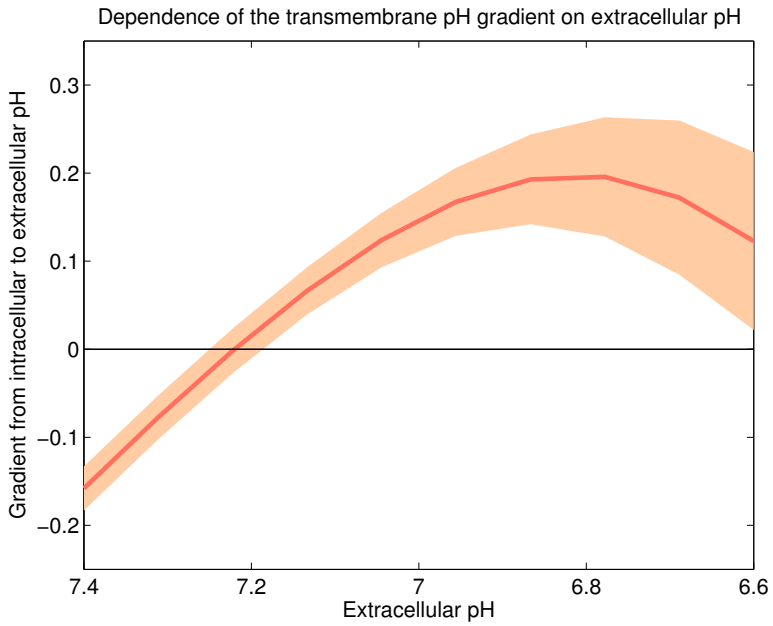

Figure 5.8: Predicted intracellular versus extracellular pH. Mean intracellular pH (curve) and standard deviation (shading) as a function of extracellular pH, from 10^3 numerical simulations of Equations (5.11)-(5.15) over a range of extracellular pH values. Parameters were fixed at the values listed in Table 5.1 or sampled randomly from the distributions in Table 5.2, and all simulations were run to an end-time of 10 minutes. The intracellular-extracellular pH relationship is what we expect to see, given the pH-dependence of the acid-extrusion and buffering mechanisms in our single-cell system. Note again that we have reversed the direction of the axes to follow convention.

5.6 Discussion

In this chapter, we have incrementally developed a comprehensive model of pH regulation in single tumour cells, beginning from first principles. To calibrate a group of our model parameters, we have employed a Bayesian approach which integrates information from a series of experimental datasets, and validated the resulting model by reproducing experimentally observed metabolic behaviours. Furthermore, we have made the prediction of a "reverse" pH gradient that is in line with both clinical observations and our expectations given the dependence on extracellular acidity of the main mechanisms governing pH regulation.

In the next chapter we will embed this single-cell model into a spatial framework that takes into account the biochemical reactions and crowding-impeded diffusion which occur in the local extracellular space of a tumour spheroid, and thereby elucidate features of the full tumour pH regulation network.

Chapter 6

A model of pH regulation in tumour spheroids

In this chapter we extend the single-cell model of the tumour pH regulation system that we developed in Chapter 5 to incorporate the spatial features of a tumour spheroid. We then calibrate this model against experimentally observed spheroid behaviours, and use it to gain novel insights that are relevant both to our general understanding of tumour acidity and to potential therapeutic approaches.

We will first discover that the pH regulation system is highly sensitive to some metabolic parameters which are difficult to measure experimentally; and that, as postulated by Parks et al. (2013), leakage of protonated lactic acid into the extracellular space plays a role belied by the low pK_a (negative log of the dissociation constant) of the molecule. We will also predict the effects of multiple targeted treatment strategies on the maintenance of a favourably small intracellular pH gradient across our model spheroid, motivated by the aim of determining whether any of the strategies can disrupt the intracellular pH sufficiently to trigger cell death. The treatment strategies we consider here were proposed recently by Parks et al. (2013), and their components have received considerable interest from the oncological community over the past several years. Lastly, we test the transmembrane pH gradient in the core of our model spheroid, which allows us to comment on the validity of assumptions implicit to the models we presented in Chapters 2-4 and to many other continuum models of tumour metabolism.

6.1 The spatial model

Herein, we will limit our scope of consideration to relatively short time-scales in order to exclude cell death, growth, and migration in our simulated spheroids, and instead focus exclusively on nutrient dynamics. For experiments involving tumour spheroids, researchers typically select samples that have grown with something close to spherical symmetry, particularly when culturing is done by the hanging drop method (Swietach et al. 2010); hence, we will make the assumption of radial symmetry in our model. This is also valid for considering the metabolic behaviour of an avascular tumour *in vivo*.

Similarly to the single-cell experimental set-ups described in Chapter 5, conditions in spheroid experiments are controlled by manipulation of the superfusate, but now the superfusate washes over the spheroid surface rather than over the exterior of a single cell. In keeping with the experimental scenarios to be considered in this chapter, we model spheroids which are moderately developed such that they are beginning to experience nutrient gradients and harshening interior conditions but have not yet attained the size necessary for the formation of central necrosis; that is, spheroids less than 0.05 centimetres in diameter (Swietach et al. 2008). Inside these intermediate spheroids, cells tend to grow densely, with cellular crowding increasing with depth inward toward the core (Cairns et al. 2011). Thus, we can assume that metabolites diffuse locally through extracellular space subject to crowding conditions, and exchange with the well-mixed superfusate at the (less crowded) spheroid edge. This edge also corresponds to the well-perfused periphery of an avascular tumour *in vivo*.

Under these assumptions, the system we develop here will describe averaged behaviours in the bulk intracellular and extracellular spaces of a tumour spheroid, without losing information about fluxes across the cell membranes. Our model will capture the components of pH regulation which are thought to be the drivers of tumour cell survival in a stressed microenvironment; these were discussed in detail in Chapter 1. For the reader's convenience we reproduce our visual summary of the tumour pH regulation network in Figure 6.1.

Under our model formulation, the bulk intracellular and extracellular spaces are overlaid on the tumour domain, with metabolites reacting inside the bulk intracellular space, passing across the intracellular-extracellular boundary (the cell membranes), and reacting locally and/or diffusing through the extracellular space. We impose a large intracellular-to-extracellular volume ratio to represent tight cellular packing (Swietach et al. 2009). We also hold constant the locations of the tumour core and edge, denoted $r = 0$ and $r = R$, respectively, with r representing the radial distance from the tumour core in polar coordinates.

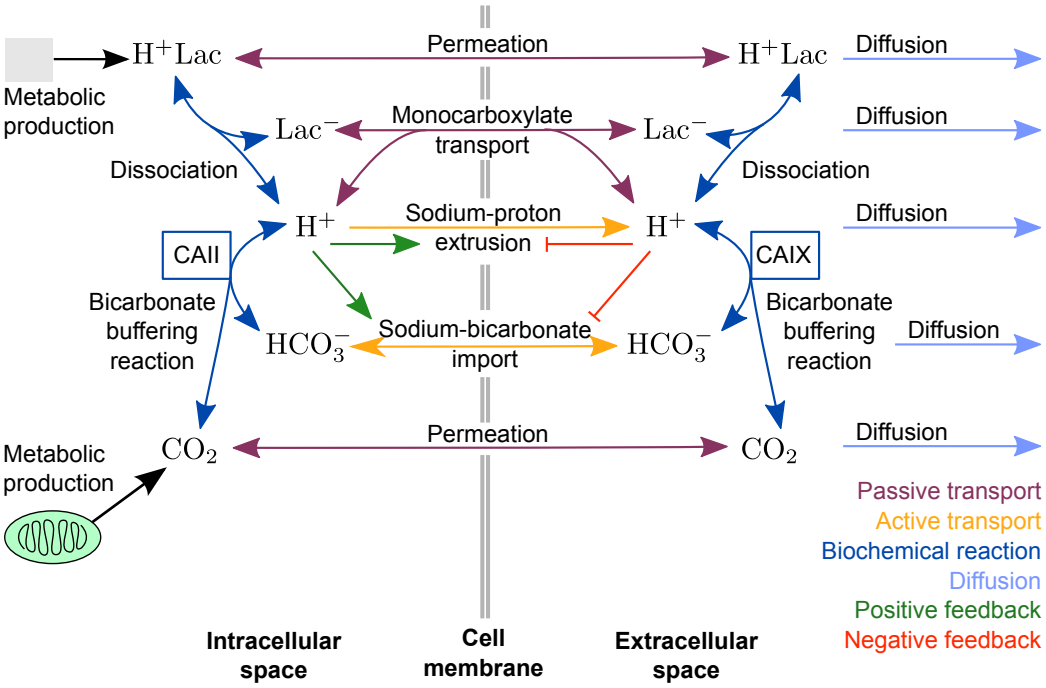

Figure 6.1: The pH regulation system in tumours. Interrelated biochemical mechanisms for handling of metabolically-derived acid loads and maintenance of pH in the intracellular space of a tumour cell, across the cell membrane, and in the local extracellular space of the microenvironment. Species in this system are protonated lactic acid (H^+Lac), lactate ions (Lac^-), free protons (H^+), bicarbonate ions (HCO_3^-), and carbon dioxide (CO_2). The bicarbonate buffering reaction is catalysed by carbonic anhydrase II (CAII) inside the cell, and by membrane-tethered carbonic anhydrase IX (CAIX) in the local extracellular space.

Although the bulk intracellular space can be viewed as a solid (cellular) phase and the bulk extracellular space as a fluid phase—following the two-phase mixture models of Chen et al. (2001), Jackson and Byrne (2002), Byrne et al. (2003), Byrne and Preziosi (2003), and Roose et al. (2003)—we instead model these as simple compartments, with the aim of focussing on the biochemical dynamics of pH regulation at a timescale smaller than that at which tumour growth and tissue-mechanical effects play significant roles. Our framework exhibits some similarities to a recent model by Al-Husari and Webb (2013b), but with explicit consideration of bicarbonate buffering and catalysis such that it more directly encapsulates the full suite of established tumour mechanisms for pH regulation.

6.1.1 Equations and terms

It is evident from Figure 6.1 that the intracellular and transmembrane processes are essentially the same as they were in our single-cell system in Chapter 5. Now, however, metabolic production is no longer constant, but rather is responsive to local microenvironmental cues, such as availability of oxygen. An average intermediately-developed spheroid (or avascular

tumour *in vivo*) has a radius (R) of roughly 300 μm, but the oxygen fall-off distance is roughly 150 μm (Rockne et al. 2010), resulting in poor perfusion in the interior. Oxidative phosphorylation requires oxygen, while the glycolytic pathway is upregulated by hypoxia-induced signalling cascades (Burgman et al. 2001, Airley et al. 2001, Williams et al. 2002, Wincewicz et al. 2007, Liu et al. 2009); thus, we will represent them both as depending upon perfusion, ω, which we can model phenomenologically with a simple function that decays with depth into the tumour:

$$\text{Perfusion} = 1 - \tanh\left(\frac{R-r}{\omega}\right). \tag{6.1}$$

The two metabolic pathways then oppose each other across space, with the rate of CO_2 production by oxidative phosphorylation, F_{oxi}, reaching its maximum at the well-perfused tumour edge, and the rate of H^+Lac production by glycolysis, F_{gly}, reaching its maximum in the hypoxic core:

$$F_{oxi} = \upsilon_C\left(1 - \tanh\left(\frac{R-r}{\omega}\right)\right), \tag{6.2}$$

$$F_{gly} = \upsilon_A \tanh\left(\frac{R-r}{\omega}\right), \tag{6.3}$$

where υ_C and υ_A are the maximal rates of CO_2 production by oxidative phosphorylation and H^+Lac production by glycolysis, respectively.

In our single-cell scenario in Chapter 5, metabolites were flushed away from the extracellular surface by the superfusate; but in the spheroid scenario, they can persist and react with one another in the local extracellular space. Thus, we have an extracellular lactic acid dissociation reaction, which follows the same chemical scheme as the intracellular reaction given by Equation (5.1). Additionally, the CO_2/HCO_3^- buffering reaction occurs in the extracellular space, following the same scheme as Equation (5.6) but now catalysed by the extracellular, tumour-expressed carbonic anhydrase IX (CAIX). We denote the catalytic activity of CAIX as α_{IX}.

In addition to reacting in the local extracellular space, we also now allow our metabolic species to diffuse, as mentioned previously. We incorporate crowding effects into this diffusion by introducing another simple function that phenomenologically captures an increasing restriction on freedom of movement as we move inward toward the core:

$$\text{Crowding} = \tanh\left(\frac{R-r}{\zeta}\right), \tag{6.4}$$

where ζ is a measure of the distance into the tumour at which crowding develops. If ζ is small, then a large extent of the tumour is crowded, while a larger ζ means that

crowding is less extensive and the above function will be relatively flatter. We note that the monotonicity of Equation (6.4) precludes consideration in this context of the peaked tumour fronts seen in Chapter 2. We incorporate Equation (6.4) as a space-restricted diffusion term; that is, for a generic metabolite M, diffusion in the extracellular space (in polar coordinates) is given by

$$\frac{\delta_M}{r^2}\frac{\partial}{\partial r}\left[r^2\left(1-\tanh\left(\frac{R-r}{\zeta}\right)\right)\frac{\partial M}{\partial r}\right], \tag{6.5}$$

where δ_M is the free-space diffusion coefficient of metabolite M. The diffusion coefficient for free protons, H^+, requires a slightly different interpretation: analogously to what occurs intrinsically in the intracellular space, free protons are taken up onto mobile species in the local extracellular environment (Swietach et al. 2009), and thus δ_H represents the *effective* diffusion coefficient of H^+ on these molecular carriers.

Taking all of this together and carrying the remaining reaction and transport mechanisms over from our single-cell framework, and letting ν denote the ratio of the total extracellular to intracellular volume, our full spheroid system is stated on the following pages.

$$\frac{\partial Hi}{\partial t} = \overbrace{\left(-\log_{10}\left(\frac{\ln(10)S\kappa_s Hi}{(\kappa_s+Hi)^2}/10^3\right)\right)^{-1}}^{\text{intrinsic buffering}}\left(\overbrace{\kappa_d Ai - \kappa_a HiLi}^{\text{H}^+\text{Lac dissociation}} + \overbrace{\alpha_{II}(\kappa_f Ci - \kappa_r HiBi)}^{\substack{\text{CAII-catalysed}\\ \text{CO}_2/\text{HCO}_3^- \text{ buffering}}} - \overbrace{\gamma_1 \frac{Hi^\eta}{Hi^\eta+\gamma_2^\eta}\left(1-\frac{He^\eta}{He^\eta+\gamma_3^\eta}\right)}^{\text{Na}^+/\text{H}^+ \text{ exchange}} - \overbrace{\frac{3}{c}\rho_L(HiLi - HeLe)}^{\text{H}^+/\text{Lac}^- \text{ co-transport}}\right), \tag{6.6}$$

$$\frac{\partial Li}{\partial t} = \overbrace{\kappa_d Ai - \kappa_a HiLi}^{\text{H}^+\text{Lac dissociation}} - \overbrace{\frac{3}{c}\rho_L(HiLi - HeLe)}^{\text{H}^+/\text{Lac}^- \text{ co-transport}}, \tag{6.7}$$

$$\frac{\partial Ai}{\partial t} = \overbrace{\upsilon_A}^{\substack{\text{glycolytic}\\ \text{metabolic}\\ \text{production}}} - \overbrace{(\kappa_d Ai - \kappa_a HiLi)}^{\text{H}^+\text{Lac dissociation}} - \overbrace{\frac{3}{c}\rho_A(Ai - Ae)}^{\text{H}^+\text{Lac permeation}}, \tag{6.8}$$

$$\frac{\partial Bi}{\partial t} = \overbrace{\gamma_4 \frac{Hi^\xi}{Hi^\xi+\gamma_5^\xi}\left(1-\frac{He^\xi}{He^\xi+\gamma_6^\xi}\right)}^{\substack{\text{Na}^+/\text{HCO}_3^- \text{ co-import}}} + \overbrace{\alpha_{II}(\kappa_f Ci - \kappa_r HiBi)}^{\substack{\text{CAII-catalysed}\\ \text{CO}_2/\text{HCO}_3^- \text{ buffering}}}, \tag{6.9}$$

$$\frac{\partial Ci}{\partial t} = \overbrace{\upsilon_C}^{\substack{\text{oxidative}\\ \text{metabolic}\\ \text{production}}} - \overbrace{\alpha_{II}(\kappa_f Ci - \kappa_r HiBi)}^{\substack{\text{CAII-catalysed}\\ \text{CO}_2/\text{HCO}_3^- \text{ buffering}}} - \overbrace{\frac{3}{c}\rho_C(Ci - Ce)}^{\text{CO}_2 \text{ permeation}}, \tag{6.10}$$

$$\frac{\partial He}{\partial t} = \overbrace{\frac{\delta_H}{r^2}\frac{\partial}{\partial r}\left[r^2\left(1-\tanh\left(\frac{R-r}{\zeta}\right)\right)\frac{\partial He}{\partial r}\right]}^{\text{effective diffusion}} + \overbrace{\kappa_d Ae - \kappa_a HeLe}^{\text{H}^+\text{Lac dissociation}} + \overbrace{\alpha_{IX}(\kappa_f Ce - \kappa_r HeBe)}^{\substack{\text{CAIX-catalysed}\\ \text{CO}_2/\text{HCO}_3^- \text{ buffering}}}$$
$$+ \nu\overbrace{\gamma_1\frac{Hi^\eta}{Hi^\eta+\gamma_2^\eta}\left(1-\frac{He^\eta}{He^\eta+\gamma_3^\eta}\right)}^{\text{Na}^+/\text{H}^+ \text{ exchange}} + \nu\overbrace{\frac{3}{c}\rho_L(HiLi - HeLe)}^{\text{H}^+/\text{Lac}^- \text{ co-transport}}, \tag{6.11}$$

$$\frac{\partial Le}{\partial t} = \overbrace{\frac{\delta_L}{r^2}\frac{\partial}{\partial r}\left[r^2\left(1-\tanh\left(\frac{R-r}{\zeta}\right)\right)\frac{\partial Le}{\partial r}\right]}^{\text{diffusion}} + \overbrace{\kappa_d Ae - \kappa_a HeLe}^{\text{H}^+\text{Lac dissociation}} + \nu\overbrace{\frac{3}{c}\rho_L(HiLi - HeLe)}^{\text{H}^+/\text{Lac}^- \text{ co-transport}}, \tag{6.12}$$

$$\frac{\partial Ae}{\partial t} = \overbrace{\frac{\delta_A}{r^2}\frac{\partial}{\partial r}\left[r^2\left(1-\tanh\left(\frac{R-r}{\zeta}\right)\right)\frac{\partial Ae}{\partial r}\right]}^{\text{diffusion}} - \overbrace{(\kappa_d Ae - \kappa_a HeLe)}^{\text{H}^+\text{Lac dissociation}} + \nu\overbrace{\frac{3}{c}\rho_A(Ai - Ae)}^{\text{H}^+\text{Lac permeation}}, \tag{6.13}$$

$$\frac{\partial Be}{\partial t} = \overbrace{\frac{\delta_B}{r^2}\frac{\partial}{\partial r}\left[r^2\left(1-\tanh\left(\frac{R-r}{\zeta}\right)\right)\frac{\partial Be}{\partial r}\right]}^{\text{diffusion}} - \overbrace{\gamma_4\frac{Hi^\xi}{Hi^\xi+\gamma_5^\xi}\left(1-\frac{He^\xi}{He^\xi+\gamma_6^\xi}\right)}^{\text{Na}^+/\text{HCO}_3^- \text{ co-import}} + \overbrace{\alpha_{IX}(\kappa_f Ce - \kappa_r HeBe)}^{\substack{\text{CAIX-catalysed}\\ \text{CO}_2/\text{HCO}_3^- \text{ buffering}}}, \tag{6.14}$$

$$\frac{\partial Ce}{\partial t} = \overbrace{\frac{\delta_C}{r^2}\frac{\partial}{\partial r}\left[r^2\left(1-\tanh\left(\frac{R-r}{\zeta}\right)\right)\frac{\partial Ce}{\partial r}\right]}^{\text{diffusion}} - \overbrace{\alpha_{IX}(\kappa_f Ce - \kappa_r HeBe)}^{\substack{\text{CAIX-catalysed}\\ \text{CO}_2/\text{HCO}_3^- \text{ buffering}}} + \nu\overbrace{\frac{3}{c}\rho_C(Ci - Ce)}^{\text{CO}_2 \text{ permeation}}. \tag{6.15}$$

It must be noted that Equation (6.14) presents a potential problem in that our term for Na^+/HCO_3^- co-import does not depend on the available extracellular bicarbonate (Be), and therefore Be runs the risk of going negative. However, we have been vigilant throughout the remainder of this chapter to ensure this does not occur in any of our numerical solutions.

6.1.2 Boundary and initial conditions

We impose zero-flux boundary conditions in the tumour core (at $r = 0$), and Dirichlet conditions at the tumour edge (at $r = R$) such that the concentrations of metabolites diffusing out from the extracellular space are equal to their concentrations at the edge. This is to represent a dynamic equilibrium between the tumour edge and the superfusate of a spheroid experiment or, equivalently, the well-perfused boundary of a tumour *in vivo*. Superfusate concentrations are denoted by a subscript s and are set to physiologically realistic values throughout this chapter: $H_s = 10^{-7.4}10^3$ mM (corresponding to a pH of 7.4), $L_s = 0$ mM, $A_s = 0$ mM, $B_s = 22$ mM, and $C_s = 1.1$ mM.

Initial conditions are set such that we avoid large transients; that is, we match the intracellular and extracellular concentrations at time $t = 0$ uniformly to the superfusate concentrations, with the exception of $Hi(r, t = 0)$ which is specified according to the experimental set-up being simulated. All numerical simulations are solved using the Method of Lines, which discretises the spatial domain by a small step, $\Delta r = 10\mu$m, and solves the resulting system of coupled differential equations through time using Matlab's inbuilt solver ODE15s. Full details of this implementation are given in Appendix B.

6.2 Validation against experimental dynamics

Taking an approach similar to that which we took in Chapter 5 for the single cell model, we fix well-determined or 'background' parameters in Equations (6.6)-(6.15) to values taken from experimental estimates in the literature. These are listed in Table 6.1. We then sample the remaining parameters from normal distributions, with means taken from experimental estimates available in the literature. As before, we choose proportionally larger standard deviations for those parameters about which we are least certain. In the case of our spheroid scenario, the parameters about which we have the least information are the metabolic production rates υ_A and υ_C and the effective free-space H^+ diffusion coefficient δ_H, as these parameters are extremely difficult to measure experimentally (Kunz-Schughart et al. 2000, Walenta et al. 2000). Distributions for all varied parameters in our spheroid system are listed in Table 6.2.

Table 6.1: Fixed parameters for Eq (6.6)-(6.15)**.** Parameters that we consider to be either experimentally well-determined (R, k_f, k_r, c, ν, and ω) or that we keep fixed to enable a consistent set-up for numerical solutions of Eq (6.6)-(6.15) (k_d, k_a, η, ξ, and ζ).

	Value	Units	Source
R	300	μm	Swietach et al. (2009)
κ_d	$6 \cdot 10^7$	min^{-1}	Not limiting
κ_a	$6 \cdot 10^8$	1/(mM·min)	Formula, $k_r = K_a k_f$
κ_f	8.4	min^{-1}	Appendix G.2
κ_r	$1.1 \cdot 10^4$	1/(mM·min)	Appendix G.2
c	6	μm	Swietach et al. (2009)
η	3	None	Bayesian fitting
ξ	3	None	Bayesian fitting
ν	0.2/0.8	None	Swietach et al. (2009)
ω	130	μm	(Carlsson and Acker 1988, Kunz-Schughart et al. 2000)
ζ	50	μm	Estimated

We now verify our spheroid model, Equations (6.6)-(6.15) with boundary and initial conditions as detailed in Section 6.1.2, by sampling from the parameter space encompassed by Tables 6.1 and 6.2 and simulating a series of experimental conditions.

By imposing an initial intracellular pH of 6.6 uniformly across the tumour—that is, by setting $Hi(r, t = 0) = 10^{-6.6}10^3$ mM—we simulate an ammonium prepulse-induced acid spike analogous to the spike induced in our verification of the single-cell sub-system in Chapter 5. We first observe for the wildtype spheroid system how the intracellular pH recovers from this acid spike over time in the core versus at the edge (Figure 6.2a). We then set $\gamma_4 = 0$ to simulate blocking of Na^+/HCO_3^- import by 44'-diisothiocyanatostilbene-22'-disulfonic acid (DIDS), and observe the over-time intracellular pH recovery in the core and at the edge (Figure 6.2b). We do the same for blocking of Na^+/H^+ exchange by setting $\gamma_1 = 0$ (Figure 6.2c), and finally set our carbonic anhydrase activity parameters to $\alpha_{II} = 1$ and $\alpha_{IX} = 1$ to simulate treatment with acetazolamide (ATZ), a membrane-permeable carbonic anhydrase inhibitor (Figure 6.2d).

The dynamics in Figure 6.2 are in good agreement with published experimental data (Figure 6.3). Similarly to the spheroids in the experiments, our model spheroids are able to recover a favourable intracellular pH (that is, close to 7.2) within ten minutes under a wildtype scenario, although recovery is slightly better at the tumour edge than in the core (Figure 6.2a). Treatment with DIDS is the most effective disrupter of this pH recovery, with the intracellular pH in the core recovering to only about 6.9 after ten minutes (Figure 6.2b), indicating that Na^+/HCO_3^- transport is important for uniform acid extrusion across spheroids. Recovery under treatment with DMA is slightly faster than this, leaving a smaller

edge-to-core gradient after ten minutes, although both the core and edge pH remain slightly more acidic than is optimal (Figure 6.2c). This suggests that Na^+/H^+ exchange may help to calibrate the intracellular pH to the optimal level, rather than primarily governing the speed of acid extrusion. Lastly, the least substantial inhibition of pH recovery is obtained by treatment with ATZ (Figure 6.2d). This supports the idea that carbonic anhydrases are subtle enzymes (Swietach et al. 2009), at least in terms of their role in intracellular pH under the stress of an acid spike.

We also demonstrate that our model correctly captures the role of CAIX in spheroid pH maintenance. We plot the simulated profiles over our spatial domain of intracellular pH (Figure 6.4a) and extracellular pH (Figure 6.4b), each with the parameter representing CAIX activity, α_{IX}, sampled from its wildtype distribution (listed in Table 6.2) or set to $\alpha_{IX} = 1$ to simulate selective inhibition by a membrane-impermeant carbonic anhydrase inhibitor. Our results are broadly in agreement with published experimental data (Figure 6.5). Note that, to remain consistent with the spheroid geometry of our model formulation, we plot distance *from* our spheroid core (in μm) along the x-axis, while Swietach et al. (2010) plot distance to the spheroid surface (i.e. distance *into* the core). Despite this difference, it is evident that the presence of active CAIX reduces the acidity of the intracellular space and maintains a more uniform intracellular pH across the tumour domain. Concurrently, CAIX *increases* the acidity of the extracellular space in the tumour core.

We now return for a moment to the acid-mediated invasion hypothesis, which was discussed in Chapter 1 and modelled in Chapters 2 and 3. The acid-mediated invasion hypothesis postulates that resistance to extracellular acidity may comprise an important feature of malignant tumour cells (Gatenby and Gawlinski 1996). As CAIX is expressed almost uniquely in cancer cells (Parks et al. 2013), the behaviours observed above may suggest a mutationally simple pathway by which tumour cells can achieve this acid resistance. That is, rather than an independent *de novo* mutation conferring acid resistance through an alteration in p53 or some other signal, it may instead be the case that extracellular acidity is simply a consequence of the intracellular pH-regulating activity of tumour-expressed CAIX.

As a final verification of our model dynamics, we simulate the effects of several treatments on the steady-state gradient in extracellular pH that is established across the tumour from edge to core. We either sample α_{IX} from the distribution listed in Table 6.2 to simulate a wildtype CAIX overexpressing tumour, or set $\alpha_{IX} = 1$ to simulate a sham-transfected (CAIX-nonexpressing) spheroid. Under these two scenarios, we first observe the gradients in the absence of any treatment; with $\rho_L = 0$ in Equation (5.8) to simulate treatment with α-cyano-4-hydroxycinnamate (CHC), an inhibitor of monocarboxylate transporters (MCTs);

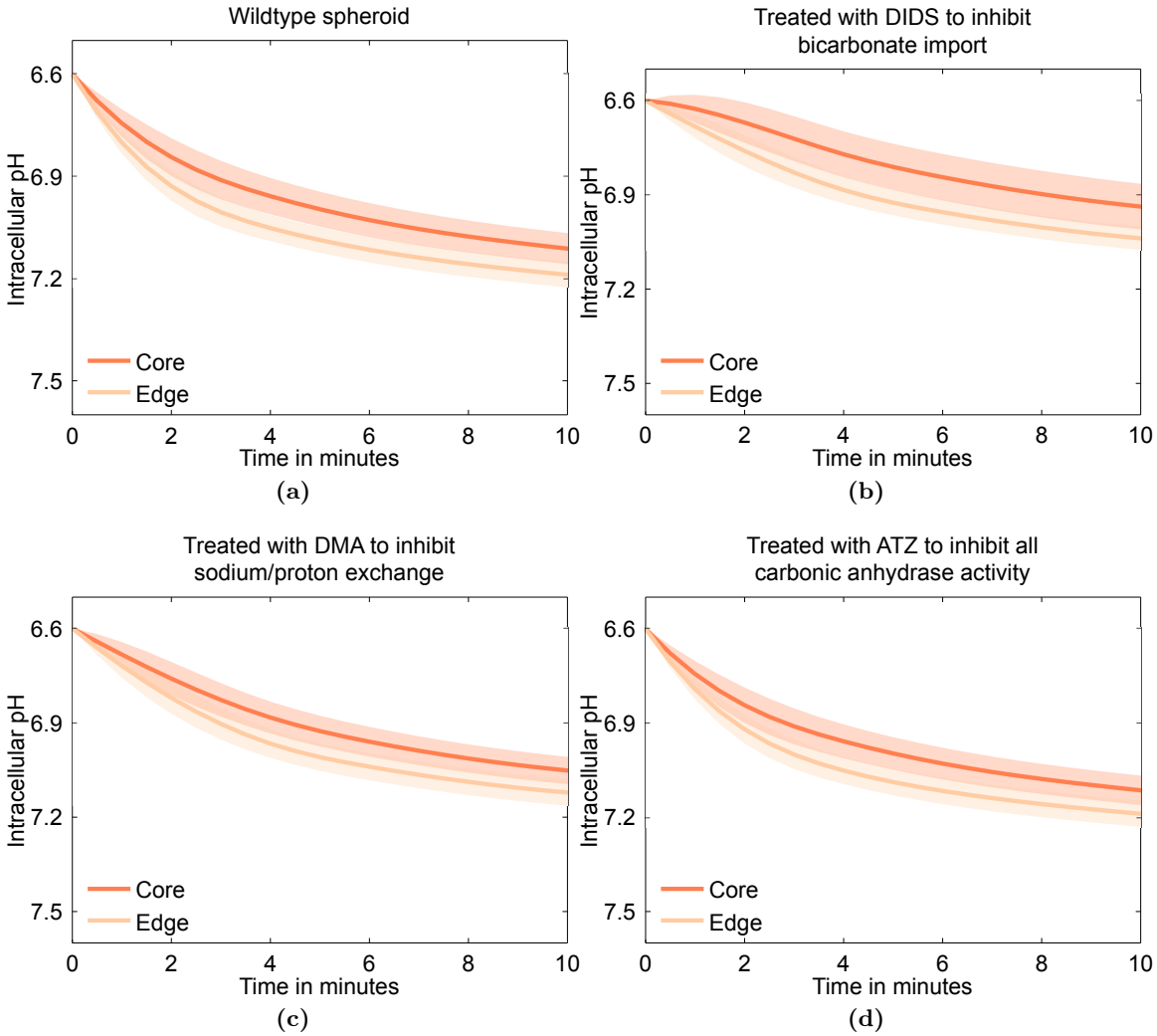

Figure 6.2: Simulated pH recovery in spheroids Means (curves) and standard deviations (shading), each from 10^3 numerical simulations of Equations (6.6)-(6.10) with an initial intracellular acid spike imposed by setting $Hi(r, t = 0) = 2.5{\cdot}10^{-4}$ mM uniformly across the spheroid, corresponding to a pH of 6.6. Parameters are either fixed at the values listed in Table 6.1 or sampled randomly from the distributions in Table 6.2, except where indicated. We show how the intracellular pH values in the tumour core (darker red) and at the tumour edge (lighter red) relax over time under a series of experimental scenarios: (a) a wildtype spheroid; (b) with $\gamma_4 = 0$ in Equation (5.5) to simulate treatment with 4,4'-diisothiocyanatostilbene-2,2'-disulfonic acid (DIDS), an inhibitor of Na^+/HCO_3^- import; (c) with $\gamma_1 = 0$ in Equation (5.4) to simulate treatment with 5-(N,N-dimethyl)amiloride (DMA), an inhibitor of Na^+/H^+ exchange; and (d) with $\alpha_{II} = \alpha_{IX} = 1$ to simulate treatment with acetazolamide (ATZ), a membrane-permeable inhibitor of carbonic anhydrase activity. Note that we have reversed the direction of the y-axes such that pH decreases as we move up the axis (i.e. acidity increases); this is done according to convention. Our simulated recovery dynamics agree with experimental results from Hulikova et al. (2011), shown for comparison in Figure 6.3.

with $\upsilon_C = 0$ in Equation (6.2) to simulate treatment with rotenone (Rot), an inhibitor of mitochondrial activity; with $\alpha_{II} = \alpha_{IX} = 1$ to simulate treatment with acetazolomide (ATZ), a membrane-permeable inhibitor of carbonic anhydrase activity; with $\upsilon_A = \upsilon_C = 0$

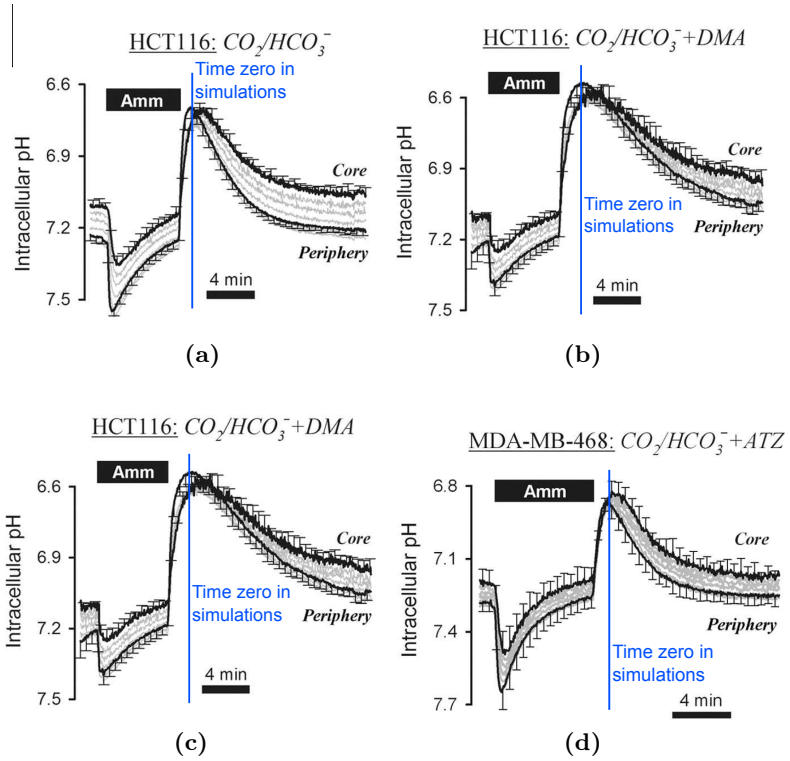

Figure 6.3: pH recovery in HCT116 spheroids. Experimental results presented by (Hulikova et al. 2011). (a) Ammonium prepulse performed on HCT116 spheroid. Bulk superfusate was buffered by 5%CO_2/22 mM HCO_3^- (pH=7.4). (b) Experiment repeated in CO_2/HCO_3^- buffer in the presence of 300 μM of 4,4'-diisothiocyanatostilbene-2,2'-disulfonic acid (DIDS) to block HCO_3^- flux. (c) Experiment repeated in the presence of 30 μM of 5-(N,N-dimethyl)amiloride (DMA) to block the major H^+ transporter, Na^+/H^+ exchange. (e) Experiment repeated on MDA-MB-468 human breast cancer cells in 100 μM acetazolamide (ATZ). Error bars indicate standard error. Images reproduced with permission from the *Journal of Biological Chemistry*.

in Equations (6.3) and (6.2) to simulate treatment with deoxyglucose to inhibit all cellular respiration by depriving the cell of glucose; and with $\upsilon_A = 0$ in Equation (6.3) to simulate treatment with galactose, which inhibits only the glycolytic pathway (Figure 6.6). These gradients are in agreement with published experimental data (Figure 6.7). We see that inhibiting monocarboxylate transporter activity does not appreciably affect the extracellular pH gradient across the tumour, and inhibiting glycolysis has only a moderate effect. More striking are the effects of mitochondrial and nonspecific carbonic anhydrase inhibition (Rot and ATZ, respectively), although inhibiting all respiration (with deoxyglucose) has the most profound impact, as is to be expected. Moreover, the effects of mitochondrial inhibition, nonspecific carbonic anhydrase inhibition, and respiration inhibition all appear to be nearly independent of whether active CAIX is present in the spheroid.

We note that Swietach et al. (2010) tested several more experimental scenarios for com-

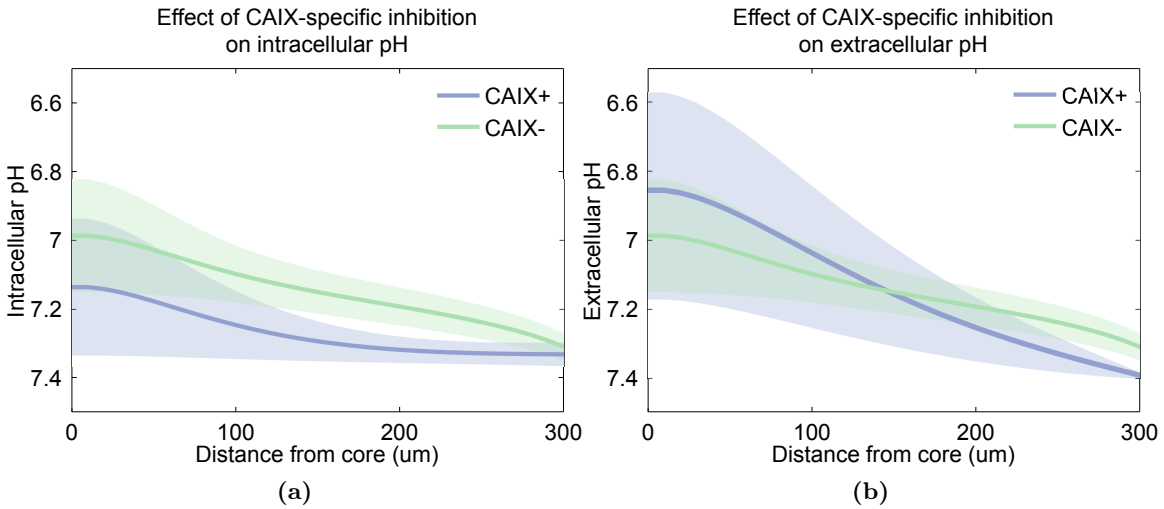

Figure 6.4: Simulated role of CAIX activity in pH gradients across spheroids. Means (curves) and standard deviations (shading), each from 10^3 long-time numerical simulations of Equations (6.6)-(6.10) with parameters fixed at the values listed in Table 6.1 or sampled randomly from the distributions in Table 6.2. Shown are the (a) intracellular pH and (b) extracellular pH profiles across the tumour space, both for the wildtype system (green) and with $\alpha_{IX} = 1$ to simulate treatment with a membrane-impermeant carbonic anhydrase inhibitor. It is evident that the role of CAIX is to maintain an intracellular pH that is closer to uniform across the tumour space, and simultaneously to acidify the extracellular environment. These simulated behaviours are in agreement with experimental results from Swietach et al. (2010), reproduced for comparison in Figure 6.5. (We note that we plot distance *from* the tumour core, rather than distance to the surface as in (Swietach et al. 2010), for consistency with our model geometry.)

pleteness in Figure 6.7, such as inhibiting mitchondria with myxothiazol (Myxo) or carbonyl cyanide *p*-(trifluoromethoxy)phenylhydrazone (FCCP) in addition to Rot, but we have not considered all of these here. This is because some of the treatments are interchangeable in terms of the parameter adjustments that we would make to simulate them (e.g. setting $\upsilon_C = 0$ could represent treatment with any of Rot, Myxo, or FCCP).

The verifications detailed here now allow us to take our model a step further and make a collection of predictions regarding the effect of treatments on the intracellular pH and the dynamics of the other species and fluxes in the system aside from Hi and He. Presented in the following section, they offer testable targets for further experimentation, and to our knowledge are novel.

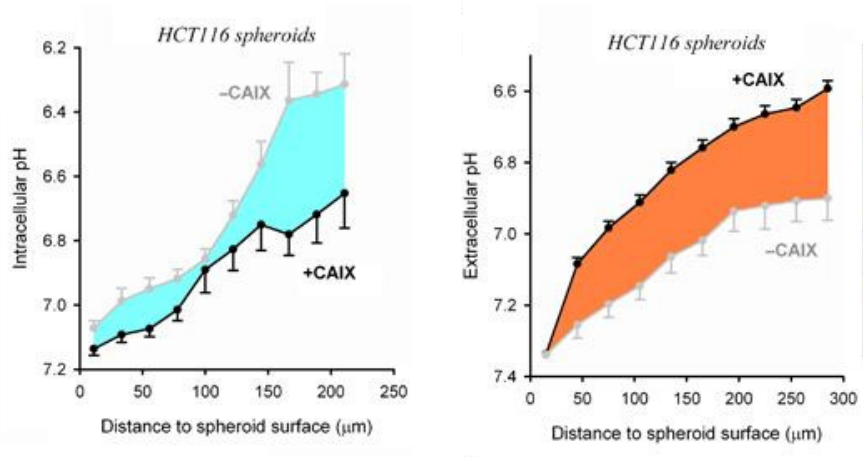

(a) **(b)**

Figure 6.5: Role of CAIX activity in pH gradients across HCT116 spheroids. Experiments determining the role of CAIX activity in shaping steady-state intracellular and extracellular pH gradients in spheroid tumours *in vitro*. (a) Steady state intracellular pH was measured confocally with carboxy-SNARF-1, a membrane-permeant pH indicator, in spheroids made of HCT116 cells overexpressing CAIX. Inhibition of CAIX with a membrane-impermeant inhibitor increased the size of intracellular pH gradients (blue shading between curves denotes alkalinising effect of CAIX). (b) Steady state extracellular pH was measured confocally with fluorescein-5-(and-6-)-sulphonic acid, a membrane-impermeant pH indicator, in spheroids made of HCT116 cells overexpressing CAIX. Inhibition of CAIX with membrane-impermeant drugs reduced extracellular pH gradients (red shading between curves denotes acidifying effect of CAIX). Images reproduced with permission from *Oncogene*.

Table 6.2: Variable parameters for Eq (6.6)-(6.15)**.** Parameters we view as random variables and sample for numerical solutions of Eq (6.6)-(6.15), calibrated by the Bayesian procedure outlined in Sections 5.2 or varied about a mean literature value. The statistic μ denotes the mean of a normal distribution, or vector of means for a multivariate normal distribution; Σ denotes the covariance matrix of a multivariate normal distribution and σ the standard deviation of a normal distribution.

	Statistics	Source	Units
β_1 β_2	$\mu = \begin{pmatrix} 53.4 \\ 2 \cdot 10^{-4} \end{pmatrix}$ $\Sigma = \begin{pmatrix} 1.7 & 10^{-5} \\ 10^{-5} & 9.8 \cdot 10^{-11} \end{pmatrix}$	Bayesian fitting of Eq (5.2) in Ch 5	mM/pH-unit mM
γ_1 γ_2 γ_3	$\mu = \begin{pmatrix} 13.6 \\ 10^{-4} \\ 2 \cdot 10^{-4} \end{pmatrix}$ $\Sigma = \begin{pmatrix} 0.04 & 5 \cdot 10^{-7} & -4 \cdot 10^{-7} \\ 5 \cdot 10^{-7} & 10^{-10} & 4 \cdot 10^{-11} \\ -3 \cdot 10^{-7} & 4 \cdot 10^{-11} & 5 \cdot 10^{-10} \end{pmatrix}$	Bayesian fitting of Eq (5.4) in Ch 5	mM/min mM mM
γ_4 γ_5 γ_6	$\mu = \begin{pmatrix} 18.1 \\ 2 \cdot 10^{-4} \\ 4 \cdot 10^{-4} \end{pmatrix}$ $\Sigma = \begin{pmatrix} 0.4 & 6 \cdot 10^{-6} & 7 \cdot 10^{-6} \\ 6 \cdot 10^{-6} & 3 \cdot 10^{-9} & 10^{-11} \\ 7 \cdot 10^{-6} & 10^{-11} & 10^{-8} \end{pmatrix}$	Bayesian fitting of Eq (5.5) in Ch 5	mM/min mM mM
α_{II}	$\mu = 4$ $\sigma = 0.8$	Swietach et al. (2009)	None
ρ_L	$\mu = 10^5$ $\sigma = 2 \cdot 10^4$	Swietach et al. (2009)	μm/(mM·min)
ρ_A	$\mu = 60$ $\sigma = 36$	Parks et al. (2013)	μm/min
ρ_C	$\mu = 60$ $\sigma = 12$	Swietach et al. (2003, 2008)	μm/min
υ_A	$\mu = 30$ $\sigma = 18$	Kunz-Schughart et al. (2000), Walenta et al. (2000)	mM/min
υ_C	$\mu = 30$ $\sigma = 18$	Kunz-Schughart et al. (2000), Walenta et al. (2000)	mM/min
α_{IX}	$\mu = 10$ $\sigma = 2$	Swietach et al. (2009)	None
δ_H	$\mu = 9.6 \cdot 10^4$ $\sigma = 5.8 \cdot 10^4$	Swietach et al. (2009)	μm^2/day
δ_L	$\mu = 7.8 \cdot 10^4$ $\sigma = 1.5 \cdot 10^4$	Lide (2004), Swietach et al. (2003)	μm^2/day
δ_A	$\mu = 7.8 \cdot 10^4$ $\sigma = 1.5 \cdot 10^4$	Lide (2004), Swietach et al. (2003)	μm^2/day
δ_B	$\mu = 9.6 \cdot 10^4$ $\sigma = 1.8 \cdot 10^4$	Lide (2004), Swietach et al. (2003, 2008)	μm^2/day
δ_C	$\mu = 7.2 \cdot 10^3$ $\sigma = 1.4 \cdot 10^3$	Swietach et al. (2003, 2008)	μm^2/day

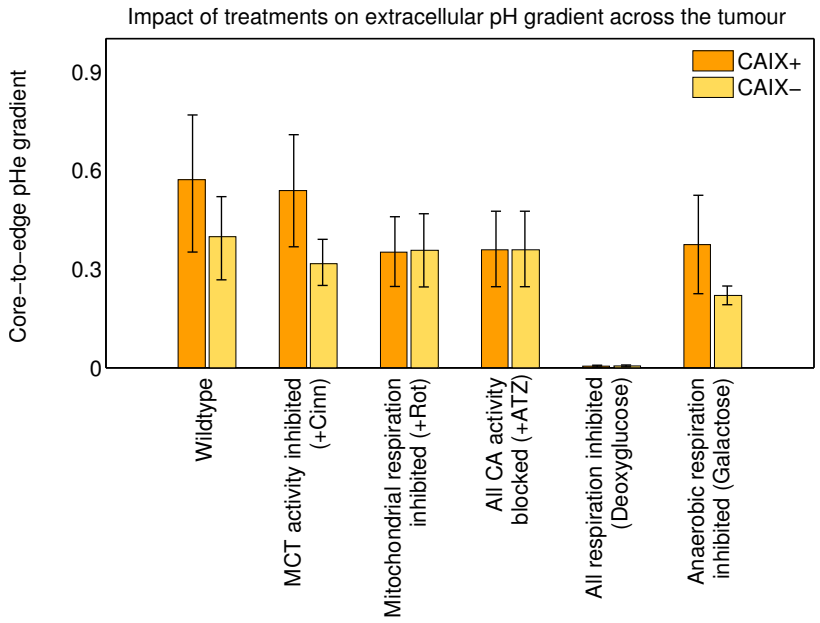

Figure 6.6: Simulated effects of treatments on extracellular pH gradients across spheroids. Means (bars) and standard deviations (errorbars) of steady-state extracellular pH gradients from the tumour edge (at $r = R$) to the core (at $r = 0$), taken from 10^3 simulations of Equations (6.6)-(6.15) with parameters set to the fixed values in Table 6.1 or sampled randomly from the distributions in Table 6.2, unless otherwise indicated. Shown are results both with α_{IX} sampled from the distribution listed in Table 6.2 to simulate a wildtype CAIX overexpressing tumour (orange), and with $\alpha_{IX} = 1$ to simulate a sham-transfected (CAIX-nonexpressing) spheroid (yellow). Bars from left to right: the untreated scenario; the spheroid with $\rho_L = 0$ to simulate treatment with α-cyano-4-hydroxycinnamate (CHC), an inhibitor of monocarboxylate transporters (MCTs); with $\upsilon_C = 0$ to simulate treatment with rotenone (Rot), an inhibitor of mitochondrial activity; with $\alpha_{II} = \alpha_{IX} = 1$ to simulate treatment with acetazolomide (ATZ), a membrane-permeable inhibitor of carbonic anhydrase activity; with $\upsilon_A = \upsilon_C = 0$ to simulate treatment with deoxyglucose to inhibit all cellular respiration; and with $\upsilon_A = 0$ to simulate treatment with galactose, which inhibits only the glycolytic pathway. These gradients are in agreement with experimental results from (Swietach et al. 2010), reproduced for comparison in Figure 6.7.

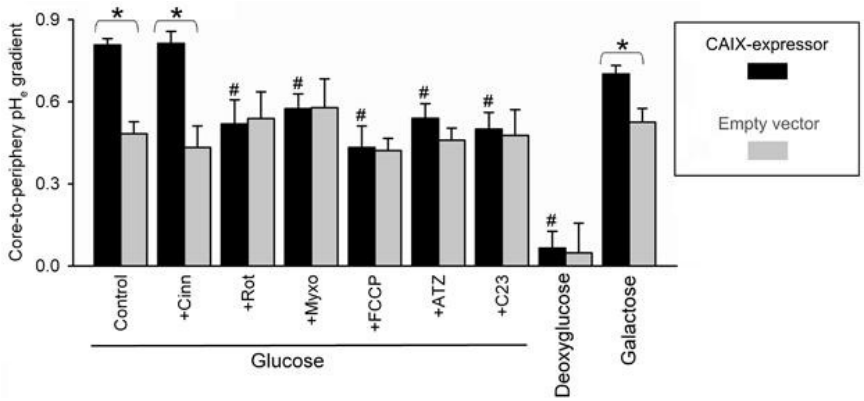

Figure 6.7: Effects of treatments on extracellular pH gradients in HCT116 spheroids. Extracellular pH at the core of spheroids made of CAIX-transfected (black) or sham-transfected (grey) HCT116 cells measured under a variety of conditions. The ability of CAIX to reduced extracellular pH was blocked by inhibiting mitochondria with rotenone (Rot), myxothiazol (Myxo) or carbonyl cyanide *p*-(trifluoromethoxy)phenylhydrazone (FCCP), but not affected by blocking lactic acid efflux with α-cyano-4-hydroxycinnamate (Cinn). Replacing medium glucose with galactose (with suppresses anaerobic respiration) had no effect on CAIX-dependent extracellular acidification. Replacing glucose with 2-deoxyglucose to decrease respiratory rate reduced extracellular acidification. * denotes statistically significant difference between empty vector and CAIX-expressor spheroid. # denotes statistically significant change in extracellular pH gradient between the empty vector and CAIX-expressor spheroid. Image reproduced with permission from *Oncogene*.

6.3 Results

6.3.1 Tissue acidity and the intracellular pH gradient share sensitivity

To explore the sensitivity of important features of the system to our fundamental model parameters, we again carry out an importance analysis using classification trees (discussed and applied in Chapter 4). We find that the importance ordering of the parameters is roughly equivalent for both the maintenance of a small intracellular pH gradient across the tumour and for maintenance of an acidic extracellular pH in the tumour core (Figure 6.8). This implies that the mechanisms keeping the intracellular pH spatially near-uniform in the tumour spheroid are the same as those which acidify the extracellular space, and supports our earlier conjecture regarding a mutationally simple path to acid resistance.

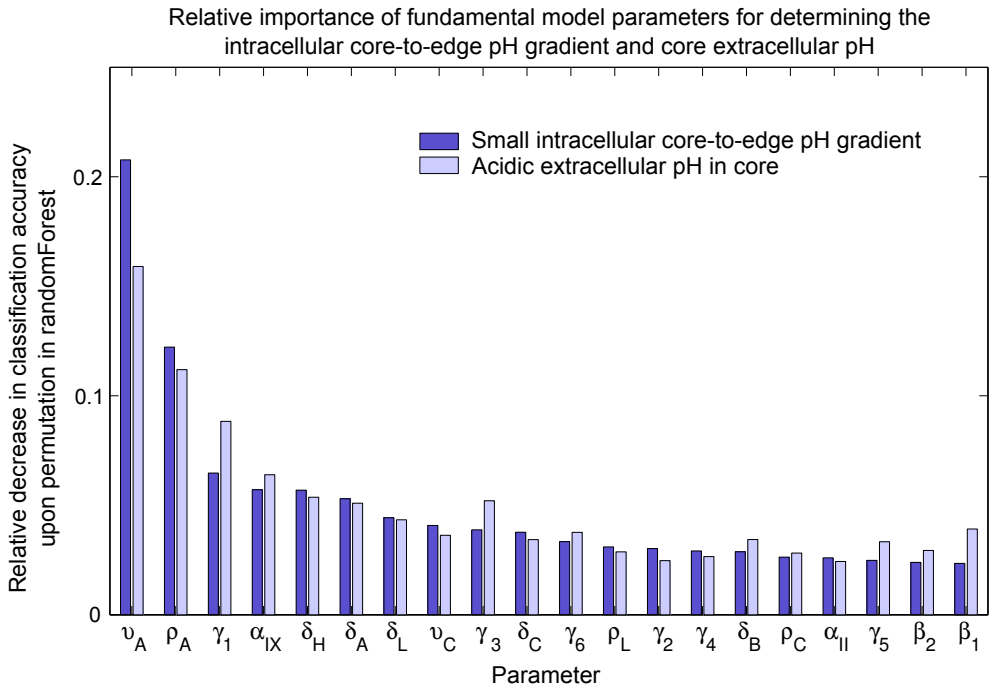

Figure 6.8: Importance of fundamental model parameters for pH characteristics. The relative importance of our fundamental model parameters for the maintenance of a near-uniform intracellular pH across the tumour space (dark purple) and the maintenance of an acidic extracellular pH in the tumour core (light purple), two conditions that correspond with well-known tumour characteristics. This analysis follows the randomForest procedure outlined in Chapter 4 and implemented in **R**, and is performed on 10^3 numerical simulations of Equations (6.6)-(6.15) subject to the boundary and initial conditions specified in Section 6.1.2, with parameter values sampled randomly from the multidimensional parameter space dictated by Table 6.2. The remaining parameters are held fixed at the values listed in Table 6.1, and all simulations are run to $t = 30$ minutes.

Although the relative importance of the parameters falls off gradually for both tumour

features in Figure 6.8, making it difficult to impose a threshold separating important from unimportant parameters, we advance some observations on the five parameters to which both features are most sensitive. The system is predicted to be most highly sensitive to the metabolic production rate of lactic acid by glycolysis (υ_A), while less sensitive to that of carbon dioxide production by oxidative phosphorylation (υ_C). Also important are the maximum rate of sodium-proton exchange (γ_1) and rate of catalysis by CAIX (α_{IX}); this result dovetails with the current opinion among oncologists that proton export and CAIX-enhanced buffering are vital components of the tumour pH regulation system.

Somewhat surprisingly, however, the rate of lactic acid permeation (ρ_A) is slightly more important for both intracellular and extracellular pH than either the rate of sodium-proton exchange or the rate of catalysis of the bicarbonate buffering reaction by CAIX. This indicates that the concerns regarding lactic acid put forward by Parks et al. (2013) are well-founded. In other words, our results indicate, in agreement with Parks et al. (2013), that lactic acid is likely to have a greater impact on the tumour pH regulation system than its low pK_a value would seem to suggest.

Finally, Figure 6.8 shows that the effective diffusion coefficient of free protons (δ_H) plays an important role in maintenance of a uniform intracellular and acidic extracellular pH. This and the metabolic lactic acid production rate (υ_A) are the parameters which are the least well-determined experimentally to date. Thus, our sensitivity analysis highlights the urgency of pinning these down more effectively through future experimentation.

6.3.2 Treatments disrupt intracellular pH without causing cell death

We are now interested in predicting the impact of a series of targeted combination treatments proposed by Parks et al. (2013). These treatments are: inhibition of CAIX combined with blocking of MCT4-mediated lactate efflux; inhibition of CAIX and blocking of lactate efflux combined with blocking of sodium-proton exchange; and inhibition of CAIX, blocking of lactate efflux, and blocking of sodium-proton exchange all combined with inhibition of mitochondrial activity. In our model, we represent inhibition of CAIX by setting $\alpha_{IX} = 1$, to remove its catalysis of the $\mathrm{CO}_2/\mathrm{HCO}_3^-$ buffering reaction; blocking of lactate efflux by setting $\rho_L = 0$ in Equation (5.8); blocking of $\mathrm{Na}^+/\mathrm{H}^+$ exchange by setting $\gamma_1 = 0$ in Equation (5.4); and inhibition of mitochondrial activity by setting $\upsilon_C = 0$ in Equation (6.2).

Applying these simulated treatments to our model, we find that all of the treatment regimens are successful in driving the extracellular bicarbonate buffering ratio, $\frac{HeBe}{Ce}$, away from its

physiological equilibrium in the tumour core (Figure 6.9a). However, we also predict that none of the treatment combinations is sufficient to drive intracellular pH in the tumour core down to a level thought to be potentially lethal; that is, down to 6.0 (Parks et al. 2013). Surprisingly, however, the combination of CAIX inhibition, blocking of lactate efflux, and blocking of sodium-proton exchange is more effective, on average, at disrupting intracellular pH than is the strategy of using all three along with mitochondrial inhibition (Figure 6.9b). This could be a non-intuitive effect of the direction of the CO^2/HCO_3^- buffering reaction in the absence of a source of CO_2, and was not predicted by Parks et al. (2013).

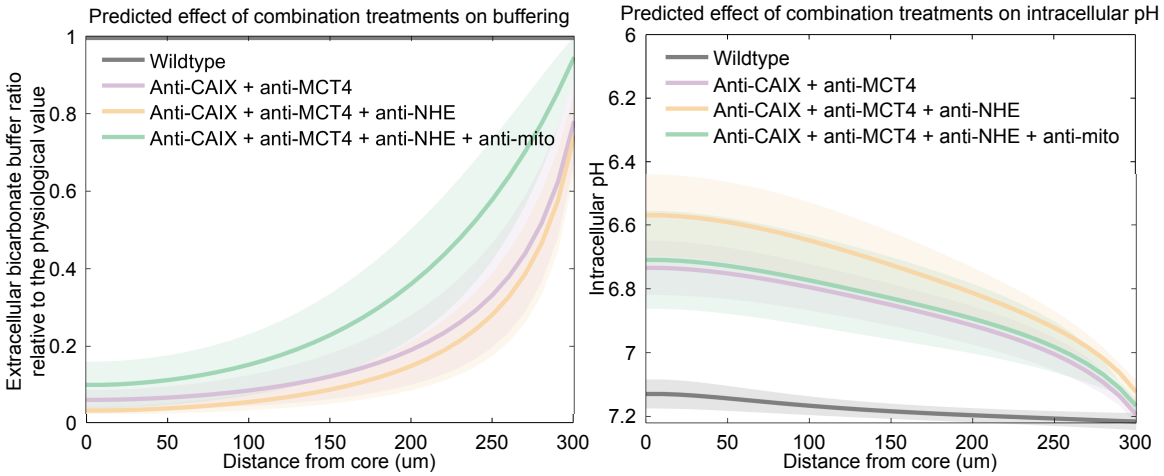

Figure 6.9: Predicted effects of combination treatments. Effects of treatment combinations on (a) the extracellular bicarbonate buffering ratio and (b) intracellular pH, both measured at the $r = 0$ boundary representing the tumour core. Shown are the means (curves) and standard deviations (shading) from numerical solutions of Equations (6.6)-(6.15) with 10^3 samples from the parameter space dictated by Tables 6.1 and 6.2, subject to the boundary and initial conditions outlined in Section 6.1.2 and run to an end-time of $t = 30$ minutes. The following scenarios are considered: a wildtype tumour (grey); CAIX inhibition combined with blocking of MCT4-mediated lactate efflux (purple); CAIX inhibition and blocking of lactate efflux combined with blocking of sodium-proton exchange (yellow); and CAIX inhibition, blocking of lactate efflux, and blocking of sodium-proton exchange all combined with inhibition of mitochondrial activity (green). The extracellular bicarbonate buffering ratio, $\frac{HeBe}{Ce}$, is calculated relative to its value under physiological conditions; that is, under a healthy extracellular pH of 7.4 and a bicarbonate concentration of 22 mM with 5% carbon dioxide (1.1 mM). While the wildtype tumour maintains a buffering ratio in equilibrium with the ratio under these physiological conditions, the treatments all cause it to drop to near zero; that is, they cause carbon dioxide to accumulate to excess in the core.

6.3.3 Spheroids retain the reverse pH gradient

Part of our motivation for undertaking this study was to examine whether it is justifiable to assume a direct relationship between acid produced metabolically in the intracellular space and extruded acid in the local extracellular space. Figure 6.10 reveals that, under our model formulation, the "reverse" pH gradient that we predicted in single cells (Figure 5.8) is indeed retained in the core of a spheroid. This is in agreement with many experimental observations of the reverse pH gradient (Webb et al. 1999a), suggesting that we have captured essential components of tumour pH regulation. Figure 6.10 additionally supports the assumption of a direct relationship between intracellular and extracellular pH that is implicitly involved in the coarse-graining of metabolic dynamics of a tumour as we did in Chapters 2-4.

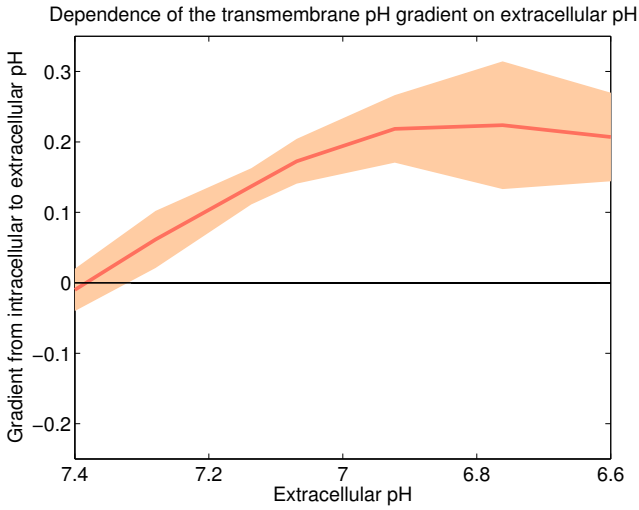

Figure 6.10: Predicted pH gradient in the spheroid core. The mean (curve) and standard deviation (shading) from a representative sample from our parameter space shows that, at the $r = 0$ boundary representing the tumour core, the transmembrane pH gradient (difference between intracellular and extracellular pH), when graphed as a function of extracellular pH, is "reversed" (i.e. is positive, meaning the intracellular pH is higher) for acidic extracellular pH values, in agreement with both our single-cell results (see Figure 5.8 for comparison) and widespread observations of such a gradient in real tumours. Parameter values are set at the values in Table 6.1 or varied according to the distributions shown in Table 6.2, and used in numerical simulations of Equations (6.6)-(6.15), subject to the initial and boundary conditions outlined in Section 6.1.2 and run to an end-time of $t = 30$ minutes.

6.4 Discussion

The thorough process of model development and validation that we have detailed here, which is an extension of the equally validated sub-model from Chapter 5, has enabled us to make several predictions regarding the pH regulation system. First, we have predicted that the pH regulation system is highly sensitive to two parameters which are difficult to measure experimentally (Figure 6.8): those governing diffusion of free protons in the extracellular space and metabolic production of lactic acid via glycolysis. This result emphasises the importance of carefully considering the uncertainty underlying fundamental model parameters, and pinpoints the directions in which further experimental effort should be expended to facilitate greater steps toward fully understanding the pH regulation system. If such experiments were to be performed, the power of the Bayesian approach we have employed in Chapter 5 could then be exploited still further, by incorporating new datasets into the distributions that represent our model parameters in a hierarchical way whereby the posterior distributions from each stage become the priors when a new set of data is collected.

We found that another factor important for determining the intracellular and extracellular pH dynamics of our model system is the rate of leakage of protonated lactic acid through trans-membrane permeation (Figure 6.8). This finding supports the warnings of Parks et al. (2013), who postulated that protonated lactic acid could have a significant impact on the system despite its low pK_a, and suggests that future modelling of pH regulation should include lactic acid specifically.

We have tested the effects of multiple targeted treatment strategies to determine whether they might cause disruption of the extracellular bicarbonate buffering ratio or intracellular pH across the tumour domain. Indeed, our model predicts that all treatment combinations of interest succeed in driving the bicarbonate buffering ratio away from the physiological equilibrium that is maintained in the blood and the wildtype tumour. Also, the combinations all lower the intracellular pH in the tumour core to acidic levels. The resulting pH measurements, however, are between roughly 6.8 and 6.4, rather than 6.2 and below; hence, according to the reasoning of Parks et al. (2013), they may be sufficient to drive the cells into only a quiescent state, rather than apoptosis or necrosis. It is possible, then, that if metabolic therapies are to destabilise a tumour enough to cause permanent damage, they will need to somehow target permeation of protonated lactic acid across the tumour (but not healthy) cell membranes.

Lastly, we have predicted that the "reverse" pH gradient exhibited by our single-cell system (Figure 6.10) is maintained in the tumour core, and is maximised at an extracellular pH

of 6.8, the value commonly taken as the optimal extracellular pH for sustained tumour proliferation. This suggests that, at least in the case of moderately-developed spheroids and on a relatively short timescale, extracellular pH may provide a serviceable approximation to the full suite of mechanisms by which tumour cells handle their metabolically-derived intracellular pH in coarse-grained models of tumour metabolic dynamics. This includes the generalised model of acid-mediated tumour invasion that we presented in Chapter 2 and 3 and the minimal model of glucose-lactate metabolic cooperation we developed in Chapter 4. To our knowledge we are the first to have explicitly examined the validity of this assumption.

Chapter 7

Discussion

The goals of this thesis were two-fold. First, we aimed to employ theoretical frameworks to explore biological hypotheses related to unresolved aspects of altered glucose metabolism in solid tumours. We have accomplished this by developing three minimal mathematical models, each of which addresses a hypothesis that is currently of interest to the oncology community. Secondly, we have illustrated the utility of combined mathematical and statistical approaches for understanding the parameter spaces of continuum models of varying complexity.

7.1 Summary

We began with a general overview of cancer metabolism in Chapter 1, briefly discussing oncology from a historical perspective. The proposal, loss of favour, and subsequent renaissance of the study of glucose metabolism were traced, with emphasis on the Warburg effect or glycolytic phenotype (constitutive enhancement of truncated glycolysis independent of oxygen supply). We then outlined three major open problems underlying the consequences of the glycolytic phenotype for tumours and their microenvironment, which together form the biological cornerstones of this thesis. Additionally, we presented an overview of continuum mathematical modelling of cancer metabolism in the literature. In subsequent chapters we developed minimal spatial models for each of our biological problems in turn, and applied a selection of appropriate theoretical methods, as follows.

In Chapter 2, we extended a canonical model of the acid-mediated invasion hypothesis by Gatenby and Gawlinski (1996); this hypothesis asserts that tumours gain a selective advantage by expressing the glycolytic phenotype if they also exhibit resistance to its acidic

byproduct. As the original model formulation was highly restrictive in terms of its underlying assumptions, our goal was to relax some of these to capture a wider range of permitted tumour behaviours that may prove to be clinically relevant, and determine whether the modelling framework could support the inclusion of greater biological detail. Numerical simulations confirmed that our extended model captures two additional types of tumour behaviour beyond those captured by the original model; and these new behaviours are non-invasive or non-aggressive, suggesting additional targets for model validation.

We then demonstrated in Chapter 3 that our extended model remained amenable to mathematical analysis, by carrying out an asymptotic analysis of the invasive behaviours in a travelling wave framework. This provided us with a comprehensive picture of the model parameter space and enabled the calculation of an explicit expression for the width of interstitial gaps that form between retreating healthy tissue and the advancing tumour front under certain parameter conditions. Interstitial gaps were a point of validation of the original model that has since proven controversial; and our findings indicate that, while gaps are not merely an artefact of the *in vitro* environment in the experimental images presented by Gatenby and Gawlinski (1996), they are perhaps exaggerated by it, and it may be preferable to exploit other targets for model validation in future.

Several other studies have adjusted the Gatenby and Gawlinski (1996) model to address problems of interest—for example, to include stromal effects (Martin et al. 2010) and tissue density (McGillen et al. 2012) and to consider acid waves that take the form of a pulse rather than a front (Holder et al. 2014)—but these studies have extended, not generalised, the modelling framework. We suggest that our model, which captures more biologically observed phenomena than the original Gatenby-Gawlinski model while preserving its structural stability and key results, may be useful for further targeted studies of the kind seen in Martin et al. (2010) or McGillen et al. (2012). We emphasise also that our study keeps the tumour and healthy proliferation rates equal and hence does not assume a growth advantage or disadvantage imparted by the Warburg effect, only an effect of the acid produced by it; this allows us to gain insight into tumour invasion while sidestepping the controversy, as yet not fully resolved, regarding the relationship between the Warburg effect and proliferation that was discussed in Chapter 1.

In Chapter 4, we carried out a theoretical test of a recent hypothesis by Sonveaux et al. (2008) that proposed a beneficial metabolic cooperation between hypoxic and normoxic tumour cells in the local vicinity of a capillary. This hypothesis has met with some skepticism in the experimental community, notably from Busk et al. (2011) who independently tested the *in vivo* implications of the hypothesis and found conflicting results. We contributed a

new perspective to the debate by presenting a minimal spatial model of the hypothesised metabolic cooperation and carrying out an in-principle test of the symbiosis hypothesis. This study was developed in collaboration with the group of Prof. Victor Pérez-García at the University of Castilla-La Mancha in Spain.

Upon applying statistical methods based on random sampling of the multidimensional parameter space of our model, we found that symbiosis occurs in a substantial portion of parameter space and largely has the expected effects, although it does not straightforwardly rescue the tumour interior from glucose deprivation. Moreover, in collaboration with Dr. Catherine Kelly of the Gray Institute for Radiation Oncology and Biology at Oxford University, we generated a set of experimental data and used it to locate U87 glioblastoma tumours in our model parameter space, observing that U87 tumours are likely to exhibit only weakly symbiotic behaviour despite their extreme malignancy. Finally, we tested the effect of an inhibitory strategy that was proposed by Sonveaux et al. (2008) and predicted that, under our modelling framework, it is unlikely to cause the expected necrosis. Taken together, these results lend clarity to one hypothesis regarding the role of metabolically-derived lactate in developing tumours.

Finally, in Chapters 5 and 6, we systematically developed a spatial model to interrogate the nonlinear tumour pH regulation system. With the exception of work by Webb et al. (1999a,b,c), Al-Husari and Webb (2013a,b), and Al-Husari et al. (2013), past modelling of altered glucose metabolism in cancer has predominantly focused on extracellular acidity; but expulsion of metabolically-derived acid from the intracellular space is far from straightforward. Understanding the pH regulation system may be particularly important because it differs from the (less robust) healthy system by expression of only a few key proteins, and thus there are strong potential targets for therapy if vulnerabilities can be identified (Colen et al. 2011, Parks et al. 2013). The tightly linked nature of the mechanisms comprising tumour pH regulation, however, renders prediction of these vulnerabilities non-trivial.

In Chapter 5 we detailed the development, from first principles, of a minimal (non-spatial) model of pH regulation in single tumour cells. We employed a Bayesian framework for estimation of key model parameters, which enabled the incorporation of information from multiple sets of experimental data. We then verified the model dynamics against experimental results in the literature, and predicted a straightforward relationship between intracellular and extracellular pH that arises from the pH-sensitivities of the regulatory components.

In Chapter 6, we extended this model to capture the full spatial scenario of a tumour spheroid, with metabolites reacting and diffusing in the local extracellular space subject to cellular crowding and limited tissue perfusion. After validating this spheroid system against

known experimental dynamics, we predicted that maintenance of both a near-uniform, favourable intracellular pH across the tumour and an acidic extracellular pH in the core are sensitive to the rates of glycolytic lactic acid production and of effective diffusion of free protons through extracellular space, for both of which little experimental data is available. Our study has thus helped to pinpoint a need for focussing future experimental effort on improving measurements of these parameters. We also echoed the concerns of Parks et al. (2013) by predicting that, despite having a low pK_a, protonated lactic acid can play a significant role in tumour pH regulation dynamics via permeation across the cell membrane. Moreover, we tested the effect on our model system of a series of treatment strategies which are currently of interest to the oncological community, and determined that, while they effectively disrupted both the extracellular bicarbonate buffering ratio and the intracellular pH, their impact on the latter was likely to be sufficient to induce only cell quiescence, rather than death. This finding unfortunately emphasises the interconnectedness and resilience of the altered metabolic networks exhibited by tumours, and reinforces the fact that, in spite of the decades of research since Warburg's seminal discovery of altered glucose processing, a definitive metabolism-based cancer treatment continues to elude us.

Lastly—and more optimistically—we tested the transmembrane pH gradient in the core of our model spheroid, and predicted that it retains the "reversal" exhibited by isolated tumour cells. Such a relationship has been implicitly assumed by the coarse-grained systems we presented in Chapters 2-4 and by many other continuum models of tumour metabolism and acidity. Thus, this study may help to lend confidence to further use of our continuum models (and many others), and suggest that they indeed can be instrumental to oncology for elucidating complex tumour dynamics, testing hypotheses, and guiding experiments.

7.2 Outlook and future directions

The models we presented in this thesis are continuum formulations, which we chose in order to facilitate analytically and numerically tractable solutions and to capture minimal representations of the dynamics of tumour and healthy cell populations. As such, they are intrinsically reliant on mean-field assumptions, which become invalid in cases of cellular clustering or low cell number. It may therefore be beneficial to develop discrete representations of these systems for comparison and elucidation of the tumour behaviours in finer detail. For example, as the interstitial gaps observed experimentally in Gatenby and Gawlinski (1996) are roughly on the scale of individual cells, it is probable that stochastic effects play a role in their formation, and a discrete realisation of the generalised continuum model

we considered in Chapter 2 and 3 could help to evaluate whether gaps could be a transient feature of tumour invasion arising from stochasticity at the tumour-host interface.

While the metabolic cooperation in Chapter 4 appears unlikely to be a significant feature of glioma tumours *in vivo* given our modelling framework, it is well established that *healthy* brain tissue does exhibit such cooperation (Pellerin and Magistretti 2004, Magistretti 2006, Pellerin et al. 2007); specifically, glutamate-mediated synaptic activity is coupled to energy metabolism by shuttling of lactate between astrocytes and neurons to ensure more efficient distribution of glucose, oxygen, and other valuable resources during neuronal signalling. Interestingly, however, the direction in which this lactate shuttling occurs (i.e. from astrocytes to neurons or from neurons to astrocytes) remains of long-standing controversy, despite the development of several biophysical models aimed at elucidating the dynamics (Aubert et al. 2007, Simpson et al. 2007, Mangia et al. 2009, Clautier et al. 2009, DiNuzzo et al. 2010). A comparison of these models by Jolivet et al. (2010) favours the system by Aubert et al. (2007), which indicates astrocyte-to-neuron transfer; but this analysis is not entirely independent due to author overlap, and further investigation could prove useful. Until the dispute is fully resolved, it may be difficult to predict the true impact of metabolic therapies, not only on glioma tumours themselves, but on the cooperative dynamics of the surrounding healthy brain tissue.

Along similar lines, it may also be worth developing a mathematical model to investigate work by Pavlides et al. (2009, 2010) that has indicated the possibility of a metabolic interaction between tumour and microenvironmental cells; that is, tumour-associated fibroblasts and stroma may exhibit aerobic glycolysis and thus 'feed' lactate to oxidative tumour cells (the so-called 'reverse' Warburg effect). Such cooperation could provide another target for therapy, if modelling were to help elucidate conditions under which it may play a significant role in tumour development.

The models we have developed in this thesis could be embedded in mechanical frameworks—for example, combining the pH regulation model from Chapter 6 with the two-phase mixture modelling of Chen et al. (2001), Jackson and Byrne (2002), Byrne et al. (2003), Byrne and Preziosi (2003), and Roose et al. (2003)—to examine the metabolic dynamics considered herein in the context of a growing, physically complex tumour. Our models do not explicitly accommodate vasculature dynamics, but instead assume the somewhat abstract feature of a fixed capillary shell; hence, they cannot be used to consider, for example, the vasoactive role of lactate (Ido et al. 2003, Hein et al. 2006) or the effect that MCT inhibition may have on angiogenesis (Sonveaux et al. 2012). We have also claimed throughout that, in addition to capturing small avascular tumours, our model systems can be considered to

describe localised pockets within a large, heterogeneous tumour; but it would be beneficial to explicitly model the global metabolic dynamics of such a tumour as a whole, as this would introduce spatial complexities and facilitate more direct comparisons with medical imaging *in vivo*. This could be accomplished by embedding our models in, for example, the multiscale frameworks developed by Alarcon et al. (2004), Bellomo and Delitala (2008), Osborne et al. (2010), and Lowengrub et al. (2010).

It also could be fruitful to extend our metabolic modelling beyond the cellular pathways directly related to glucose breakdown. For example, glutamatergic signalling (activation of multiple intracellular signalling pathways by binding of glutamate) has been shown to function aberrantly in both glioma and melanoma tumours, as well as being implicated in other diseases such as schizophrenia and Alzheimer's disease (Prickett and Samuels 2012). Additionally, including important metabolic components such as lipid synthesis pathways and the oxidising/reducing agents NAD^+/NADH could help to directly resolve lingering controversy over the relationship between the glycolytic phenotype and proliferation rate. These latter factors in particular have, generally speaking, been omitted from explicit inclusion in modelling studies of both tumour and healthy metabolism, leading to an implicitly ATP-centred viewpoint. Integrating them with existing modelling may thus enable the prediction and observation of heretofore overlooked dynamics that could prove important for the development of novel anti-cancer strategies.

On the experimental side, the mathematical results we presented in Chapters 2-6 could be supplemented further. For example, regarding the acid-mediated invasion hypothesis (Chapters 2 and 3), experiments could help to pin down the range of permissible widths for the interstitial gap and determine its comparative frequency of occurrence in fixed versus unfixed specimens *in vitro*.

Recent technological advances have placed microfluidics, a class of devices for precisely manipulating the flow of fluids through microchannels, at the leading edge of experimental cancer research (Whitesides 2006, Huang et al. 2011, Zhang and Nagrath 2013). By geometrically constraining the manipulation of fluids to a sub-millimetre scale, microfluidics allow for more precise and tightly controlled analogues of conventional culture or spheroid experiments. Applications have been increasing in molecular biology and now include studies of tumour cell migration and cell culturing for spheroid formation (Hsiao et al. 2009, Chung et al. 2009, Irimia and Toner 2009). These powerful methods could be exploited for improved estimation of the rates of glucose production by aerobic glycolysis and carbon dioxide production by oxidative phosphorylation, which were important parameters in our models of metabolic cooperation in glioma (Chapter 4) and pH regulation in spheroids

(Chapter 6) but to date have been poorly characterised experimentally. Non-tumour cell types present in the microenvironment, such as fibroblasts, could also be included (Das and Chakraborty 2013) to aid in parameterisation of the potential modelling extensions discussed here.

7.3 Final remarks

To sum up, this thesis has employed mathematical modelling to elucidate previously-unresolved features of altered glucose metabolism in tumours that are presently of interest to the oncology community. Two overarching motivations have governed these efforts: on the one hand, we have combined our modelling studies with new sets of experimental data for more thorough testing of the biological hypotheses of interest, and on the other hand, we have illustrated the power of a resourceful mathematical-statistical approach for building a comprehensive understanding of the dynamics of such models.

To our knowledge, we are the first to apply the statistics-inspired and Bayesian approaches detailed herein to continuum models in mathematical oncology. In doing so, we hope that we have illustrated the considerable gains that can potentially be made through continual feedback and collaboration between the mathematical, statistical, and experimental communities in oncology and beyond. We believe that such collaborations are more than the sum of their parts, and offer countless exciting opportunities for driving forward our understanding of even the most daunting medical and biological challenges that we must face today and in the future.

Appendices

Appendix A

Linear stability analysis

Here we briefly discuss linear stability analysis for a representative simple system of ordinary differential equations,

$$\frac{dx}{dt} = f(x, y), \tag{A.1}$$

$$\frac{dy}{dt} = g(x, y). \tag{A.2}$$

Phase trajectories of this system are solutions of

$$\frac{dx}{dy} = \frac{f(x, y)}{g(x, y)}. \tag{A.3}$$

There is a unique curve through any point (x_0, y_0), except for a singular point, here denoted (x_s, y_s), at which

$$f(x_s, y_s) = g(x_s, y_s) = 0. \tag{A.4}$$

Expanding f and g in Taylor series and retaining only the linear terms, we obtain

$$\frac{dx}{dy} = \frac{ax + by}{cx + dy}, \tag{A.5}$$

and the matrix A,

$$A = \begin{bmatrix} a & b \\ c & d \end{bmatrix} = \begin{bmatrix} f_x & f_y \\ g_x & g_y \end{bmatrix}_{(x_s, y_s)}, \tag{A.6}$$

evaluated at the given stationary point (x_s, y_s).

The linear form is equivalent to the system

$$\frac{dx}{dt} = ax + by, \tag{A.7}$$

$$\frac{dy}{dt} = cx + dy. \tag{A.8}$$

Solutions to this system give the parametric forms of phase curves, with t as the parametric parameter. Let λ_1 and λ_2 be eigenvalues of the matrix A; i.e. taking the determinant of A and setting it to zero,

$$\begin{vmatrix} a-\lambda & b \\ c & d-\lambda \end{vmatrix} = 0, \tag{A.9}$$

yields the eigenvalues

$$\lambda_1, \lambda_2 = \frac{1}{2}\left(a + d \pm \sqrt{(a+d)^2 - 4((a-\lambda)(d-\lambda) - bc)}\right). \tag{A.10}$$

If λ_1 and λ_2 are distinct and real, then the stationary point is either a node singularity or a saddle point. If λ_1 and λ_2 are both negative, such that $\lambda_1 < \lambda_2 < 0$, then the stationary point is a stable node and trajectories will tend to it as $t \longrightarrow \infty$. If λ_1 and λ_2 are both positive, such that $\lambda_1 > \lambda_2 > 0$, then the stationary point is an unstable node, and the system will not approach it as $t \longrightarrow \infty$. Additionally, if λ_1 and λ_2 have different signs, then the stationary point is a saddle point singularity, which is unstable: except for strictly along the eigenvector which corresponds to the negative eigenvalue, any small perturbation from (x_s, y_s) grows exponentially.

If λ_1 and λ_2 are distinct and complex, i.e. $\lambda_1, \lambda_2 = \alpha + i\beta$ with $\beta \neq 0$, then an approach to the stationary point will be oscillatory. The point is a stable spiral if $\alpha < 0$, an unstable spiral if $\alpha > 0$, or a centre if $\alpha = 0$. In this last case, the linear stability is insufficient to determine whether it is actually a spiral, and it becomes necessary to look at higher-order terms.

Finally, if λ_1 and λ_2 are not distinct, such that $\lambda_1 = \lambda_2 = \lambda$, then solutions will generally involve terms similar to $te^{\lambda t}$ and the stationary point will be a node singularity, although in some cases, if the solution does not contain a $te^{\lambda t}$ term then it may instead be a star singularity, stable if $\lambda < 0$ and unstable otherwise.

Further discussion can be found in the classic textbook by Murray (2002).

Appendix B

Numerical solution of partial differential equations

B.1 Finite differences of derivatives

Finite difference methods are computational techniques for replacing the derivatives in differential equations by finite difference approximations, to yield a system of algebraic equations which can be solved numerically (LeVeque 2007). The choice of difference approximation depends upon the desired level of accuracy. For example, to approximate the first-order derivative $\frac{du(x)}{dx}$, we can choose either of two one-sided approximations to the function $u(x)$,

$$D_+u(x) = \frac{u(x+\Delta x) - u(x)}{\Delta x}, \tag{B.1}$$

$$D_-u(x) = \frac{u(x) - u(x-\Delta x)}{\Delta x}, \tag{B.2}$$

where D_+ denotes the left side approximation, D_- denotes the right side approximation, and Δx denotes the spatial grid step. These one-sided approximations are accurate to first order; that is, the size of the error is proportional to Δx. If we instead take a centred difference approximation,

$$D_cu(x) = \frac{u(x+\Delta x) - u(x-\Delta x)}{2\Delta x}, \tag{B.3}$$

we obtain second-order accuracy, with the error proportional to $(\Delta x)^2$.

Second-order derivatives are calculated by repeatedly applying first-order difference approximations. For example, the second-order difference approximation $D^2u(x)$ can be found as

follows:

$$D^2u(x) = D_+D_-u(x) \tag{B.4}$$
$$= \frac{1}{\Delta x}\left(D_-u(x+\Delta x) - D_-u(x)\right) \tag{B.5}$$
$$= \frac{1}{\Delta x}\left(\frac{u(x+\Delta x)-u(x)}{\Delta x} - \frac{u(x)-u(x-\Delta x)}{\Delta x}\right) \tag{B.6}$$
$$= \frac{u(x-\Delta x)-2u(x)+u(x+\Delta x)}{(\Delta x)^2}. \tag{B.7}$$

Considering the system

$$\frac{d^2u(x)}{dx^2} = f(x) \text{ for } 0 \le x \le 1, \tag{B.8}$$

the solution can be computed with a grid consisting of values $U_0, U_1, ..., U_m, U_{m+1}$ where U_j is an approximation to the solution $u(x_j)$. Here, we have $x_j = j\Delta x$ and the mesh width $\Delta x = 1/(m+1)$. Taking finite differences of the second derivative in Equation (B.8) yields

$$\frac{1}{(\Delta x)^2}(U_{j-1} - 2U_j + U_{j+1}) = f(x_j) \text{ for } j = 1, 2, ..., m. \tag{B.9}$$

B.2 Finite differences of boundary conditions

If Equation (B.8) has Dirichlet (constant-value) boundary conditions, then the value for u at the boundary is specified and can be used directly. For example, for the boundary conditions $u(0) = \alpha$, $u(1) = \beta$, we have $U_0 = \alpha$ and $U_{m+1} = \beta$, and the solution is calculated on the grid comprised of $U_0, U_1, ..., U_m, U_{m+1}$ as before.

If Equation (B.8) has Neumann (zero- or constant-flux) boundary conditions, then a centred approximation is preferable as it contributes second-order accuracy (LeVeque 2007). The use of a centred approximation to the derivative at the boundary requires the introduction of a ghost point, as follows. If Equation (B.8) has the boundary condition $u'(0) = \gamma$, then the ghost point U_{-1} is introduced and the following two equations are used:

$$\frac{1}{(\Delta x)^2}(U_{-1} - 2U_0 + U_1) = f(x_0), \tag{B.10}$$
$$\frac{U_1 - U_{-1}}{\Delta x} = \gamma. \tag{B.11}$$

Eliminating U_{-1} from these equations by substitution, we obtain the approximation

$$\frac{1}{\Delta x}(-U_0 + U_1) = \gamma + \frac{\Delta x}{2}f(x_0). \tag{B.12}$$

B.3 Finite differences in polar coordinates

Consider a differential equation for u in the cylindrical or spheroical polar coordinate r,

$$\frac{\partial u}{\partial t} = \bigtriangledown_r^2 u, \tag{B.13}$$

with boundary condition $\partial u/\partial r = 0$ at $r = 0$.

In the Cartesian coordinate x, Equation (B.13) becomes $\partial u/\partial r = \partial^2 u/\partial x^2$ and can be discretised using central differences. In cylindrical polar coordinates, Equation (B.13) takes the form

$$\frac{\partial u}{\partial t} = \frac{\partial^2 u}{\partial r^2} + \frac{1}{r}\frac{\partial u}{\partial r}, \tag{B.14}$$

which has a singularity due to the factor of $1/r$. To circumvent this, we can take the expansion

$$\dot{u}(r,t) = \dot{u}(0,t) + r\ddot{u}(0,t) + \frac{1}{2}r^2\dddot{u}(0,t) + ..., \tag{B.15}$$

where $\dot{}$ denotes differentiation with respect to the cylindrical coordinate r. Since we have from the boundary conditions that $\dot{u}(0,t) = 0$, by rearrangement the limiting value of $\frac{1}{r}\frac{\partial u}{\partial r}$ as $r \longrightarrow 0$ can be replaced by $\frac{\partial^2 u}{\partial r^2}$ at $r = 0$ (Smith 1985). Hence, at the $r = 0$ boundary the normal finite difference equation can be replaced by

$$\frac{\partial u}{\partial t} = 2\frac{\partial^2 u}{\partial u^2}. \tag{B.16}$$

In spherical polar coordinates, Equation (B.13) takes the form

$$\frac{\partial u}{\partial t} = \frac{\partial^2 u}{\partial r^2} + \frac{2}{r}\frac{\partial u}{\partial r}, \tag{B.17}$$

and by a calculation similar to that for cylindrical coordinates, at the $r = 0$ boundary we can replace the finite difference equation with

$$\frac{\partial u}{\partial t} = 3\frac{\partial^2 u}{\partial r^2}. \tag{B.18}$$

B.4 The upwind method for spatial discretisation

Traditional centred finite differences are often unstable when applied to hyperbolic partial differential equations. An alternative is the upwind method (LeVeque 2007), which uses an asymmetric approximation rather than a centred finite difference.

For an example advection equation,

$$\frac{\partial u}{\partial t} + a\frac{\partial u}{\partial x} = 0, \tag{B.19}$$

with a denoting a constant and an initial condition $u(x,0) = f(x)$, the exact solution can be found and is $u(x,t) = f(x - at)$ where the solution translates with speed a. If $a > 0$, then the solution translates from left to right, while if $a < 0$ then it translates from right to left. The following approximation can accommodate the inherent asymmetry in the solution.

If $a > 0$, such that the solution translates from left to right, we can use the approximation

$$u_x(x_j, t) \approx \frac{1}{\Delta x}(U_j - U_{j-1}), \tag{B.20}$$

which is stable if $0 \leq ak/\Delta x \leq 1$.

If $a < 0$, such that the solution translates from right to left, we can use the approximation

$$u_x(x_j, t) \approx \frac{1}{\Delta x}(U_{j+1} - U_j), \tag{B.21}$$

which is stable if $-1 \leq ak/\Delta x \leq 0$.

Upwind methods are first-order accurate. We leave discussion of higher-order methods to LeVeque (2007).

B.5 The Method of Lines

The Method of Lines is an efficient approach for numerically solving partial differential equations, whereby the spatial variable is discretised and the resulting system of coupled orderinary differential equations is solved through time (Schiesser 1991, Schiesser and Griffiths 2009).

Considering the one-dimensional heat equation

$$\frac{\partial u}{\partial t} = k\frac{\partial^2 u}{\partial x^2}, \quad \text{with} \quad x \in [0,1], \tag{B.22}$$

and imposing the initial condition $u(x,0) = f(x)$ and Dirichlet boundary conditions $u(0,t) = g_0(t)$ and $u(1,t) = g_1(t)$ for $t > 0$, we can apply a set of finite difference equations on a discrete grid with grid points (x_i, t_n), where $x_i = i\Delta x$ and $t_n = nk$. Here, Δx is the spatial step and k the time step. Letting $U_i^n \approx u(x_i, t_n)$ represent the numerical approximation at (x_i, t_n), the Method of Lines discretises Equation (B.22) using centred differences in space at grid point x_i by

$$U_i' = \frac{1}{(\Delta x)^2}(U_{i-1}(t) - 2U_i + U_{i+1}(t)) \quad \text{for} \quad i = 1, 2, ..., m, \tag{B.23}$$

with $'$ denoting differentiation with respect to time. This produces a coupled system of m ordinary differential equations, which can then be solved in time using a standard solver. In this thesis we use the inbuilt Matlab solver ODE15s, described in the following section.

B.6 The inbuilt Matlab solver ODE15s

ODE15s is an inbuilt Matlab solver appropriate for solving stiff systems of ordinary differential equations; that is, systems which exhibit regions of rapid transient movement along with smooth and slowly-varying solutions. The fast-changing regions require a very small time step, but this is unnecessary during the slow-varying transient and can severely slow the calculations or cause them to fail altogether. Numerical methods with a large stability region in the left-hand region of the stability plane are useful in cases of stiff systems, as they allow us to take large steps when the solution is varying slowly. Explicit methods have bounded stability regions, however, and hence it is necessary to use implicit methods, such as backward Euler, which have unbounded stability regions (LeVeque 2007).

ODE15s is a variable-order, multistep solver with a maximum order of five (Shampine and Reichelt 1997). The numerical solution for a desired $u(t)$ can be computed by U^n where $t = n$. Unlike single-step methods, which calculate U^{t+1} using only U^n, multistep methods calculate U^{t+1} from several previous values, such as U^n and U^{n-1}.

The solver algorithm is based on numerical differentiation formulae and employs backward differences (Shampine and Reichelt 1997). In turn, numerical differentiation formulae are based on backward differentiation of the form

$$\alpha_0 U^n + \alpha_1 U^{n+1} + ... + \alpha_r U^{n+r} = k\beta_r f(U^{n+r}), \tag{B.24}$$

where the coefficients $\alpha_0, ..., \alpha_r$ and β_r are determined by polynomial interpolation of U^{n+r} (LeVeque 2007).

Multistep methods allow the derivation of an r-step method with rth order accuracy. For example, the two-step backward differentiation formula $3U^{n+2} - 4U^{n+1} + U^n = 2kf(U^{n+2})$ is second-order accurate (LeVeque 2007).

B.7 Interpolation measurement of wavespeeds

To calculate invasive tumour wavespeeds in our numerical simulations in Chapters 2 and 3, we employed a linear interpolation method. That is, we obtained the numerical solution of the tumour density at two time-points, U^{τ} and $U^{\tau+\Delta t}$. At each time point, we used linear interpolation to find the midpoint of the tumour front, by locating where along the spatial domain it attained half its maximum value; that is, the x-coordinate ξ at which $U_{\xi} = \frac{1}{2}\max\{U(x)\}$. We then subtracted these midpoint coordinates and divided them by the difference in time ($\Delta\tau$) to determine the tumour wavespeed.

The use of linear interpolation at the wavefront introduces error. Denoting the grid points as (ξ_i, τ_n), where $\xi_i = i\Delta t$ and $\tau_n = nk$, with Δx representing the spatial step and k the time step, the error is bounded by the size of Δx and the second derivative of U. In other words, for mesh points ξ_i and ξ_{i+1} between which our solution is interpolated, the error, E, is bounded by

$$E \leq \frac{(\xi_i - \xi_{i+1})^2}{8}\max_{\xi_i \leq \xi \leq \xi_{i+1}}|U''(\xi)|. \tag{B.25}$$

In addition to this interpolation error, we also have error contributed by the ordinary differential equation solver, which is the maximum of the relative and absolute error tolerances. In Matlab, the default absolute error tolerance for the ODE15s solver is 10^{-6} and the relative error tolerance is 10^{-3}. In Chapters 2 and 3 we reduce both error tolerances to 10^{-12}.

B.8 Verification of numerics

Throughout this thesis, we employed standard procedures for ensuring the validity of our numerical results. Our numerical schemes were first run using a test system with a known solution. For example, we tested our Method of Lines implementation and numerical wavespeed calculation using the Fisher equation. Figure B.1 shows the accuracy of our numerical solution as compared to the known analytical wavespeed.

Additionally, we ensured the stability of our numerical schemes by progressively shrinking the grid spacing. We then chose the smallest spacings that balanced accuracy with rapidity of the numerical integration. We also compared our numerical solutions to analytical solutions or approximations where possible (namely, in Chapter 3).

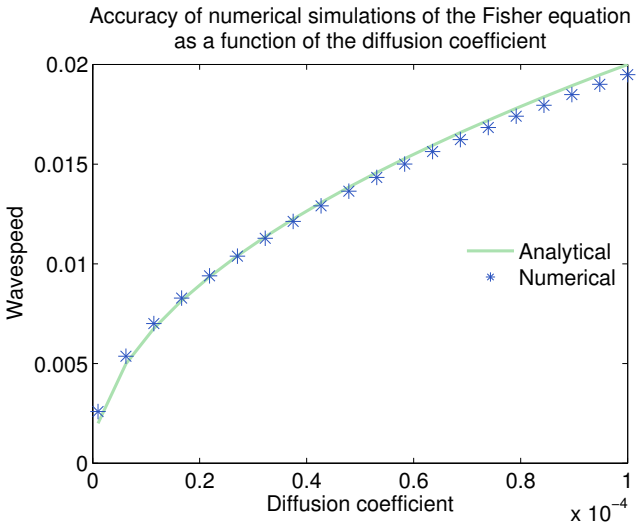

Figure B.1: Verification of numerical methods. Accuracy of numerical approximations for the travelling wavespeed of the Fisher equation (blue stars), solved with our Method of Lines implementation and measured using our wavespeed interpolation method, as compared to the analytical solution (green) as a function of the diffusion coefficient.

Appendix C

Perturbation theory

Perturbation theory is a large collection of methods for finding approximate solutions to problems which contain a small parameter, typically denoted ϵ, and which simplify in some way—for example, by becoming linear or exactly solvable—when $\epsilon = 0$. Such a problem can be viewed as a small perturbation from an underlying simpler system, and the aim is then to determine the behaviour of the solution as the perturbation shrinks to nothing (i.e. ϵ approaches zero, herein denoted $\epsilon \to 0$).

The solution to a perturbation problem is expressed as an asymptotic expansion, or formal series of functions that, when truncated after a finite number of terms, provides an approximation to the solution as its argument tends toward a particular point; typically this is a power series in the small parameter ϵ evaluated as $\epsilon \to 0$. Formulating the solution in such a way quantifies the deviation of the system from the underlying simpler problem. This is a powerful approach because the leading-order term in the asymptotic series elucidates the salient features of the solution, with higher-order terms contributing corrective refinements on the order of ϵ or smaller (Bender and Orszag 1999).

C.1 Regular vs. singular perturbation theory

Broadly, perturbation problems can be divided into two classes: regular and singular. Different asymptotic methods exist for dealing with each of these classes. A regular problem is one whose perturbation series takes the form of a power series in ϵ which has a non-vanishing radius of convergence; that is, the exact solution for a small (but nonzero) ϵ smoothly approaches the unperturbed solution as $\epsilon \to 0$.

A singular problem does not exhibit such smooth behaviour; instead, its perturbation series either has a vanishing radius of convergence or does not take the form of a power series at

all. This class of problem arises when the exact solution for $\epsilon = 0$ (the unperturbed solution) either fails to exist or is fundamentally different in character from solutions obtained in the limit as $\epsilon \to 0$ (the perturbative solution). In such a case, care must be taken to distinguish between the exact solution of the unperturbed problem and the leading-order perturbative solution, especially if the former does not exist. In contrast, for a regular problem these two solutions are the same.

A particular type of singular perturbation problem arises in Chapter 3: a differential equation whose highest-order derivative is multiplied by the small parameter ϵ. In the limit as $\epsilon \to 0$, the unperturbed solution to this type of equation loses its ability to satisfy the boundary conditions and thus disappears. This behaviour can be seen in the following very simple example from Bender and Orszag (1999):

The boundary-value problem

$$\begin{aligned} \epsilon y'' - y' &= 0, \\ y(0) &= 0, \\ y(1) &= 1, \end{aligned}$$

is singular because its associated unperturbed problem,

$$\begin{aligned} -y' &= 0, \\ y(0) &= 0, \\ y(1) &= 1, \end{aligned}$$

has no solution; the solution to the unperturbed first-order differential equation, $y = k$ where k is a constant, cannot satisfy both boundary conditions.

Such a system exhibits a **boundary layer**, or localised region of rapid variation for small ϵ which develops into a discontinuity in the limit as $\epsilon \to 0$. Constructing an analytical expression for a leading-order approximation—which is often sufficient to provide a good idea of the system behaviour, although a full perturbative approximation can be developed if needed—requires the technique of asymptotic matching, discussed below.

C.2 Asymptotic matching

The global properties of the solution to a differential equation with a boundary layer can be approximated using the technique of asymptotic matching, which rests on the principle of breaking the interval on which a boundary-value problem is posed into two or more

overlapping subintervals. On each subinterval, perturbation theory can be applied to find an asymptotic approximation for the solution of the differential equation that is valid on that subinterval. These solutions are then matched by requiring that the asymptotic approximations take the same functional form within the overlapping region of each pair of subintervals. The following simple example, condensed from Holmes (2013), illustrates this process.

Suppose we have the second-order ordinary differential equation

$$\epsilon y'' + 2y' + 2y = 0, \quad 0 < x < 1, \tag{C.1}$$

with boundary conditions $y(0) = 0$ and $y(1) = 1$. If $\epsilon = 0$, then the problem is no longer second-order, and hence we have a singular perturbation problem as introduced in Section C.1. Assuming initially that the solution can be expanded in powers of ϵ, i.e. that

$$y(x) \approx y_o(x) + \epsilon y_1(x) + \epsilon^2 y_2(x) + ...,$$

substituting this expansion into Equation C.1 and taking the leading-order terms yields the equation $y_o' + y_o = 0$, which has the general solution

$$y_o = ae^{-x}, \tag{C.2}$$

where a is an arbitrary constant. Unfortunately, this solution cannot simultaneously satisfy both boundary conditions, and hence is incapable of describing the solution over the entire interval $0 \leq x \leq 1$.

If we know there is a boundary layer at $x = 0$ (for example by inspecting numerical simulations of Equation C.1), then we can introduce a transformation to 'stretch' the region near $x = 0$ as ϵ becomes small. This boundary-layer coordinate is given by $\bar{x} = x/\epsilon^\alpha$ where $\alpha > 0$. Transforming Equation C.1 accordingly via the chain rule, and letting $Y(\bar{x})$ denote the new solution, we have:

$$\epsilon^{1-2\alpha}\frac{d^2Y}{d\bar{x}^2} + 2\epsilon^{-\alpha}\frac{dY}{d\bar{x}} + 2Y = 0, \tag{C.3}$$

with the boundary condition $Y(0) = 0$. The appropriate expansion for this boundary layer, which describes the solution in the immediate vicinity of the point $x = 0$, is

$$Y(\bar{x}) \approx Y_o(\bar{x}) + \epsilon^\gamma Y_1(\bar{x}) + ... \quad \text{where } \gamma > 0.$$

Substituting this expansion into Equation C.3 and introducing the appropriate balancing of scales with $\alpha = 1$, the problem to solve at asymptotic order $1/\epsilon$ is now $Y_o'' + 2Y_o' = 0$ for $0 < \bar{x} < \infty$, with the boundary condition $Y_o(0) = 0$. The general solution of this problem is

$$Y_o(\bar{x}) = A(1 - e^{-2\bar{x}}), \tag{C.4}$$

where A is an arbitrary constant. This is known as the inner solution.

Assuming there are no other layers present in the system, it is reasonable to expect that the outer solution, Equation (C.2), applies everywhere outside the immediate vicinity of $x = 0$; this means that it should satisfy the other boundary condition at $x = 1$, which results in the solution $y_o = e^{1-x}$.

It now remains to determine the constant A in the inner solution, Equation C.4. Figure C.1a shows that both the outer and inner expansion are approximations of the same function; therefore, they must be the same in the region of overlap. To ensure this, we require that the value of y_o as we enter the boundary layer (i.e. as $x \to 0$) is equal to the value of Y_o as we emerge from it (i.e. as $\bar{x} \to \infty$). From this condition we find (and can see in Figure C.1a) that $A = e^1$. With this, the inner solution becomes $Y_o(\bar{x}) = e^1 - e^{1-2\bar{x}}$.

We have the solution in two pieces, one valid near $x = 0$ and one valid everywhere else, but neither is uniformly valid over the whole interval $0 \leq x \leq 1$, and so we now need to combine them. To do this, we simply add the approximations together and subtract the overlap:

$$\begin{aligned} y &\approx y_o(x) + Y_o(x/\epsilon) - y_o(0) \\ &\approx e^{1-x} - e^{1-2x/\epsilon}. \end{aligned}$$

This composite expansion gives a close approximation of the exact solution over the entire integral, as can be seen in Figure C.1b, and the two converge as ϵ shrinks. We note that the composite solution satisfies the boundary condition at $x = 0$ exactly and at $x = 1$ asymptotically; this is acceptable because the expansion also satisfies the original differential equation asymptotically.

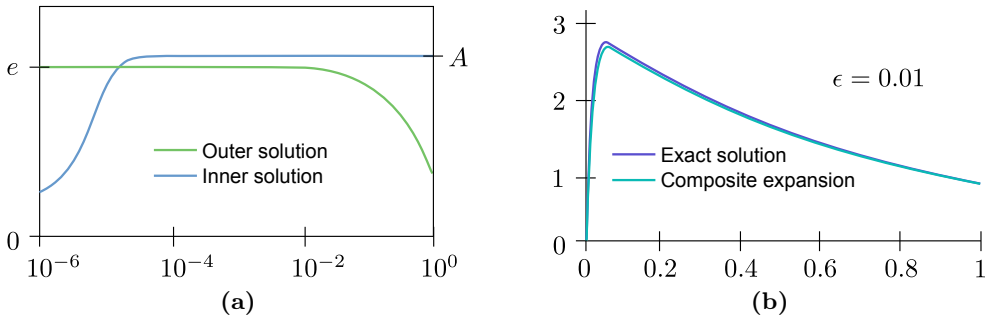

Figure C.1: Illustration of asymptotic matching. (a) Overlap of inner and outer solutions for the simple example problem presented here, and (b) correspondence of the composite expansion with the exact solution.

In general, the technique of asymptotic matching produces a sequence of asymptotic approximations to the solution of the differential equation which, by construction, satisfy all the boundary conditions imposed at various points along the interval; and its end result is an approximate solution to the boundary-value problem that is valid over the entire interval (Bender and Orszag 1999). Of course, many subtleties are involved in this method—for example, when one of the expansions is unbounded and hence lacks a limit—but we leave further discussion to Holmes (2013).

Appendix D

Laplace's method for asymptotic expansion of integrals

If we consider an integral in which a large parameter, here denoted χ, appears in an exponential,

$$I(\chi) = \int_a^b f(t)e^{\chi\phi(t)}dt,$$

where $f(t)$ and $\phi(t)$ are real continuous functions, then we can apply a technique known as Laplace's Method to obtain the asymptotic behaviour of the integral as $\chi \to +\infty$.

The central idea behind Laplace's Method is that if the real continuous function $\phi(t)$ has its maximum on the interval $a \leq t \leq b$ at the point $t = c$, and if $f(c) \neq 0$, then only the immediate vicinity of $t = c$ will contribute to the full asymptotic expansion of $I(\chi)$ for large χ. That is, we can approximate the integral $I(\chi)$ by $I(\chi;\epsilon)$, where

$$I(\chi;\epsilon) = \begin{cases} \int_{c-\epsilon}^{c+\epsilon} f(t)e^{\chi\phi(t)}dt & \text{if } a < c < b, \\ \int_a^{a+\epsilon} f(t)e^{\chi\phi(t)}dt & \text{if } c = a, \\ \int_{b-\epsilon}^{b} f(t)e^{\chi\phi(t)}dt & \text{if } c = b, \end{cases}$$

with ϵ being an arbitrary positive number such that the restricted integration range $c-\epsilon \leq t \leq c+\epsilon$ is a subinterval of $a \leq t \leq b$. Crucially, the full asymptotic expansion of $I(\chi;\epsilon)$ as χ approaches infinity must not depend on ϵ, and also must be identical to the full asymptotic expansion of $I(\chi)$ as $\chi \to +\infty$; both of these requirements are satisfied because the integral over the regions outside of $I(\chi;\epsilon)$ is exponentially small compared to $I(\chi)$ as $\chi \to +\infty$. The utility of exploiting the shape of $e^{\chi\phi(t)}$ in this way becomes clear when we choose ϵ to be small, as this allows us to replace $f(t)$ and $\phi(t)$ by their Taylor or asymptotic series expansions about the point $t = c$.

Implementation of Laplace's Method involves three steps. First, as described above, $I(\chi)$ is approximated by $I(\chi;\epsilon)$ via restriction of the original integration range to a narrow region around the location of the maximum of $\phi(t)$. Secondly, $f(t)$ and $\phi(t)$ are expanded in series which are valid near the location of the maximum of $\phi(t)$; this in turn expands $I(\chi;\epsilon)$ into a series of integrals. Thirdly, for convenient evaluation of the terms in the series for $I(\chi;\epsilon)$, the integration region of each integral is extended to infinity. Each change of the limits of integration introduces only exponentially small errors. When we apply Laplace's Method in Chapter 3, we consider it sufficient to obtain a leading-order approximation to our integral of interest; but the method can be extended to include higher-order expansion terms as in Bender and Orszag (1999).

Appendix E

Nondimensionalisation of Equations (4.7)-(4.10)

For convenience we repeat the full dimensional spatial model for dual glucose-lactate metabolism from Chapter 4 here:

$$
\begin{aligned}
C_t &= \frac{\Delta_C}{r^2}[r^2 C_r]_r + \rho C\left(1 - \frac{C}{C_*}\right) - \delta\left(\psi_G + \psi_A + \psi_N\right) C, \\
G_t &= \frac{\Delta_G}{r^2}[r^2 G_r]_r - \kappa_G \frac{\alpha_G G}{\alpha_G G + \alpha_L L + \eta_G} C, \\
L_t &= \frac{\Delta_L}{r^2}[r^2 L_r]_r + 2\kappa_G \frac{\alpha_G G}{\alpha_G G + \alpha_L L + \eta_G} C - \kappa_L \frac{\alpha_L L}{\alpha_G G + \alpha_L L + \eta_L} \psi_H C, \\
O_t &= \frac{\Delta_O}{r^2}[r^2 O_r]_r - 3\kappa_L \frac{\alpha_L L}{\alpha_G G + \alpha_L L + \eta_L} \psi_H C,
\end{aligned}
$$

with t representing the time in days, r the one-dimensional distance in centimetres, C the tumour density in $1/\text{cm}^3$, G the glucose concentration in mM, L the lactate concentration in mM, and O the oxygen concentration in mM. The parameters Δ_C, Δ_G, Δ_L, and Δ_O denote the diffusion coefficients of tumour cells, glucose, lactate, and oxygen, respectively; κ_G and κ_L the maximal rates of consumption of glucose and lactate, respectively; η_G and η_L the half-saturation points for uptake of glucose and lactate, respectively; ρ and δ the rates of tumour cell proliferation and necrosis, respectively; and ψ_H, ψ_G, ψ_A, and ψ_N simple switch functions capturing tumour sensitivity to hypoxia, glucose deprivation, acidosis, and

anoxia, respectively:

$$\psi_G = \begin{cases} 0 & \text{if } G > \sigma_G, \\ 1 & \text{otherwise;} \end{cases}$$

$$\psi_A = \begin{cases} 1 & \text{if } L > \sigma_A, \\ 0 & \text{otherwise; and} \end{cases}$$

$$\psi_N = \begin{cases} 0 & \text{if } O > \sigma_N, \\ 1 & \text{otherwise;} \end{cases}$$

$$\psi_H = \begin{cases} 1 & \text{if } O > \sigma_H, \\ 0 & \text{otherwise;} \end{cases}$$

with σ_G denoting the minimum glucose concentration that cells require for survival, σ_A the lactate concentration corresponding to the maximum tolerable level of tissue acidity, σ_N the oxygen threshold for severe anoxia, and σ_H the oxygen threshold for hypoxia. The dimensional parameters are summarised in Table E.1.

Table E.1: Parameters in Equations (4.7)-(4.10). Values or ranges for the dimensional parameters in our model of dual glucose-lactate metabolism from Chapter 4.

Parameter	Value	Units	Source
C_*	$5 \cdot 10^7$	$1/\text{cm}^3$	Tracqui et al. (1995)
Δ_C	$5.7 \cdot 10^{-6}$	cm^2/day	Rockne et al. (2010)
Δ_G	0.0346	cm^2/day	Jiang et al. (2005)
Δ_L	0.0518	cm^2/day	$1.5\Delta_G$, due to size
Δ_O	0.864	cm^2/day	Rockne et al. (2010)
ρ	1/17	1/day	Rockne et al. (2010)
δ	1/10	1/day	Estimated
σ_H	0.0278	mM	Daşu et al. (2003)
σ_G	0.1	mM	Chosen to be small
σ_A	20	mM	Chosen to be large
σ_N	0.001	mM	Chosen to be small
J_G	10^3	1/cm	(McEwen and Reagan 2004)
J_O	10^3	1/cm	(Blum 1960)
J_L	10	1/cm	Assumed moderate for functioning vessels
G_v	5	mM	Physiological (Sherwood 2007)
L_v	$[0, 6]$	mM	Physiological (Figley 2011)
O_v	0.0834	mM	Physiological (Sherwood 2007)
κ_G	$[1, 10^5]$	$\text{mM}\cdot\text{cm}^3/\text{day}$	Mendoza-Juez et al. (2012)
κ_L	$[1, 10^5]$	$\text{mM}\cdot\text{cm}^3/\text{day}$	Mendoza-Juez et al. (2012)
η_G	0.5	mM	Mendoza-Juez et al. (2012)
η_L	$[0.01, 10]$	mM	Mendoza-Juez et al. (2012)
α_G	$[1, 10^3]$	none	Mendoza-Juez et al. (2012)
α_L	$[1, 10^3]$	none	Mendoza-Juez et al. (2012)

We can nondimensionalise this system by scaling time by the cell proliferation rate, space by the tumour diffusion coefficient, the tumour density by the tissue carrying capacity, and the metabolites by their concentrations in the vessel. That is, we make the substitutions $\tilde{t} = \gamma t$, $\tilde{r} = \sqrt{\gamma/\Delta_C}r$, $\tilde{C} = C/C_*$, $\tilde{G} = G/G_v$, $\tilde{L} = L/(2G_v)$, and $O = O/O_v$, and define the dimensionless parameters $D_G = \Delta_G/\Delta_C$, $D_L = \Delta_L/\Delta_C$, $D_O = \Delta_O/\Delta_C$, $d = \delta/\gamma$, $g = \kappa_G C_*/(\gamma G_v)$, $v = O_v/G_v$, $a = \alpha_L/\alpha_G$, $k = \kappa_L/\kappa_G$, $n_G = \eta_G/(\alpha_G G_v)$, and $n_L = \eta_L/\alpha_L G_v$. Dropping the tildes for convenience, the system becomes

$$C_t = \frac{1}{r^2}[r^2 C_r]_r + C(1-C) - d(f_A + f_G + f_N)C \tag{E.1}$$

$$G_t = \frac{D_G}{r^2}[r^2 G_r]_r - g\frac{G}{G + 2aL + n_G}C \tag{E.2}$$

$$L_t = \frac{D_L}{r^2}[r^2 L_r]_r + g\frac{G}{G + 2aL + n_G}C - gk\frac{L}{G/a + 2L + n_L}f_O C \tag{E.3}$$

$$O_t = \frac{D_O}{r^2}[r^2 O_r]_r - 6\frac{gk}{v}\frac{L}{G/a + 2L + n_L}f_O C \tag{E.4}$$

where the sensitivity switch functions are now

$$f_G = \begin{cases} 0 & \text{if } G > s_G, \\ 1 & \text{otherwise;} \end{cases} \tag{E.5}$$

$$f_A = \begin{cases} 1 & \text{if } L > s_A, \\ 0 & \text{otherwise; and} \end{cases} \tag{E.6}$$

$$f_N = \begin{cases} 0 & \text{if } O > s_N, \\ 1 & \text{otherwise;} \end{cases} \tag{E.7}$$

$$f_H = \begin{cases} 1 & \text{if } O > s_H, \\ 0 & \text{otherwise;} \end{cases} \tag{E.8}$$

with $s_H = \sigma_H/O_v$, $s_G = \sigma_G/G_v$, $s_A = \sigma_A/(2G_v)$, and $s_N = \sigma_N/O_v$.

This nondimensionalisation puts the variables and parameters into the ranges or values listed in Table E.2.

Table E.2: Parameters in Equations (E.1)-(E.4). Values or ranges for the nondimensionalised variables and parameters in Equations (E.1)-(E.4).

Variable	Nondimensional range
t	$[0, 10]$
r	$[0, 2]$
C	$[0, 1]$
G	$[0, 1]$
L	$\mathcal{O}(1)$
O	$[0, 1]$

Parameter	Derivation	Nondimensional value or range
D_G	Δ_G/Δ_C	$6 \cdot 10^3$
D_L	Δ_L/Δ_C	$0 \cdot 10^3$
D_O	Δ_O/Δ_C	$1.5 \cdot 10^5$
d	δ/γ	1.7
s_H	σ_H/O_v	0.33
s_G	σ_G/G_v	0.02
s_A	$\sigma_A/(2G_v)$	2
s_N	σ_N/O_v	0.012
j_G	$J_G\sqrt{\Delta_C/\gamma}$	4.1
j_O	$J_O\sqrt{\Delta_C/\gamma}$	4.1
j_L	$J_L\sqrt{\Delta_C/\gamma}$	4.1
g_v	G_v/G_v	1
l_v	$L_v/(2G_v)$	$[0, 1]$
o_v	O_v/O_v	1
v	O_v/G_v	0.02
a	α_L/α_G	$[10^{-3}, 10^3]$
k	κ_L/κ_G	$[0.1, 10]$
g	$\kappa_G C_*/(\gamma G_v)$	$[3.4, 34]$
n_G	$\eta_G/(\alpha_G G_v)$	$[2 \cdot 10^{-4}, 20]$
n_L	$\eta_L/(\alpha_L G_v)$	$[2 \cdot 10^{-5}, 200]$

Appendix F

Experimental data sets

F.1 Lactate metabolism in U87 glioma cells

These experiments were designed by Jessica McGillen and Dr. Catherine Kelly, and performed by Dr. Kelly.*

A set of experiments was performed to examine the metabolic characteristics of U87 glioma cultures *in vitro* using three metrics: glucose uptake, extracellular acidification, and oxygen consumption. Glucose was measured using a radiolabelled analogue, [18F] fluorodeoxyglucose (FDG), which has similar uptake kinetics to glucose. The experimental methods are described in detail in Chapter 4, and we present the data here, in Tables F.1-F.3.

*Gray Institute for Radiation Oncology and Biology, Oxford University

Table F.1: Rate of oxygen consumption in U87 glioma cells. Relative oxygen consumption rate in cultured U87 glioma cells, measured with the Seahorse XF Analyser, after the addition of exogenous lactate at varying concentrations (columns). Eight replicates were taken at each concentration (rows) and all measurements were normalised to cell density. These data are graphed in Chapter 4 (Figure 4.10b).

	Concentration of exogenous lactate					
	0 mM	3 mM	6 mM	9 mM	12 mM	15 mM
	0.9876271377	1.0175177706	1.1442815047	1.2128417511	1.1932827529	1.1341156639
Normalised	0.9945825267	1.0543300643	1.0754863531	1.1593454226	1.1866903196	1.2317917962
relative	1.0111985808	0.9986416542	1.1768415062	1.2077034677	1.1543309036	1.2373879005
oxygen	1.1135001026	1.0292171335	1.077972934	1.1796015123	1.2496233185	1.2202248722
consumption	1.036774399	0.9889682867	1.1428470943	1.1885601448	1.1945541068	1.1587325268
rate	0.9585132586	1.0167226201	1.1174676987	1.0039692435	1.1755487484	1.2231765568
	0.8965796779	1.035559579	1.1096546698	1.167501273	1.2447254641	1.4062721991
	1.0012243169	1.0113565352	1.0717141114	1.2026988582	1.3078569476	1.2354102462

Table F.2: Rate of extracellular acidification in U87 glioma cells. Relative extracellular acidification rate in cultured U87 glioma cells, measured with the Seahorse XF Analyser, after the addition of exogenous lactate at varying concentrations (columns). Eight replicates were taken at each concentration (rows) and all measurements were normalised to cell density. These data are graphed in Chapter 4 (Figure 4.10a).

	Concentration of exogenous lactate					
	0 mM	3 mM	6 mM	9 mM	12 mM	15 mM
	0.9231644026	0.9467730982	0.7785001664	0.7567007432	0.7692287601	0.7357509588
Normalised	0.9202509674	0.9722415673	0.8021891705	0.7232783205	0.7773338907	0.7989420249
relative	0.9864178597	0.937660968	0.8891600186	0.7732388927	0.7823930129	0.8365165395
extracellular	0.9919029593	1.0297183134	0.8554536441	0.7821919821	0.719787442	0.7359797162
acidification	1.0749524381	0.9530409856	0.8203578301	0.7456790514	0.7515318988	0.7435438262
rate	1.2070651413	0.8981172046	0.7836000538	0.7390429359	0.7848735084	0.7702080471
	0.9245206597	0.830854532	0.8007288473	0.7377557897	0.7840037128	0.8101066276
	0.9717255719	1.051645511	0.7875583573	0.7731629977	0.7436179786	0.8047839825

Table F.3: Glucose uptake in U87 glioma cells. Relative radioactivity of [18F] fluorodeoxyglucose (FDG), counted using a Beckman Coulter Counter, after the addition of exogenous lactate at varying concentrations (columns). Three replicates were taken at each concentration (rows). These data are graphed in Chapter 4 (Figure 4.10c).

	Concentration of exogenous lactate					
	0 mM	3 mM	6 mM	9 mM	12 mM	15 mM
[18F] fluoro-	960534.97	923360.09	925424.33	925526.85	949125.58	901955.55
deoxyglucose	976203.8	930074.24	971597.14	953730.56	940002.11	919079.17
activity	994980.38	952607.17	992458.47	947694.82	980438.18	936298.82

F.2 Buffering and flux dynamics in HCT116 cells

These data were generously contributed by Dr. Pawel Swietach[†].

We have three sets of *in vitro* data from flux experiments on HCT116 human colon carcinoma cells. These data are displayed in Tables F.4-F.6, with the experimental methods summarised in the table captions, and are plotted in Figures F.1-F.3.

Table F.4: Experimental data on intrinsic intracellular buffering power. Intrinsic buffering was determined in HCT116 human colon carcinoma cells superfused with Hepes buffer, an artificial buffer that is nominally free of the physiological buffer CO_2/HCO_3. The protocol (Swietach 2011) consisted of acid loading a cell by using the classic technique of prepulsing with ammonium (NH_4^+), and then recording the resulting fall of intracellular pH (Roos and Boron 1981). The successive decreases in intracellular pH produced by stepping down the extracellular ammonium concentration were used to estimate the buffering power, β (mM) as $\beta = \Delta[NH_4^+]_i/\Delta pH_i$, where the subscript i denotes an intracellular species and where $[NH_4^+]_o \cdot 10^{pH_o - pH_i}$, under the assumption that the pK of ammonium dissociation is the same in the extracellular and intracellular compartment (Roos and Boron 1981). These data are plotted in Figure F.1.

Intracellular pH	Buffering power in mM/pH unit	Standard error
6.3909	27.1266	1.7138
6.5496	29.4961	1.0318
6.6557	31.4941	2.6629
6.7464	31.2528	2.9088
6.8489	28.5886	1.7101
6.9592	29.2323	1.5311
7.0463	28.8779	1.5234
7.1496	24.0605	1.0273
7.2483	18.5715	0.7378
7.3417	16.1852	0.9366
7.4564	11.5327	0.6677
7.5451	10.3138	0.536
7.6308	9.1777	1.7804

[†]Department of Physiology, Anatomy, and Genetics, Oxford University

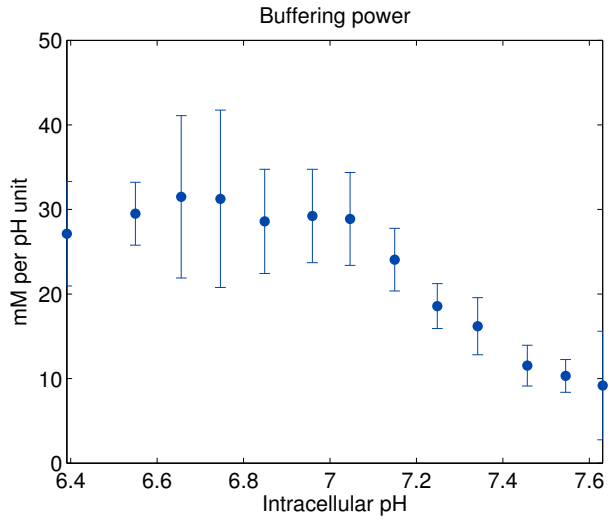

Figure F.1: Data for intrinsic buffering power. Plot of the data in Table F.4, with error-bars showing standard deviations (standard errors multiplied by the square root of the number of measurements).

Table F.5: Data for Na^+/H^+ exchange. Measurements of the rate of efflux of H^+, in mM per minute, from an experiment in single HCT116 human colon carcinoma cells *in vitro*, performed in Hepes. A membrane-permeable pH fluorophore (carboxy-SNARF-1) was used to detect the flux of protons across the cell membrane following an ammonium prepulse, with the extracellular pH set to the listed values by flushing of the superfusate. These data are plotted in Figure F.2.

Extracellular pH	Intracellular pH	Flux (mM/min)	Standard error
6.4	6.4288	2.091	0.39844
6.4	6.4783	1.2496	0.24168
6.4	6.5267	0.85235	0.16798
6.4	6.5774	0.80705	0.11774
6.4	6.6259	0.63155	0.088986
6.4	6.6756	0.52162	0.079151
6.4	6.7248	0.55844	0.069196
6.4	6.7732	0.46118	0.076502
6.4	6.8237	0.48315	0.084445
6.4	6.872	0.41818	0.10365
6.4	6.9221	0.58412	0.13462
6.4	6.9719	0.39585	0.27092
6.4	7.0145	0.43996	0.46667
6.8	6.4297	2.0608	0.80319
6.8	6.4788	1.3576	0.49998
6.8	6.5273	1.1166	0.33581
6.8	6.576	1.2711	0.23974
6.8	6.626	1.2264	0.18344
6.8	6.6761	1.0543	0.16394
6.8	6.7244	0.94927	0.13392
6.8	6.7753	0.93913	0.11966

Continued on next page

Table F.5 – *Continued from previous page*

Extracellular pH	Intracellular pH	Flux (mM/min)	Standard error
6.8	6.8246	0.87156	0.12672
6.8	6.8746	0.75315	0.1229
6.8	6.9245	0.74316	0.1138
6.8	6.9746	0.62808	0.13052
6.8	7.0236	0.52768	0.13579
6.8	7.0709	0.37749	0.14061
6.8	7.1242	0.43226	0.22372
6.8	7.1735	0.51531	0.33542
6.8	7.2254	0.19364	0.30765
6.8	7.271	0.036162	0.29989
7.1	6.4268	5.7491	1.2012
7.1	6.4752	5.629	1.0327
7.1	6.5282	5.1443	0.81918
7.1	6.5756	4.5687	0.53138
7.1	6.6247	4.1301	0.42326
7.1	6.6762	3.3025	0.33341
7.1	6.7257	2.8495	0.26742
7.1	6.7765	2.2023	0.22428
7.1	6.8261	1.3286	0.16252
7.1	6.8774	1.1264	0.13802
7.1	6.925	0.53864	0.094244
7.1	6.9747	0.42898	0.088286
7.1	7.0237	0.46255	0.10551
7.1	7.0737	0.19729	0.091642
7.1	7.1223	0.19382	0.10028
7.1	7.1713	0.17687	0.14677
7.4	6.4265	10.391	1.4228
7.4	6.4759	11.956	1.0059
7.4	6.5261	9.8477	0.87648
7.4	6.578	9.049	0.68737
7.4	6.627	8.0301	0.44582
7.4	6.676	7.4476	0.38643
7.4	6.7267	5.9919	0.29798
7.4	6.7768	4.4625	0.23007
7.4	6.8259	3.3737	0.1552
7.4	6.8759	2.6283	0.12203
7.4	6.9262	2.3453	0.11191
7.4	6.9763	1.738	0.085195
7.4	7.0256	1.364	0.072029
7.4	7.0753	1.0055	0.064464
7.4	7.125	0.84957	0.059711
7.4	7.1736	0.76912	0.058108
7.4	7.2243	0.71528	0.057996
7.4	7.2734	0.53499	0.055182

Continued on next page

Table F.5 – *Continued from previous page*

Extracellular pH	Intracellular pH	Flux (mM/min)	Standard error
7.4	7.324	0.51072	0.062688
7.4	7.3737	0.42618	0.064805
7.4	7.4229	0.32304	0.071606
7.4	7.4702	0.32118	0.11624
7.4	7.5201	0.25059	0.20743
7.8	6.4301	12.0232	1.4494
7.8	6.4742	10.458	1.6209
7.8	6.5257	9.3807	1.2238
7.8	6.5763	8.8691	0.74892
7.8	6.6259	8.3561	0.66007
7.8	6.6772	6.8737	0.53892
7.8	6.7272	6.0228	0.40078
7.8	6.7762	5.2012	0.3171
7.8	6.8252	4.0229	0.26689
7.8	6.8755	3.4777	0.20284
7.8	6.9253	2.6956	0.16441
7.8	6.9761	2.4425	0.13556
7.8	7.026	1.5961	0.10323
7.8	7.0761	0.9877	0.076588
7.8	7.124	0.6628	0.063148
7.8	7.1742	0.84222	0.070305
7.8	7.2244	0.58724	0.066769
7.8	7.2754	0.46626	0.05679
7.8	7.3241	0.39297	0.054971
7.8	7.3755	0.26629	0.049869
7.8	7.4237	0.13147	0.05237
7.8	7.4701	0.13134	0.067359
7.8	7.5137	0.34652	0.17239

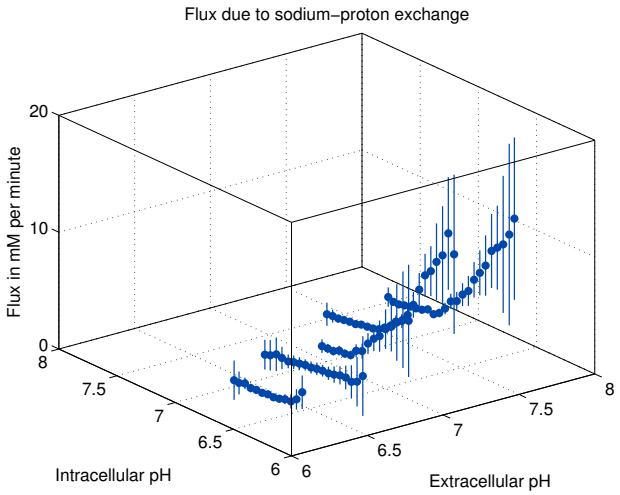

Figure F.2: Data for Na^+/H^+ exchange. Plot of the data in Table F.5, with errorbars showing standard deviations (standard errors multiplied by the square root of the number of measurements for each level of extracellular pH).

Table F.6: Data for CO_2/HCO_3 import. Measurements of the rate of influx of HCO_3^-, in mM per minute, from an experiment in single HCT116 human colon carcinoma cells *in vitro*, performed in physiological (CO_2/HCO_3^-) buffer. A membrane-permeable pH fluorophore (carboxy-SNARF-1) was used to detect the flux of protons across the cell membrane following an ammonium prepulse, with the extracellular pH set to the listed values by flushing of the superfusate. These data are plotted in Figure F.3.

Extracellular pH	Intracellular pH	Flux (mM/min)	Standard error
6.4	6.4262	2.2311	0.27338
6.4	6.4754	1.7502	0.23761
6.4	6.5261	1.9547	0.18876
6.4	6.5759	1.4677	0.16188
6.4	6.6251	1.3107	0.14316
6.4	6.6747	1.104	0.14222
6.4	6.7245	1.1505	0.13499
6.4	6.7736	0.87008	0.14714
6.4	6.8224	0.97492	0.19816
6.4	6.8714	0.91668	0.26942
6.4	6.9219	1.3374	0.50749
6.4	6.9711	0.91164	0.55458
6.8	6.4255	3.6731	1.2342
6.8	6.4782	4.1708	0.87128
6.8	6.5259	3.7243	0.59341
6.8	6.5759	3.7423	0.55443
6.8	6.6269	3.532	0.37239
6.8	6.6763	3.1152	0.28827
6.8	6.7262	2.9443	0.22245
6.8	6.7762	2.2747	0.18941

Continued on next page

Table F.6 – *Continued from previous page*

Extracellular pH	Intracellular pH	Flux (mM/min)	Standard error
6.8	6.8256	2.0114	0.15696
6.8	6.875	1.7186	0.14458
6.8	6.9259	1.1495	0.12355
6.8	6.9753	0.86399	0.11297
6.8	7.023	0.70178	0.1237
6.8	7.0697	0.7949	0.18018
7.1	6.427	8.4519	1.0162
7.1	6.4772	8.0024	0.8123
7.1	6.5262	8.1597	0.6077
7.1	6.5757	6.5089	0.49037
7.1	6.6256	6.7493	0.43185
7.1	6.6758	5.7081	0.33044
7.1	6.7258	5.343	0.29239
7.1	6.7757	4.0363	0.25275
7.1	6.8259	3.7731	0.19639
7.1	6.8763	2.7527	0.16314
7.1	6.9259	2.2221	0.14118
7.1	6.977	1.4359	0.11067
7.1	7.0251	0.88529	0.096993
7.1	7.0724	0.79646	0.12478
7.1	7.1234	0.83793	0.18512
7.1	7.165	0.66601	0.39044
7.4	6.4246	16.297	1.914
7.4	6.4754	15.416	1.6595
7.4	6.5274	13.96	1.1337
7.4	6.5764	12.442	0.9208
7.4	6.6249	10.716	0.59812
7.4	6.6753	10.479	0.5432
7.4	6.7253	9.8827	0.4716
7.4	6.7764	7.4027	0.35944
7.4	6.8256	6.5754	0.28496
7.4	6.8758	5.855	0.24042
7.4	6.9257	4.7009	0.21587
7.4	6.9754	3.9244	0.17447
7.4	7.0263	3.3438	0.16854
7.4	7.0749	2.631	0.16683
7.4	7.1246	1.9282	0.17534
7.4	7.1724	1.5848	0.23256
7.8	6.4272	18.187	2.3511
7.8	6.4775	16.337	2.488
7.8	6.5277	14.253	2.0475
7.8	6.576	12.958	1.1773
7.8	6.6252	11.401	1.0681
7.8	6.676	10.776	0.70226

Continued on next page

Table F.6 – *Continued from previous page*

Extracellular pH	Intracellular pH	Flux (mM/min)	Standard error
7.8	6.7266	9.8738	0.63934
7.8	6.7752	8.9278	0.45125
7.8	6.8246	6.5126	0.33924
7.8	6.8766	6.0059	0.31918
7.8	6.9262	4.3209	0.30173
7.8	6.9757	3.3604	0.24253
7.8	7.0272	2.1849	0.20782
7.8	7.0758	1.3865	0.16462
7.8	7.1238	1.0976	0.16012
7.8	7.1703	1.242	0.23277

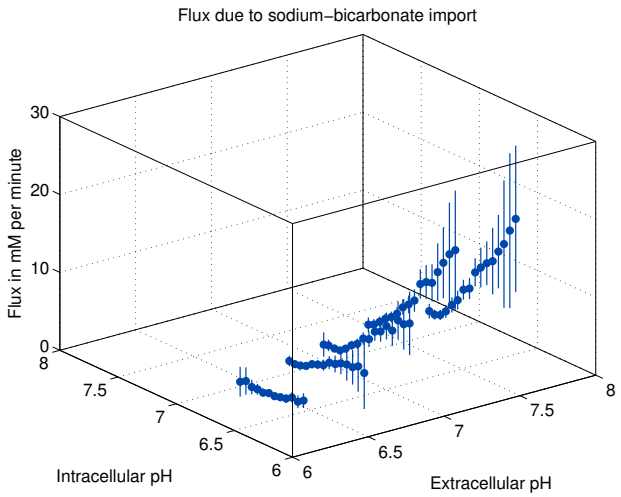

Figure F.3: Data for Na^+/HCO_3^- import. Plot of the data in Table F.6, with errorbars showing standard deviations (standard errors multiplied by the square root of the number of measurements for each level of extracellular pH).

Appendix G

Biochemistry

G.1 pH calculations

Denoting free protons by H^+ and molar concentration by square brackets, pH is defined as

$$\mathrm{pH} = -\log_{10}[\mathrm{H}^+], \tag{G.1}$$

with $[H^+]$ in M (moles/litre).

The Henderson-Hasselbalch equation relates the pH of a weak acid in solution to the concentrations of the protonated and unprotonated forms (Henderson 1908). For a given weak acid A, letting [HA] denote its concentration in protonated form, $[A^-]$ the concentration of the conjugate base, and pK_a the negative log of the acid dissociation constant (that is, of the equilibrium constant of the acid-base reaction), the Henderson-Hasselbalch equation is:

$$\mathrm{pH} = pK_a + \log_{10}\left(\frac{[\mathrm{A}^-]}{[\mathrm{HA}]}\right). \tag{G.2}$$

G.2 The bicarbonate buffering reaction

Letting CO_2 denote carbon dioxide, H_2O water, H_2CO_3 carbonic acid, HCO_3^- a bicarbonate ion, and H^+ a free proton, the full scheme for the bicarbonate buffering reaction is:

$$\mathrm{CO_2} + \mathrm{H_2O} \underset{k_2}{\overset{k_1}{\rightleftharpoons}} \mathrm{H_2CO_3} \underset{k_4}{\overset{k_3}{\rightleftharpoons}} \mathrm{H^+} + \mathrm{HCO_3^-}. \tag{G.3}$$

First examining the left-hand side,

$$\mathrm{CO_2} + \mathrm{H_2O} \underset{k_2}{\overset{k_1}{\rightleftharpoons}} \mathrm{H_2CO_3}, \tag{G.4}$$

it is generally the case that H_2O is in sufficient bulk that its concentration is negligibly affected by this reaction, and thus conventional notation incorporates the constant concentration of H_2O into the reaction rate k_1. The reaction in Equation (G.4) proceeds slowly in solution, but is greatly accelerated by the presence of carbonic anhydrase enzymes. At equilibrium, by the law of mass action we have

$$\frac{[H_2CO_3]}{[CO_2]} = \frac{k_1}{k_2} = K_a^{\text{left}}, \tag{G.5}$$

where $K_a^{\text{left}} \approx 0.0013$ (Hainsworth 1986). Thus, relatively little carbonic acid (H_2CO_3) is present in solution.

Next examining the right-hand side of Equation (G.3),

$$H_2CO_3 \underset{k_4}{\overset{k_3}{\rightleftharpoons}} H^+ + HCO_3^-, \tag{G.6}$$

we have by the law of mass action that

$$\frac{[H^+][HCO_3^-]}{[H_2CO_3]} = \frac{k_3}{k_4} = K_a^{\text{right}}. \tag{G.7}$$

At a healthy physiological pH of 7.4, we have $K_a^{\text{right}} \approx 10^{-3.2}$ (Hainsworth 1986). Rearranging the above equation, we find that

$$\frac{[HCO_3^-]}{[H_2CO_3]} = \frac{K_a^{\text{right}}}{[H^+]} \approx 15850, \tag{G.8}$$

and thus carbonic acid is almost entirely dissociated at physiological pH.

Eliminating carbonic acid from Equations (G.4) and (G.6) and introducing k_f and k_r to denote the apparent forward and reverse rate constants, respectively, we obtain

$$CO_2 + H_2O \underset{k_r}{\overset{k_f}{\rightleftharpoons}} H^+ + HCO_3^- \text{ and} \tag{G.9}$$

$$\frac{[H^+][HCO_3^-]}{[CO_2]} = K_a^{\text{L}} K_a^{\text{R}} = K_a^{\text{A}}, \tag{G.10}$$

where K_a^A is the apparent buffer equilibrium constant. The apparent pK_a of the bicarbonate buffer in human blood is 6.1 (Hainsworth 1986), and hence $K_a^{\text{A}} = 10^{-6.1}$ M. We take an estimate of $k_f = 8.4$ per minute from Leem and Vaughan-Jones (1998) and apply the formula $k_f = k_r K_a^{\text{A}}$ to find $k_r = 1.11 \cdot 10^4$ per mM per minute. These (apparent) forward and reverse reaction rates are used in Chapter 5 and 6.

G.3 Buffering capacity

A buffer solution retains an almost constant pH when a small amount of acid or base is added. The quantitative measure of this resistance to pH changes is the buffering capacity or power of the solution (Hulanicki 1987).

The buffering capacity, β, is defined as the quantity of strong acid or base that would need to be added to one litre of the buffer solution to change its pH by one unit:

$$\beta = \frac{\mathrm{d}n}{\mathrm{dpH}}, \tag{G.11}$$

where n is the number of chemical equivalents of added strong acid or base. In turn, a chemical equivalent is a measure of the reactive capacity of a given molecule; hence, n is effectively the number of moles of a (highly reactive) strong acid or base.

Let us assume that the volume of a given buffer solution is 1L, such that we can treat concentration and number of moles interchangeably. The total molar concentration of the buffer species, here denoted S, is given by

$$S = [\mathrm{HA}] + [\mathrm{A}^-], \tag{G.12}$$

where $[\mathrm{HA}]$ and $[\mathrm{A}^-]$ represent the molar concentrations of the protonated and unprotonated forms, respectively, of the buffer species in the chemical reaction

$$\mathrm{HA} \rightleftharpoons \mathrm{A}^- + \mathrm{H}^+. \tag{G.13}$$

From the definition of the acid dissociation constant K_a (Hainsworth 1986), which is

$$K_a = \frac{[\mathrm{H}^+][\mathrm{A}^-]}{[\mathrm{HA}]}, \tag{G.14}$$

we have that

$$[\mathrm{HA}] = \frac{[\mathrm{H}^+][\mathrm{A}^-]}{K_a} \tag{G.15}$$

and hence

$$S = \frac{[\mathrm{H}^+][\mathrm{A}^-]}{K_a} + [\mathrm{A}^-]. \tag{G.16}$$

With our assumption of 1L of solution, $[\mathrm{A}^-]$ is equal to the number of (equivalent) moles of strong base that is added to the system, such that

$$n = \frac{K_a S}{K_a + [\mathrm{H}^+]}. \tag{G.17}$$

Now we can calculate the derivative via an application of the chain rule:

$$\begin{aligned}\beta &= \frac{\mathrm{d}n}{\mathrm{dpH}} \\ &= \frac{\mathrm{d}n}{\mathrm{d}[\mathrm{H}^+]}\frac{\mathrm{d}[\mathrm{H}^+]}{\mathrm{dpH}} \\ &= -\frac{K_a S}{(K_a + [\mathrm{H}^+])^2}(-\ln(10)[\mathrm{H}^+]) \\ &= \frac{\ln(10) K_a S [\mathrm{H}^+]}{(K_a + [\mathrm{H}^+])^2}. \end{aligned} \tag{G.18}$$

Note that buffer capacity is proportional to the concentration of the buffering species, i.e. dilute concentrations have little buffering capacity.

Further, note that we have not considered the role of self-ionisation of water, which is to provide buffering in the absence of any classic buffering species, as this only becomes an important factor at extremely non-physiological pH values of close to 1 and close to 13.

References

JA Adam. Mathematical models of perivascular spheroid development and catastrophe-theoretic description of rapid metastatic growth/tumour remission. *Invasion and Metastasis*, 16:247–267, 1996.

R Airley, J Loncaster, S Davidson, M Bromley, S Roberts, A Patterson, R Hunter, I Stratford, and C West. Glucose transporter Glut-1 expression correlates with tumour hypoxia and predicts metastasis-free survival in advanced carcinoma of the cervix. *Clinical Cancer Research*, 7:928–934, 2001.

AC Aisenberg. *The Glycolysis and Respiration of Tumours (Cancer Commission of Harvard University)*. New York Academic Press, 1961.

M Al-Husari and SD Webb. Regulation of tumour intracellular pH: A mathematical model examining the interplay between H+ and lactate. *Journal of Theoretical Biology*, 322: 58–71, 2013a.

M Al-Husari and SD Webb. Theoretical predictions of lactate and hydrogen ion distributions in tumours. *PLOS One*, 8:e72020, 2013b.

M Al-Husari, C Murdoch, and SD Webb. A cellular automaton model examining the effects of oxygen, hydrogen ions and lactate on early tumour growth. *Journal of Mathematical Biology*, 67:1–35, 2013.

T Alarcon, HM Byrne, and PK Maini. Towards whole-organ modelling of tumour growth. *Progress in Biophysics and Molecular Biology*, 85:451–472, 2004.

KO Alfarouk, AK Muddathir, and MEA Shayoub. Tumour acidity as evolutionary spite. *Cancers*, 3:408–414, 2011.

ARA Anderson, MAJ Chaplain, EL Newman, RJC Steele, and AM Thompson. Mathematical modelling of tumour invasion and metastasis. *Journal of Theoretical Medicine*, 2:192–154, 2000.

ARA Anderson, AM Weaver, PT Cummings, and V Quaranta. Tumour morphology and phenotypic evolution driven by selective pressure from the microenvironment. *Cell*, 127: 905–915, 2006.

RP Araujo and DLS McElwain. A history of the study of solid tumour growth: the contribution of mathematical modelling. *Bulletin of Mathematical Biology*, 66:1039–1091, 2004.

M Archetti. Evolutionary dynamics of the Warburg effect: glycolysis as a collective action problem among cancer cells. *Journal of Theoretical Biology*, 341:1–8, 2014.

NJ Armstrong, KJ Painter, and JA Sherratt. A continuum approach to modelling cell-cell adhesion. *Journal of Theoretical Biology*, 243:98–113, 2006.

BH Arve and AI Liapis. Oxygen tension in tumours predicted by diffusion with absorption model involving a moving free boundary. *Mathematical and Computational Modelling*, 10:159–174, 1988.

A Aubert, L Pellerin, PJ Magistretti, and R Costalat. A coherent neurobiological framework for functional neuroimaging provided by a model integrating compartmentalised energy metabolism. *Proceedings of the National Academy of Sciences USA*, 104:4188–4193, 2007.

M Bai and DJ Bornhop. Recent advances in receptor-targeted fluorescent probes for in vivo cancer imaging. *Current Medicinal Chemistry*, 19:4742–4758, 2012.

D Basanta, B Ribba, E Watkin, B You, and A Deutsch. Computational analysis of the influence of microenvironment on carcinogenesis. *Mathematical Biosciences*, 229:22–29, 2011.

M Bélanger, I Allaman, and PJ Magistretti. Brain energy metabolism: focus on astrocyte-neuron metabolic cooperation. *Cell Metabolism*, 14:724–738, 2011.

N Bellomo and M Delitala. From the mathematical kinetic and stochastic game theory to modelling mutations, onset, progression and immune competition of cancer cells. *Physics of Life Reviews*, 5:183–206, 2008.

N Bellomo, NK Li, and PK Maini. On the foundations of cancer modelling: selected topics, speculations, and perspectives. *Mathematical Models and Methods in Applied Sciences*, 18:593–646, 2008.

CM Bender and SA Orszag. *Advanced Mathematical Methods for Scientists and Engineers I: Asymptotic Methods and Perturbation Theory*. Springer-Verlag New York, 1999.

JM Berg, JL Tymoczko, and L Stryer. *Biochemistry*. WH Freeman and Co, 2002.

E Berra, E Benizri, A Ginouvés, V Volmat, D Roux, and J Pouysségur. HIF prolyl-hydroxylase 2 is the key oxygen sensor setting low steady-state levels of HIF-1a in normoxia. *The EMBO Journal*, 22:4082–4090, 2003.

A Bertuzzi, A Fasano, A Gandolfi, and C Sinisgalli. ATP production and necrosis formation in a tumour spheroid model. *Mathematical Models of Natural Phenomena*, 2:30–46, 2007.

A Bertuzzi, A Fasano, A Gandolfi, and C Sinisgalli. Necrotic core in EMT6/Ro tumour spheroids: Is it caused by an ATP deficit? *Journal of Theoretical Biology*, 262:142–150, 2010.

L Bianchini and A Fasano. A model combining acid-mediated tumour invasion and nutrient dynamics. *Nonlinear Analysis: Real World Applications*, 10:1955–1975, 2009.

JJ Blum. Concentration profiles in and around capillaries. *American Journal of Physics*, 198:991, 1960.

WF Boron. Regulation of intracellular pH. *Advances in Physiology Education*, 28:160–179, 2004.

K Boubaker, M Flepp, P Sudre, H Furrer, A Haensel, B Hirschel, K Boggian, JP Chave, E Bernasconi, M Egger, M Opravil, M Rickenbach, P Francioli, and A Telenti. Hyperlactatemia and antiretroviral therapy: the Swiss HIV cohort study. *Clinical Infectious Diseases*, 33:1931–1937, 2001.

F Boumezbeur, KF Peterson, GW Cline, GF Mason, KL Behar, GI Shulman, and DL Rothman. The contribution of blood lactate to brain energy metabolims in humans measured by dynamic 13C nuclear magnetic resonance spectroscopy. *The Journal of Neuroscience*, 30:13983–13991, 2010.

AK Bouzier-Sore, P Canioni, and M Merle. Effect of exogenous lactate on rat glioma metabolism. *Journal of Neuroscience Research*, 65:543–548, 2001.

R Breiman. Random Forests. *Machine Learning*, 45:5–32, 2001.

P Burgman, JA O'Donoghue, JL Humm, and CC Ling. Hypoxia-induced increase in FDG uptake in MCF7 cells. *Journal of Nuclear Medicine*, 42:170–175, 2001.

AC Burton. Rate of growth of solid tumours as a problem of diffusion. *Growth*, 30:157–176, 1966.

M Busk, S Walenta, W Mueller-Klieser, T Steiniche, S Jakobsen, MR Horsman, and J Overgaard. Inhibition of tumour lactate oxidation: consequences of the tumour microenvironment. *Radiotherapy and Oncology*, 99:404–411, 2011.

HM Byrne. A weakly nonlinear analysis of a model of avascular solid tumour growth. *Journal of Mathematical Biology*, 39:59–89, 1999.

HM Byrne. Dissecting cancer through mathematics: from the cell to the animal model. *Nature Reviews Cancer*, 10:221–230, 2010.

HM Byrne and MAJ Chaplain. Modelling the role of cell-cell adhesion in the growth and development of carcinomas. *Mathematical Computation and Modelling*, 24:1–17, 1996.

HM Byrne and SA Gourley. The role of growth factors in avascular tumour growth. *Mathematical and Computer Modelling*, 26:35–55, 1997.

HM Byrne and L Preziosi. Modelling solid tumour growth using the theory of mixtures. *Mathematical Medicine and Biology*, 20:341–366, 2003.

HM Byrne, JR King, DLS McElwain, and L Preziosi. A two-phase model of solid tumour growth. *Applied Mathematics Letters*, 16:567–573, 2003.

HM Byrne, T Alarcon, MR Owen, SD Webb, and PK Maini. Modelling aspects of cancer dynamics: a review. *Philosophical Transactions of the Royal Society A*, 364:1563–1578, 2006.

R Cairns, I Harris, and T Mak. Regulation of cancer cell metabolism. *Nature Reviews Cancer*, 11:85–95, 2011.

RA Cardone, V Casavola, and SJ Reshkin. The role of disturbed pH dynamics and the Na+/H+ exchanger in metastasis. *Nature Reviews Cancer*, 5:786–795, 2005.

J Cariboni, D Gatelli, R Liska, and A Saltelli. The role of sensitivity analysis in ecological modelling. *Ecological Modelling*, 203:2007, 2007.

J Carlsson and H Acker. Relations between pH, oxygen partial pressure and growth in cultured cell spheroids. *International Journal of Cancer*, 42:715–720, 1988.

JJ Casciari, SV Sotirchos, and RM Sutherland. Variations in tumour cell growth rates and metabolism with oxygen concentration, glucose concentration, and extracellular pH. *Journal of Cellular Physiology*, 151:386–394, 1992.

JR Casey, S Grinstein, and J Orlowski. Sensors and regulators of intracellular pH. *Nature Reviews Molecular Cell Biology*, 11:50–61, 2010.

JC Chambard and J Pouyssegur. Intracellular pH controls growth factor-induced ribosomal protein S6 phosphorylation and protein synthesis in the G0-G1 transition of fibroblasts. *Experimental Cell Research*, 164:282–294, 1986.

KW Chang, S Laconi, KA Mangold, S Hubchak, and DG Scarpelli. Multiple genetic alterations in hamster pancreatic ductal adenocarcinomas. *Cancer Research*, 55:2560–2568, 1995.

MAJ Chaplain. Avascular growth, angiogenesis and vascular growth in solid tumours: the mathematical modelling of the stages of tumour development. *Mathematical and Computer Modelling*, 23:47–87, 1996.

MAJ Chaplain, DL Benson, and PK Maini. Nonlinear diffusion of a growth inhibitory factor in multicell spheroids. *Mathematical Biosciences*, 121:1–13, 1994.

MAJ Chaplain, M Ganesh, and IG Graham. Spatio-temporal pattern formation on spherical surfaces: numerical simulation and application to solid tumour growth. *Journal of Mathematical Biology*, 42:387–423, 2001.

S Cheeti, BK Warrier, and CH Lee. The role of monocarboxylate transporters in uptake of lactic acid in HeLa cells. *International Journal of Pharmaceutics*, 325:48–54, 2006.

CY Chen, HM Byrne, and JR King. The influence of growth-induced stress from the surrounding medium on the development of multicell spheroids. *Journal of Mathematical Biology*, 43:191–220, 2001.

J Chiche, K Ilc, MC Brahimi-Horn, and J Pouyssegur. Membrane-bound carbonic anhydrases are key pH regulators controlling tumour growth and cell migration. *Advances in Enzyme Regulation*, 50:20–33, 2010.

A Christoforides, JD Carpten, GJ Weiss, MJ Demeure, DD vonHoff, and DW Craig. Identification of somatic mutations in cancer through Bayesian-based analysis of sequenced genome pairs. *BMC Genomics*, 14:302–313, 2013.

S Chung, R Sudo, PJ Mack, CR Wan, V Vickerman, and RD Kamm. Cell migration into scaffolds under co-culture conditions in a microfluidic platform. *Lab on a Chip*, 9:269–275, 2009.

R Clarke, RB Dickson, and N Bruenner. The process of malignant progression in human breast cancer. *Annals of Oncology*, 1:401–407, 1990.

M Clautier, FB Bolger, JP Lowry, and P Wellstead. An integrative dynamic model of brain energy metabolism using in vivo neurochemical measurements. *Journal of Computational Neuroscience*, 27:391–414, 2009.

CB Colen, Y Shen, F Ghoddoussi, P Yu, TB Francis, BJ Koch, MD Monterey, MP Galloway, AE Sloan, and SP Mathupala. Metabolic targeting of lactate efflux by malignant glioma inhibits invasiveness and induces necrosis: an in vivo study. *Neoplasia*, 13:620–632, 2011.

V Cristini, J Lowengrub, and Q Nie. Nonlinear simulation of tumour growth. *Journal of Mathematical Biology*, 46:191–224, 2003.

RD Cutler, TC Edwards, KH Beard, A Cutler, KT Hess, J Gibson, and JJ Lawler. Random forests for classification in ecology. *Ecology*, 88:2783–2792, 2007.

A Daşu, I Tuma-Daşu, and M Karlsson. Theoretical simulation of tumour oxygenation and results from acute and chronic hypoxia. *Physics in Medicine and Biology*, 48:2829–2842, 2003.

PD Dale, JA Sherratt, and PK Maini. Mathematical modelling of corneal epithelial wound healing. *Mathematical Biosciences*, 124:127–147, 1994.

T Das and S Chakraborty. Perspective: flicking with flow: can microfluidics revolutionise the cancer research? *Biomicrofluidics*, 7:1–20, 2013.

G De'ath and KE Fabricius. Classification and regression trees: a powerful yet simple technique for ecological data analysis. *Ecology*, 81:3178–3192, 2000.

RJ DeBerardinis and CB Thompson. Cellular metabolism and disease: what do metabolic outliers teach us? *Cell*, 148:1132–1144, 2012.

RJ DeBerardinis, JJ Lum, G Hatzivassiliou, and CB Thompson. The biology of cancer: metabolic reprogramming fuels cell growth and proliferation. *Cell Metabolism*, 7:11–20, 2008.

K Degenhardt, R Mathew, B Beaudoin, K Bray, D Anderson, G Chen, C Mukherjee, Y Shi, C Gélinas, Y Fan, DA Nelson, S Jin, and E White. Autophagy promotes tumour cell survival and restricts necrosis, inflammation, and tumourigenesis. *Cancer Cell*, 10:51–64, 2006.

FL Degner and RM Sutherland. Mathematical modelling of oxygen supply and oxygenation in tumour tissues: prognostic, therapeutic and experimental implications. *International Journal of Radiation Oncology and Biological Physics*, 15:391–397, 1988.

M DiNuzzo, S Mangia, B Maraviglia, and F Giove. Changes in glucose uptake rather than lactate shuttle take centre stage in subserving neuroenergetics: evidence from mathematical modelling. *Journal of Cerebral Blood Flow and Metabolism*, 30:586–602, 2010.

A d'Onofrio and IPM Tomlinson. A nonlinear mathematical model of cell turnover, differentiation, and tumourigenesis in the intestinal crypt. *Journal of Theoretical Biology*, 244: 267–374, 2007.

L Dubois, S Peeters, NG Lieuwes, N Geusens, A Thiry, S Wigfield, F Carta, A Mcintyre, A Scozzafava, JM Dogne, CT Supuran, AL Harris, B Masereel, and P Lambin. Specific inhibition of carbonic anhydrase IX activity enhances the in vivo therapeutic effect of tumour irradiation. *Radiotherapy and Oncology*, 99:424–431, 2011.

HF Dvorak, DR Senger, and AM Dvorak. Fibrin as a component of the tumour stroma: origins and biological significance. *Cancer and Metastasis Reviews*, 2:41–73, 1983.

RL Elstrom, DE Bauer, M Buzzai, R Karnauskas, MH Harris, DR Plas, H Zhuang, RM Cinalli, A Alavi, CM Rudin, and CB Thompson. Akt stimulates aerobic glycolysis in cancer cells. *Cancer Research*, 64:3892–3899, 2004.

V Estrella, T Chen, M Lloyd, J Wojtkowiak, HH Cornnell, A Ibrahim-Hashim, K Bailey, Y Balagurunathan, JM Rothberg, BF Sloane, J Johnson, RA Gatenby, and RJ Gillies. Acidity generated by the tumour microenvironment drives local invasion. *Cancer Research*, 73:1524–1535, 2013.

VR Fantin, J St-Pierre, and P Leder. Attenuation of LDH-A expression uncovers a link between glycolysis, mitochondrial physiology, and tumour maintenance. *Cancer Cell*, 9: 425–434, 2006.

A Fasano, MA Herrero, and MR Rodrigo. Slow and fast invasion waves in a model of acid-mediated tumour growth. *Mathematical Biosciences*, 220:45–56, 2009.

O Feron. Pyruvate into lactate and back: from the Warburg effect to symbiotic energy fuel exchange in cancer cells. *Radiotherapy and Oncology*, 92:329–333, 2009.

LM Ferreira. Cancer metabolism: the Warburg effect today. *Experimental Molecular Pathology*, 89:372–380, 2010.

IJ Fidler and IR Hart. Biological diversity in metastatic neoplasms: origins and implications. *Science*, 217:998–1003, 1982.

J Fieberg and KJ Jenkins. Assessing uncertainty in ecological systems using global sensitivity analyses: a case example of simulated wolf reintroduction effects on elk. *Ecological Modelling*, 187:259–280, 2005.

CR Figley. Lactate transport and metabolism in the human brain: implications for the astrocyte-neuron lactate shuttle hypothesis. *The Journal of Neuroscience*, 31:4768–4770, 2011.

RA Fisher. The wave of advance of adventageous genes. *Annals of Eugenics*, 7:353–369, 1937.

JV Frangioni. New technologies for human cancer imaging. *Journal of Clinical Oncology*, 26:4012–4021, 2008.

HB Frieboes, X Zheng, CH Sun, B Tromberg, R Gatenby, and V Cristini. An integrated computational/experimental model of tumour invasion. *Cancer Research*, 66:1597–1604, 2006.

A Friedman. Mathematical analysis and challenges arising from models of tumour growth. *Mathematical Models and Methods in Applied Sciences*, 17:1751–1772, 2007.

RA Gatenby. Population ecology issues in tumour growth. *Cancer Research*, 51:2542–2547, 1991.

RA Gatenby and ET Gawlinski. A reaction-diffusion model of cancer invasion. *Cancer Research*, 56:5745–5753, 1996.

RA Gatenby and RJ Gillies. Why do cancers have high aerobic glycolysis? *Nature Reviews Cancer*, 4:891–899, 2004.

RA Gatenby and PK Maini. Mathematical oncology: cancer summed up. *Nature*, 421:321, 2003.

RA Gatenby and TL Vincent. Application of quantitative models from population biology and evolutionary game theory to tumour therapeutic strategies. *Molecular Cancer Therapeutics*, 2:919–927, 2003.

RA Gatenby, TL Vincent, and RJ Gillies. Evolutionary dynamics in carcinogenesis. *Mathematical Models and Methods in Applied Sciences*, 15:1619–1638, 2005.

RA Gatenby, K Smallbone, PK Maini, F Rose, J Averill, RB Nagle, L Worrall, and RJ Gillies. Cellular adaptations to hypoxia and acidosis during somatic evolution of breast cancer. *British Journal of Cancer*, 97:646–653, 2007.

RA Gatenby, AS Silva, RJ Gillies, and BR Frieden. Adaptive therapy. *Cancer Research*, 69:4894–4903, 2009.

M Gerlinger, AJ Rowan, S Horswell, J Larkin, D Endesfelder, E Gronroos, P Martinez, N Matthews, A Stewart, P Tarpey, I Varela, B Phillimore, S Begum, NQ McDonald, A Butler, D Jones, K Raine, C Latimer, CR Santos, M Nohadani, AC Eklund, B Spencer-Dene, G Clark, L Pickering, G Stamp, M Gore, Z Szallasi, J Downward, PA Futreal, and C Swanton. Intratumour heterogeneity and branched evolution revealed by multiregion sequencing. *New England Journal of Medicine*, 366:883–892, 2012.

RJ Gillies and RA Gatenby. Hypoxia and adaptive landscapes in the evolution of carcinogenesis. *Cancer and Metastasis Reviews*, 26:311–317, 2007.

RJ Gillies, D Verduzco, and RA Gatenby. Evolutionary dynamics of cancer and why targeted therapy does not work. *Nature Reviews Cancer*, 12:487–493, 2012.

N Gillings. Radiotracers for positron emission tomography imaging. *MAGMA*, 26:149–158, 2013.

LB Gladden. Lactate metabolism: a new paradigm for the third millenium. *The Journal of Physiology*, 558:5–30, 2004.

ME Glickman and DA van Dyk. *Topics in Biostatistics*. Springer: Methods in Molecular Biology series, 2007.

JM Grange, JL Stanford, and CA Stanford. Campbell de Morgan's 'Observations on cancer', and their relevance today. *Journal of the Royal Society of Medicine*, 95:296–299, 2002.

HP Greenspan. Models for the growth of a solid tumour by diffusion. *Sudies in Applied Mathematics*, 52:317–340, 1972.

HP Greenspan. On the growth and stability of cell cultures and solid tumours. *Journal of Theoretical Biology*, 56:229–242, 1976.

U Grossmann. Profiles of oxygen partial pressure and oxygen consumption inside multicellular spheroids. *Recent Results in Cancer Research*, 95:150–159, 1984.

U Haberkorn, SI Ziegler, F Oberdorfer, H Trojan, D Haag, P Peschke, MR Berger, A Altmann, and G Van-Kaick. FDG uptake, tumour proliferation and expression of glycolysis associated genes in animal tumour models. *Nuclear Medicine and Biology*, 21:827–834, 1994.

R Hainsworth. *Acid-Base Balance*. Manchester University Press, 1986.

SI Hajdu, MJ Thun, LM Hannan, and A Jemal. A note from history: landmarks in the history of cancer, part 1. *Cancer*, 117:1097–1102, 2011.

D Hanahan and RA Weinberg. The hallmarks of cancer. *Cell*, 100:57–70, 2000.

D Hanahan and RA Weinberg. Hallmarks of cancer: the next generation. *Cell*, 144:646–674, 2011.

T Hastie, R Tibshirani, and J Friedman. *The Elements of Statistical Learning: Data Mining, Inference, and Prediction*. Springer Series in Statistics, 2009.

H Hatzikirou, A Deutsch, C Schaller, M Simon, and K Swanson. Mathematical modelling of glioblastoma tumour development: a review. *Mathematical Models and Methods in Applied Sciences*, 15:1779–1794, 2005.

TW Hein, W Xu, and L Kuo. Dilation of retinal arteriols in response to lactate: role of nitric oxide, guanylyl cyclase, and ATP-sensitive potassium channels. *Investigative Ophthalmology and Visual Science*, 47:693–699, 2006.

LJ Henderson. Concerning the relationship between the strength of acids and their capacity to preserve neutrality. *American Journal of Physiology*, 21:173–179, 1908.

K Herholz, W Heindel, PR Luyten, JA denHollander, U Pietrzyk, J Voges, H Kugel, G Friedmann, and WD Heiss. In vivo imaging of glucose consumption and lactate concentration in human gliomas. *Annals of Neurology*, 31:319–327, 1992.

AB Holder, MR Rodrigo, and MA Herrero. A model for acid-mediated tumour growth with nonlinear acid production term. *Applied Mathematics and Computation*, 15:176–198, 2014.

MH Holmes. *Introduction to Perturbation Methods*. Springer Science+Business Media New York, 2013.

T Homma and A Saltelli. Importance measures in global sensitivity analysis of nonlinear models. *Reliabiliy Engineering and System Safety*, 52:1–17, 1996.

AY Hsiao, Y Torisawa, YC Tung, S Sud, RS Taichman, KJ Pienta, and S Takayama. Microfluidic system for formation of PC-3 prostate cancer co-culture spheroids. *Biomaterials*, 30:3020–3027, 2009.

Y Huang, B Agrawal, D Sun, JS Kuo, and JC Williams. Microfluidics-based devices: new tools for studying cancer and cancer stem cell migration. *Biomicrofluidics*, 5:1–17, 2011.

WE Huckabee. Abnormal resting blood lactate: the significance of hyperlactatemia in hospitalized patients. *The American Journal of Medicine*, 30:833–839, 1961.

A Hulanicki. *Reactions of Acids and Bases in Analytical Chemistry*. Halstead Press, 1987.

A Hulikova, RD Vaughan-Jones, and P Swietach. Dual role of CO2/HCO3- buffer in the regulation of intracellular pH of three-dimensional tumour growths. *Journal of Biological Chemistry*, 286:13815–13826, 2011.

A Hulikova, AL Harris, RD Vaughan-Jones, and P Swietach. Regulation of intracellular pH in cancer cell lines under normoxia and hypoxia. *Journal of Cellular Physiology*, 228: 743–752, 2013.

DA Hume and MJ Weidemann. Role and regulation of glucose metabolism in proliferating cells. *Journal of the National Cancer Institute*, 62:3–8, 1979.

Y Ido, K Chang, and JR Williamson. NADH augments blood flow in physiologically activated retina and visual cortex. *Proceedings of the National Academy of Sciences USA*, 101:653–658, 2003.

D Irimia and M Toner. Spontaneous migration of cancer cells under conditions of mechanical confinement. *Integrative Biology*, 1:489–556, 2009.

BA Jabour, Y Choi, CK Hoh, SD Rege, JC Soong, RB Lufkin, WN Hanafee, J Maddahi, L Chaiken, and J Bailet. Extracranial head and neck: PET imaging with 2-F18-fluoro-2-deoxy-D-glucose and MR imaging correlation. *Radiology*, 186:27–35, 1993.

TL Jackson and HM Byrne. A mechanical model of tumour encapsulation and transcapsular spread. *Mathematical Biosciences*, 180:307–328, 2002.

BW Jakoby, Y Bercier, M Conti, ME Casey, B Bendriem, and DW Townsend. Physical and clinical performance of the mCT time-of-flight PET/CT scanner. *Physical Medicine and Biology*, 56:2375–2389, 2011.

FC James and CE McCulloch. Multivariate analysis in ecology and systematics: panacea or Pandora's box? *Annual Review of Ecology and Systematics*, 21:129–166, 1990.

T Jean, C Frelin, P Vigne, P Barbry, and M Lazdunski. Biochemical properties of the Na+/H+ exchange system in rat brain synaptosomes: interdependence of internal and external pH control of the exchange activity. *Journal of Biological Chemistry*, 260:9678–9684, 1985.

Y Jiang, J Pjesivac-Grbovic, C Cantrell, and JP Freyer. A multiscale model for avascular tumour growth. *Biophysical Journal*, 89:3884–3894, 2005.

R Jolivet, I Allaman, L Pellerin, PJ Magistretti, and B Weber. Comment on recent modelling studies of astrocyte-neuron metabolic interactions. *Journal of Cerebral Blood Flow and Metabolism*, 30:1982–1986, 2010.

AF Jones, HM Byrne, JS Gibson, and JW Dold. A mathematical model of the stress induced during avascular tumour growth. *Journal of Mathematical Biology*, 40:473–499, 2000.

F Kallinowski, P Vaupel, S Runkel, G Berg, HP Fortmeyer, KH Baessler, K Wagner, W Mueller-Klieser, and S Walenta. Glucose uptake, lactate release, ketone body turnover, metabolic micromilieu, and pH distributions in human breast cancer xenografts in nude rats. *Cancer Research*, 48:7264–7272, 1988.

KM Kennedy and MW Dewhirst. Tumour metabolism of lactate: the influence and therapeutic potential for MCT and CD147 regulation. *Future Oncology*, 6:127–159, 2010.

SK Kershaw, HM Byrne, DJ Gavaghan, and JM Osborne. Colorectal cancer through simulation and experiment. *IET Systems Biology*, 7:57–73, 2013.

AR Kherlopian, T Song, Q Duan, MA Neimark, MJ Po, JK Gohagan, and AF Laine. A review of imaging techniques for systems biology. *BMC Systems Biology*, 2:74, 2008.

F Kirchhoff, R Dringen, and C Giaume. Pathways of neuron-astrocyte interactions and their possible role in neuroprotection. *European Archives of Psychiatry and Clinical Neuroscience*, 251:159–169, 2001.

JP Kirkpatrick, DM Brizel, and MW Dewhirst. A mathematical model of tumour oxygen and glucose mass transport and metabolism with complex reaction kinetics. *Radiation Research*, 159:336–344, 2003.

AN Kolmogorov, IG Petrovsky, and NS Piskunov. An investigation of the diffusion equation combined with an increase in mass and its application to a biological problem. *Moscow University Bulletin of Mathematics*, 1:1–25, 1937.

N Komarova. Spatial stochastic models for cancer initiation and progression. *Bulletin of Mathematical Biology*, 17:1573–1599, 2006.

N Komarova. Stochastic modelling of loss- and gain-of-function mutation in cancer. *Mathematical Models and Medicine in Applied Sciences*, 17:1647–1674, 2007.

N Komarova, A Sengupta, and MA Nowak. Mutation-selection networks of cancer initiation: tumour suppressor genes and chromosomal instability. *Journal of Theoretical Biology*, 223:433–450, 2003.

WH Koppenol, PL Bounds, and CV Dang. Otto Warburg's contributions to current concepts of cancer metabolism. *Nature Reviews Cancer*, 11:325–337, 2011.

H Krebs. Otto Heinrich Warburg, 1883-1970. *Biographical Memoirs of Fellows of the Royal Society*, 18:628–699, 1972.

G Kroemer and J Pouyssegur. tumour cell metabolism: cancer's Achilles' heel. *Cancer Cell*, 13:472–482, 2008.

LA Kunz-Schughart, J Doetsch, W Mueller-Klieser, and K Groebe. Proliferative activity and tumourigenic conversion: impact on cellular metabolism in 3D culture. *American Journal of Physiology*, 278:765–780, 2000.

H Land, LF Parada, and RA Weinberg. Tumourigenic conversion of primary embryo fibroblasts requires at least two cooperating oncogenes. *Nature*, 304:596–602, 1983.

D Lay. *Linear Algebra and Its Applications*. Addison-Wesley New York, 2000.

CH Leem and RD Vaughan-Jones. Out-of-equilibrium pH transients in the guinea-pig ventricular myocyte. *Journal of Physiology*, 509:471–485, 1998.

CH Leem, D Lagadic-Gossmann, and RD Vaughan-Jones. Characterization of intracellular pH regulation in the guinea-pig ventricular myocyte. *Journal of Physiology*, 517:159–180, 1999.

R LeVeque. *Finite Difference Methods for Ordinary and Partial Differential Equations: Steady-State and Time-Dependent Problems (Classics in Applied Mathematics)*. Society for Industrial and Applied Mathematics, 2007.

J Levraut, JP Ciebiera, S Chave, O Rabary, P Jambou, M Carles, and D Grimaud. Mild hyperlactatemia in stable septic patients is due to impaired lactate clearance rather than

overproduction. *American Journal of Respiratory and Critical Care Medicine*, 157:1021–1026, 1998.

D Lide. *CRC Handbook of Chemistry and Physics*. CRC Press, 2004.

Y Liu, YM Li, RF Tian, WP Liu, Z Fei, QF Long, XA Wang, and X Zhang. The expression and significance of HIF-1a and GLUT-3 in glioma. *Brain Research*, 1304:149–154, 2009.

JS Lowengrub, HB Frieboes, F Jin, YL Chuang, X Li, P Macklin, SM Wise, and V Cristini. Nonlinear modelling of cancer: bridging the gap between cells and tumours. *Nonlinearity*, 23:1–91, 2010.

F Lucien, K Brochu-Gaudreau, D Arsenault, K Harper, and CM Dubois. Hypoxia-induced invadopodia formation involves activation of NHE-1 by the p90 ribosomal S6 kinase (p90RSK). *PLOS One*, 6:e28851, 2011.

SY Lunt and MG Vander Heiden. Aerobic glycolysis: meeting the metabolic requirements of cell proliferation. *Annual Review of Cellular and Developmental Biology*, 27:441–464, 2011.

W Ma, HJ Sung, JY Park, S Matoba, and PM Hwang. A pivotal role for p53: balancing aerobic respiration and glycolysis. *Journal of Bioenergetics and Biomembranes*, 39:243–246, 2007.

K Måaseide and E Rofstad. Mathematical modelling of chronical hypoxia in tumours considering potential doubling time and hypoxic cell lifetime. *Radiotherapy and Oncology*, 54:171–177, 2000.

DJC MacKay. *Information Theory, Inference, and Learning Algorithms*. Cambridge University Press, 2003.

P Macklin and J Lowengrub. Nonlinear simulation of the effect of microenvironment on tumour growth. *Journal of Theoretical Biology*, 245:677–704, 2007.

PJ Magistretti. Neuron-glia metabolic coupling and plasticity. *Journal of Experimental Biology*, 209:2304–2311, 2006.

EA Maher, I Marin-Valencia, RM Bachoo, T Mashimo, J Raisanen, KJ Hatanpaa, A Jindal, FM Jeffrey, C Choi, C Madden, D Mathews, JM Pascual, BE Mickey, CR Malloy, and RJ DeBerardinis. Metabolism of U-13C glucose in human brain tumours in vivo. *NMR in Biomedicine*, 25:1234–1244, 2012.

D Majumdar, XH Peng, and DM Shin. The medicinal chemistry of theragnostics, multimodality imaging and applications of nanotechnology in cancer. *Current Topics in Medicinal Chemistry*, 10:1211–1226, 2010.

S Mangia, IA Simpson, SJ Vannucci, and A Carruthers. The in vivo neuron-to-astrocyte lactate shuttle in human brain: evidence from modelling of measured lactate levels during visual stimulation. *Journal of Neurochemistry*, 109:55–62, 2009.

JE Manning-Fox, D Meredith, and AP Halestrap. Characterisation of human monocarboxylate transporter 4 substantiates its role in lactic acid efflux from skeletal muscle. *Journal of Physiology*, 529:285–293, 2000.

NV Mantzaris, S Webb, and HG Othmer. Mathematical modelling of tumour-induced angiogenesis. *Journal of Mathematical Biology*, 49:111–187, 2004.

B Marchant, J Norbury, and HM Byrne. Biphasic behaviour in malignant invasion. *Mathematical Medicine and Biology*, 23:173–196, 2006.

S Marino, IB Hogue, CJ Ray, and DE Kirschner. A methodology for performing the global uncertainty and sensitivity analysis in systems biology. *Journal of Theoretical Biology*, 254:178–196, 2008.

GR Martin and RK Jain. Noninvasive measurement of interstitial pH profiles in normal and neoplastic tissue using fluorescence ratio imaging microscopy. *Cancer Research*, 54: 5670–5674, 1994.

NK Martin. Mathematical Modelling of Tumour Acidity: Buffer Therapy and Stromal Effects. *DPhil thesis, University of Oxford*, 2009.

NK Martin, EA Gaffney, RA Gatenby, and PK Maini. Tumour-stromal interactions in acid-mediated invasion: a mathematical model. *Journal of Theoretical Biology*, 267:461–470, 2010.

NK Martin, EA Gaffney, RA Gatenby, RJ Gillies, IF Robey, and PK Maini. A mathematical model of tumour and blood pHe regulation: the HCO3-/CO2 buffering system. *Mathematical Biosciences*, 230:1–11, 2011.

JH Marxsen, P Stengel, K Doege, P Heikkinen, T Jokilehto, T Wagner, W Jelkmann, P Jaakkola, and E Metzen. Hypoxia-inducible factor-1 (HIF-1) pomotes its degradation by induction of HIF-alpha-prolyl-4-hydroxylases. *Biochemical Journal*, 381:761–767, 2004.

S Mathupala, YH Ko, and PL Pedersen. The pivotal roles of mitochondria in cancer: Warburg and beyond and encouraging prospects for effective therapies. *Biochimica et Biophysica Acta*, 1797:1225–1230, 2010.

PC McDonald, JY Winum, CT Supuran, and S Dedhar. Recent developments in targeting carbonic anhydrase IX for cancer therapeutics. *Oncotarget*, 3:84–97, 2012.

DLS McElwain and LE Morris. Apoptosis as a volume loss mechanism in mathematical models of solid tumour growth. *Mathematical Biosciences*, 39:147–157, 1978.

DLS McElwain and PJ Ponzo. A mathematical model for the growth of a solid tumour with non-uniform oxygen consumption. *Mathematical Biosciences*, 35:267–279, 1977.

BS McEwen and LP Reagan. Glucose transporter expression in the central nervous system: relationship to synaptic function. *European Journal of Pharmacology*, 490:13–24, 2004.

JB McGillen, NK Martin, IF Robey, EA Gaffney, and PK Maini. Applications of mathematical analysis to tumour acidity modelling. *RIMS Kôkyûroku Bessatsu*, B31:31–59, 2012.

B Mendoza-Juez, A Martinéz-González, GF Calvo, and V Pérez-García. A mathematical model for the glucose-lactate metabolism of in vitro cancer cells. *Bulletin of Mathematical Biology*, 74:1125–1142, 2012.

LMF Merlo, JW Pepper, BJ Reid, and CC Maley. Cancer as an evolutionary and ecological process. *Nature Reviews Cancer*, 6:924–935, 2006.

M Meyerson, S Gabriel, and G Getz. Advances in understanding cancer genomes through second-generation sequencing. *Nature Reviews Genetics*, 11:685–696, 2010.

F Michor, Y Iwasa, and MA Nowak. Dynamics of cancer progression. *Nature Reviews Cancer*, 4:197–205, 2004.

GR Mirams, AG Fletcher, PK Maini, and HM Byrne. A theoretical investigation of the effect of proliferation and adhesion on monoclonal conversion in the colonic crypt. *Journal of Theoretical Biology*, 312:143–156, 2012.

M Morange. From the regulatory vision of cancer to the oncogene paradigm, 1975-1985. *Journal of the History of Biology*, 30:1–29, 1997.

R Moreno-Sánchez, S Rodrígo-Enríquez, A Marín-Hernández, and E Saavedra. Energy metabolism in tumour cells. *Federation of European Biochemical Societies Journal*, 274: 1393–1418, 2007.

W Mueller-Klieser. Method for the determination of oxygen consumption rates and diffusion coefficients in multicellular spheroids. *Biophysical Journal*, 46:343–348, 1984.

S Mukherjee. *The Emperor of All Maladies: A Biography of Cancer*. Fourth Estate, 2010.

JD Murray. *Mathematical Biology: I. An Introduction*. Interdisciplinary applied mathematics. Springer, 3rd edition, 2002.

D Neri and CT Supuran. Interfering with pH regulation in tumours as a therapeutic strategy. *Nature Reviews Drug Discovery*, 10:767–777, 2011.

KJ Newell and IF Tannock. Reduction of intracellular pH as a possible mechanism for killing cells in acidic regions of solid tumours: effects of carbonylcyanide-3-chlorophenylhydrazone. *Cancer Research*, 49:4477–4482, 1989.

ES Norris, JR King, and HM Byrne. Modelling the response of spatially structured tumours to chemotherapy: drug kinetics. *Mathematical and Computer Modelling*, 43:820–837, 2006.

PC Nowell. The clonal evolution of tumour cell populations. *Science*, 194:23–28, 1976.

JM Osborne, A Walter, SK Kershaw, GR Mirams, AG Fletcher, P Pathmanathan, D Gavaghan, OE Jensen, PK Maini, and HM Byrne. A hybrid approach to multi-scale modelling of cancer. *Philosophical Transactions of the Royal Society A*, 368:5013–5028, 2010.

KJ Painter and JA Sherratt. Modelling the movement of interacting cell populations. *Journal of Theoretical Biology*, 225:327–339, 2003.

KJ Painter, NJ Armstrong, and JA Sherratt. The impact of adhesion on cellular invasion processes in cancer and development. *Journal of Theoretical Biology*, 264:1057–1067, 2010.

F Pappenberger, I Iorgulescu, and KJ Beven. Sensitivity analysis based on regional splits and regression trees (SARS-RT). *Environmental Modelling and Software*, 21:976–990, 2006.

HJ Park, JC Lyons, T Ohtsubo, and CW Song. Acidic environment causes apoptosis by increasing caspase activity. *British Journal of Cancer*, 80:1892–1897, 1999.

SK Parks, J Chiche, and J Pouysségur. pH control mechanisms of tumour survival and growth. *Journal of Cellular Physiology*, 226:299–308, 2011.

SK Parks, J Chiche, and J Pouysségur. Disrupting proton dynamics and energy metabolism for cancer therapy. *Nature Reviews Cancer*, 13:611–623, 2013.

DW Parsons, S Jones, X Zhang, JCH Lin, RJ Leary, P Angenendt, P Mankoo, H Carter, IM Siu, GL Gallia, A Olivi, R McLendon, BA Rasheed, S Keir, T Nikolskaya, Y Nikolsky, DA Busam, H Tekleab, LA Diaz, J Hartigan, DR Smith, RL Strausberg, SKN Marie, SMO Shinjo, H Yan, GJ Riggins, DD Bigner, R Karchin, N Papadopoulos, G Parmigiani, B Vogelstein, VE Velculescu, and KW Kinzler. An integrated genomic analysis of human glioblastoma multiforme. *Science*, 321:1807–1812, 2008.

S Pavlides, D Whitaker-Menezes, R Castello-Cros, N Flomenberg, AK Witkiewicz, PG Frank, MC Casimiro, C Wang, P Fortina, S Addya, RG Pestell, UE Martinez-Outschoorn, F Sotgia, and MP Lisanti. The reverse Warburg effect: aerobic glycolysis in cancer associated flibroblasts and the tumour stroma. *Cell Cycle*, 8:3984–4001, 2009.

S Pavlides, A Tsirigos, I Vera, N Flomenberg, PG Frank, MC Casimiro, C Wang, RG Pestell, UE Martinez-Outschoorn, A Howell, F Sotgia, and MP Lisanti. Transciptional evidence for the 'Reverse Warburg Effect' in human breast cancer tumour stroma and metastasis: similarities with oxidative stress, inflammation, Alzheimer's disease, and 'Neuron-Glia Metabolic Coupling'. *Aging*, 2:185–199, 2010.

L Pellerin and PJ Magistretti. Neuroenergetics: calling upon astrocytes to satisfy hungry neurons. *The Neuroscientist*, 10:53–62, 2004.

L Pellerin, AK Bouzier-Sore, A Aubert, S Serres, M Merle, R Costalat, and PJ Magistretti. Activity-dependent regulation of energy metabolism by astrocytes: an update. *Glia*, 55: 1251–1262, 2007.

AJ Perumpanani, JA Sherratt, J Norbury, and HM Byrne. Biological inferences from a mathematical model for malignant invasion. *Invasion and Metastasis*, 16:209–221, 1996.

AJ Perumpanani, JA Sherratt, and J Norbury. Mathematical modelling of capsule formation and multinodularity in benign tumour growth. *Nonlinearity*, 10:1599–1614, 1997.

GJ Pettet, CP Please, MJ Tindall, and DLS McElwain. The migration of cells in multicell tumour spheroids. *Bulletin of Mathematical Biology*, 63:231–257, 2000.

T Pfeiffer, S Schuster, and S Bonhoeffer. Cooperation and competition in the evolution of ATP-producing pathways. *Science*, 292:504–507, 2001.

KJ Pienta, N McGregor, R Axelrod, and DE Axelrod. Ecological therapy for cancer: defining tumours using an ecosystem paradigm suggests new opportunities for novel cancer treatments. *Translational Oncology*, 1:158–164, 2008.

J Pouyssegur, C Sardet, A Franchi, G L'Allemain, and S Paris. A specific mutation abolishing Na+/H+ antiport activity in hamster fibroblasts precludes growth at neutral and acidic pH. *Proceedings of the National Academy of Sciences USA*, 81:4833–4837, 1984.

J Pouyssegur, F Dayan, and NM Mazure. Hypoxia signalling in cancer and approaches to enforce tumour regression. *Nature*, 441:437–443, 2006.

TD Prickett and Y Samuels. Molecular pathways: dysregulated glutamatergic signalling pathways in cancer. *Clinical Cancer Research*, 18:4240–4246, 2012.

JG Rajendran, DA Mankoff, and F O'Sullivan. Hypoxia and glucose metabolism in malignant tumours: evaluation by 18F fluoromisonidazole and 18F fluorodeoxyglucose positron emission tomography imaging. *Clincal Cancer Research*, 10:2245–2252, 2004.

IF Robey and NK Martin. Bicarbonate and dichloroacetate: evaluating pH altering therapies in a mouse model for metastatic breast cancer. *BMC Cancer*, 11:235–245, 2011.

IF Robey, BK Baggett, ND Kirkpatrick, DJ Roe, J Dosescu, BF Sloane, AI Hashim, DL Morse, N Raghunand, RA Gatenby, and RJ Gillies. Bicarbonate increases tumour pH and inhibits spontaneous metastases. *Cancer Research*, 69:2260–2268, 2009.

R Rockne, JK Rockhill, M Mrugala, AM Spence, I Kalet, K Hendrickson, A Lai, T Cloughesy, EC Alvord, and KR Swanson. Predicting the efficacy of radiotherapy in individual glioblastoma patients in vivo: a mathematical modelling approach. *Physics in Medicine and Biology*, 55:3271–3285, 2010.

S Rodríguez-Enríquez, PA Vital-González, FL Florez-Rodríquez, A Marín-Hernández, L Ruiz-Azuara, and R Moreno-Sánchez. Control of cellular proliferation by modulation of oxidative phosphorylation in human and rodent fast-growing tumour cells. *Toxicology and Applied Pharmacology*, 215:208–217, 2006.

EK Rofstad, B Mathiesen, K Kindem, and K Galappathi. Acidic extracellular pH promotes experimental metastasis of human melanoma cells in athymic nude mice. *Cancer Research*, 66:6699–6707, 2006.

A Roos and WF Boron. Intracellular pH. *Physiological Reviews*, 61:296–434, 1981.

T Roose, PA Netti, LL Munn, Y Boucher, and RK Jain. Solid stress generated by spheroid growth estimated using a linear poroelasticity model. *Microvascular Research*, 66:204–212, 2003.

T Roose, SJ Chapman, and PK Maini. Mathematical models of avascular tumour growth. *Society for Industrial and Applied Mathematics Review*, 49:179–208, 2007.

D Rotin, B Robinson, and IF Tannock. Influence of hypoxia and an acidic environment on the metabolism and viability of cultured cells: potential implications for cell death in tumours. *Cancer Research*, 46:2821–2826, 1986.

D Rotin, P Wan, S Grinstein, and IF Tannock. Cytotoxicity of compounds that interfere with the regulation of intracellular pH: a potential new class of anticancer drugs. *Cancer Research*, 47:1497–1504, 1987.

A Saltelli and P Annoni. How to avoid a perfunctory sensitivity analysis. *Environmental Modelling and Software*, 25:1508–1517, 2010.

A Saltelli, M Ratto, T Andres, F Campolongo, J Cariboni, D Gatelli, M Saisana, and S Tarantola. *Global Sensitivity Analysis*. John Wiley and Sons, 2008.

G Schaller and M Meyer-Hermann. Continuum versus discrete model: comparison for multicellular tumour spheroids. *Philosophical Transactions of the Royal Society A*, 364: 1443–1464, 2006.

WE Schiesser. *The Numerical Method of Lines: Integration of Partial Differential Equations*. Academic Press, 1st edition, 1991.

WE Schiesser and GW Griffiths. *A Compendium of Partial Differential Equation Models: Method of Lines Analysis With Matlab*. Cambridge University Press, 2009.

GL Semenza. HIF-1: upstream and downstream of cancer metabolism. *Current Opinion in Genetics and Development*, 20:97–106, 2010.

L Shampine and M Reichelt. The Matlab ODE suite. *SIAM Journal on Scientific Computing*, 18:1–22, 1997.

JA Sherratt. Cellular growth control and travelling waves of cancer. *SIAM Journal on Applied Mathematics*, 53:1713–1730, 1993.

JA Sherratt. Travelling wave solutions of a mathematical model for tumour encapsulation. *SIAM Journal on Applied Mathematics*, 60:392–407, 1999.

JA Sherratt. Wavefront propagation in a competition equation with a new motility term modelling contact inhibition between cell populations. *Proceedings of the Royal Society A*, 456:2365–2386, 2000.

JA Sherratt, SA Gourley, NJ Armstrong, and KJ Painter. Boundedness of solutions of a non-local reaction-diffusion model for adhesion in cell aggregation and cancer invasion. *European Journal of Applied Mathematics*, 20:123–144, 2009.

L Sherwood. *Human physiology: from cells to systems*. Brooks/Cole Publishing, 2007.

D Shibata. Heterogeneity and tumour history. *Science*, 336:304–305, 2012.

T Shlomi, T Benyamini, E Gottlieb, R Sharan, and E Ruppin. Genome-scale metabolic modeling elucidates the role of proliferative adaptation in causing the Warburg effect. *Public Library of Science Computational Biology*, 7:e1002018, 2011.

AS Silva, JA Yunes, RJ Gillies, and RA Gatenby. The potential role of systemic buffers in reducing intratumoural extracellular pH and acid-mediated invasion. *Cancer Research*, 69:2677–2684, 2009.

MJ Simpson, A Merrifield, KA Landman, and BD Hughes. Simulating invasion with cellular automata: connecting cell-scale and population-scale properties. *Physical Review E*, 76: 1–12, 2007.

K Smallbone, D Gavaghan, RA Gatenby, and PK Maini. The role of acidity in solid tumour growth and invasion. *Journal of Theoretical Biology*, 235:476–484, 2005.

GD Smith. *Numerical Solution of Partial Differential Equations: Finite Difference Methods*. Oxford University Press, 1985.

P Sonveaux, F Végran, T Schroeder, MC Wergin, J Verrax, ZN Rabbani, CJ de Saedeleer, KM Kennedy, C Diepart, BF Jordan, MJ Kelley, B Gallez, ML Wahl, O Feron, and MW Dewhirst. Targeting the lactate-fueled respiration selectively kills hypoxic tumour cells in mice. *Journal of Clinical Investigation*, 118:3930–3942, 2008.

P Sonveaux, T Copetti, CJ De Saedeleer, F Vegran, and J Verrax. Targeting the lactate transporter MCT1 in endothelial cells inhibits lactate-induced HIF-1 activation and tumour angiogenesis. *PLOS One*, 7:e33418, 2012.

SL Spencer, MJ Berryman, JAQ Garcia, and D Abbot. An ordinary differential equation model for the multistep transformation to cancer. *Journal of Theoretical Biology*, 231: 515–524, 2004.

AK Stewart, CE Kurschat, RD Vaughan-Jones, and SL Alper. Putative re-entrant loop 1 of AE2 transmembrane domain has a major role in acute regulation of anion exchange by pH. *Journal of Biological Chemistry*, 284:6126–6139, 2009.

MR Stratton, PJ Campbell, and PA Futreal. The cancer genome. *Nature*, 458:719–724, 2009.

KR Swanson, HLP Harpold, DL Peacock, R Rockne, C Pennington, L Kilbride, R Grant, JM Wardlaw, and EC Alvord. Velocity of radial expansion of contrast-enchancing gliomas and the effectiveness of radiotherapy in individual patients: a proof of principle. *Clinical Oncology*, 20:301–308, 2008.

P Swietach. *Personal communication*, 2011.

P Swietach, M Zaniboni, AK Stewart, A Rossini, KW Spitzer, and RD Vaughan-Jones. Modelling intracellular H+ ion diffusion. *Progress in Biophysics and Molecular Biology*, 83:69–100, 2003.

P Swietach, RD Vaughan-Jones, and A Harris. Regulation of tumour pH and the role of carbonic anhydrase 9. *Cancer and Metastasis Reviews*, 26:299–310, 2007.

P Swietach, S Wigfield, P Cobden, CT Supuran, AL Harris, and RD Vaughan-Jones. tumour-associated carbonic anhydrase 9 spatially coordinates intracellular pH in three-dimensional multicellular growths. *Journal of Biological Chemistry*, 283:20473–20483, 2008.

P Swietach, S Patiar, CT Supuran, AL Harris, and RD Vaughan-Jones. The role of carbonic anhydrase 9 in regulating extracellular and intracellular pH in three-dimensional tumour cell growths. *Journal of Biological Chemistry*, 284:20299–20310, 2009.

P Swietach, A Hulikova, RD Vaughan-Jones, and AL Harris. New insights into the physiological role of carbonic anhydrase IX in tumour pH regulation. *Oncogene*, 29:6509–6521, 2010.

M Terpstra, R Gruetter, WB High, M Mescher, L DelaBarre, M Merkle, and M Garwood. Lactate turnover in rat glioma measured by in vivo nuclear magnetic resonance spectroscopy. *Cancer Research*, 58:5083–5088, 1998.

IPM Tomlinson. Game-theory models of interactions between tumour cells. *European Journal of Cancer*, 33:1495–1500, 1997.

P Tracqui, GC Cruywagen, DE Woodward, GT Bartoo, EC Alvord, and JD Murray. A mathematical model of glioma growth: the effect of chemotherapy on spatio-temporal growth. *Cell Proliferation*, 28:17–31, 1995.

W van Saarloos. Front propagation into unstable states: marginal stability as a dynamical mechanism for velocity selection. *Physical Review A*, 37:211–229, 1988.

MG Vander Heiden, LC Cantley, and CB Thompson. Understanding the Warburg effect: the metabolic requirements of cell proliferation. *Science*, 324:1029–1033, 2009.

H Varmus, W Pao, K Politi, K Podsypanina, and YC Du. Oncogenes come of age. *Cold Spring Harbor Symposia in Quantitative Biology*, 70:1–9, 2005.

P Vaupel, O Thews, and M Hoeckel. Treatment resistance of solid tumours. *Medical Oncology*, 18:243–259, 2001.

R Venkatasubramanian, MA Henson, and NS Forbes. Incorporating energy metabolism into a growth model of multicellular tumour spheroids. *Journal of Theoretical Biology*, 242:440–453, 2006.

B Vogelstein, ER Fearon, SR Hamilton, SE Kern, AC Preisinger, M Leppert, AM Smits, and JL Bos. Genetic alterations during colorectal-tumour development. *New England Journal of Medicine*, 319:525–532, 1988.

P Voisin, V Bouchaud, M Merle, P Diolez, L Duffy, K Flint, JM Franconi, and AK Bouzier-Sore. Microglia in close vicinity of glioma cells: correlation between phenotype and metabolic alterations. *Frontiers in Neuroenergetics*, 2:131, 2010.

J Volpe. Genetic instability of cancer: why a metastatic tumour is unstable and a benign tumour is stable. *Cancer Genetics and Cytogenetics*, 34:125–134, 1988.

D Vriens, JA Disselhorst, WJG Oyen, LF de Geus-Oei, and EP Visser. Quantitative assessment of heterogeneity in tumour metabolism using FDG-PET. *International Journal of Radiation Oncology and Biological Physics*, 82:25–731, 2012.

S Walenta, J Doetsch, W Mueller-Klieser, and LA Kunz-Schughart. Metabolic imaging in multicellular spheroids of oncogene-transfected fibroblasts. *Journal of Histochemistry and Cytochemistry*, 48:509–522, 2000.

O Warburg. *The Metabolism of Tumours*. Arnold Constable London, 1930.

O Warburg. On the origin of cancer cells. *Science*, 123:309–314, 1956.

JP Ward and JR King. Mathematical modelling of the effects of mitotic inhibitors on avascular tumour growth. *Journal of Theoretical Medicine*, 1:287–311, 1999.

JP Ward and JR King. Mathematical modelling of drug transport in tumour multicell spheroids and monolayer cultures. *Mathematical Biosciences*, 181:177–207, 2003.

BA Webb, M Chimenti, MP Jacobson, and DL Barber. Dysregulated pH: a perfect storm for cancer progression. *Nature Reviews Cancer*, 11:671–677, 2011.

SD Webb, JA Sherratt, and RG Fish. Mathematical modelling of tumour acidity: regulation of intracellular pH. *Journal of Theoretical Biology*, 196:237–250, 1999a.

SD Webb, JA Sherratt, and RG Fish. Alterations in proteolytic activity at low pH and its association with invasion: a theoretical model. *Clinical and Experimental Metastasis*, 17: 397–407, 1999b.

SD Webb, JA Sherratt, and RG Fish. Mathematical modelling of tumour acidity: regulation of intracellular pH. *Journal of Theoretical Biology*, 196:237–250, 1999c.

SD Webb, MR Owen, HM Byrne, C Murdoch, and CE Lewis. Macrophage-based anti-cancer therapy: modelling different modes of tumour targeting. *Bulletin of Mathematical Biology*, 69:1747–1776, 2007.

LM Wein, JT Wu, AG Ianculescu, and RK Puri. A mathematical model of the impact of infused targeted cytotoxic agents on brain tumours: implications for detection, design, and delivery. *Cell Proliferation*, 35:343–361, 2002.

GM Whitesides. The origins and future of microfluidics. *Nature*, 442:368–373, 2006.

KJ Williams, BA Telfer, RE Airley, HP Peters, MR Sheridan, AJ van-der Kogel, AL Harris, and IJ Stratford. A protective role for HIF-1 in response to redox manipulation and glucose deprivation: implications for tumourigenesis. *Oncogene*, 21:282–290, 2002.

A Wincewicz, M Sulkowska, M Koda, and S Sulkowski. Clinicopathological significance and linkage of the distribution of HIF-1a and GLUT-1 in human primary colorectal cancer. *Pathology and Oncology Research*, 13:15–20, 2007.

J Wu, R Dhingra, M Gambhir, and JV Remais. Sensitivity analysis of infectious disease models: methods, advances and their application. *Journal of the Royal Society Interface*, 10:20121018, 2013.

M Yalom. *A History of the Breast*. New York: Alfred A. Knopf, 1997.

Z Zhang and S Nagrath. Microfluidics and cancer: are we there yet? *Biomedical Microdevices*, 15:595–609, 2013.

XL Zu and M Guppy. Cancer metabolism: facts, fantasy, and fiction. *Biochemical and Biophysical Research Communications*, 313:459–465, 2004.